

NORTHWESTERN UNIVERSITY

Probing and Functionalizing Emerging Two-Dimensional Materials at the Nanoscale

A DISSERTATION

SUBMITTED TO THE GRADUATE SCHOOL

IN PARTIAL FULLFILLMENT OF THE REQUIREMENTS

for the degree

DOCTOR OF PHILOSOPHY

Field of Applied Physics

By

Xiaolong Liu

EVANSTON, ILLINOIS

December 2018

© Copyright by Xiaolong Liu 2018

All Rights Reserved

Abstract

Probing and Functionalizing Emerging Two-Dimensional Materials at the Nanoscale

Xiaolong Liu

Two-dimensional (2D) materials and heterostructures have attracted significant attention for a variety of nanoelectronic and optoelectronic applications. At the atomically thin limit, the material characteristics and functionalities are dominated by surface chemistry and interface coupling. Therefore, methods for comprehensively characterizing and precisely controlling surfaces and interfaces are required to realize the full technological potential of 2D materials. In Chapter 1 of this thesis, I first introduce the surface and interface properties that govern the performance of 2D materials and review the experimental approaches that resolve surface and interface phenomena down to the atomic scale. I then experimentally explore the surface and interface characteristics of three emerging 2D materials and their heterostructures including black phosphorus (BP), transition metal dichalcogenides (e.g., MoS₂), and borophene (i.e., 2D boron). The characterization tools used span across a suite of surface science techniques, but primarily involve electron microscopy and scanning probe microscopy at the atomic/molecular scale.

In particular, an atomic-scale microscopic and spectroscopic study is first performed to characterize the thermal degradation of mechanically exfoliated 2D BP in Chapter 2. From *in situ* scanning/transmission electron microscopy, decomposition of 2D BP is observed to occur at ~400°C in vacuum, in contrast to the 550°C bulk BP sublimation temperature. Taking advantage of the chemical instability of BP and the high-spatial resolution of atomic force microscopy (AFM), I then demonstrated nanopatterning and layer-by-layer thinning of BP with conductive AFM

anodic oxidation, where the liquid-phase patterning byproduct is readily removed by water rinsing. An alternating current method is developed to enable direct nanopatterning and thinning on insulating substrates such as SiO₂/Si, leading to field-effect transistors with patterned channels showing significant improvements in current modulation by up to a factor of 50.

The research is further extended to MoS₂ monolayers grown via chemical vapor deposition on epitaxial graphene (EG) on SiC in Chapter 3, which are suitable for ultra-high vacuum (UHV) scanning tunneling microscopy (STM) and spectroscopy (STS) studies. After achieving rotationally commensurate growth of MoS₂, I interrogate point and line defects in monolayer MoS₂ at the atomic scale. As a result of rotational commensurability, a much lower total defect density is observed. In addition, grain boundaries are limited to mostly having 30° and 60° tilt angles with band gap reductions to ~0.8 eV and ~0.5 eV, respectively. By functionalizing such heterostructures with 2,7-dioctyl[1]benzothieno[3,2-b][1]benzothiophene (C₈-BTBT), the molecules are found to self-assemble well on MoS₂, forming a well-defined mixed-dimensional heterostructure with clean interfaces. The first C₈-BTBT layer on rotationally commensurate MoS₂/EG is found to be insensitive to structural defects and electronic perturbations from the underlying MoS₂.

In Chapter 4, the focus is shifted to an emerging 2D material - borophene. I start with atomic scale UHV STM/STS characterizations of borophene line defects corroborated by density functional theory calculations. Line defects in mixed-phase borophene are found to adopt structures that match the constituent units of the other phase and energetically favor spatially periodic self-assembly that gives rise to new borophene phases, ultimately blurring the distinction between borophene crystals and defects. Low temperature measurements further reveal subtle electronic features that are consistent with a charge density wave, which are modulated by line defects. Such borophene polymorphs are then imaged with carbon monoxide-functionalized non-

contact AFM (CO-AFM) and STM (CO-STM) probes revealing for the first time features that are consistent with boron-boron covalent bonds. CO-STM is identified as an equivalent and comparatively more accessible technique to unambiguously determine borophene structures. Upon deposition of an organic molecule perylene-3,4,9,10-tetracarboxylic dianhydride (PTCDA) on sub-monolayer borophene samples, lateral heterostructures spontaneously form with an electronically abrupt borophene/PTCDA interface. Covalent functionalization of borophene via molecular oxygen is also explored at the atomic scale, and an effective in situ passivation scheme involving Al_2O_3 capping layers is developed to protect borophene from ambient degradation for at least 3 months.

Finally, a brief summary and future outlook is given in Chapter 5. Under the background of ever-increasing interest in low-dimensional materials worldwide, this thesis is aimed to provide some fundamental understandings at the atomic/molecular level, and hopefully contribute to the effort of identifying new technological solutions for the pressing energy, environment, and health challenges we are facing.

Acknowledgements

My PhD journey won't be possible without support, advice, and inspiration from others. It is truly fortunate for me to have Prof. Mark C. Hersam as my PhD advisor. I am indebted to Mark for providing me with the opportunity of carrying out research in his research group with great flexibility and ample financial support. I treasure the fruitful discussions and brainstorming we had in the past five years. Moreover, I appreciate his patience, understanding, trust, and inspiration throughout my PhD life, especially when I was confused, disappointed and defeated. I'm also glad that I've been influenced by him working vigorously and efficiently, and thinking optimistically. I also want to take the opportunity to acknowledge Prof. Michael J. Bedzyk and Prof. Nathaniel Stern for serving as my thesis committee members, and the Ryan Fellowship offered by the International Institute of Technology at Northwestern University.

I want to thank my research mentors, Dr. EunKyung Cho and Dr. Joshua D. Wood, who practically led me to the world of ultrahigh-vacuum (UHV) scanning tunneling microscopy in my first year. They tolerated my naïve and endless questions, and trained me with great patience on complicated experimental instruments. Josh has been highly energetic and set an exemplary standard of efficient multitasking. I also appreciate past senior lab members in the UHV lab including Dr. Chun-Hong Sham, Dr. Vincent Demers-Carpentier, Dr. Christopher Ryder, Dr. Andrew J. Mannix, and Dr. Itama Jade Balla. Especially, Jade has been not only a great collaborator on chemical vapor deposition, but also a genuine friend in and out of research labs. I believe his straightforwardness and confidence has influenced everyone around him. I want to thank current junior students and postdocs in the UHV lab including Dr. Shaowei Li, Dr. Qiucheng

Li, Matthew S. Rahn and Eden B. Aklile. They are the new blood to this challenging yet fascinating research field. Their help with instrument maintenance and modification is greatly appreciated.

I feel proud to have worked with Hersam group members outside the UHV lab as well. Dr. Jian Zhu, Dr. Kan-Sheng Chen, Dr. Joohoon Kang, and Hadallia Bergeron have been not only great colleagues but also friends in life. In the lab, Dr. Kan-Sheng Chen provided great assistance and patience into training me as a proficient user of our atomic force microscope. Dr. Jian Zhu and Dr. Joohoon Kang has been quite knowledgeable and helpful regarding research of colloidal systems. Together with Jade, Hadallia has devoted tremendous amount of effort into ex situ sample growth and optimization. It would have been a lot harder for me if they were not there. I also thank other group members including Dr. Junmo Kang, Dr. Vinod Sangwan, Spencer A. Wells and David Lam for successful collaborations.

Research collaborations outside the Hersam group are a key component of my PhD study. I have been fortunate to collaborate with Prof. Michael J. Bedzyk and his student Dr. Gavin P. Campbell on structural determination of heterostructures using synchrotron X-rays. I also thank Prof. Erik Luijten and Dr. Zonghui Wei for the opportunity to work together on selective self-assembly of organics using molecular dynamics. Recent collaborations with Prof. Boris I. Yakobson, Dr. Zhuhua Zhang, and Luqing Wang from Rice University on topics of borophene have been fruitful, and it has been a great pleasure to conduct research in such a highly collaborative environment. Finally, I thank staff members including Dr. Jinsong Wu and Dr. Xinqi Chen of NUANCE, the cryogenic facility manager Stephen Jacobson, and Reggie Lee and Alex Villatoro from the Tech loading dock for their assistance and hard work.

Last but not least, I am most grateful to my family in China. My easy choice of studying abroad was a hard and possibly heart-breaking choice to them. While they were proud and excited

talking to people, I knew how much they wished I could stay - after all, I'm the only child. I thank my grandparents and my mother for raising me up, for all their supports, encouragement and unconditional love. I would not be who I am now without them. I also thank my father for his love, albeit late. Finally, I want to thank my then-girlfriend now-wife Zonghui Wei, who went through the 9-year undergraduate and PhD grind with me together. Regardless of happiness or sadness, she probably understands me most, and supports me with all she has. I feel rich with so many wonderful people at the end of this special journey.

List of Abbreviations

1L	Monolayer
2D	Two-dimensional
2L	Second layer
AC	Alternating current
AFM	Atomic force microscopy
ALD	Atomic layer deposition
ARPES	Angle-resolved photoemission spectroscopy
BP	Black phosphorus
C8-BTBT	2,7-dioctyl[1]benzothieno[3,2-b][1]benzothiophene
CAFM	Conductive atomic force microscopy
CBM	Conduction band minimum
CO	Carbon monoxide
CO-AFM	Carbon monoxide functionalized atomic force microscopy
CO-STM	Carbon monoxide functionalized scanning tunneling microscopy
CTE	Coefficient of thermal expansion
CVD	Chemical vapor deposition
DC	Direct current
DCT	Dry contact transfer
DFT	Density functional theory
DGU	Density gradient ultracentrifugation

DOS	Density of states
EDS	Energy-dispersive X-ray spectroscopy
EELS	Electron energy loss spectroscopy
EFM	Electrostatic force microscopy
EG	Epitaxial graphene
FET	Field effect transistor
GB	Grain boundary
GNR	Graphene nanoribbon
HAADF	High-angle annular dark field
HH	Hollow hexagon
IETS	Inelastic electron tunneling spectroscopy
IR	Infrared
KPFM	Kelvin-probe force microscopy
LFM	Lateral force microscopy
LJ	Lennard-Jones
MBE	Molecular beam epitaxy
MD	Molecular dynamics
MFM	Magnetic force microscopy
nc-AFM	Non-contact atomic force microscopy
NDR	Negative differential resistance
PC-AFM	Photoconductive atomic force microscopy
PL	Photoluminescence

PLD	Pulsed laser deposition
PTCDA	Perylene-3,4,9,10-tetracarboxylic dianhydride
SBH	Schottky barrier height
SHG	Second harmonic generation
SNOM	Scanning near-field optical microscopy
SPP	Surface plasmon polariton
SQUID	Superconducting quantum interference device
STEM	Scanning transmission electron microscopy
SThM	Scanning tunneling hydrogen microscopy
STM	Scanning tunneling microscopy
STS	Scanning tunneling spectroscopy
SUM	Scanning ultrasound microscopy
TDTR	Time-domain thermal reflectance
TEM	Transmission electron microscopy
TFT	Thin film transistor
TMDC	Transition metal dichalcogenide
Tof-SIMS	Time-of-flight secondary ion mass spectrometry
UFM	Ultrasonic force microscopy
UHV	Ultrahigh vacuum
VBM	Valence band maximum
XPS	X-ray photoelectron spectroscopy
XTEM	Cross-sectional transmission electron microscopy

For my maternal grandfather

Table of Contents

Abstract	3
Acknowledgements.....	6
List of Abbreviations	9
List of Figures.....	16
Chapter 1: Introduction	30
1.1. Two-Dimensional Materials and Heterostructures.....	30
1.2. Surface and Interface Phenomena	31
1.2.1. Geometrical Distortions at Surfaces.....	32
1.2.2. Interfacial Coupling.....	35
1.2.3. Surface and Interface Electronic States.....	38
1.3. Synthesis and Preparation of 2D Materials.....	39
1.3.1. Top-Down Approaches	39
1.3.1.1. Exfoliation in Dry Environments	39
1.3.1.2. Solution-Phase Exfoliation.....	41
1.3.2. Bottom-Up Growth	42
1.3.2.1. Chemical Vapor Deposition.....	42
1.3.2.2. Atomic Layer Deposition.....	42
1.3.2.3. Physical Vapor Deposition.....	43
1.3.2.4. Solution-Phase Growth	44
1.4. Characterizing Surfaces and Interfaces.....	44

1.4.1. Atomic Resolution Microscopy Methods.....	14
1.4.2. Spatially Resolved Property Measurements	45
1.4.2.1. Characterizing Mechanical and Thermal Properties.....	52
1.4.2.2. Characterizing Electronic Properties	54
1.4.2.3. Characterizing Subsurface Properties.....	58
1.4.3. Characterization with Optical Techniques	60
Chapter 2: Few-Layer BP: Thermal Stability and Layer-by-Layer Thinning.....	65
2.1 Introduction to BP: a Highly Anisotropic Elemental 2D Material.....	65
2.1.1. Structural Anisotropy	66
2.1.2. Optical Anisotropy.....	68
2.1.3. Vibrational Anisotropy.....	71
2.1.4. Electronic and Electrical Anisotropy	73
2.1.5. Thermal and Mechanical Anisotropy.....	75
2.2 Thermal Stability of BP	78
2.3 Patterning and Thinning of BP via Scanning Probe Nanolithography.....	85
Chapter 3: MoS ₂ Monolayers on EG: Defect Engineering and Chemical Functionalization	99
3.1 Introduction: TMDC Monolayers and Heterostructures with Graphene.....	99
3.2 Point and Line defects in Rotationally Commensurate MoS ₂ /EG Heterostructures .	102
3.3 Mixed-Dimensional Heterostructures of C8-BTBT with MoS ₂ /EG	115
Chapter 4: Borophene: Characterization, Functionalization, and Passivation	126
4.1 Introduction to Borophene	126
4.2 Defects in Borophene	127

	15
4.3 CO-Functionalized Scanning Probe Microscopy of Borophene Structures	141
4.4 Non-Covalent Functionalizations of Borophene: a Borophene-Organic Lateral Heterostructure.....	153
4.5 Borophene Oxidation and Effective Passivation.....	163
Chapter 5: Summary and Future Outlook.....	170
5.1 Summary.....	126
5.2 Future Outlook	126
5.2.1 BP and Bulk van der Waals Materials	171
5.2.2 Synthetic 2D Materials.....	173
5.2.3 Research Directions Enabled by New Capabilities.....	174
References	176
Vita.....	202

List of Figures

Figure 1.1. (a) Surface relaxation. (b) Surface reconstruction. (c) Interfacial strain. (d) Interfacial charge transfer. (e) Interfacial magnetic coupling. (f) Termination-dependent interfaces.

.....32

Figure 1.2. (a) Scotch-tape micromechanical exfoliation. (b) Micromechanically exfoliated graphene flake. Reproduced from ref.¹ Copyright 2004, AAAS. (c) Liquid-phase exfoliation by sonication. (d) Liquid-phase exfoliated BP. Reproduced from ref.¹⁹ Copyright 2015, American Chemical Society. (e) Direct growth via CVD. (f) CVD-grown monolayer MoS₂. Reproduced from ref.⁵⁴ Copyright 2013, Nature Publishing Group. (g) Direct growth via MBE. (h) MBE-grown monolayer NbSe₂. Reproduced from ref.¹⁰² Copyright 2016, Nature Publishing Group.

.....40

Figure 1.3. (a) Schematic of STM with hydrogen functionalization, and electron tunneling process. (b) Examples showing: (I) STM imaging of PTCDA molecules without chemical bonding details. Reproduced from ref.¹⁵² Copyright 2010, American Chemical Society. (II) Scanning tunneling hydrogen microscopy (STHM) of a PTCDA molecule. Reproduced from ref.¹⁵³ Copyright 2008, IOP Publishing. (III) dI/dV map of a PTCDA molecule with a CO-functionalized tip. Reproduced from ref.¹⁵⁴ Copyright 2014, American Physical Society. (IV) d^2I/dV^2 map of a CoPC molecule with a CO functionalized tip. Reproduced from ref.¹⁵⁵ Copyright 2014, AAAS. (c) Schematic of AFM with CO molecule functionalization, and the van der Waals interaction between the tip and sample. The red and green regions correspond to repulsive and attractive mode AFM, respectively. (d) (I) Atomic resolution Δf image of graphene. Reproduced from ref.¹⁵⁶ Copyright 2012, American Chemical Society. (II) Δf image of 8-hq molecule cluster showing chemical bonds with a CO-functionalized tip. Reproduced from ref.¹⁵⁷ Copyright 2013, AAAS. (III) Current and force images revealing angular symmetry of chemical bonds. Reproduced from ref.¹⁵⁸ Copyright 2012, AAAS. (e) Schematic of STEM and TEM. STEM utilizes a focused electron beam (purple), whereas TEM uses a collimated beam (pink). (f): (I) Cross-sectional TEM image of few-layer BP revealing a buckled structure. Reproduced from ref.¹⁵⁹ Copyright 2015, American Vacuum Society. (II) Atomic resolution TEM image of solution-processed BP and (III) the corresponding SAED pattern. Reproduced from ref.¹⁰⁹ Copyright 2016, National Academy of Sciences.

.....46

Figure 1.4. (a) AFM topography images of exfoliated graphene revealing periodic structures along different directions. (b) Lateral force microscopy image revealing 3 regions with different frictional properties. (c) Transverse force image of the same domain with enhanced contrast of frictional differences. (a-c): Reproduced from ref.¹⁷⁹ Copyright 2016, Nature Publishing Group. (d) Schematic of EFM measurement (top), EFM phase image (middle), and calculated potential profiles across a MoS₂/pentacene to pentacene interface. Reproduced from ref.¹⁹⁰ Copyright 2016, American Chemical Society. (e) A KPFM image of a WS₂-MoS₂ lateral heterostructure and corresponding band alignment. Reproduced from ref.¹⁹¹ Copyright 2015, American Chemical Society.

.....55

Figure 1.5. (a) AFM topography image of a polymer film covering a trench-structured substrate showing uniform coating over the silicon nitride surface. (b) The corresponding SUM image showing buried voids in the coated polymer. (a,b): Reproduced from ref.²²⁰ Copyright 2005, AAAS. (c) AFM topography image of a 15 nm thick MoS₂ flake exfoliated onto a ridge-structured substrate. (d) The corresponding UFM image showing subsurface ridge structures. (c,d): Reproduced from ref.²²⁴ Copyright 2017, IOP Publishing.

.....59

Figure 1.6. (a) Schematic illustration of the SHG process. (b) Structures of monolayer MoS₂ and hBN with broken inversion symmetry. (c) 2-layers and 4-layers of MoS₂ and hBN have minimum SHG intensities. Reproduced from ref.²²⁸ Copyright 2013, American Chemical Society. (d) SHG intensity for two stacked MoS₂ monolayers with roughly inverted (top) and aligned (bottom) geometries. (a,d): Reproduced from ref.²²⁷ Copyright 2014, American Chemical Society. (e) PL map of a WS₂-MoS₂ lateral heterostructure with constant optical pump at the center (red spot). (f) PL spectra measured at the blue and red spots in (e). (e,f): Reproduced from ref.²³¹ Copyright 2017, Nature Publishing Group. (g) Schematic of a nano-IR setup. (h) Image of IR scattering amplitude of a graphene/hBN heterostructure. (i) AFM topography showing the boundary between moiré patterned and graphene regions. (g-i): Reproduced from ref.²³² Copyright 2015, Nature Publishing Group. (j) Schematic of TA measurements of pentacene on MoS₂. (k) Dynamics of the MoS₂ B-exciton from three samples. (j,k): Reproduced from ref.⁷² Copyright 2017, American Chemical Society.

.....61

Figure 2.1. Structural anisotropy of BP. (a) Schematic of BP crystal structure. Distinct bond lengths and bond angles are labeled. (b) High-resolution STM and TEM images of BP. The STM image reveals zigzag rows along the zigzag direction, whereas the TEM image shows a rectangular lattice. Reproduced from ref.²⁵⁸ Copyright 2016, Wiley-VCH. (c) TEM image of BP and (d) the corresponding indexed SAED pattern. The crystallographic orientation can be determined in both cases. (c,d) Reproduced from ref.²⁵⁹ Copyright 2015, Nature Publishing Group.

.....67

Figure 2.2. Optical anisotropy of BP. (a) Band structure of BP along the armchair (Z-L) and zigzag (Z-T') directions determined by ARPES measurements. Reproduced from ref.²⁵² Copyright 2014, Nature Publishing Group. (b) Simulated ground state exciton wavefunction for monolayer BP. The wavefunction is more delocalized along the armchair direction (x-axis). (c) Polarization-dependent PL spectra of BP, where the x-axis is along the armchair direction. Greatly enhanced PL is observed when excitation and detection are parallel and along the armchair direction. (b,c) Reproduced from ref.²⁶⁷ Copyright 2015, Nature Publishing Group. (d) Photocurrent maps of a BP photodetector with different light polarization angles, showing angle-dependent photocurrent. Reproduced from ref.²⁶⁶ Copyright 2015, Nature Publishing Group.

.....69

Figure 2.3. Vibrational anisotropy of BP. (a) Six Raman-active modes of BP. Only A_g¹, A_g², and B_{2g} are active when the incident laser is perpendicular to the BP plane. Reproduced from ref.²⁷⁴ Copyright 2015, American Chemical Society. (b) Observations of angle-dependent Raman

intensities, where each mode has intensity varying periodically with the change of relative angle between the BP crystal and laser polarization. Reproduced from ref.²⁷³ Copyright 2015, Wiley-VCH.

.....71

Figure 2.4. Electrical anisotropy of BP. (a) Temperature-dependent mobilities of bulk BP along the **a** (zigzag), **b** (out-of-plane), and **c** (armchair) directions. Mobility along the armchair direction is uniformly highest, followed by mobilities along the zigzag and the out-of-plane directions. Reproduced from ref.²⁵⁴ Copyright 1983, The Physical Society of Japan. (b) Correlated IR transmission and conductivity on the same BP flake. The maximum transmission and conductivity occur in the same direction (armchair). Reproduced from ref.²⁵³ Copyright 2014, Nature Publishing Group. (c) Band structure of potassium-doped BP at the transition from semiconductor to metal. The dispersion along the armchair direction is linear, whereas the dispersion along the zigzag direction is quadratic. Reproduced from ref.²⁸² Copyright 2015, AAAS. (d) Biaxial strain dependence of monolayer BP mobilities along the x (zigzag) and y (armchair) directions. Increasing strain decreases mobility along the armchair direction and increases mobility along the zigzag direction. Reproduced from ref.²⁸³ Copyright 2014, American Chemical Society.

.....74

Figure 2.5. Thermal and mechanical anisotropy of BP. (a) Thickness-dependent and direction-dependent thermal conductivity of BP. The thermal conductivity along the zigzag direction is higher than that of the armchair direction for all thicknesses. (b) Temperature-dependent Raman shift of BP Raman modes. (a,b) Reproduced from ref.²⁸⁵ Copyright 2015, Nature Publishing Group. (c). Left column: measured multimode resonance of a circular BP mechanical resonator. Middle column: simulated anisotropic resonator. Right column: simulated isotropic resonator. Reproduced from ref.²⁸⁷ Copyright 2016, American Chemical Society.

.....76

Figure 2.6. TEM images of exfoliated BP and *in situ* heating of BP. a) Low-magnification TEM bright field image of a BP flake. Scale bar is 2 μm . *Inset*: SAED pattern of the flake. Scale bar is 5 nm^{-1} . (b) High-magnification TEM bright field image of BP showing lattice fringes. Scale bar is 2 nm. (c-g) TEM bright field images (false colored) of a thin BP flake after (c) introduction to the TEM and heated at (d) 200 $^{\circ}\text{C}$, (e) 300 $^{\circ}\text{C}$, (f) 400 $^{\circ}\text{C}$, and (g) 500 $^{\circ}\text{C}$, respectively. All heating times are 20 min long. Scale bars are 200 nm. *Insets*: SAED patterns for each heating stage. Scale bars are 5 nm^{-1} . Irregular patterns and amorphization occur past 400 $^{\circ}\text{C}$. EDS spectra of BP flake (h) before and (i) after 400 $^{\circ}\text{C}$ *in situ* heating. In both cases, a P K α peak is apparent.

.....79

Figure 2.7. Dynamics of *in situ* BP sublimation. Low-magnification TEM images for annealing conditions of: (a) unannealed, (b) 20 min at 200 $^{\circ}\text{C}$, (c) 20 min at 300 $^{\circ}\text{C}$, (d) 5 min at 400 $^{\circ}\text{C}$, (e) 8 min at 400 $^{\circ}\text{C}$, (f) 12 min at 400 $^{\circ}\text{C}$, (g) 20 min at 400 $^{\circ}\text{C}$, (h) 20 min at 500 $^{\circ}\text{C}$, respectively. When the flake is heated at 400 $^{\circ}\text{C}$ for 5 min, the flake begins to decompose, as denoted by the yellow and red arrows in (d-f). The degradation continues until 500 $^{\circ}\text{C}$, after which a thin skeleton remains. Scale bars are 2 μm .

.....80

Figure 2.8. Formation of eye-shaped cracks in BP during sublimation. (a-c) Zoomed-in image of the flake in Fig. 2.7, heated for 5 min, 8 min, and 12 min at 400 °C, respectively. Eye-shaped cracks (yellow) form and grow. The blue arrow indicates the propagation direction. (d) SAED pattern of the flake at 300 °C, showing the [001] crack propagation direction. (e, f) Temperature-induced increase in BP lattice parameters a and c . (g) In-plane lattice schematic for BP. (h-j) Snapshots from a BP sublimation model, describing the formation of eye-shaped cracks along the [001] direction (blue arrow).

.....82

Figure 2.9. *In situ* STEM heating of BP and corresponding EELS spectra. STEM transmitted electron images of BP after (a) introduction to the STEM and heated at (b) 200 °C for 20 min, (c) 300 °C for 20 min, (d) 400 °C for 2 min, (e) 400 °C for 10 min, (f) 400 °C for 20 min, (g) 500 °C for 20 min. Consistent with *in situ* TEM heating, BP sublimation begins at ~400 °C. (h, i) STEM TE image of BP exposed to ambient for 5 min and 24 hr after *in situ* heating, respectively. Scale bars are 2 μm . (j) P L edge and derivative EELS spectra during each stage of *in situ* heating. P L_{2,3} ELNES line shapes qualitatively change after 400 °C.

.....84

Figure 2.10. Demonstration of DC CAFM patterning of BP crystals. (a) High crystal quality of BP source material is confirmed by UHV STM ($V_{\text{sample}} = 0.2 \text{ V}$, $I_{\text{tunneling}} = 60 \text{ pA}$) and TEM imaging. (b) Schematic illustration of the patterning setup. (c-e) Tapping mode AFM images of checkerboard patterns made at different sample biases. (f) Bias voltage used for patterning the logo of Northwestern University, and the corresponding (g) tapping mode AFM and (h) contact mode AFM images of the as-patterned sample.

.....87

Figure 2.11. Chemical characterization of patterning byproducts. (a,b) Tapping mode AFM images of patterned letter ‘N’ (a) before and (b) after water rinsing. (c) Dark-field optical image (left) and tapping mode AFM image (right) of an as-patterned checkerboard pattern. (d) ToF-SIMS spectrum, and (e) peak mappings of the checkerboard pattern. (f) Raman spectra taken at patterned regions with increasing amount of oxide. Inset: optical images of the patterns where the Raman spectra were taken as indicated by the black, blue, and red dots.

.....89

Figure 2.12. DC patterning of micromechanically exfoliated BP flakes on n^+ -Si substrates. (a) Contact mode AFM images of arrays of patterned dots at different sample bias, and (b) the corresponding tapping mode AFM images. (c) An example of monolayer patterning of the initials ‘BP’. (d) Successive patterning on a BP flake at the same location results in deeper etching.

.....91

Figure 2.13. AC patterning of BP on dielectric substrates. (a) Schematic illustration of the patterning setup. (b) Optical image of a BP flake directly patterned on 300 nm Si/SiO₂. (c) Contact mode AFM images of the flake before and after patterning. (d) Patterning with increasing voltage amplitude and constant frequency (1 MHz). (e) Patterning with increasing frequency and constant

voltage amplitude (1.8 V). (f) Schematic, optical microscopy image, and AFM image of BP FETs fabricated with AC patterned BP (between electrodes A and B) and pristine BP (between electrodes B and C) on 300 nm Si/SiO₂. (g) Transfer curves of the BP FETs shown in (f). The linear-scale plot shows a moderate decrease in on-state current, and the logarithmic-scale plot reveals a significant increase in current on-off ratio from 200 to 10⁴ following CAFM patterning.

.....93

Figure 2.14. Extraction of contact resistance from I - V relationship. The conductive AFM tip is in contact with a BP flake on n⁺-doped Si wafer while varying the applied sample bias. From the resulting I - V curve, the contact resistance is estimated to be $\sim 2 \times 10^{11} \Omega$.

.....94

Figure 2.15. Raman maps of patterned BP flakes. (a) Optical microscope image of an AC patterned BP flake on 300 nm SiO₂ after water rinsing. The white dashed square indicates the thinned region. (b) Tapping mode AFM image of the yellow dashed square region in (a). (c) Height profiles along the black (top) and blue (bottom) dashed lines in (b), indicating an initial flake thickness of 14.6 nm and a thinning thickness of 5.4 nm (~ 11 layers). (d) Raman spectra taken at the patterned (blue dot in (b)) and the unpatterned (red dot in (b)) regions, showing nearly identical line shapes. (e-g) Raman intensity maps of the BP A_g^1 , B_{2g} , and A_g^2 modes of the patterned flake in (b). (h-j) Full width at half maximum (FWHM) maps of the BP A_g^1 , B_{2g} , and A_g^2 modes of the patterned flake in (b). No detectable change (e.g., broadening) is observed, implying high crystal quality of the patterned region. (k) Raman map of the integrated area ratio of A_g^1 to A_g^2 of the BP Raman modes. The ratios are mostly above 0.5 with no contrast between the patterned and pristine regions. Since defective BP would have a lower ratio below 0.3, it can be concluded that CAFM patterning introduces minimal defects to the remaining BP crystal.³¹⁶

.....95

Figure 2.16. XTEM images of patterned BP. (a) XTEM image of the Pt/Au/BP/Si structure. Pt and Au are coated to protect BP from damage. Inset: AFM image of as-patterned BP on Si (~ 4 nm thinner in the patterned square). (b) XTEM image of the boundary between patterned and pristine BP regions. (c) XTEM image of the pristine BP region. The BP lattice is present under an amorphous surface layer of ~ 3.7 nm. (d) XTEM image of the patterned BP region showing a similar amorphous layer of ~ 3.9 nm above the crystalline BP lattice. These results shows that the BP crystallinity is preserved after CAFM patterning and water rinsing.

.....97

Figure 3.1. Rotationally commensurate van der Waals epitaxy of MoS₂ on EG. (a) Schematic of GIWAXS measurement. k_i : incident wave vector, k_f : scattering wave vector, α : incident angle, β : out-of-plane angle, 2θ : in-plane angle, ϕ : sample rotation angle, ν : detector rotation angle. (b) Q_{xy} 2D reciprocal space map of MoS₂/EG projected from $Q_z = 0.08 \text{ \AA}^{-1}$ to 0.12 \AA^{-1} by synchrotron GIWAXS. The \mathbf{b}^* reciprocal space vectors are indicated by arrows. (c) Real-space model of the

MoS₂/EG heterostructure with MoS₂ lattice aligned with that of EG. (d) Projected first order peaks of MoS₂ and SiC onto ϕ showing sharp distributions. (e) Referring to (b), in-plane scattered intensity along Q_y direction at Q_x = 0. The determined real-space lattice constants of MoS₂, EG, and SiC are $3.16 \pm 0.01 \text{ \AA}$, $2.46 \pm 0.01 \text{ \AA}$, and $3.07 \pm 0.01 \text{ \AA}$, respectively.

.....102

Figure 3.2. High crystal quality CVD-grown MoS₂ on EG. (a) AFM height image of predominantly monolayer MoS₂ domains on EG with aligned crystal orientations. (b) Raman spectrum of MoS₂ with E_{2g}¹ and A_{1g} modes separated by 20.6 cm⁻¹. (c) Current and differential tunneling conductance spectra of monolayer MoS₂ on EG showing a band gap of 2 eV. (d) Moiré patterns from the MoS₂/EG heterostructure probed at different scanning conditions.

.....103

Figure 3.3. Schematic illustration of the formation of Moiré patterns. The observed Moiré pattern ($V_{\text{sample}} = -0.6 \text{ V}$, $I_{\text{tunneling}} = 3 \text{ nA}$) in the STM image of (a) can be explained by stacking MoS₂ (yellow) and graphene (black) lattices together with the same lattice orientation shown in the schematic in (b).

.....105

Figure 3.4. Point defects in monolayer MoS₂. (a) An STM topography image showing 4 types of point defects as indicated by the green, yellow, red, and white arrows. $V_{\text{sample}} = -1 \text{ V}$, $I_{\text{tunneling}} = 800 \text{ pA}$. (b-d) Atomic-scale imaging of representative point defects with an additional type-5 defect indicated by the blue arrow in (d). $V_{\text{sample}} = -1 \text{ V}$, $I_{\text{tunneling}} = 800 \text{ pA}$. (e-g) Bias-dependent images of type-1 and type-2 defects. $I_{\text{tunneling}} = 800 \text{ pA}$.

.....107

Figure 3.5. 30° and 60° GBs for rotationally commensurate monolayer MoS₂ on EG. (a,c) AFM height images of 30° and 60° GBs with the GB regions emphasized in the insets, respectively. The angles between the intersecting edges for the two types of GBs are 90° and 120°, respectively. (b,d) Schematics and STM topography images of 30° and 60° GBs. The GBs are indicated by black arrows in the STM images. $V_{\text{sample}} = -1 \text{ V}$, $I_{\text{tunneling}} = 50 \text{ pA}$.

.....108

Figure 3.6. Atomic and electronic properties of 30° GBs. (a) An atomically resolved STM topography image of a 30° GB with the contrast adjusted by height median matching. The zigzag directions of the top and bottom grains are indicated by the green and blue arrows, respectively. The GB direction is indicated by the black arrow, which is rotated 45° from the zigzag direction of the top grain. $V_{\text{sample}} = -0.6 \text{ V}$, $I_{\text{tunneling}} = 5.2 \text{ nA}$. (b) Top: a zoomed-in STM image of the GB region marked by the rectangle in (a). Bottom: a structural model for the 30° GB with the green, blue, and black arrows corresponding to the zigzag directions of the top and bottom grains and the GB direction, respectively. (c). A series of STS spectra taken across a 30° GB with tip positions marked by the colored dots in the inset. The STS spectra show band gap narrowing across the GB. Adjacent points are separated by 5 Å.

.....110

Figure 3.7. Band profiles across (a) 30° and (b) 60° GBs based on the series of dI/dV spectra across 30° and 60° GBs shown. The Fermi level is indicated by the white dashed line, which shows that the band gap narrowing results from the rise of the valence band maximum. For both GBs, the typical decay length of such electronic disturbances is ~2 nm in each direction from the GB. Although the GBs are narrow in real space (a few atomic sites wide), these longer range electronic effects will be reflected in constant current STM images and lead to the GBs appearing wider than expected in STM. It is worth noting that the extraction of band edges are based on individual STS spectra, and not the apparent boundaries of the high density of states (DOS) regions, since the initial rise of dI/dV curves at band edges does not contribute to high contrast in these two-dimensional plots. The red regions are saturated dI/dV signals due to the high DOS at GBs.

.....111

Figure 3.8. Bias-dependent images of MoS₂ GBs. (a-e) As the sample bias is increased from a negative to a positive value, the apparent height of the 30° GB in decreases. This effect is due to the high dI/dV value in the negative bias range at the GB, which effectively lifts the tip during constant current scanning as it approaches GBs with negative sample bias. (f) Zoomed-in image of the region marked by the rectangle in (c). At this bias, the GB shows more structural details and closely matches the proposed model, which is partially superimposed. (g) Large-scale STM images of an MoS₂ GB at different sample biases. The line profiles across the GB at different biases are shown on the right side, demonstrating the aforementioned behavior of decreasing GB apparent height with increasing bias.

.....112

Figure 3.9. Atomic and electronic properties of 60° GBs. (a) An atomically resolved STM topography image of a 60° GB. The zigzag directions of the top and bottom grains are indicated by the green and blue arrows, respectively. The GB direction is indicated by the black arrow, which is 19° rotated from the zigzag direction of the bottom grain. $V_{\text{sample}} = -0.8$ V, $I_{\text{tunneling}} = 50$ pA. (b) Top: a zoomed-in STM image of the GB region marked by the rectangle in (a). A fast Fourier transform was applied to this image to better emphasize the superstructure of the GB edge. Bottom: a structural model for the 60° GB with the green, blue, and black arrows corresponding to the zigzag directions of the top and bottom grains and the GB direction, respectively. (c). A series of STS spectra taken across a 60° GB with tip positions marked by the colored dots in the inset. The STS spectra show band gap narrowing across the GB. Adjacent points are separated by 5 Å.

.....114

Figure 3.10. (a) Structure of the C8-BTBT molecule and schematic of the C8-BTBT/MoS₂/graphene mixed-dimensional heterostructure. (b) AFM height and (c) phase image of sub-monolayer C8-BTBT deposited on MoS₂/EG. (d) AFM height image of an area with bilayers of C8-BTBT. (e) Extracted height profiles from the corresponding traces shown in d. (f) STM image of the MoS₂/EG boundary covered by monolayer C8-BTBT. Inset: extracted height profile measured along the green line.

.....116

Figure 3.11. (a) AFM height and (b) phase images of C₈-BTBT deposited on MoS₂/EG. The red arrows indicate the fuzzy boundaries of the depressed regions (i.e., exposed EG). Such fuzziness is likely from the moving molecules caused by the scanning AFM tip. On the other hand, other step edges such as the MoS₂ (green arrow) and graphene (blue arrows) step edges covered uniformly by C₈-BTBT remain abrupt. (c) AFM height image of an area with multiple layers of C₈-BTBT. The red arrows indicate triangular MoS₂ domains where multi-layer C₈-BTBT doesn't grow onto.

.....118

Figure 3.12. (a) STM images of self-assembled 1L C₈-BTBT on EG and (b) MoS₂, respectively. (c,d) STM images of two chiral structures of 1L C₈-BTBT and their schematics on MoS₂. (e) 1L C₈-BTBT self-assembles continuously over point defects (indicated by arrows) in the underlying MoS₂ and (f) EG.

.....119

Figure 3.13. (a) STM image of a pristine monolayer MoS₂ surface showing the presence of protruded (blue arrow) and depressed (white arrows) point defects. (b) STM image of a pristine EG surface showing not only the atomic lattices and the $6\sqrt{3}$ reconstruction, but also the presence of protruded point defects (blue arrow). (c) STM images of 1L C₈-BTBT covered MoS₂ and (d) EG, where the molecular self-assembly is not perturbed by the underlying point defects (white and blue arrows). (e) 1L C₈-BTBT continuously covers the step edge (white arrow) of graphene and point defects (blue arrow).

.....121

Figure 3.14. (a) Distribution of α defined by the relative acute angle between the edge of a MoS₂ domain and the stripe orientation of 1L C₈-BTBT (red lines). (b) Schematic illustration of the orientation of 1L C₈-BTBT on MoS₂. (c-e) STM images of 30°, 60°, and 21.1° GBs of MoS₂ covered by 1L C₈-BTBT and schematic illustrations, respectively. In d, the layer-numbers of the MoS₂ are labeled. Inset in e: a zoomed-in STM image of the interface region.

.....122

Figure 3.15. (a) STM image of 1L C₈-BTBT on EG with 60° rotations between different domains. (b) A pristine defect free region of EG showing both the honeycomb graphene lattice and the larger scale $6\sqrt{3}$ reconstruction. (c) Left: STM image of 1L C₈-BTBT on EG. Right: The Fourier transform of the image on the left shows not only spots corresponding to the ordered molecular stripes (blue circles), but also points corresponding to the $6\sqrt{3}$ reconstruction (yellow circles) that are rotated by 16.6° from the molecular stripes. By choosing only the points corresponding to the $6\sqrt{3}$ reconstruction, the filtered image (bottom right) indeed confirms the $6\sqrt{3}$ reconstruction. (d) Given the fact that the lattice of graphene is rotated by 30° with respect to that of the $6\sqrt{3}$ reconstruction, the orientation of the 1L C₈-BTBT on EG could be determined as schematically shown.

.....123

Figure 3.16. (a) STS spectra of 1L C8-BTBT on EG and MoS₂ (measured at 6 positions on each region). (b) Differential conductance from a series of STS spectra taken across a 60° GB of MoS₂ covered by 1L C8-BTBT (inset).

.....124

Figure 4.1. Growth of pristine borophene on Ag(111) thin films. (a,b) Large-scale (a) STM topography and (b) STS map of borophene grown on Ag(111). (c,d) Atomic-resolution STM images of (c) $\nu_{1/6}$ and (d) $\nu_{1/5}$ borophene sheets with inter-row spacings of 0.54 ± 0.03 nm and 0.45 ± 0.02 nm, respectively. (e) Six STS spectra taken on different positions of the $\nu_{1/6}$ and $\nu_{1/5}$ borophene sheets showing metallic behavior. (f,g) *In situ* XPS spectra of the (f) B 1s and (g) O 1s core levels indicating pristine borophene growth. STM bias voltages: (a,b) $V_s = -1$ V, (c) $V_s = -0.35$ V, (d) $V_s = -1.2$ V.

.....128

Figure 4.2. Temperature dependence of borophene growth in the range of 350°C - 500°C. (a-g) Representative STM images of borophene grown at different temperatures. The regions corresponding to the $\nu_{1/6}$ and $\nu_{1/5}$ phases are labeled with red and blue rectangles, respectively. Outside this temperature window, growth yields primarily 3D boron particles. (h) Areal percentage of $\nu_{1/5}$ phase borophene as function of growth temperature. This plot reveals that low temperature growth (e.g., 350°C) favors the $\nu_{1/6}$ phase while high temperature growth (e.g., 500°C) favors the $\nu_{1/5}$ phase, with a gradual transition over this 150°C window.

.....129

Figure 4.3. Models used in DFT calculations of $\nu_{1/6}$ (left) and $\nu_{1/5}$ (right) borophene sheets (red balls) on Ag(111) surface (white balls). The blue boxes in both images represent the structural supercells used in the calculations. The two sheets have nearly identical chemical potentials as provided below each panel, supporting the co-existence of the two structures experimentally.

.....130

Figure 4.4. Presence of line defects in borophene. (a,b) (a) Derivative image of the (b) STM topography of borophene islands revealing the presence of parallel line defects. The $\nu_{1/6}$ and $\nu_{1/5}$ borophene regions are labeled, and their respective line defects are indicated by the blue and red arrow heads. (c) Schematic depiction of the distribution of line defects in $\nu_{1/6}$ (red) and $\nu_{1/5}$ (blue) borophene domains based on the image in (a). The line defects are colored oppositely. (d) STS map of the same region, showing minimal electronic contrast within the borophene sheets. STM bias voltages: (b,d) $V_s = -0.65$ V.

.....131

Figure 4.5. DFT-calculated density of states (DOS) of the $\nu_{1/5}$ and $\nu_{1/6}$ line defects in (a) $\nu_{1/6}$ and (b) $\nu_{1/5}$ borophene sheets, respectively. The contributions from the $\nu_{1/5}$ and $\nu_{1/6}$ structures are colored blue and red, respectively. The DOS contributed by the line defect is shown blue in (a) and red in (b), both rescaled by 10 times for clarity; the DOS in grey contains the projection of substrate. The total density of states (black) suggests both line defects are metallic.

.....132

Figure 4.6. Atomic structures of borophene line defects. (a,b) STM images of line defects in $\nu_{1/6}$ and $\nu_{1/5}$ borophene sheets indicated by blue and red arrow heads, respectively. (c) Regions of the blue, gray, and green boxes in (a,b), corresponding to the boundary of $\nu_{1/6}$ and $\nu_{1/5}$ sheets, line defect in $\nu_{1/6}$, and line defect in $\nu_{1/5}$, respectively. (d) Schematic representations of the three regions in (c). (e) Relaxed structure models (top) and zoomed-in structures (bottom) corresponding to the three regions in (c). The $\nu_{1/6}$ and $\nu_{1/5}$ structures are shaded red and blue, respectively. (f) Cross-sectional views of the relaxed structures in (e), showing no out-of-plane buckling. (g) Simulated STM images based on the structures in (e), showing close agreement with the experimental data. STM bias voltages: (a) $V_s = -0.38$ V, (b) $V_s = -0.91$ V.

.....133

Figure 4.7. Self-assembly of borophene line defects and formation of new phases. (a) Schematic models of perpendicularly interfacing $\nu_{1/6}$ and $\nu_{1/5}$ sheets (shaded red and blue, respectively), where the boron rows in each sheet are perpendicular to each other. The large lattice mismatch causes high interfacial energies. (b) The structures of $\nu_{1/6}$ and $\nu_{1/5}$ rows (top), and an example of forming a new boron phase by assembling $\nu_{1/6}$ and $\nu_{1/5}$ rows (bottom). (c) A borophene sheet containing domains with different periodic assemblies of $\nu_{1/6}$ and $\nu_{1/5}$ rows, including two new phases of borophene ($\nu_{7/36}$ and $\nu_{4/21}$ sheets). STM bias voltage: $V_s = -1.3$ V.

.....134

Figure 4.8. The relative change of total energy at 728 K of different line defect configurations. A $\nu_{1/6}$ row in a $\nu_{1/5}$ sheet is shifted from the periodic configuration (A) to the right resulting in aperiodic configurations (B, C, and D). The increase of energy indicates that spatially periodic line defects are the most energetically favorable.

.....135

Figure 4.9. Electronic modulations at low temperature. (a) STS spectra of $\nu_{1/6}$ and $\nu_{1/5}$ phase borophene measured at ~ 4 K, revealing a gap feature at the Fermi level. (b) STM topography and (c) STS map of a $\nu_{1/5}$ borophene domain. The inset in (b) shows the borophene orientation. (d,e) Fourier transforms of the images in (b,c). The yellow and blue arrow heads indicate points corresponding to the inter-row spacing and the 3×2 superstructure, respectively. (f) STM topography and (g) STS map of a mixed-phase borophene domain. (h) Direct comparison of the $\nu_{1/5}$ borophene regions enclosed by the yellow and green rectangles in (f) and (g). The blue arrow heads indicate the apparent 3×2 superstructure. STM bias voltages: (b) $V_s = 50$ mV, (f) $V_s = -40$ mV, (h) $V_s = -40$ mV.

.....136

Figure 4.10. Origin of the superstructure. (a), 100 STS spectra taken across the region shown in the STM topography along the green line. Periodic modulations of the topography and local density of states (LDOS) in regions of pure $\nu_{1/5}$ phase borophene are indicated by the blue arrow heads. The straight and parallel patterns across the -0.15 V to 0.15 V bias range indicate that the superstructure periodicity does not change with energy. (b-d) STM topography images of $\nu_{1/5}$ phase borophene domains that are free of defects and far away from material boundaries at different sample biases. (e-g) The corresponding Fourier transforms of the images in (b-d). Since the

periodicity of the superstructure remain the same at different sample biases, the periodicity is independent of energy.

.....137

Figure 4.11. DFT calculations of the Fermi surfaces of $\nu_{1/5}$ phase borophene at doping levels of (a) 0 eV, (b) 0.2 eV, and (c) 1.0 eV. The inset in (a) denotes the crystal orientation. The blue and red lines are Fermi surface contours of different electronic bands, while the light-purple thick lines indicate the location of approximate nesting. The purple arrows indicate the Fermi surface nesting vector. The Brillouin zone is marked by the gray lines. The linear-motif structure of $\nu_{1/5}$ phase borophene results in the anisotropic Brillouin zone and a dog-bone, nearly-rectangular Fermi contour. With increasing doping level (known to occur due to electron transfer from Ag), the quasi-1D characteristic of its Fermi contour becomes more obvious. The two segments of the Fermi surface that are connected by the Fermi surface nesting vector $\mathbf{q} \approx 2/3\mathbf{b}_y$ also increase. The direction and especially the size of this vector are consistent with the experimentally observed superstructure in the y direction with a periodicity of 3 boron rows.

.....139

Figure 4.12. Low temperature STM/STS characterization of $\nu_{4/21}$ -phase borophene. (a) STM topography, (b) STS map, and (c) calculated LDOS map of $\nu_{4/21}$ phase borophene. The 3×2 superstructure is no longer present. Instead, the $\nu_{1/5}$ rows appear darker and the $\nu_{1/6}$ rows appear brighter in the STS map, corroborated by the calculated LDOS map.

.....140

Figure 4.13. Imaging $\nu_{1/5}$ phase borophene with bare and functionalized probes. (a) Bare-tip STM image of intermixed $\nu_{1/5}$ (colored blue) and $\nu_{1/6}$ (colored red) phase borophene. (b) A neighboring Ag(111) surface, where the angle between the HH rows of borophene (horizontal) in a and the Ag atomic chains is 30° as expected. (c) Schematic illustration of the rotational orientation of $\nu_{1/5}$ and $\nu_{1/6}$ phase borophene on Ag(111). The arrows mark the unit cells of the HH lattices in each phase. (d) Bare-tip STM image of $\nu_{1/5}$ phase borophene. (e) Inelastic electron tunneling spectroscopy on borophene with a CO-functionalized tip. (f) CO-AFM image of $\nu_{1/5}$ phase borophene. (g) Simulated CO-AFM image of $\nu_{1/5}$ phase borophene with overlaid atomic structure. (h) CO-STM and (i) dynamic CO-STM image of $\nu_{1/5}$ phase borophene. The red arrows in f, h, and i denote the unit cells corresponding to the HH lattice. $V_s = -10$ mV in a, 20 mV in b, 100 mV in d, -7 mV in h, and 15 mV in i.

.....142

Figure 4.14. Milder imaging conditions with dynamic CO-STM. (a) A typical STM image of $\nu_{1/5}$ phase borophene with a bare metal tip (W). (b) A series of CO-STM images of the same region with increasing tunneling current, where the HH lattice is more clearly resolved with high tunneling current. (c) Dynamic CO-STM image of the same region (~ 1 nm tip oscillation). While the HH lattice is clearly resolved, the imaging condition compared to (b) is much milder due to the fact that the highest tunneling current in the dynamic mode is much higher than the average tunneling current. As a result, the CO-stability on the tip apex is enhanced.

.....145

Figure 4.15. Imaging $\nu_{1/6}$ - 30° phase borophene structures with bare and functionalized probes. Bare-tip STM images of (a), a $\nu_{1/6}$ - 30° phase borophene domain and (b), a neighboring $\nu_{1/5}$ phase borophene, where the HH rows in each phase are perpendicular (yellow arrows). (c) Schematic of $\nu_{1/6}$ - 30° phase borophene. (d) Bare-tip STM image of a polycrystalline $\nu_{1/6}$ - 30° phase borophene with multiple 60° GBs (yellow arrows). (e) Bare-tip, (f) CO-AFM, (g) simulated CO-AFM, and (h) CO-STM images of the $\nu_{1/6}$ - 30° phase borophene. The atomic structure is overlaid in g. (i) Bare-tip, (j) CO-AFM, (k) simulated CO-AFM, and (l) CO-STM images of a 60° GB of $\nu_{1/6}$ - 30° phase borophene. The atomic structure is overlaid in k. $V_s = -3$ mV in a, 4 mV in b, -34 mV in d, 9 mV in e, 4 mV in h, -34 mV in i, and 4 mV in l.

.....146

Figure. 4.16. Additional simulated CO-AFM images. (a,b) Schematics and simulated CO-AFM images of (a) the $\nu_{1/6}$ - 30° phase borophene and (b) the triangular lattice (the brighter pink lines indicate upward buckling). Clearly, the simulated image of the triangular lattice significantly deviates from experimental observation.

.....147

Figure 4.17. Resolving $\nu_{1/5}$ - 30° phase borophene and its intermixing with the $\nu_{1/6}$ - 30° phase. (a) Schematic of $\nu_{1/5}$ - 30° phase borophene. (b) Bare-tip, and (c) CO-STM images of an undulated $\nu_{1/5}$ - 30° phase borophene. The yellow circles in c indicate the staggered HH pattern. (d) Schematic of the undulations resulting from a lattice mismatch between borophene and Ag(111). (e) CO-STM image of the phase boundary between a $\nu_{1/6}$ - 30° (left) and a $\nu_{1/5}$ - 30° phase borophene. (f-i) CO-STM images of $\nu_{1/5}$ - 30° -structured line defects in $\nu_{1/6}$ - 30° phase borophene with different widths. The yellow circles denote the staggered arrangement of the HH patterns, and the structure schematics are given in the bottom row. $V_s = -3$ mV in b and c, -7 mV in e and f, -1 mV in g, 4 mV in h, and -7 mV in i.

.....148

Figure 4.18. Imaging rotationally incommensurate phases of borophene with functionalized probes. (a) Derivative image of bare-tip STM topography of a $\nu_{1/5}$ (left) and $\nu_{1/5}$ - 6° (right) phase borophene domains. The insets are the zoomed-in images in the red and green squares. (b) CO-STM image of the $\nu_{1/5}$ - 6° phase borophene. (c) Schematic of rotationally incommensurate borophene phases, where α denotes the angle by which the sheet is rotated from $\nu_{1/5}$ phase borophene. (d) CO-AFM image of the $\nu_{1/5}$ - 6° phase borophene with overlaid atomic structure. (e) CO-STM image of a $\nu_{1/5}$ - 22° phase borophene with self-assembled $\nu_{1/6}$ - 22° -structured line defects. (f) Qualitative phase diagram of borophene growth with respect to temperature. $V_s = 190$ mV in a, -2 mV in b, and 22 mV in e.

.....149

Figure 4.19. Additional images of $\nu_{1/5}$ - 22° , $\nu_{4/21}$ - 22° , and $\nu_{1/5}$ - 9° phase borophene. (a) Large-scale derivative image of bare-tip STM topography of a $\nu_{1/5}$ - 22° phase borophene domain with a $\nu_{4/21}$ - 22° phase on the right. Since the HH row direction is $\sim 52^\circ$ rotated from the Ag atomic chain direction (yellow arrows), the rotation angle α with respect to $\nu_{1/5}$ is thus 22° . The inset shows the zoomed-in image of the region in the red square. (b) Zoom-in derivative image of bare-tip STM topography of the $\nu_{4/21}$ - 22° domain shown in (a). The yellow arrow heads indicate positions of the

periodic $v_{1/6}$ - 22° -structured line defects in the $v_{1/5}$ - 22° phase borophene, forming equivalently the $v_{4/21}$ - 22° phase. (c) Large-scale derivative image of bare-tip STM topography of a $v_{1/5}$ - 9° phase borophene neighboring a $v_{1/5}$ phase borophene. The inset shows the zoomed-in image of the region in the orange square. While the HH rows of the $v_{1/5}$ phase borophene is perpendicular (or 30° rotated) to the Ag atomic chains, the angle between the HH rows of the $v_{1/5}$ - 9° phase borophene and the Ag atomic chains is $\sim 81^\circ$ (yellow arrows). Therefore, the phase is 9° rotated from the $v_{1/5}$ phase and thus denoted as $v_{1/5}$ - 9° . $V_s = 15$ mV in a, 10 mV in b and c.

.....151

Figure 4.20. Borophene/PTCDA lateral heterostructure. (a) Large-scale STM image of a borophene/PTCDA lateral heterostructure and the cross-sectional profile along the white dashed line ($V_s = -1.7$ V, $I_t = 90$ pA). Borophene to PTCDA step edges, Ag to PTCDA step edges, and Ag atomic step edges under PTCDA and borophene are indicated by the yellow, gray, green, and blue arrows, respectively. Inset: PTCDA molecule structure. (b) Schematic of a borophene/PTCDA lateral heterostructure. (c) Unit cell of the PTCDA herringbone structure. (d) STM image of a borophene/PTCDA lateral heterostructure with the green, yellow, and blue boxes indicating regions of PTCDA, borophene, and Ag, respectively ($V_s = -1.1$ V, $I_t = 90$ pA). (e to g) STM images of the square regions indicated in (d). The pair of yellow and blue arrows indicate the lattice orientations of borophene and Ag(111) ((e): $V_s = -0.45$ V, $I_t = 140$ pA, (f): $V_s = -1.1$ V, $I_t = 500$ pA, (g): $V_s = -70$ mV, $I_t = 6.1$ nA).

.....155

Fig. 4.21. Molecular dynamics simulation results. (a) $\Delta G(z)$, $\Delta H(z)$, $T\Delta S(z)$ as a function of center-of-mass distance z to the homogeneous substrate of a single PTCDA molecule with $\Delta H_{\text{ads}} = 10k_B T$. (b) ΔG_{ads} and probability ratio of finding a molecule beyond and within a threshold $z_0 = 5.635$ Å from the substrate, as a function of ΔH_{ads} . (c) Surface coverage as a function of ΔH_{ads} . Inset: simulation snapshots of PTCDA adsorption and self-assembly on homogeneous Ag(111) substrates at different ΔH_{ads} . (d) Self-assembled structure of PTCDA on heterogeneous borophene/Ag(111) substrates with $\Delta H_{\text{ads,B}} = 10k_B T$, $16k_B T$, $18k_B T$, and $22k_B T$.

.....158

Figure 4.22. Spectroscopic properties of the borophene/PTCDA lateral heterostructure. (a) *In situ* XPS spectra of the B 1s core-level, and (b) C 1s core-level before and after the formation of the borophene/PTCDA lateral heterostructure. (c) Differential tunneling conductance spectra of Ag(111), borophene, and PTCDA. (d) STS map of a borophene/PTCDA lateral heterostructure overlaid on a three-dimensionally rendered STM topography image ($V_s = -1$ V, $I_t = 90$ pA). (e) Spatially resolved STS spectra across the interfaces of borophene/Ag, and (f) borophene/PTCDA. The vertical black lines in (e) and (f) indicate the positions of the Ag surface state feature and the LUMO+1 orbital of PTCDA far from the borophene/Ag and borophene/PTCDA interfaces, respectively.

.....161

Figure. 4.23. (a,b) STM and STS images of pristine submonolayer borophene. (c) *In situ* XPS spectra of pristine borophene and borophene exposed to ambient for 1 min and 5 min. (d) *In situ* XPS spectra of borophene exposed to increasing amount of molecular oxygen.

Figure. 4.24. (a-g) STM images of $\nu_{1/5}$ phase borophene. (h) STM image of borophene with well-defined particles. (i) A series of STS taken across pristine and oxidized borophene edges, presented as heatmaps.

.....165

Figure 4.25. STM image of oxidized $\nu_{1/5}$ phase borophene after annealing at 500°C for >30 min. The presence of the particles indicate that they are chemically bonded to borophene.

.....166

Figure. 4.26. (a,b) Ambient AFM images of borophene encapsulated with 1.3 nm and 3.7 nm alumina. (c,d) Corresponding AFM phases images of (a,b), respectively. (e,f) B1s XPS spectra of 1.3 nm and 3.7 nm alumina encapsulated borophene.

.....167

Figure. 4.27. (a-d) XPS spectra of Al2p, O1s, Mo3d, and Ag3d core levels, respectively.

.....168

Figure. 4.28. Ambient AFM images and optical microscopy image of alumina encapsulated borophene over a large substrate.

.....169

Chapter 1: Introduction

This chapter is based partially on the following publication:

X. Liu, and M. C. Hersam, Interface Characterization and Control of 2D Materials and Heterostructures, *Advanced Materials*, **2018**, DOI: 10.1002/adma.201801586.

1.1. Two-Dimensional Materials and Heterostructures

Two-dimensional (2D) materials, a class of atomically thin materials pioneered by Geim and Novoselov following their study of the exotic physical properties of graphene in 2004,^{1,2} present unique opportunities for a range of fundamental studies and applied technologies. While strict 2D lattices were historically believed to be unstable due to presumed thermal fluctuations that destroy long-range order,³⁻⁶ the isolation of graphene demonstrated that atomically thin materials could exist even with minimal interaction with supporting substrates. More recently, the existence criteria for low-dimensional materials have been revisited,⁷ with anharmonic coupling between bending and stretching modes providing a means for stabilizing 2D lattices with 3D ripples.^{8,9} Nevertheless, while it is now widely accepted that 2D materials can exist in isolation, the vast majority of experimental studies and applications require 2D materials to be directly interfaced with neighboring materials. Since 2D materials possess exceptionally high surface area to volume ratios, the resulting interfaces with substrates, surface functionalization, and encapsulation layers play a significant if not dominant role in determining properties.

After more than a decade of research efforts spurred by graphene, the arena of 2D materials is now populated with superconductors (e.g., NbSe₂¹⁰), metals (e.g., borophene^{11,12} and NbTe₂^{13,14}), semimetals (e.g., graphene^{15,16}), semiconductors (e.g., black phosphorus (BP)¹⁷⁻¹⁹ and MoS₂^{20,21}), and insulators (e.g., hexagonal BN²² and Bi₂Se₃²³). Including graphene, most of the 2D materials

are integral parts of bulk layered van der Waals crystals. In addition, recent work has demonstrated synthetic 2D materials with atomic lattices that do not resemble their bulk counterparts including borophene,^{11,12,24,25} silicene,²⁶⁻²⁸ germanene,²⁹ and stanene.^{30,31} Geometrically, the atomically thin nature of 2D materials offers high mechanical flexibility and optical transparency, opportunities for building functional heterostructures, and minimal dielectric screening, which are ideal platforms for wearable electronics, sensors, displays, and related technologies. Fundamentally, 2D materials enable the study of a range of quantum mechanical phenomena and phase transitions at the atomically thin limit. Examples include the transition from indirect to direct bandgap of MoS₂ as the material is thinned to the monolayer scale,²¹ layer-dependent bandgap energy of phosphorene,³² massless charge carriers in graphene,³³ and structural transformations of GaN at the few-layer limit.³⁴

Given the increasing research interest and rapid advances in the field of 2D materials and heterostructures, this chapter will present an overview of common surface of interface phenomena that govern the properties of 2D materials and heterostructures, as well as common material preparation and characterization techniques.

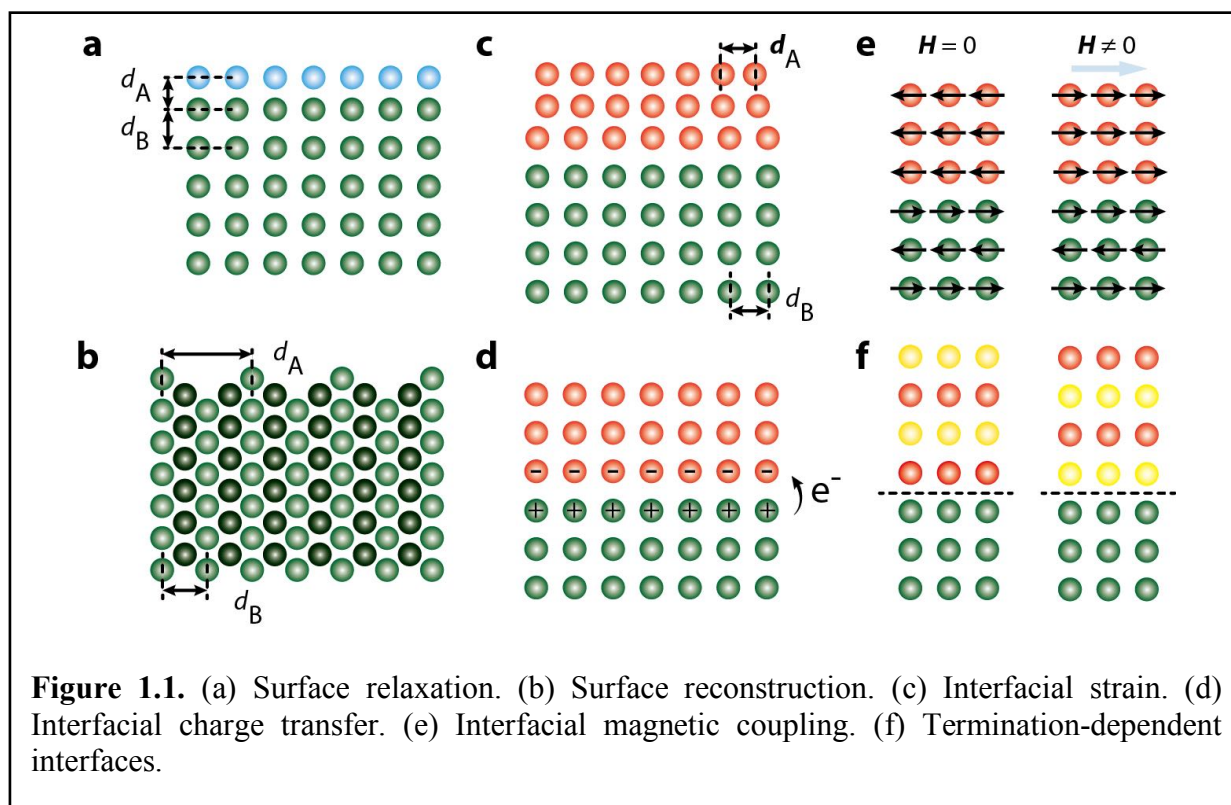
1.2. Surface and Interface Phenomena

Decades of work in surface science have repeatedly confirmed that the properties of surfaces deviate from those of the bulk. As the dimensions of objects move to the nanoscale, the surface area to volume ratio increases significantly with atomically thin materials being the extreme case where all atoms are at the surface. Therefore, the study of 2D materials can benefit from a careful consideration of lessons learned from prior surface science studies. Towards this

end, this section introduces common surface and interface phenomena observed in conventional bulk materials and how they manifest themselves in the 2D limit.

1.2.1. Geometrical Distortions at Surfaces

Since atoms in crystals are interacting and collectively respond to changes, the discontinuity of a crystal lattice at a surface often leads to the contraction of the surface layer into the bulk due to the absence of atoms pulling on the other side. This surface relaxation phenomenon is depicted in **Fig. 1.1a**, where the lattice spacing at the surface (d_A) becomes smaller than that in the bulk (d_B). Finnis and Heine provided insight into this phenomenon with pairwise interactions and perturbation theory.^{35,36} Energetically, the crystal lowers the total energy by allowing the surface atoms to relax. The kinetic energy of electrons are also lowered if the electron distribution becomes smoother, resulting in electrons rearranging themselves to minimize the corrugation of



electron density at the surface, which in turn displaces the top layer of atoms toward the bulk.³⁷ However, it should be noted that the decrease of the spacing between the first and second atomic layers is not ubiquitous for all materials. For example, the surfaces of some metals exhibit anomalous outward surface relaxation including Be (0001)³⁸ and Pt(111).³⁹ More generally, a few atomic layers near the surface take part in the surface relaxation, with oscillatory expansion and contraction of interlayer gaps typically leading to energy minimization.⁴⁰⁻⁴³ Surface atoms can also displace laterally to further lower the surface energy, resulting in surface reconstruction. Surfaces with low atomic density and high surface energy (e.g., the (110) surface compared to the (111) surface of face centered cubic metals) have a greater chance of surface reconstruction. **Fig. 1.1b** schematically shows the cross-sectional view of a missing-row reconstruction on the (110) surface of a transition metal, where the lateral periodicity at the reconstructed surface (d_A) is twice as large as the bulk (d_B). Since dangling bonds are reactive and one dangling bond per atom leads to metallic behavior, the surfaces of semiconductors tend to be semiconducting or insulating by eliminating dangling bonds through surface reconstruction.

Surface relaxation and reconstruction, or more generally, surface structural distortions driven by energy minimization have significant implications for 2D materials and 2D heterostructures since any geometrical distortion changes the details of the 2D atomic structure. For example, the Jahn-Teller distortion has been widely used to explain spontaneous symmetry breaking of molecular systems when spatially degenerate electronic ground states exist in the undistorted structure. While graphene is mostly flat, pseudo-Jahn-Teller distortions have been invoked to understand the formation of highly puckered 2D materials including black and blue phosphorene, silicene, and germanene,⁴⁴⁻⁴⁶ where the electronic states are nondegenerate but possess small splitting and strong vibronic coupling.⁴⁷ On the other hand, the larger gaps between

the ground state and higher states in graphene suppress the instability towards distortion.⁴⁵ In principle, 2D materials can be manipulated through the promotion or suppression of the pseudo-Jahn-Teller distortion, which in turn offers control over the surface and interface characteristics. Although not yet experimentally realized, theoretical proposals exist along these lines including the transition of silicene and graphitic carbon nitride monolayers from puckered to flat structures via Li⁴⁶ and Be doping,⁴⁸ respectively.

Another example of how geometrical relaxations influence the structure and properties of 2D materials is shape relaxation.⁴⁹⁻⁵¹ While the conventional Wulff construction based on boundary energy minimization implies size-independent crystal shapes and straight or convex crystal edges,⁵² both synthesized 3D thin films⁴⁹ and 2D materials (e.g., monolayer MoS₂^{53,54}) have shown deviations from the Wulff construction including concave and size-dependent crystal shapes. By considering long-range interactions such as elasticity, these experimental deviations can be reproduced theoretically.⁴⁹ Specifically, in smaller crystals, boundary energy dominates and the Wulff construction applies. However, as crystals grow larger, elastic energy becomes non-negligible, resulting in concave shapes since elastic relaxation lowers the formation energy of the crystal by increasing its perimeter. This mechanism influences the details of grain boundaries (GBs), crystal structures, and edge-termination-dependent properties of polycrystalline 2D films (e.g., higher hydrogen evolution activity of Mo-edges in MoS₂⁵⁵⁻⁵⁷), especially for large-area transition metal dichalcogenide (TMDC) monolayers grown by chemical vapor deposition (CVD) as will be detailed later. Finally, the surface structure of a 3D material is the lowest free energy structure that is kinetically accessible under the growth conditions. When applied to 2D materials, kinetic accessibility can determine the overall crystal structure, as has been observed recently in borophene^{11,12} and monolayer MoTe₂^{58,59} polymorphs that are tuned by growth temperature.

1.2.2. Interfacial Coupling

The integration of dissimilar materials underlies most functional devices, which implies the near ubiquity of interfaces in applied technologies. Indeed, it has been said that “the interface is the device,”⁶⁰ especially in the context of multi-material heterostructures. The most extreme manifestation is 2D heterostructures where 2D materials serve as the building blocks for creating functional interfaces. In the context of electronics, strong interfacial interactions are a prerequisite for making low-resistance electrical contacts. Consequently, achieving reliable Ohmic contacts to low-dimensional materials has been challenging, and for 2D materials, the first-order concern is to choose a metal that minimizes the Schottky barrier. However, geometric considerations allow additional means for tailoring electrical contacts in the low-dimensional limit. For example, end-bonded carbon nanotubes possess exceptionally low contact resistance through Mo-carbide formation,⁶¹ with further recent improvements achieved with Co catalysts to reduce the reaction temperature.⁶² Similarly, 1D edge contacts have been shown to outperform surface contacts for 2D vertical heterostructures.⁶³

Epitaxial growth is the conventional means of achieving well-defined interfaces between two covalently bonded bulk materials with similar lattice constants. Small but non-zero differences in lattice constants imply a gradual distortion of the lattices in a buffer layer that accommodates the strain as is schematically shown in **Fig. 1.1c**, where the lattice constant of the film (d_A) is slightly smaller than that of the substrate (d_B). While large lattice mismatch results in strain build-up and the formation of misfit dislocations, epitaxial growth of Si on SiGe cleverly takes advantage of such interfacial strain to enhance the charge carrier mobility of Si.⁶⁴ Another requirement for forming a well-defined interface is valence-matching, meaning that the bonds created by atoms on

each side of the interface should have two electrons.⁶⁵ Otherwise, residual charge builds up and distorts the interfacial atomic arrangements during the growth, which has been a problem for the nearly perfectly lattice matched system of Ge on GaAs (lattice constants are 5.66 Å and 5.65 Å, respectively).

In contrast to the covalent bonding at conventional epitaxial interfaces, the relatively weak van der Waals forces between the layers in 2D material heterostructures strongly relaxes the requirements of lattice-matching and valence-matching, ultimately enabling a broader heterostructure phase space.⁶⁶ Albeit weak, the van der Waals interaction still mediates various types of coupling across the interface. For example, charges redistribute at interfaces to balance the chemical potential, which influences phenomena such as screening, band bending, and depletion. While interfacial charge transfer takes place (**Fig. 1.1d**) in both conventional 3D heterostructures and 2D van der Waals heterostructures, significant differences exist. Firstly, the minimal electronic hybridization across van der Waals gaps limits charge transfer processes to relatively inefficient tunneling and hopping. Secondly, the increased exciton binding energy due to reduced dielectric screening can rival band offsets that would otherwise dictate charge transfer processes. Nevertheless, recent developments have shown cases where charge transfer in van der Waals heterostructures can be ultrafast including MoS₂/WS₂,⁶⁷⁻⁶⁹ MoS₂/graphene,⁷⁰ WS₂/quantum dot,⁷¹ and MoS₂/organic heterostructures.⁷² In 2D superconductors,⁷³ interfacial coupling can also strongly influence the superconducting critical temperature. For example, FeSe is one of the most studied 2D superconductors with a bulk superconducting critical temperature (T_c) of ~8 K.⁷⁴ However, by growing monolayer FeSe on SrTiO₃, T_c is significantly enhanced to temperatures of ~100 K,⁷⁵ due to interface-enhanced electron-phonon coupling.⁷⁶⁻⁷⁸

In addition to electronic coupling, the spin degree of freedom introduces interfacial magnetic coupling. The exchange interaction between spins determines parallel or anti-parallel alignment of neighboring spins, corresponding to ferromagnetic and antiferromagnetic ordering. An example is shown in **Fig. 1.1e**, where an interface is created between a ferromagnetic layer (top, orange) and an antiferromagnetic layer (bottom, green). Under zero external magnetic field (i.e., $H = 0$, left panel), the type of ordering at the interface is determined by the exchange interaction, which is assumed to be antiferromagnetic in this case. By applying an external magnetic field (i.e., $H \neq 0$, right panel), the magnetization of the ferromagnetic layer can be flipped above a critical field strength since the overall energy is lowered by aligning spins with the external magnetic field, even though the exchange interaction increases at the interface. Recently, ferromagnetism has been observed in the 2D limit in monolayer CrI_3 as a result of magnetic anisotropy.⁷⁹ Furthermore, through the exchange interaction and ultrafast charge transfer, the valley polarization of monolayer WSe_2 has been modified when integrated with CrI_3 in a vertical heterostructure.⁸⁰

While the constituent materials alone typically determine the interfacial behavior in heterostructures, the details of the surface termination can also play a role in select cases. For example, in polar materials, two possible interfaces are created depending on the termination of the top material, as shown in **Fig. 1.1f**. This situation is most common for complex oxides⁸¹ such as the extensively studied $\text{LaAlO}_3\text{-SrTiO}_3$ heterostructure,⁸²⁻⁸⁴ where two possible interfaces of $(\text{LaO})^+ / (\text{TiO}_2)^0$ or $(\text{AlO}_2)^- / (\text{SrO})^0$ exist. These two interfaces result in two types of polarity discontinuities, ultimately leading to either an n-type or a p-type interface, with a high-mobility electron gas only existing at the n-type interface. This significant difference in electronic properties

led to the development of growth methods with half-unit-cell resolution to better control interfacial coupling.⁸⁵

1.2.3. Surface and Interface Electronic States

Since band theories are based on periodic lattices, the discontinuity of a crystal lattice at a boundary (e.g., surfaces and interfaces) is expected to alter local electronic properties. Bulk electronic states typically decay exponentially into vacuum (except surface resonance derived from bulk states) and define the band structure of crystals, while surface states are spatially localized and decay both into the bulk and vacuum.^{86,87} Energetically, surface states often exist in the band gap of semiconductors or in the local gaps of metals. Historically, surface states are categorized as Shockley states, which are applied to more delocalized systems such as noble metals and narrow-gap semiconductors, or Tamm states, which are used to describe more tightly bound systems such as transition metals with d-electrons and wide-gap semiconductors.⁸⁸ Surface states are generally sensitive to surface modifications such as reconstructions, defects, and coupling with other materials. Similarly, interfacial states may arise in the band gap of two interfacing semiconductors or at the GB of a polycrystalline material. For 2D materials and heterostructures, if the interfacial states are delocalized and cross the Fermi level, a metallic pathway is created that directly impacts charge transport. More exotically, the metallic surface states of a topological insulator are protected by time-reversal symmetry, which makes them robust against local non-magnetic disturbances.⁸⁹ Through additional interfacial coupling with a superconductor, artificial topological superconductor heterostructures are predicted to host Majorana fermions for fault-tolerant quantum computation.⁹⁰ Towards this end, 2D heterostructures based on NbSe₂/Bi₂Se₃⁹¹ and FeTe/Bi₂Te₃⁹² are being actively explored.

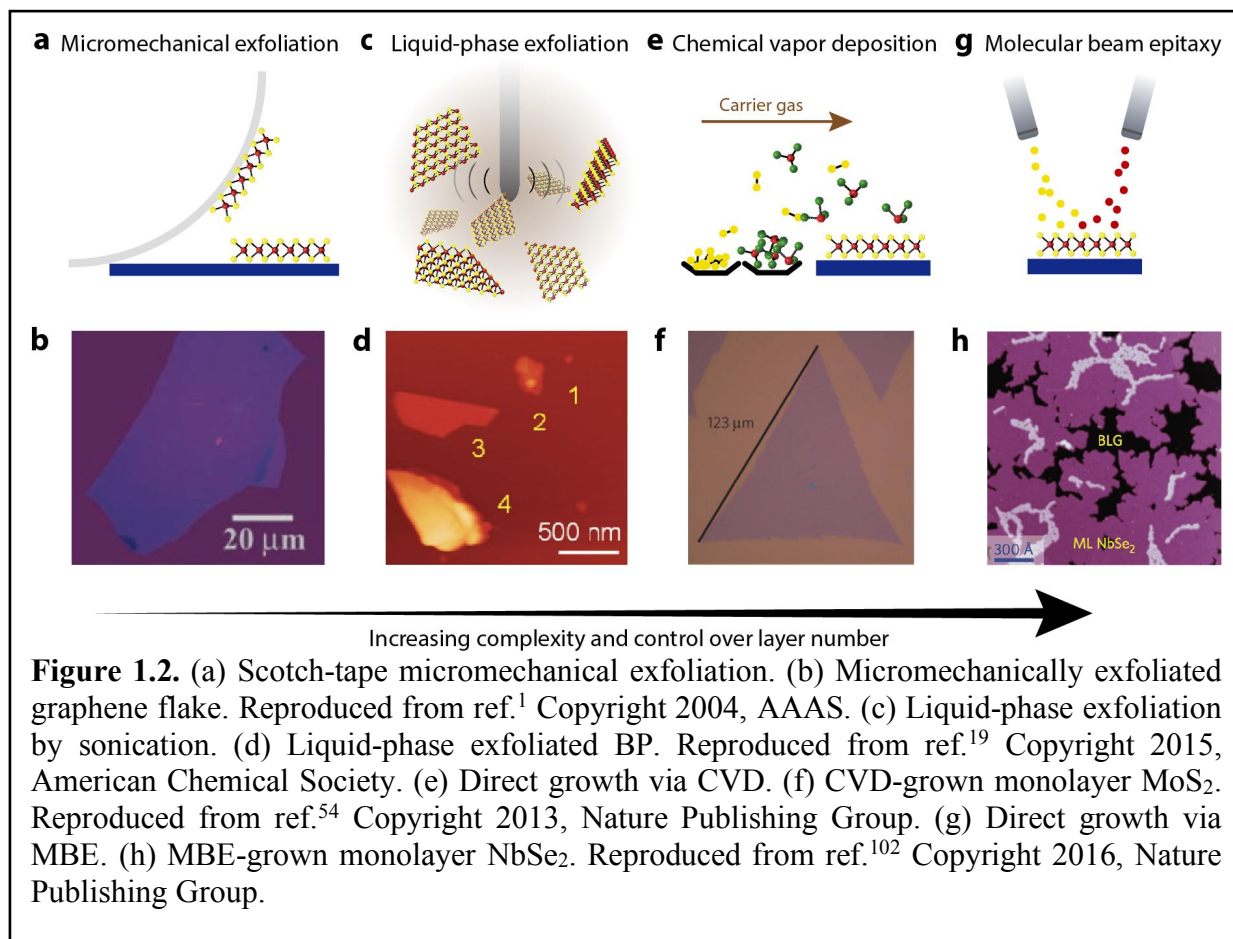
1.3. Synthesis and Preparation of 2D Materials

The interfaces of 2D heterostructures are heavily influenced by the fabrication methods used to produce their constituent 2D materials. The preparation conditions also control defect structures and surface cleanliness. For example, ultrahigh vacuum (UHV) growth provides the most pristine crystal surface, whereas solution-based exfoliation often leaves solvent or surfactant residues. Therefore, it is necessary to summarize the experimental approaches for preparing 2D materials before reviewing strategies for characterizing and controlling their surfaces and interfaces. Given the existence of in-depth review articles focused solely on the synthesis and preparation of 2D materials,⁹³⁻⁹⁷ this section provides a broad overview of common techniques rather than attempting to be an exhaustive treatment of the subject.

1.3.1. Top-Down Approaches

1.3.1.1. Exfoliation in Dry Environments

Scotch tape exfoliation is the simplest and most commonly adopted method in research laboratories for preparing 2D materials from layered van der Waals crystals. This approach falls within the more general category of micromechanical exfoliation (**Fig. 1.2a**), which also employs exfoliation media beyond adhesive tape such as polymers, thermal release tape, and fiberglass. Micromechanical exfoliation relies on the relatively weak inter-layer van der Waals interaction compared to stronger in-plane covalent bonding, and results in flakes with a wide thickness distribution (monolayer to bulk) and lateral dimensions (typically 0.1 to 100 μm). Although this method generally results in irregular lateral shapes (**Fig. 1.2b**), micromechanically exfoliated flakes can be highly faceted if the layered van der Waals crystal possesses a high in-plane structural



and mechanical anisotropy (e.g., ReS₂⁹⁸ and BP⁹⁹). The effectiveness of this method heavily relies on the bonding between layers being weaker than the bonding to the target substrate. For example, since BP has a higher interlayer bonding energy than graphite, hBN, and most TMDCs,^{100,101} BP crystals are generally more difficult to exfoliate, resulting in a relatively high proportion of thick BP flakes. Efforts to increase the yield of thin flakes include enhancing adhesion to the target substrate via Au adlayers^{103,104} and heat treatments.¹⁰⁵ A related strategy is the dry contact transfer (DCT) method¹⁰⁶ in which 2D materials are directly exfoliated on chemically reactive substrates (e.g., pristine Si surfaces) in UHV. Ball-milling is another dry exfoliation method (e.g., in the presence of dry ice), although it is also often performed in solvents,¹⁰⁷ which is more scalable than traditional micromechanical exfoliation. In addition to exfoliation via surface normal forces, ball

milling introduces significant shear forces that delaminate layers with relatively high yield, albeit in a manner that results in relatively small lateral flake sizes ($<1 \mu\text{m}$).

1.3.1.2. Solution-Phase Exfoliation

Solution-based exfoliation is the leading strategy for producing large quantities¹⁰⁸ of thin 2D flakes. The resulting dispersions have been implemented in roll-to-roll processing, providing a pathway to applications in thin-film transistors, printed electronics, and related additive manufacturing technologies.⁹³ In solution-based exfoliation, bulk layered van der Waals materials or powders are subjected to local mechanical stresses that are produced by collapsing cavitation bubbles during ultrasonication or shear mixing in liquid media (**Fig. 1.2c**). The resulting exfoliated 2D materials are stabilized by surfactants in aqueous solutions or via high boiling point organic solvents that match the surface energy of the targeted 2D material. To preserve the surface integrity of air-unstable materials such as BP (**Fig. 1.2d**), anhydrous organic solvents¹⁹ and deoxygenated aqueous solutions¹⁰⁹ are employed. Furthermore, since solution-phase exfoliation typically suffers from imperfect control over flake thickness, lateral dimensions, and surface chemistry, post-processing methods such as density gradient ultracentrifugation (DGU) have been developed to improve structural and chemical monodispersity.⁹³ Another solution-phase exfoliation method that produces relatively large and thin 2D layers is based on ion intercalation,^{110,111} where 2D layers are separated by mild sonication after intercalated ions (e.g., Li^+) weaken the inter-layer bonding. However, ion intercalation methods often introduce chemical modifications, etching, and even phase transformations, which can substantially modify the properties of the resulting 2D flakes. Further details and examples of solution-phase exfoliation methods are delineated in recent reviews.^{93,112-114}

1.3.2. Bottom-Up Growth

1.3.2.1. Chemical Vapor Deposition

Since top-down exfoliation tends to yield relatively small flakes, direct growth methods are employed in applications that require large-area films. In the context of 2D materials, CVD was first utilized to produce graphene on metal substrates in both ambient¹⁵ and UHV conditions.¹¹⁵ Later developments enabled the synthesis of millimeter-sized,¹¹⁶ centimeter-sized,^{117,118} and even decimeter-sized¹¹⁹ single-crystal graphene domains. Similarly, CVD is among the most popular means of preparing TMDCs with controlled stoichiometry, layer number, domain size, and GBs. As depicted in **Fig. 1.2e**, volatile precursors (e.g., MoO₃ and S) are co-evaporated and then reacted to form desired deposits (e.g., MoS₂) on the surface of targeted substrates. **Fig. 1.2f** shows an example of CVD-grown monolayer MoS₂.⁵⁴ A summary of typical CVD precursors and growth conditions for TMDCs is given in a recent review article.¹²⁰ In addition, several variations of the CVD method have been demonstrated. For example, plasma-enhanced CVD of graphene allows the use of lower substrate temperatures and growth times, which minimizes contamination from metal substrates.¹²¹ In addition, metal-organic CVD of TMDCs improves growth homogeneity over large areas,^{122,123} while aromatic-molecule-assisted CVD promotes the growth of large domains at lower temperatures¹²⁴ and facilitates lateral and vertical stitching of dissimilar 2D materials into heterostructures.¹²⁵

1.3.2.2. Atomic Layer Deposition

Atomic layer deposition (ALD) is a subset of the more general CVD process. Its primary difference is that the reactive precursors are introduced alternately as opposed to concurrently.

Following the introduction of the first precursor, the chamber is purged with inert gas to leave behind only a surface layer. The introduction of the second precursor results in chemical reactions that will self-terminate once all of the surface sites have reacted, after which residual precursor is pumped out. Since ALD is a self-terminating process, it has been utilized to grow oxide layers on 2D materials as gate dielectrics with precise thickness control.¹²⁶ A detailed perspective article¹²⁷ summarizes the precursors used for different 2D materials. The growth of 2D materials directly via ALD, however, has been limited to TMDCs.¹²⁸⁻¹³² In this context, ALD growth offers advantages over CVD in terms of growth temperature (as low as 60°C)¹²⁹ and scalability,¹³¹ although post-growth annealing is typically required to improve crystallinity.

1.3.2.3. Physical Vapor Deposition

Physical vapor deposition includes multiple techniques such as molecular beam epitaxy (MBE), sputtering, and pulsed laser deposition (PLD). For the synthesis of 2D materials, MBE offers the highest level of control over layer thickness and stoichiometry. In particular, complex oxide materials that are platforms for studying superconductivity have only been reliably grown by oxide MBE and PLD. The growth proceeds with elemental source materials evaporated in UHV from Knudsen cells (low temperature) or electron-beam evaporators (high temperature) (**Fig. 1.2g**). The growth rate is typically low to promote epitaxial growth. While MBE has been mostly applied to grow 2D compounds, such as NbSe₂¹⁰² (**Fig. 1.2h**), elemental 2D materials have also been demonstrated.^{11,12,24-28,30,31} The capability of continuous growth of multiple layers of alternating materials is especially useful for creating 2D heterostructures and superlattices.⁸¹

Instead of using thermal evaporators, target materials are deposited using intense laser ablation in the process of PLD. Recently, this technique has been used to produce numerous 2D

materials including graphene,¹³³ hBN,¹³⁴ MoS₂,¹³⁵ InSe,¹³⁶ and BP.¹³⁷ The advantage of PLD lies in its high deposition rate and direct transfer of the stoichiometry of the target material. However, a common issue is that the thickness is not well controlled, and the resulting films are highly polycrystalline or even amorphous.¹³⁷ A thorough summary of the application of PLD to growing 2D materials is provided in a recent review.¹³⁸

1.3.2.4. Solution-Phase Growth

For printed electronics and additive manufacturing, direct growth of 2D materials from solution-phase precursors eliminates the need for top-down exfoliation. Indeed, direct growth of 2D materials and heterostructures from the solution phase has been demonstrated for CdSe,¹³⁹ PbSe,¹⁴⁰ 2D perovskites,¹⁴¹ Sb₂Te₃/Bi₂Te₃ heterostructures,¹⁴² and various TMDCs.¹⁴³⁻¹⁴⁵ For colloidal synthesis, the templating effect of a 2D substrate is missing. Therefore, in addition to choosing appropriate precursors, a key challenge is to introduce anisotropic growth, which could result from lattice anisotropy or through defect and ligand engineering.¹⁴⁶ Recent reviews summarize the latest advances in colloidal synthesis of 2D materials.^{146,147}

1.4. Characterizing Surfaces and Interfaces

While surfaces are readily characterized via microscopy methods, buried interfaces in conventional bulk heterostructures are not directly accessible without cross-sectional techniques. However, in the case of 2D vertical heterostructures, the atomically thin layers are electronically and optically transparent under certain experimental conditions, thus enabling characterization of not only buried layers, but also interfaces. For example, electrons can tunnel through monolayer hBN into underlying conductors in scanning tunneling microscopy (STM).¹⁴⁸ In this section,

microscopy and spectroscopy methods for characterizing 2D surfaces and interfaces are reviewed.

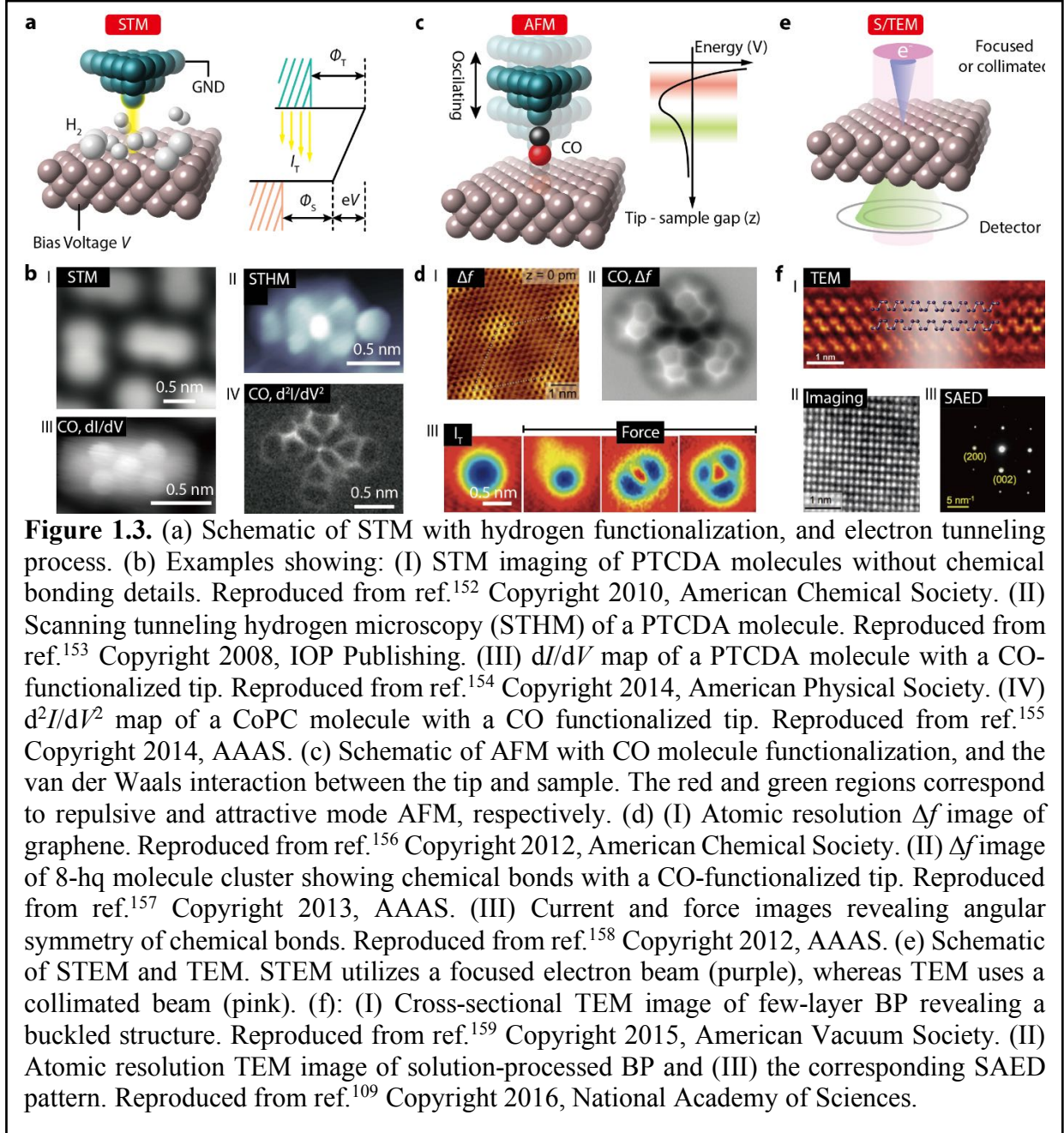
1.4.1. Atomic Resolution Microscopy Methods

STM has been one of the most important tools for characterizing surfaces. Through piezoelectric motors,¹⁴⁹ an atomically sharp metal tip is approached toward a sample surface, which is biased at a voltage V . When the tip apex and sample surface are sufficiently close, typically ~ 1 nm, electrons efficiently tunnel through the tip-sample junction resulting in a tunneling current I_T as schematically shown in **Fig. 1.3a**. The tunneling junctions can also be functionalized with small molecules (e.g., hydrogen), which can lead to enhanced imaging contrast in some cases. With $V > 0$, electrons tunnel from the occupied states of the tip to the unoccupied states of the sample (right panel in **Fig. 1.3a**). For electrons with energy ε with respect to the Fermi level ($\varepsilon=0$) of the sample, the current due to electrons tunneling from the tip to the sample can be expressed as:^{150,151}

$$I_{t-s}(\varepsilon) = -4\pi e \frac{|M|^2}{\hbar} \rho_t(\varepsilon - eV) f(\varepsilon - eV) \rho_s(\varepsilon) [1 - f(\varepsilon)] \quad (1)$$

where M is the tunneling matrix element, $\rho_s(\varepsilon)$ is the electronic density of states (DOS) of the sample, $\rho_t(\varepsilon)$ is the DOS of the tip, and $f(\varepsilon)$ is the Fermi-Dirac distribution. Similarly, the tunneling current from the sample to the tip can be expressed as:

$$I_{s-t}(\varepsilon) = -4\pi e \frac{|M|^2}{\hbar} \rho_t(\varepsilon - eV) f(\varepsilon) \rho_s(\varepsilon) [1 - f(\varepsilon - eV)] \quad (2)$$



The overall net current flowing from the tip to the sample is calculated through an integration over energy:

$$I_T = \int_{-\infty}^{\infty} (I_{t-s}(\varepsilon) - I_{s-t}(\varepsilon)) d\varepsilon = -\frac{4\pi e}{\hbar} \int_{-\infty}^{\infty} |M|^2 \rho_t(\varepsilon - eV) \rho_s(\varepsilon) [f(\varepsilon - eV) - f(\varepsilon)] d\varepsilon \quad (3)$$

STM tips are typically metals (e.g., W, Pt, or PtIr), where the DOS is featureless around the Fermi level such that $\rho_t(\varepsilon)$ can be approximated as $\rho_t(0)$. In addition, at sufficiently low temperatures, the Fermi-Dirac distribution is close to a step function. If we further assume a s-wave tip, $|M|^2$ is independent of energy:¹⁶⁰

$$|M|^2 = e^{-2d\sqrt{2m\phi/\hbar^2}} \quad (4)$$

where d is the tip-sample gap, m is the electron mass, and ϕ is the tunneling barrier height determined by the work functions of the tip (ϕ_T) and sample (ϕ_S) (**Fig. 1.3a**, right). Therefore, equation (3) can be simplified as:

$$I_T \approx -\frac{4\pi e}{\hbar} e^{-2d\sqrt{2m\phi/\hbar^2}} \rho_t(0) \int_0^{eV} \rho_s(\varepsilon) d\varepsilon \quad (5)$$

Evidently, the tunneling current exponentially decays with increasing tip-sample distance. For a cone-shaped STM tip, this result implies that the tunneling current is highly localized at the tip apex, which enables both high vertical resolution (~ 0.01 Å) and lateral resolution (~ 1 Å). Furthermore, the differential tunneling conductance is directly proportional to the sample DOS at energy eV :

$$\frac{dI_T}{dV} \approx -\frac{4\pi e}{\hbar} e^{-2d\sqrt{2m\phi/\hbar^2}} \rho_t(0) \rho_s(eV) \quad (6)$$

which allows STM to simultaneously probe the structural and electronic properties of surfaces. Experimentally, the differential tunneling conductance is often obtained using a lock-in amplifier to improve signal-to-noise ratio.

STM topography images are a convolution of structural and electronic properties, which complicates the identification of real-space atomic arrangements. For example, when imaging molecules, STM images are typically far less detailed than the actual molecular atomic structure due to contributions from delocalized molecular orbitals. To illustrate this issue, **Fig. 1.3b-I** shows

an STM image of self-assembled perylene-3,4,9,10-tetracarboxylic dianhydride (PTCDA) molecules,¹⁵² where individual molecules show minimal intra-molecular contrast. However, by functionalizing the tunneling junction with hydrogen,¹⁵³ sharp intra-molecular structure is revealed (**Fig. 1.3b-II**) as well as inter-molecular interactions. While the exact mechanism of this enhanced resolution was not determined in this initial study, later theoretical calculations suggested that the geometrical lateral relaxation of the adsorbed molecular species is responsible for the increased spatial resolution.¹⁵⁴ Carbon monoxide (CO) can also be used to functionalize the STM tip to improve spatial resolution. As shown in **Fig. 1.3b-III**, intramolecular contrast is obtained in the differential tunneling conductance map,¹⁵⁴ which is spatially modulated by the interactions between the CO-functionalized tip and the surface. This bond-resolved imaging technique is especially useful for resolving unknown bonding structures of new materials and heterostructure interfaces. In the context of 2D materials, heterostructures between pristine graphene nanoribbons (GNRs) and fluorenone-functionalized GNRs are indistinguishable in standard STM imaging, but are readily identified with CO-functionalized STM tips.¹⁶¹ Although elastic tunneling from band to band dominates the tunneling current in STM, local excitations (e.g., excitations of vibrational states) in the tip or sample offer additional inelastic tunneling pathways, which are resolvable in the second-order differential tunneling conductance (d^2I/dV^2), typically known as inelastic electron tunneling spectroscopy (IETS). **Fig. 1.3b-IV** shows an IETS map of a CoPc molecule, where intramolecular chemical bonding is apparent.¹⁵⁵ However, since this technique requires low temperatures (<1 K) and long acquisition times, it is generally only used in cases where vibrational information is critically needed.

In atomic force microscopy (AFM), tips couple to surfaces through mechanical forces such as the van der Waals interaction (**Fig. 1.3c**, right) that depend on the tip-sample gap (z). In AFM,

the probe is integrated with a force sensor, which is typically a nanoscale harmonic oscillator with a spring constant k . The oscillator is often in the form of a silicon cantilever or a quartz tuning fork (e.g., qPlus¹⁶² or KlibriSensor¹⁶³) with oscillation frequencies in the kHz to MHz range. When the AFM tip is brought close to the sample surface, an additional force is exerted on the tip, $F_{ts}(z) = -\frac{\partial V}{\partial z}$, and the point of $F_{ts}(z) = 0$ separates the regions of attractive (green) and repulsive (red) interactions as shown in **Fig. 1.3c**. The equivalent spring constant is $k' = k + k_{ts}(z) = k - \frac{\partial F_{ts}}{\partial z} = k + \frac{\partial^2 V}{\partial z^2}$, and the effective resonant frequency is $f' \propto \sqrt{k'}$.¹⁶⁴ While k is always positive for the physical force sensor, $k_{ts}(z)$ is positive at small tip-sample distances and becomes negative at large tip-sample distances.

AFM can be operated in static mode, where the tip-sample interaction is kept constant (e.g., contact-mode) by monitoring the bending of the cantilever, or in dynamic mode (also known as non-contact AFM (nc-AFM)), where the tip vibrates and has intermediate interaction with the sample surface. If the oscillator is driven by a sinusoidal signal at its resonant frequency f_0 and has no interaction with the surface, the sinusoidal oscillation of the cantilever will have a phase lag of $\pi/2$ compared to the driving signal. This phase difference is larger if the driven frequency is higher than the resonant frequency, while the opposite behavior occurs below the resonant frequency. Consequently, if the tip-sample interaction results in positive k_{ts} (e.g., in the repulsive regime), f' will be larger than f_0 and the phase difference will be smaller than $\pi/2$. In amplitude-modulation mode AFM, where the oscillator is excited with a constant amplitude during scanning, inhomogeneous surfaces will result in spatially varying van der Waals coupling and thus spatially inhomogeneous phase differences. Therefore, phase mapping provides complementary material-specific information compared to topography images. In the case of 2D lateral heterostructures,

the similar thickness of two adjacent materials may show little contrast in topography, but the interface can be clearly identified due to the phase difference on each side. Even for the same material, subtle differences in its electronic and chemical properties can result in high contrast in phase imaging. For example, in the case of epitaxial graphene grown on SiC, while monolayer and bilayer graphene regions are difficult to distinguish in topographic imaging, they are immediately distinguishable via phase mapping.¹⁶⁵ A drawback of the amplitude-modulation mode is that the change in the tip vibration amplitude takes place on a time scale of $\tau_{am} \approx 2Q/f_0$, where Q is the quality factor.¹⁶⁴ In UHV where Q reaches values up to 100,000, amplitude-modulation mode possesses small bandwidths. On the other hand, if the change of oscillation frequency is recorded at a constant tip height (i.e., frequency-modulation), the time constant is significantly reduced to $\tau_{fm} \approx 1/f_0$.¹⁶⁴ By using rigid sensors such as quartz tuning forks ($k \sim 1000$ N/m), the required oscillation amplitudes can be kept sufficiently low (e.g., 1 Å) to resolve the short-range forces that give rise to atomic corrugation. An example is given in **Fig. 1.3d-I**, where the honeycomb lattice of graphene is atomically resolved.¹⁵⁶

Like STM, AFM spatial resolution can be enhanced by functionalizing the tip with CO. After the first report of resolving intramolecular structure with CO-functionalized AFM by IBM in 2009,¹⁶⁶ intermolecular hydrogen bonding networks were observed in 2013 with the same technique¹⁵⁷ (**Fig. 1.3d-II**). Theories invoking Pauli repulsion,^{166,167} CO relaxation,¹⁵⁴ and short-range electrostatic forces^{168,169} have been proposed and supported by matching experimental and simulated images, although the underlying imaging mechanism is still being debated.^{170,171} When applied to 2D materials, CO-functionalized AFM has provided unambiguous structural identification of the lateral interface of two mirror-domains (i.e., mirror twin boundaries) of monolayer MoSe₂,¹⁷² which is otherwise highly blurred in STM due to the delocalized DOS near

the Fermi level. In addition to the capability of scanning insulating samples, another added benefit of UHV AFM is its high force sensitivity. In frequency modulation mode, the frequency shift $\Delta f = f' - f_0 = f_0 k_{ts}/2k$ is a direct measure of the derivative of the tip-sample interaction in the z direction. The high sensitivity in force measurement allows the investigation of the angular dependence of atomic bonding with apparent sub-atomic resolution.^{173,174} In **Fig. 1.3c-III**, the tunneling current distribution of a CO molecule in constant-height STM imaging with a W probe is rotationally symmetric,¹⁵⁸ which is expected for the CO molecule standing up on the copper surface. On the other hand, the short-range force distribution in the out-of-plane direction derived from AFM imaging using 3 different tips exhibits single, dual, and triple minima, which is a result of directional bonding between the tip atom and the CO molecule that depends on the atomic configuration of each tip.¹⁵⁸

Transmission electron microscopy (TEM) offers another atomic-resolution technique that images through materials instead of only at the surface (**Fig. 1.3e**). Cross-sectional TEM is especially powerful for probing buried interfaces in 2D materials and vertical heterostructures. For instance, **Fig. 1.3f-I** shows the cross-section of a 3-layer thick BP flake (~ 1.5 nm) prepared via focused ion beam milling.¹⁵⁹ Electron microscopy also offers analytical modes of operation including energy-dispersive X-ray spectroscopy (EDS) and electron energy loss spectroscopy (EELS) that provide chemical sensitivity down to the atomic scale.

In TEM, a collimated beam of electrons with energies in the range of 60 keV to 2 MeV are directed at thin-film samples with thicknesses under 100 nm (**Fig. 1.3e**). The high electron energy provides a small de Broglie wavelength of $\lambda = 1.22/\sqrt{E}$, where E is the electron energy in eV, and λ has units of nm.¹⁷⁵ With a commonly used 200 keV electron beam, λ will be around 2.7 pm, which enables atomically resolved imaging. For example, the atomic lattice of a 2D BP flake is

clearly resolvable¹⁰⁹ as shown in **Fig. 1.3f-II**. The electron diffraction capability of TEM provides another means of determining crystallinity and crystallographic orientation. **Fig. 1.3f-III** shows a characteristic selected area electron diffraction pattern of 2D BP,¹⁰⁹ where a variable-sized aperture defines the imaging areas. Alternatively, in a scanning transmission electron microscope (STEM), a convergent beam of electrons is used to scan the sample line by line (**Fig. 1.3e**). Transmitted electrons at each imaging pixel are used to reconstruct a full image. The versatility in constructing an image from different fractions of transmitted, diffracted, or even back scattered electrons provides information about the chemical properties of the sample. For example, when constructing an image using a high-angle annular dark field (HAADF) detector, the image contrast scales with the atomic number due to increased scattering of electrons by heavier elements.

1.4.2. Spatially Resolved Property Measurements

Although atomic-scale imaging provides the most direct measure of physical structure, many materials properties are manifested over larger length scales. Consequently, spatially resolved property measurements can often be probed without the need of a UHV environment, which simplifies experimental characterization. In this section, we review the basic principles and applications of spatially resolved methods for characterizing the properties of surfaces and interfaces of 2D materials.

1.4.2.1. Characterizing Mechanical and Thermal Properties

By probing vertical and lateral forces on a Si cantilever, ambient AFM allows the stiffness and frictional properties of materials to be characterized.¹⁷⁶ For example, it has been shown that surface friction of numerous 2D materials (e.g., graphene, MoS₂, NbSe₂, and hBN) decreases with

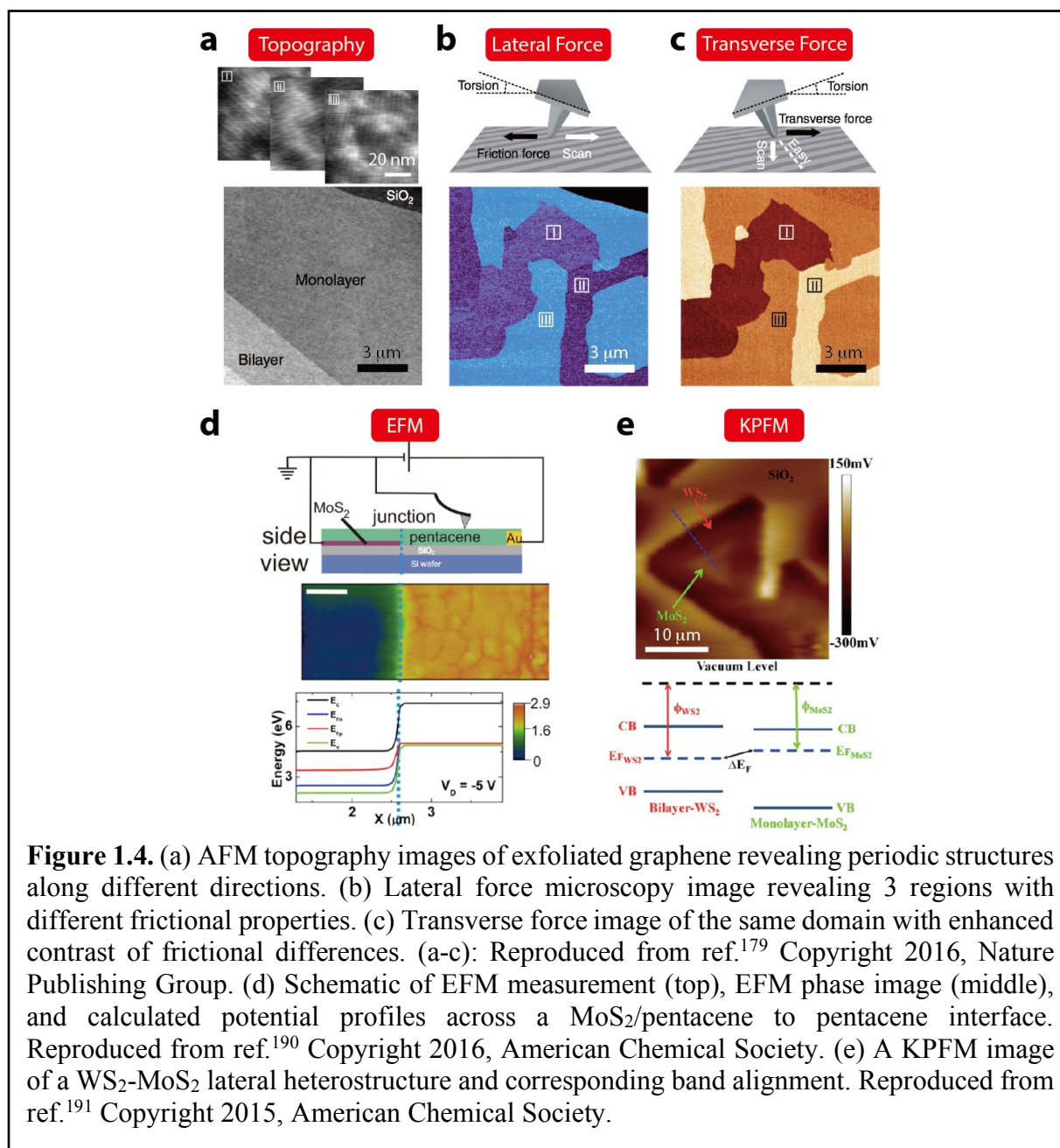
increasing numbers of layers, which is consistent with the increased susceptibility to out-of-plane deformation for thinner layers.¹⁷⁷ In addition, atomic-scale friction measurements have revealed a stick-slip sliding phenomenon consistent with the Prandtl-Tomlison model.¹⁷⁸ On a larger scale, different materials or friction anisotropies can be resolved using lateral force microscopy (LFM). **Fig. 1.4a** (bottom) shows a topography image of an exfoliated graphene flake on SiO₂, where the monolayer region shows high homogeneity.¹⁷⁹ When the same monolayer graphene is imaged with LFM (**Fig. 1.4b**, top), the lateral force image (**Fig. 1.4b**, bottom) shows domain structures. This contrast is more pronounced in the transverse force channel, where the fast scan direction is along the cantilever, but the lateral tilt of the cantilever is recorded (**Fig. 1.4c**). These results hint at the existence of anisotropic friction domains in the isotropic graphene monolayer. The initial interpretation suggested the formation of rippled graphene domains in three equivalent directions that give rise to anisotropic friction as a result of anisotropic graphene puckering.¹⁸⁰ However, a later study¹⁷⁹ employing higher resolution AFM imaging revealed well-defined periodic stripes within each frictional domain as shown in **Fig. 1.4a** (top). The lack of these periodic structures on samples imaged in vacuum suggests that the origin of these stripes are ambient adsorbates that self-assemble and modulate the frictional forces in each domain. Grain boundaries in 2D materials are also easily discernable due to their different frictional properties.¹⁸¹

For probing thermal properties, scanning thermal microscopy (SThM)^{182,183} allows the spatial distribution of both temperature and thermal conductivity to be measured depending on the probe used. The first type of probe involves a temperature sensor (e.g., nanoscale thermocouple junction or Schottky diode) integrated at the tip apex that can directly measure sample temperatures locally. The second type of probe employs a nanoscale resistor, which can measure temperature by monitoring the change of resistance by passing a small current with negligible Joule heating,

or local thermal conductivity by passing a large current and monitoring the conduction of heat to the sample reflected in the change of voltage. The temperature resolution in ambient conditions is ~ 1 K,¹⁸⁴ but can be improved to ~ 15 mK in UHV environments using an Au-Cr thermocouple.¹⁸⁵ Temperature resolution down to ~ 1 μ K was recently realized in a scanning superconducting quantum interference device (SQUID) with spatial resolution of ~ 50 nm that revealed local dissipation centers at graphene edges in a hBN/graphene/hBN heterostructure.¹⁸⁶

1.4.2.2. Characterizing Electronic Properties

Similar to STM, the application of a tip-sample voltage in AFM with an electrically conductive tip provides local electronic coupling to the sample. This electronic coupling can modulate force measurements as in electrostatic force microscopy (EFM) and Kelvin probe force microscopy (KPFM), or directly give rise to imaging signals as in conductive AFM (CAFM). The capacitance C of the tip-sample junction in AFM is dependent on the tip-sample distance z . With a large z beyond the short range van der Waals interaction (**Fig. 1.3c**) and a surface potential difference V between the tip and the sample, the net force acting on the tip is $F_{ts}(z) = \frac{1}{2} \frac{\partial C}{\partial z} V^2$. Since $\frac{\partial C}{\partial z} < 0$, the force is attractive ($F_{ts}(z) < 0$). The potential difference V is composed of the tip-sample bias V_b and the work function difference V_{CPD} (also known as contact potential difference): $V = V_b + V_{CPD}$. In both EFM and KPFM, the topography of the sample is first obtained and then the tip retraces the sample with a larger separation (tens of nm) to detect the long range electrostatic force. In EFM, the tip is oscillating and biased during the retrace and the change of the oscillating phase due to $F_{ts}(z)$ is detected in a manner that is analogous to the phase image of amplitude-modulation AFM. The phase shift beyond $\pi/2$ is $\Delta\phi = \frac{Q}{k} \frac{\partial F_{ts}}{\partial z} = \frac{QV^2}{2k} \frac{\partial^2 C}{\partial z^2}$, which is proportional to



the square of the surface potential difference between the tip and sample.¹⁸⁷ Early studies widely employed EFM to image graphene and showed strong layer-dependency of the surface potential.^{188,189} Together with the layer-dependent surface friction discussed earlier, this characterization revealed the importance of interfacial interactions in determining the properties of few-layer 2D materials. In addition to isolated 2D materials, EFM has recently been applied to

2D heterostructures. **Fig. 1.4d** shows an example of using EFM to reveal the band profile in a MoS₂/pentacene heterostructure, which is a gate-tunable p-n junction diode. In this case, a reverse bias is applied to the diode (**Fig. 1.4d**, top), resulting in a spatially inhomogeneous electrostatic potential. The sharp jump of the EFM phase at the edge of the MoS₂ flake under the continuous pentacene layer (**Fig. 1.4d**, middle) indicates a large potential drop that agrees with band profile calculations (**Fig. 1.4d**, bottom). This method has also been applied to resolve the large potential drop across bisecting GBs in CVD-grown MoS₂ memristor devices.¹⁹²

Unlike the qualitative surface potential distribution provided by EFM, KPFM provides quantitative mapping of V_{CPD} by nulling the contact potential difference using an external DC bias. In KPFM retrace, the tip is not piezoelectrically driven. Instead, an AC voltage $V_{AC} = A\sin(\omega t)$ at the resonance frequency of the cantilever, $\omega = 2\pi f_0$, and a DC voltage V_{DC} are applied to the tip so that the potential difference between the tip and sample is $V = V_{AC} + V_{DC} + V_{CPD}$. The electrostatic force caused by the AC voltage ($F_{ts} = \frac{1}{2} \frac{\partial C}{\partial z} V^2$) thus has an AC term with frequency ω being $\frac{\partial C}{\partial z} (V_{DC} + V_{CPD}) A \sin(\omega t)$. This force drives oscillation of the cantilever, but is minimized if the applied V_{DC} cancels V_{CPD} (i.e., $V_{CPD} = -V_{DC}$). Hence, the work function distribution can be quantified by minimizing the cantilever oscillation and calibrating the tip work function. **Fig. 1.4e** (top) shows a KPFM surface potential map of a CVD-grown WS₂/MoS₂ lateral heterostructure, revealing the work function difference between the two interfacing materials.¹⁹¹ A type-II band alignment is deduced and schematically shown at the bottom of **Fig. 1.4e**. Further applications of KPFM include extracting band offsets in MoS₂ heterostructures with different layer numbers,^{193,194} mapping surface potential differences in MoS₂/ZnS¹⁹⁵ and MoS₂/WSe₂¹⁹⁶ lateral heterostructures, and examining the electrical properties of MoS₂ GBs.¹⁹⁷ Although EFM and KPFM have shown

high sensitivity to electrostatic interactions, even higher charge resolution down to the single electron limit has been realized using scanning single-electron transistor microscopy.¹⁹⁸ The probe in this method is a nanoscale tunneling device governed by the Coulomb blockade effect, where the tunneling current is modulated by the electric field of the sample. Charge detection sensitivity down to 0.01e has been demonstrated, which allows the electron-hole puddles in graphene to be resolved.¹⁹⁹ Like electrostatic forces, magnetic interactions are also long range, which allows them to be detected using a similar strategy to EFM. While early reports showed evidence of layer-dependent magnetism in few-layer graphene and MoS₂ using magnetic force microscopy (MFM),²⁰⁰ non-magnetic contributions including electrostatic interactions may also have been contributing to the observed imaging contrast.^{201,202} With the recent discovery of the 2D ferromagnet CrI₃,⁷⁹ MFM is likely to be revisited for 2D material characterization.

Unlike the aforementioned non-contact techniques, CAFM assesses local electrical conductivity by directly measuring the current flowing through the tip in contact-mode AFM. For instance, CAFM imaging readily reveals graphene from ungraphitized regions for epitaxial graphene on SiC.^{203,204} In lateral heterostructures of MoS₂/WS₂, the conductivity drops gradually within an 8 nm transition region from MoS₂ to WS₂,²⁰⁵ which is consistent with the relatively small band offset between WS₂ (2.03 eV) and MoS₂ (1.87 eV). Interestingly, when the MoS₂/WS₂ lateral heterostructure interface is covered with another layer of WS₂, the local conductivity at the lateral interface is enhanced by an order of magnitude over a 10 nm region.²⁰⁵ Further insight into this highly conductive interface has been provided by UHV scanning tunneling spectroscopy (STS), revealing local band bending that may trap charge carriers.²⁰⁵ By integrating CAFM with a light source introduced to the back side of a transparent sample, nanoscale photocurrent can also be

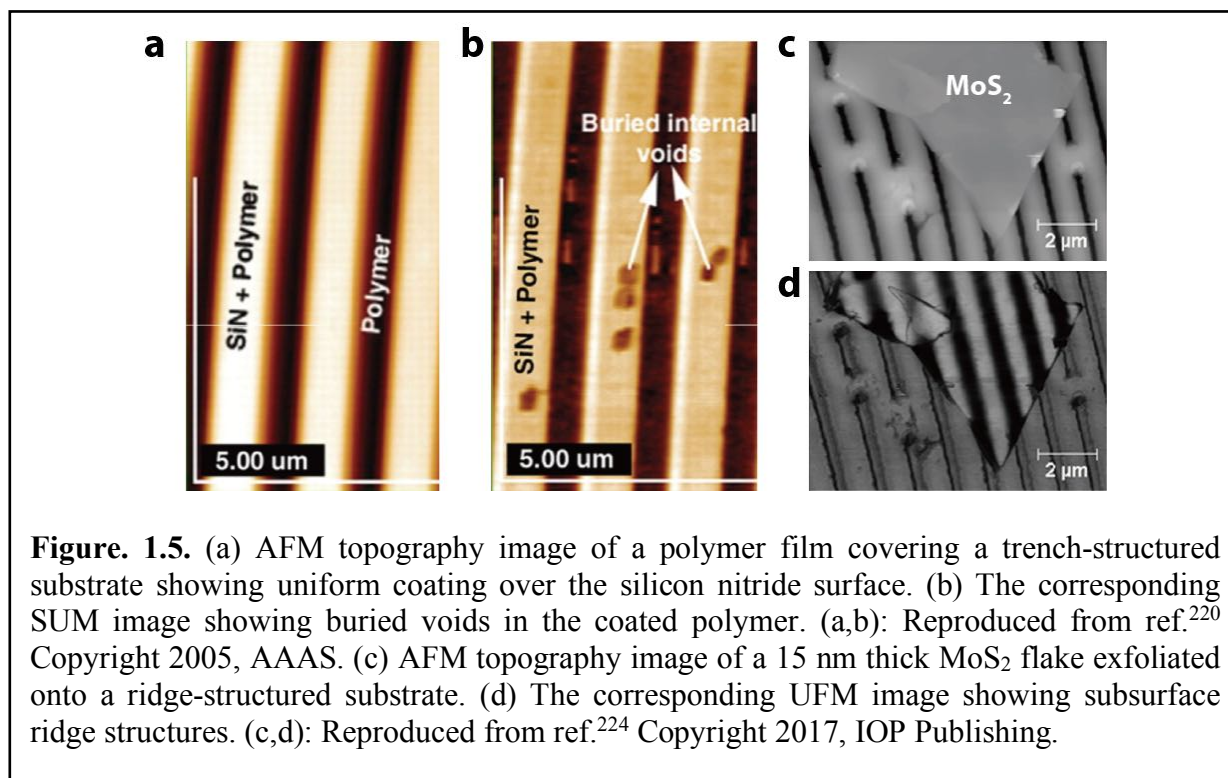
spatially mapped. This photoconductive AFM (PC-AFM) technique has been applied to organics,^{206,207} photovoltaic cells,^{208,209} and WSe₂/MoS₂ lateral heterostructures.²¹⁰

CAFM also allows local current-voltage (I - V) measurements to be performed by sweeping the voltage and measuring the current while the tip is held stationary. This CAFM I - V spectroscopy has been applied to graphene,^{211,212} hBN,²¹³ and TMDCs.^{194,214,215} In particular, under small biases, the tunneling resistance of MoS₂ has been found to be mechanically tunable by the compressing force of the CAFM tip,²¹⁴ which suggests the possibility of tunneling-based nano-electro-mechanical switches. CAFM spectroscopy has also revealed negative differential resistance (NDR) in manually stacked 2D heterostructures²¹⁶ and CVD-grown MoS₂/WSe₂/graphene and WSe₂/MoSe₂/graphene heterostructures.²¹⁷ The NDR features in these TMDC-based heterostructures are spectrally narrower than those of graphene/hBN/graphene heterostructures,²¹⁸ with peak-to-valley current ratios that are comparable to traditional resonant tunneling diodes.²¹⁹ CAFM also allows characterization of local Schottky barrier heights (SBHs). In addition to probing layer-dependent SBHs in MoS₂,¹⁹⁴ CAFM revealed a linear correlation between local SBH and local resistance in MoS₂, suggesting a common source of inhomogeneity such as sulfur vacancy concentration variations.²¹⁵ For graphene, interfacial charge transfer with substrates was found to be responsible for the low SBHs of epitaxial graphene grown on SiC (0.36 eV)²¹¹ and transferred graphene on AlGaN (0.4 eV).²¹²

1.4.2.3. Characterizing Subsurface Properties

Since buried interfaces play a significant role in the properties of 2D vertical heterostructures, subsurface imaging techniques are highly desirable. Many scanning probe methods allow subsurface probing by detecting the mechanical response at high oscillation

frequencies as in ultrasonography. For example, in scanning ultrasound microscopy (SUM),^{220,221} a high-frequency acoustic wave on the order of MHz or higher is launched from the bottom of the sample while another wave with slightly different frequency is launched from the AFM cantilever.

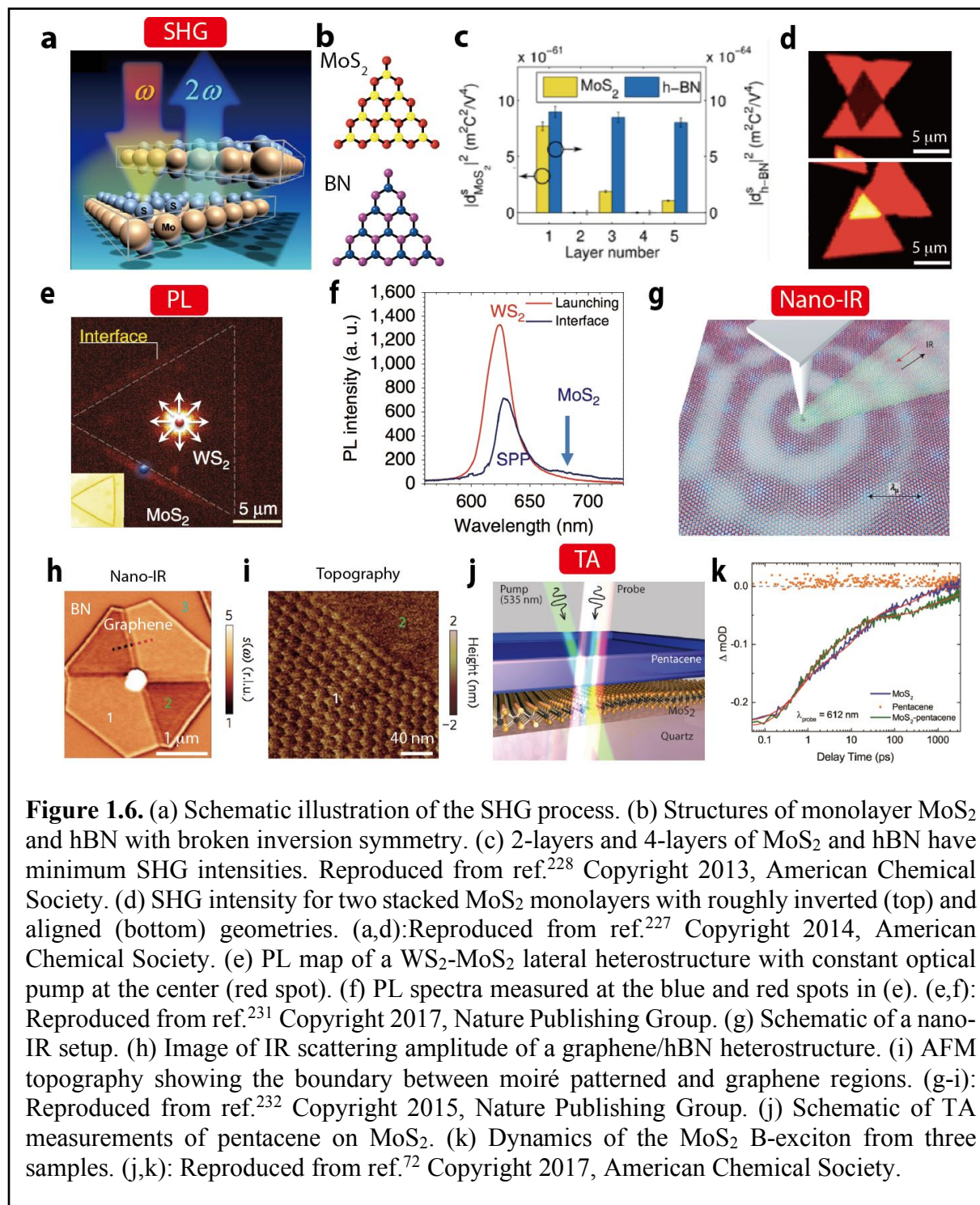


A surface acoustic standing wave resulting from interference of the two launched waves is modulated by subsurface inhomogeneities and detected by the AFM cantilever. This method has been used to resolve internal structural voids²²⁰ (**Fig. 1.5a,b**) and intracellular structures.²²¹ On the other hand, in scanning microwave microscopy an electromagnetic wave (in the microwave range) is transmitted by the AFM cantilever and the reflected signal is also collected by the cantilever and analyzed through a vector network analyzer to deduce the power ratio of the incident and reflected waves.²²² This technique has been shown to resolve not only the lateral location of a buried (14 nm deep) thin layer (0.2 nm thick) of phosphorus in Si, but also its vertical depth.²²³ In ultrasonic force microscopy (UFM), ultrasonic vibration of the sample stage at a frequency much higher than

the AFM cantilever resonant frequency periodically modulates the indentation depth of the contact-mode AFM tip into the sample. At a critical vibration amplitude, the contact is broken, which depends on the local mechanical stiffness. By comparing the topography (**Fig. 1.5c**) and UFM (**Fig. 1.5d**) images, suspended and supported regions of MoS₂ on textured substrates has been resolved.²²⁴ In a similar technique called contact resonance atomic force microscopy, the substrate vibration is kept at the resonant frequency of the coupled tip-sample system. Spatial variations of the sample stiffness due to subsurface features shifts the resonant frequency and thus allows subsurface atomic structures such as the buffer-layer, monolayer, and bilayer graphene regions of epitaxial graphene on SiC to be resolved.²²⁵ A complete survey of nanoscale subsurface imaging techniques has been provided in a recent review article.²²⁶

1.4.3. Characterization with Optical Techniques

Compared to scanning probe methods, optical spectroscopy is not a surface-sensitive technique but rather measures the adsorption and emission of light down to the depth of light penetration. While the atomic distances in crystals are far smaller than the wavelength of visible light, the crystal symmetry imposed by the atomic structures has profound influence on optical processes. For example, Raman tensors relating scattered light with incident light are dependent on crystal structure with anisotropic and chiral structures typically resulting in anisotropic and chiral optical responses. On the other hand, second-harmonic generation (SHG) is an even order nonlinear optical effect that only takes place in crystals without inversion symmetry. As depicted in **Fig. 1.6a**, due to anharmonic interactions, photons with twice the energy of the incident ones are emitted, resulting in a doubling of the frequency (2ω) of the incident light (ω).²²⁷ In addition to indexing crystallographic orientations resembling angle-dependent Raman and absorption



spectroscopy, SHG has been utilized to reveal interfacial lattice alignment of 2D bilayer heterostructures. Monolayers (and odd number of layers) of MoS₂ (and other 2H-phase TMDCs)

and hBN have broken inversion-symmetry due to inequivalent atomic sites as shown in **Fig. 1.6b**. Via AB stacking or interlayer rotation of 60° , inversion symmetry is restored in bilayers (and even number of layers) of MoS₂ and hBN, which minimizes the SHG signal (**Fig. 1.6c,d**).^{227,228} For centrosymmetric 2D materials like BP, third harmonic generation is more suitable.^{229,230} Although the signal intensity is much lower for higher order multiphoton processes, high-harmonic generations up to 13th order have been detected in MoS₂.²³³

Compared with nonlinear optical microscopy, photoluminescence (PL) and absorption spectroscopies offer quick and straightforward characterization of interfacial charge and energy transfer in 2D heterostructures. Using PL spectroscopy, a vast amount of literature has focused on interlayer excitons in heterostructures with type-II band alignment, where optically excited electrons and holes relax into individual layers but remain bounded. The recombination of these spatially indirect excitons emit light with a lower energy than the intralayer excitons and thus can be distinguished via PL spectroscopy. The intensity of interlayer exciton emission dictates the extent of interfacial charge transfer and thus the electronic coupling strength.²³⁴ Most of the studies along these lines have been carried out on TMDC heterojunctions with rich exciton and valley physics.^{235,236} Specifically for the MoSe₂/WSe₂ heterostructure, the interlayer exciton shows nontrivial temperature-dependent energy and linewidth,²³⁷ as well as a long lifetime (~ 1.8 ns) that is an order of magnitude longer than intralayer excitons.²³⁸ This heterostructure has also been utilized in an interlayer electroluminescent device.²³⁹ Similarly, excitation intensity dependent PL has been shown in the MoS₂/WS₂ heterostructure.²⁴⁰ While weak interlayer coupling and charge transfer has been observed in mechanically stacked MoS₂/WS₂ heterostructures,²⁴¹ interlayer exciton emission is only observed in CVD-grown MoS₂/WS₂ vertical heterostructures with well-defined interfaces,²⁴² which shows that interlayer exciton emission is a sensitive indicator of

interfacial interactions. With similar optical techniques, fast interfacial energy transfer involving WS_2 excitons resonantly exciting MoSe_2 excitons has been revealed.²⁴³ However, as shown in **Fig. 1.6e**, a different approach is taken for characterizing the 1D interface of a MoS_2/WS_2 lateral heterostructure. In this case, an excitation laser is incident at the center WS_2 region. With the aid of a silver plasmonic substrate, the excitonic energy is transferred to surface plasmon polaritons (SPPs) that then propagate to the lateral interface with MoS_2 .²³¹ In this case, both WS_2 and MoS_2 PL emission is detected (**Fig. 1.6f**), demonstrating the possibility of cascaded excitonic energy transfer assisted by SPPs.

Optical spectroscopy offers great versatility, but typically has diffraction-limited spatial resolution. However, when it is combined with localized optical excitation or detection with a scanning probe tip, the diffraction limit can be exceeded. Examples include tip-enhanced Raman and fluorescence spectroscopy, where the electric field is locally enhanced by the tip apex.^{244,245} Similarly, scanning near-field optical microscopy (SNOM) beats the diffraction limit by utilizing the evanescent field of a laser beam through the hole in an AFM tip to locally excite the sample.²⁴⁶ As schematically shown in **Fig. 1.6g**, infrared (IR) light is focused on the AFM tip over a graphene/hBN vertical heterostructure.²³² Scattering-type SNOM is then used to perform nano-IR measurements, where the scattered IR light is collected in the far field.²⁴⁷ By mapping the IR back-scattering at a selected frequency, two domain structures are revealed with contrasting scattering amplitudes (**Fig. 1.6h**). The high-resolution topography image in **Fig. 1.6i** suggests that the IR imaging contrasts results from different registries between the graphene and underlying hBN.

Finally, optical spectroscopy offers much higher temporal resolution than conventional scanning probe techniques. Time-resolved optical spectroscopy is typically based on the pump-probe technique, where a strong pump pulse optically excites the sample, and a weaker probe pulse

examines the dynamics of excited states as a function of pump-probe pulse delay. **Fig. 1.6j** provides an example of this method being applied to a pentacene/MoS₂ heterostructure.⁷² Pump-probe optical spectroscopy is particularly well-suited for the study of interfacial charge and energy transfer dynamics.^{238,248-250} For instance, in MoS₂/WS₂ heterostructures, ultrafast charge transfer⁶⁷ and the formation of interlayer hot excitons²⁴⁹ have been revealed using transient absorption (TA) and ultrafast visible/IR spectroscopy, respectively. Similarly, the kinetics of MoS₂ excitons in a pentacene/MoS₂ vertical p-n junction is shown in **Fig. 1.6k** as measured with TA.⁷²

Chapter 2: Few-Layer BP: Thermal Stability and Layer-by-Layer Thinning

This chapter is based partially on the following publications:

X. Liu*, C. R. Ryder*, S. A. Wells, and M. C. Hersam, Resolving the In-Plane Anisotropic Properties of Black Phosphorus, *Small Methods* **2017**, *1*, 1700143.

X. Liu, K.-S. Chen, S. A. Wells, I. Balla, J. Zhu, J. D. Wood, and M. C. Hersam, Scanning Probe Nanopatterning and Layer-by-Layer Thinning of Black Phosphorus, *Advanced Materials* **2017**, *29*, 1604121.

X. Liu*, J. D. Wood*, K.-S. Chen, E. Cho, and M. C. Hersam, In Situ Thermal Decomposition of Exfoliated Two-Dimensional Black Phosphorus, *Journal of Physical Chemistry Letters* **2015**, *6*, 773-778.

*These authors contribute equally.

2.1 Introduction to BP: a Highly Anisotropic Elemental 2D Material

As introduced in Chapter 1, layered materials consist of sheets of atoms that are bonded strongly in the in-plane direction and weakly in the out-of-plane direction. This fundamental anisotropy has been utilized in the past decade to exfoliate and study these materials in the 2D limit. The resulting 2D nanomaterials exhibit novel layer-dependent physical properties that differ from their bulk counterparts, and show significant promise for new technologies.²⁵¹

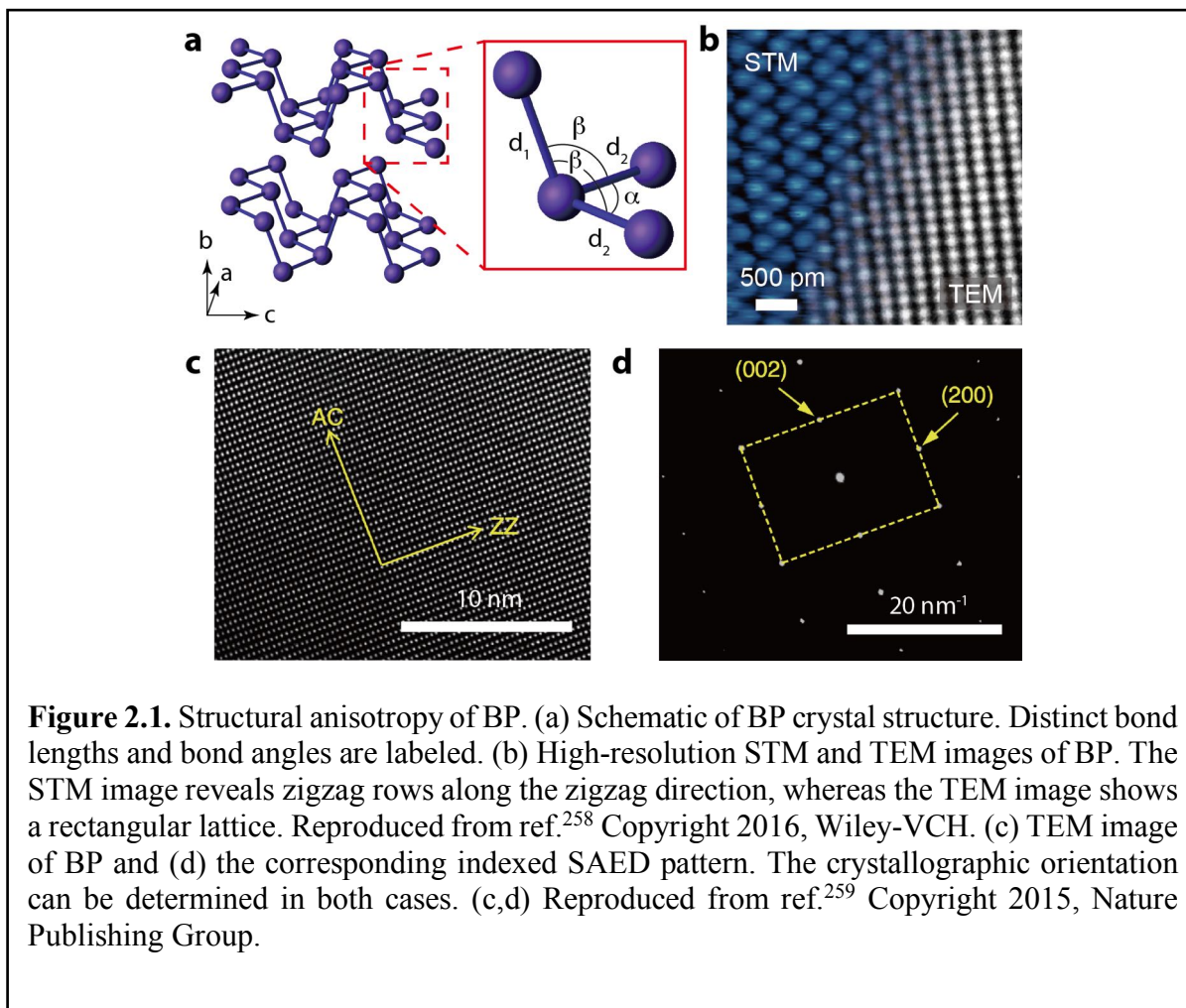
BP is a layered material that has recently been examined in this context.^{252,253} BP is a high mobility semiconductor with an additional in-plane anisotropy due to its differing bond lengths and bond angles along its orthogonal in-plane directions.²⁵⁴ The finite, direct bandgap and high charge carrier mobility of BP present advantages over previously studied 2D nanomaterials such as graphene and transition metal dichalcogenides. Consequently, exfoliated BP has produced noteworthy performance in prototype nanoscale electronic and optoelectronic devices.^{252,253,255}

Among the most distinctive characteristics of BP is its in-plane anisotropy, which provides opportunities for fundamental studies and applications that are otherwise not possible with higher symmetry materials.²⁵⁶ As the prototypical 2D nanomaterial with in-plane anisotropy, BP also serves as a model system that is informing investigations of other emerging anisotropic 2D nanomaterials including ReS₂,²⁵⁷ and borophene.^{11,12} Therefore, organized based on various anisotropic properties of BP, this introduction section of Chapter 2 is aimed to provide an overview of the material properties and characterization techniques of this emerging 2D material, setting the foundation for the exploration of thermal stabilities and layer-by-layer thinning of 2D BP that would be discussed later in the chapter.

2.1.1. Structural Anisotropy

BP is the most stable phosphorus allotrope, and exists as a layered van der Waals crystal with an orthorhombic structure at room temperature and pressure. As shown in **Fig. 2.1a**, the two in-plane directions are defined as **a** and **c**, and the out-of-plane direction is defined as **b**. The unit cell dimensions of bulk BP are $a = 3.314 \text{ \AA}$, $b = 10.478 \text{ \AA}$, and $c = 4.376 \text{ \AA}$, with the inter-layer distance being 5.239 \AA .²⁶⁰ Similar to graphene, each phosphorus atom is bound to three neighbors. However, unlike graphene, BP displays out-of-plane distortion resulting in a ridge structure along the zigzag direction (i.e., **a** direction) and a puckered structure along the armchair direction (i.e., **c** direction), and thus non-equal bond lengths ($d_1 = 2.244 \text{ \AA}$, $d_2 = 2.224 \text{ \AA}$) and bond angles ($\alpha = 96.34^\circ$, $\beta = 102.09^\circ$). This structure leads to substantial in-plane anisotropy and resembles the hinge-like structure seen in artificially engineered auxetic materials. As a result, monolayer BP exhibits a negative Poisson ratio.^{261,262}

The anisotropic in-plane structure of BP can be visualized via microscopy and diffraction methods. By cleaving a bulk crystal to expose the a - c plane, STM images reveal atomic chains of BP along the zigzag direction as demonstrated in the left portion of **Fig. 2.1b**.^{258,263,264} Exfoliated BP layers can also be visualized with high-resolution TEM (right portion of **Fig. 2.1b**).^{18,259} The



in-plane orientation of BP sheets is determined by comparing the lattice spacing along two orthogonal directions, or by performing SAED (**Fig. 2.1c, d**). While these methods are imperative for determining crystallographic orientations of BP sheets with nanoscale lateral dimensions, larger samples with dimensions greater than the wavelength of visible light can also be analyzed with optical methods as discussed below.

2.1.2. Optical Anisotropy

The electronic structure of monolayer BP has markedly different behavior along the in-plane armchair and zigzag directions as determined by angle-resolved photoemission spectroscopy (ARPES) in **Fig. 2.2a**. Consequently, the dielectric function of BP is anisotropic, leading to variations in the real and imaginary parts of the complex refractive index as a function of crystallographic direction.²⁶⁵ Furthermore, transitions from the valence band maximum to the conduction band minimum are symmetry forbidden for the zigzag direction.^{265,266} These characteristics result in BP having anisotropic optical properties, which have been observed predominantly in measurements involving linearly polarized light at different angles with respect to the BP crystal structure.

Exfoliated BP exhibits a linear dichroism, which has been observed in polarization-dependent optical absorption,^{266,268} extinction,²⁵³ transmission,²⁶⁶ and reflection measurements.^{32,266,269} The earliest characterization was performed on thick exfoliated samples via infrared spectroscopy, where light polarized along the armchair direction showed greater extinction in the infrared range.²⁵³ These measurements also revealed a distinct peak at the bulk-like optical bandgap of ~ 0.3 eV, which was absent in measurements along the zigzag direction.²⁵³ Similar observations were subsequently made in thinner samples, with BP exhibiting enhanced absorption for incident light polarized along the armchair direction at visible wavelengths.^{268,270} Recently interband excitation resonances were observed in the reflectance spectrum of 1 to 5 layer thick exfoliated BP for armchair-polarized light, resulting in overall greater reflectance for light polarized along the armchair-direction compared to the zigzag direction.³² The anisotropic dielectric function and birefringence of BP also lead to polarization-dependent optical contrast at

visible wavelengths. In particular, the optical contrast of exfoliated BP on SiO₂/Si and fused silica substrates has been observed to change (i.e., the red, blue, and green levels varied in intensity)

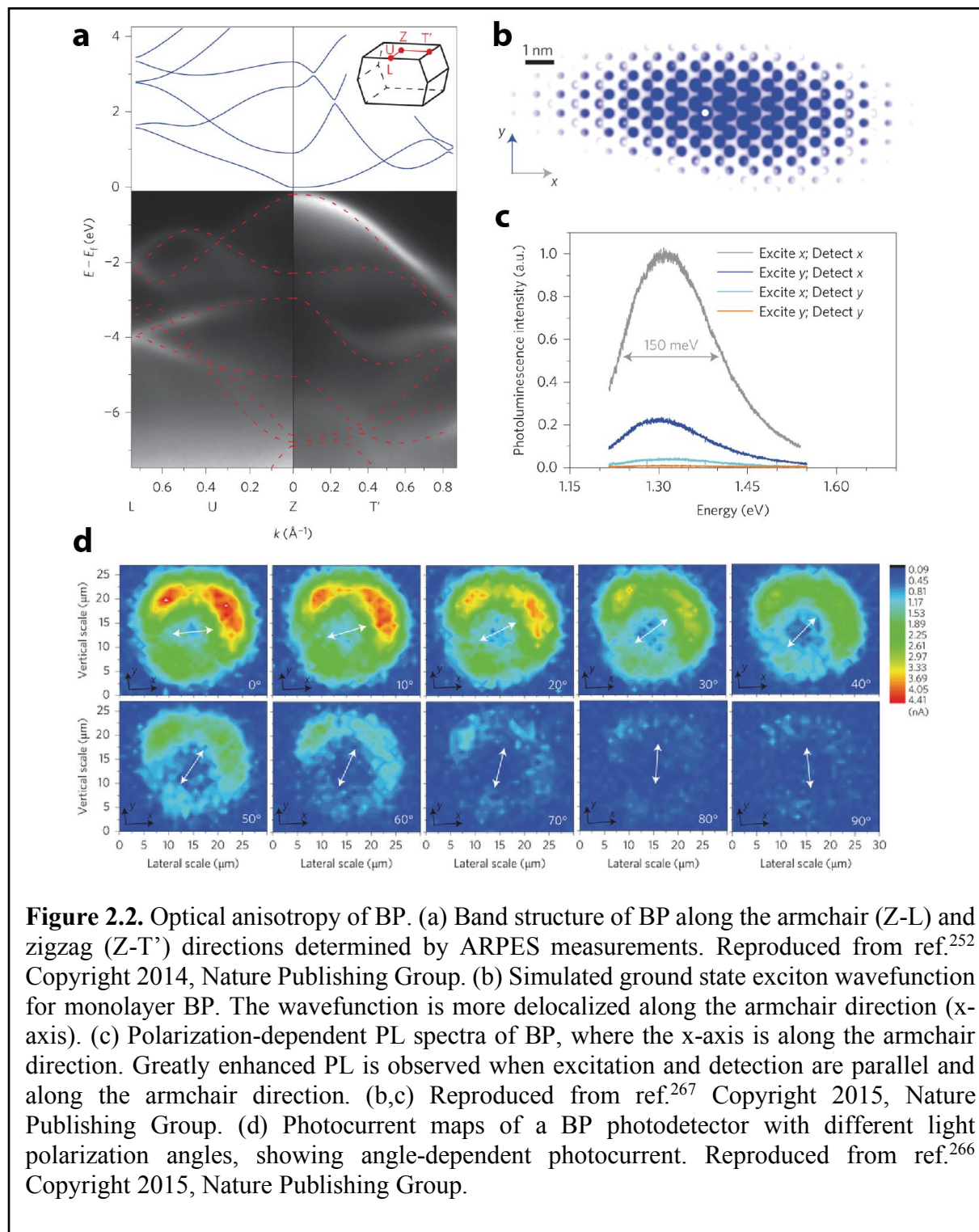


Figure 2.2. Optical anisotropy of BP. (a) Band structure of BP along the armchair (Z-L) and zigzag (Z-T') directions determined by ARPES measurements. Reproduced from ref.²⁵² Copyright 2014, Nature Publishing Group. (b) Simulated ground state exciton wavefunction for monolayer BP. The wavefunction is more delocalized along the armchair direction (x-axis). (c) Polarization-dependent PL spectra of BP, where the x-axis is along the armchair direction. Greatly enhanced PL is observed when excitation and detection are parallel and along the armchair direction. (b,c) Reproduced from ref.²⁶⁷ Copyright 2015, Nature Publishing Group. (d) Photocurrent maps of a BP photodetector with different light polarization angles, showing angle-dependent photocurrent. Reproduced from ref.²⁶⁶ Copyright 2015, Nature Publishing Group.

under white light illumination when rotating the sample with respect to a fixed polarizer.²⁶⁹

The anisotropic electronic structure of BP also manifests itself in a crystallographic direction dependence for the recombination of charge carriers. The exciton wavefunctions of monolayer BP have been calculated to have significant directionality, with the probability density being more disperse in the armchair direction (**Fig. 2.2b**).²⁷¹ The PL emission of monolayer BP is similarly enhanced when measured parallel to the armchair direction (**Fig. 2.2c**). However, due to the linear dichroism of BP, this emission is also strongly dependent on the excitation polarization. The combination of these two effects yields PL emission that is ~100 times greater for measurements made with both the excitation and detection oriented parallel to the armchair direction as compared to measurements along the zigzag direction.²⁶⁷

Overall, the photon-electron interactions are more pronounced when incident light is polarized along the BP armchair direction as opposed to the zigzag direction. Therefore, optical absorbance, transmittance, and reflection characterization provides a means for indexing the crystallographic directions of BP. Optical anisotropy further provides opportunities for polarization-dependent linear and nonlinear optical device applications based on exfoliated BP. For example, BP photodetectors exhibit enhanced photoresponsivity for light polarized along the armchair direction (**Fig. 2.2d**),^{266,272} which has been further amplified by applying a gate field to form a vertical *p-n* junction.²⁶⁶ The anisotropic nonlinear optical properties of exfoliated BP have also been utilized to create polarized ultrafast optical pulse generators via anisotropic saturable absorption²⁷⁰ in addition to polarized frequency converters via anisotropic third harmonic generation.^{229,230} Moreover, the plasmon dispersion of BP is anisotropic, thus providing another degree of freedom in BP-based plasmonic devices.

2.1.3. Vibrational Anisotropy

Raman spectroscopy is a commonly employed technique for characterizing 2D nanomaterials, and has been widely used in exfoliated BP studies. Raman spectroscopy measures

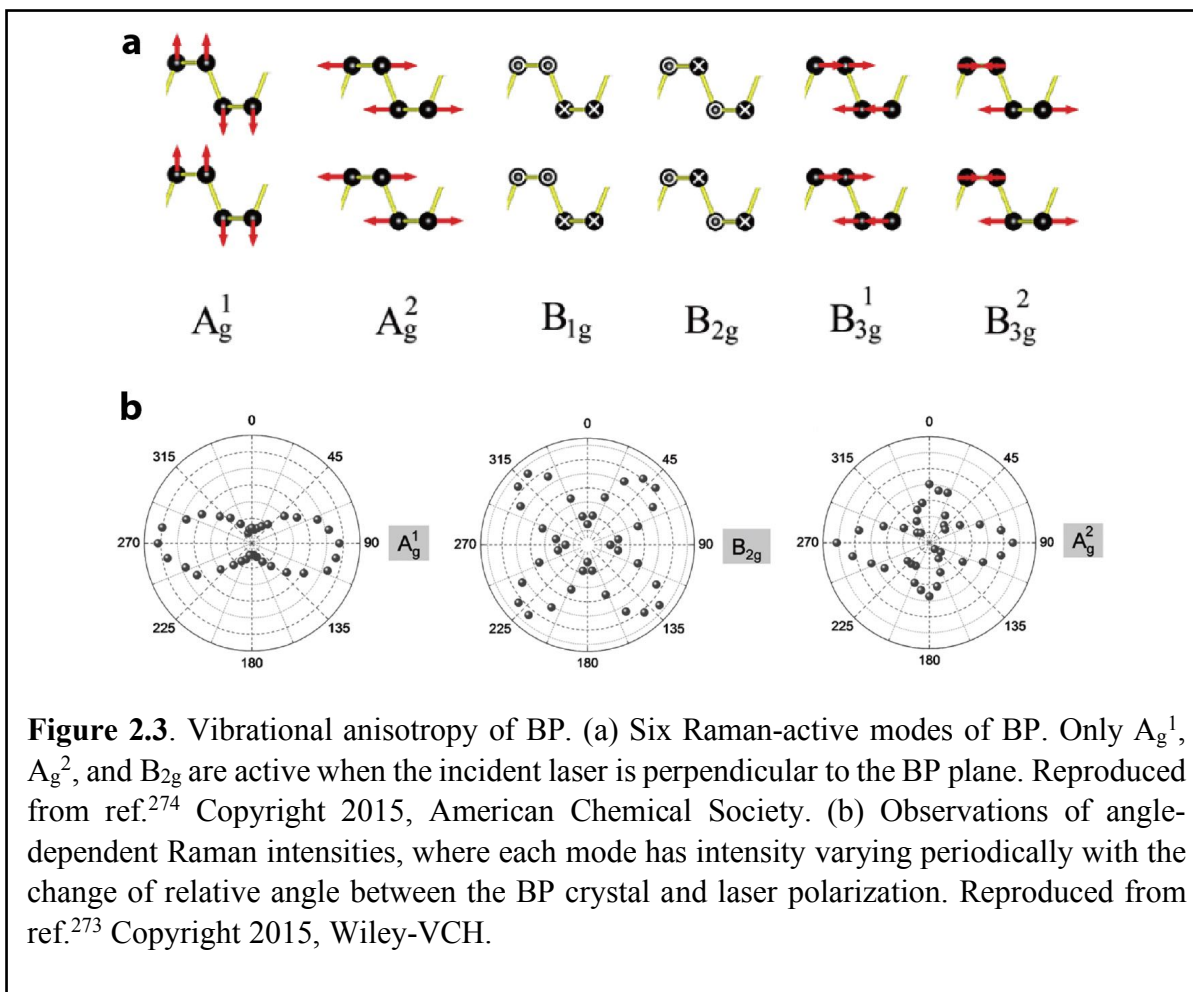


Figure 2.3. Vibrational anisotropy of BP. (a) Six Raman-active modes of BP. Only A_g^1 , A_g^2 , and B_{2g} are active when the incident laser is perpendicular to the BP plane. Reproduced from ref.²⁷⁴ Copyright 2015, American Chemical Society. (b) Observations of angle-dependent Raman intensities, where each mode has intensity varying periodically with the change of relative angle between the BP crystal and laser polarization. Reproduced from ref.²⁷³ Copyright 2015, Wiley-VCH.

light, typically originating from a laser, which has been inelastically scattered by lattice vibrations.

The scattered light intensity I is dependent on the polarizations of the incident (\mathbf{e}_i) and scattered light (\mathbf{e}_s), and the Raman tensor (\mathbf{R}) of the Raman mode:²⁷³ $I \propto |\mathbf{e}_i \times \mathbf{R} \times \mathbf{e}_s|^2$. Consequently, crystallographic information is embedded in the measured Raman response, which suggests that crystallographic indexing can be achieved through systematic analysis of the polarization-dependent Raman spectra.

Bulk BP has six Raman-active modes with three of them (A^1_g , B_{2g} , and A^2_g) being Raman active when the incident laser is aligned perpendicular to the basal plane (**Fig. 2.3a**).²⁷³ The A^1_g mode is an out-of-plane vibration, whereas the B_{2g} and A^2_g modes are in-plane vibrations along the zigzag and armchair directions, respectively. Thus, the in-plane B_{2g} and A^2_g modes are sensitive to uniaxial strain along the zigzag direction, while the A^1_g mode is more sensitive to strain along the armchair direction.²⁷⁵ Experimentally, the three Raman modes of BP periodically vary in intensity when the relative angle between the incident laser polarization and the BP crystal orientation is rotated.^{253,267,276} For example, early experimental observations demonstrated that the A^2_g (B_{2g}) mode intensity is highest (lowest) when the laser is polarized along the armchair direction.

Analysis of the intensity variations of the BP Raman modes is simplified by using polarization filters on the excitation light *and* the Raman scattered light, and by orienting these polarizations either parallel or perpendicular with respect to each other.^{268,273,274,277} For example, **Fig. 2.3b** shows periodic variations of the Raman intensities when the polarizations are parallel. In this condition, it has been observed that the A^2_g mode exhibits the highest intensity when the laser is polarized along the armchair direction (i.e., the horizontal direction in **Fig. 2.3b**), and thus polarized measurements of the A^2_g mode intensity have been used for identifying the crystal orientation of BP.²⁷³ In the same polarization orientation, the dependence of the B_{2g} mode (**Fig. 2.3b**) typically has four maxima that are equivalent in intensity and occur when the polarization is incident between the armchair and zigzag directions. The intensity minima of the B_{2g} mode occur when the polarization is along the armchair and zigzag directions where the B_{2g} mode is symmetry-forbidden. Likewise, the symmetry of the low-frequency interlayer Raman breathing modes produces a polarization dependence that can be used to determine the crystallographic orientation of BP.²⁷⁷

However, it should be noted that Raman spectroscopy of exfoliated BP involves both anisotropic optical properties (e.g., linear dichroism and linear birefringence) and anisotropic electron-phonon interactions. Therefore, to properly fit the polarization dependence of the high frequency Raman modes (e.g., the A_g^1 and the A_g^2 modes), details of the optical absorption need to be considered. Specifically, the imaginary parts of the dielectric function tensor should be included in the analysis, as the elements of the Raman tensor \mathbf{R} are determined from the derivative of the corresponding dielectric function tensor elements with respect to normal coordinates.^{268,274} Furthermore, the Raman response varies as a function of the excitation laser wavelength and BP flake thickness, which creates counterintuitive results in some cases where the maximum intensity of the A_g modes occur along the zigzag direction instead of the armchair direction.^{268,278} This reversal in the intensity dependence as a function of BP in-plane crystallography may account for some apparently contradictory results in the literature that assigned the high conductivity axis of BP to the zigzag direction.²⁷⁹ Therefore, significant care must be taken when attempting to index BP crystallography with polarized Raman measurements.

2.1.4. Electronic and Electrical Anisotropy

Due to the anisotropic dispersion relation of BP along the armchair and zigzag directions, the effective masses of holes and electrons are smaller along the armchair direction than those along the zigzag direction,^{266,280} resulting in high electronic anisotropy. Using multi-face Hall effect measurements on bulk BP single crystals, the highest mobility and conductivity have been observed along the armchair direction, while the zigzag and the out-of-plane directions show lower and lowest mobilities, respectively (**Fig. 2.4a**).²⁵⁴ The ratio of the mobilities holds constant at all temperatures, indicating that the degree of anisotropy in the band structure or anisotropy of

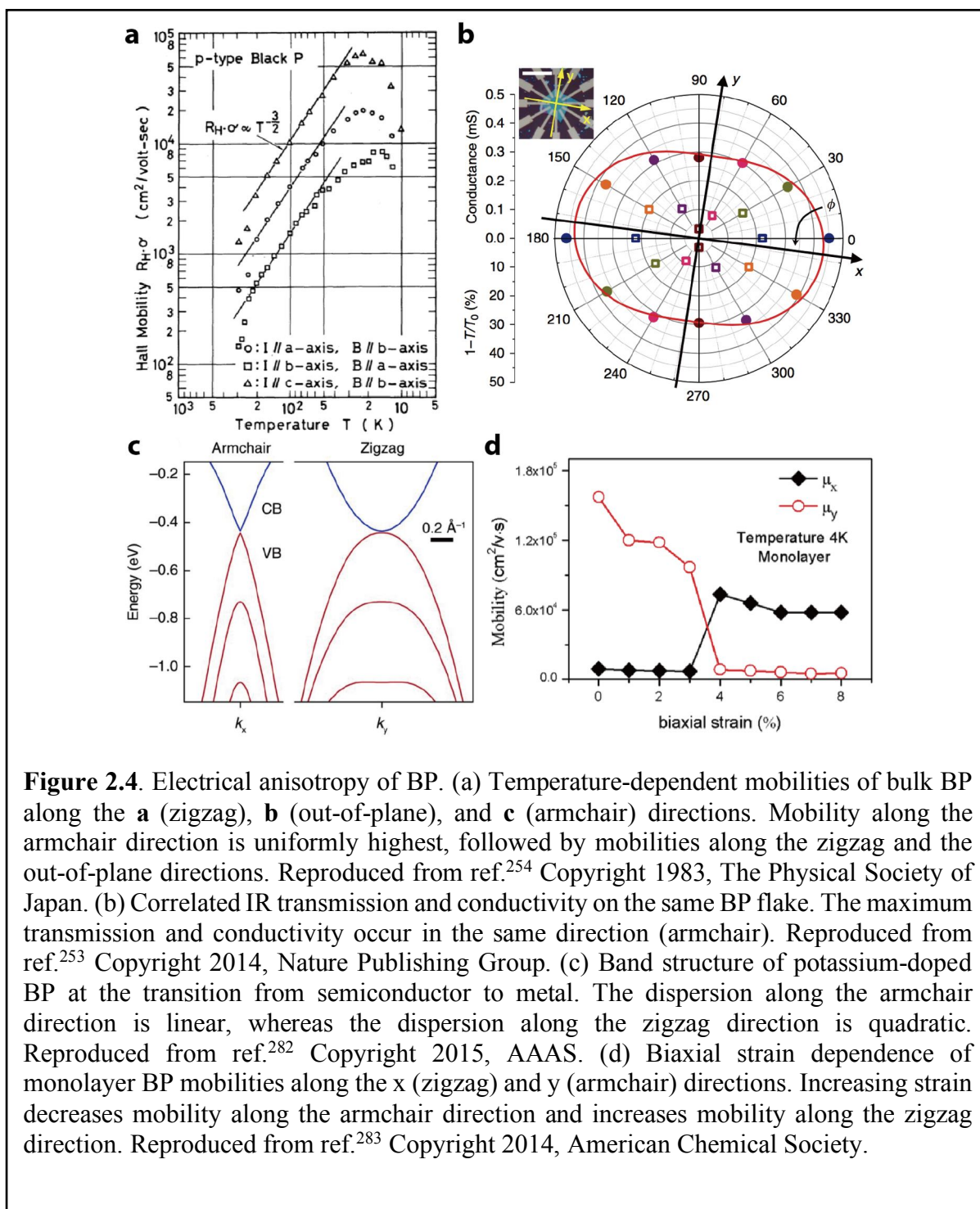


Figure 2.4. Electrical anisotropy of BP. (a) Temperature-dependent mobilities of bulk BP along the **a** (zigzag), **b** (out-of-plane), and **c** (armchair) directions. Mobility along the armchair direction is uniformly highest, followed by mobilities along the zigzag and the out-of-plane directions. Reproduced from ref.²⁵⁴ Copyright 1983, The Physical Society of Japan. (b) Correlated IR transmission and conductivity on the same BP flake. The maximum transmission and conductivity occur in the same direction (armchair). Reproduced from ref.²⁵³ Copyright 2014, Nature Publishing Group. (c) Band structure of potassium-doped BP at the transition from semiconductor to metal. The dispersion along the armchair direction is linear, whereas the dispersion along the zigzag direction is quadratic. Reproduced from ref.²⁸² Copyright 2015, AAAS. (d) Biaxial strain dependence of monolayer BP mobilities along the x (zigzag) and y (armchair) directions. Increasing strain decreases mobility along the armchair direction and increases mobility along the zigzag direction. Reproduced from ref.²⁸³ Copyright 2014, American Chemical Society.

scattering do not substantially evolve with decreasing temperature. These observations have been confirmed for few-layer BP, where the measured electrical conductance^{253,273,281} and carrier

mobilities^{259,281} along the armchair direction are typically higher than those along zigzag directions (**Fig. 2.4b**).²⁵³ This electrical anisotropy manifests itself in large sample-to-sample variations for reported two-terminal BP transistor mobilities when the crystal orientation is not explicitly determined.

The electronic anisotropy of BP is further evident upon external perturbation. For example, the non-equivalent effective mass suggests that excitons in BP should respond differently along the two orthogonal in-plane directions and have different polarizabilities under an external in-plane electric field. While a Stark shift is expected universally for excitons, the shift of binding energies is direction-dependent in BP due to its anisotropic band structure.²⁸⁴ In the extreme case, when BP is chemically doped with potassium, the enhanced Stark effect begins to close the bandgap of BP.²⁸² At the critical doping level when BP becomes a semimetal, a linear dispersion (i.e., massless carriers) is obtained along the armchair direction, whereas a quadratic dispersion is present along the zigzag direction (**Fig. 2.4c**). Numerically, increasing biaxial or uniaxial strain causes the material to become more isotropic, with the zigzag and armchair mobilities being equal at 3-4% biaxial strain or 5-6% zigzag-direction uniaxial strain.²⁸³ Further increases in strain are predicted to reverse the mobility trend in BP, yielding a material with higher mobilities in the zigzag direction as shown in **Fig. 2.4d**.

2.1.5. Thermal and Mechanical Anisotropy

Recently, several reports have demonstrated higher thermal conductivity along the zigzag direction compared to the armchair direction in exfoliated BP.^{259,285,286} The anisotropic thermal conductivity of BP has been attributed to its anisotropic phonon dispersion (**Fig. 2.5a**), whereas the electronic contribution to the thermal conductivity is effectively negligible.²⁸⁵ The thermal

conductivity anisotropy is orthogonal to the electrical conductivity anisotropy, which has potential utility in thermoelectrics.²⁸⁸

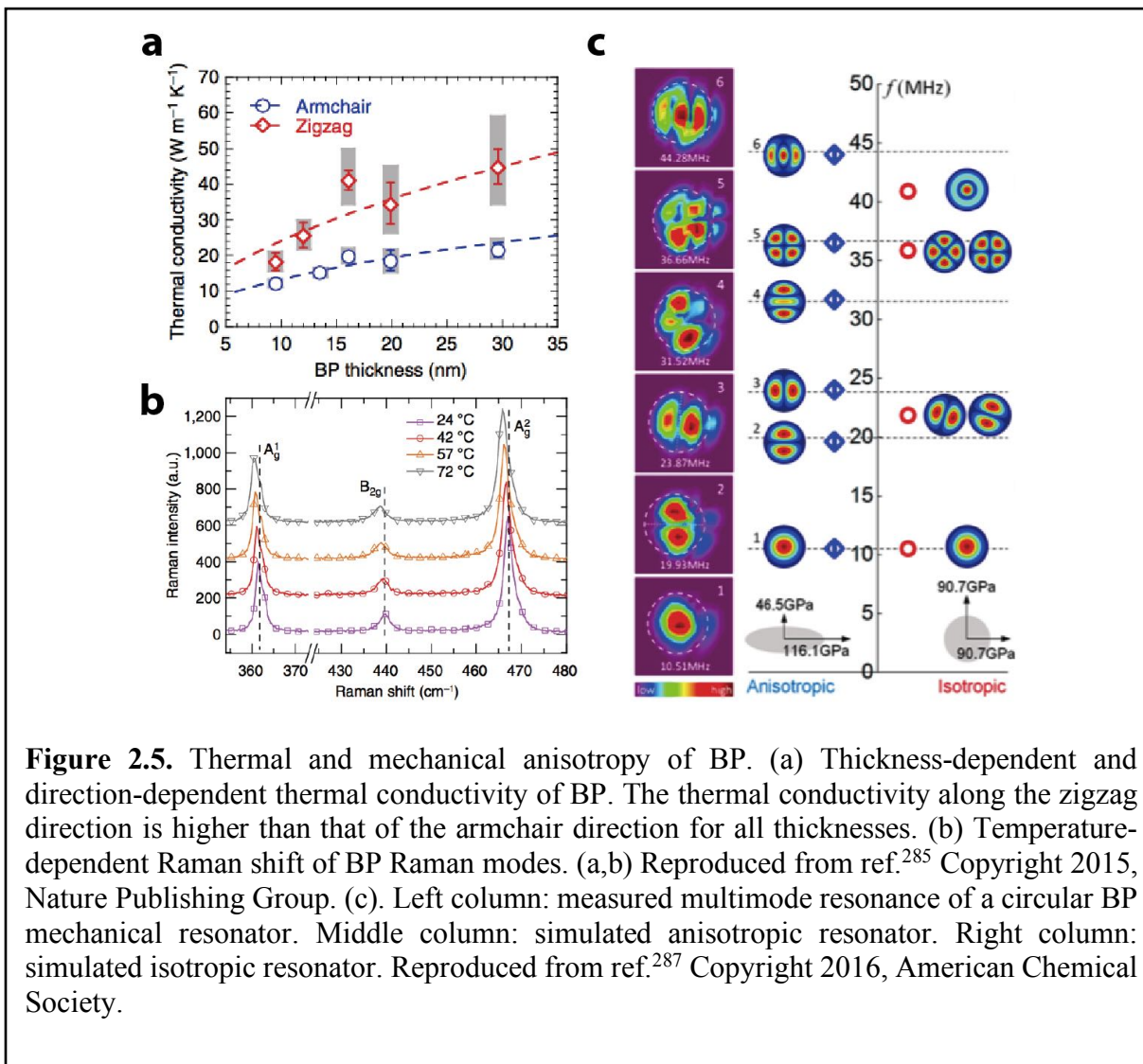


Figure 2.5. Thermal and mechanical anisotropy of BP. (a) Thickness-dependent and direction-dependent thermal conductivity of BP. The thermal conductivity along the zigzag direction is higher than that of the armchair direction for all thicknesses. (b) Temperature-dependent Raman shift of BP Raman modes. (a,b) Reproduced from ref.²⁸⁵ Copyright 2015, Nature Publishing Group. (c). Left column: measured multimode resonance of a circular BP mechanical resonator. Middle column: simulated anisotropic resonator. Right column: simulated isotropic resonator. Reproduced from ref.²⁸⁷ Copyright 2016, American Chemical Society.

Thermal conductivity measurements along in-plane BP directions have been achieved in several ways. Direct measurements have been performed on suspended BP ribbons that were lithographically defined along either the armchair or zigzag directions.²⁵⁹ In Raman thermography measurements, it was found that all three of the BP high-frequency Raman modes shift with temperature changes (**Fig. 2.5b**), with the A_{2g} mode being most sensitive, and that measurements in the in-plane directions could be made by using a slit aperture to achieve an excitation laser focal

line.²⁸⁵ Thermal conductivity of exfoliated BP has also recently been determined by time-domain thermal reflectance (TDTR) measurements by orienting the pump and probe laser beam offsets in these directions, and measuring the variation in reflectance with laser heating.²⁸⁶ It is well-known that BP is susceptible to chemical degradation and that oxide species form on the surface in ambient conditions.¹⁷ While the aforementioned techniques are dissimilar, it is notable that TDTR measurements yielded the highest thermal conductivities for exfoliated BP and found lower thermal conductivities for samples that likely had greater oxidation.²⁸⁶ The Seebeck coefficient has also been determined to be greater in the zigzag direction than the armchair direction. However, unlike the thermal conductivity, the Seebeck coefficient has a large electronic contribution due to its proportional dependence on charge carrier effective mass.²⁸⁹

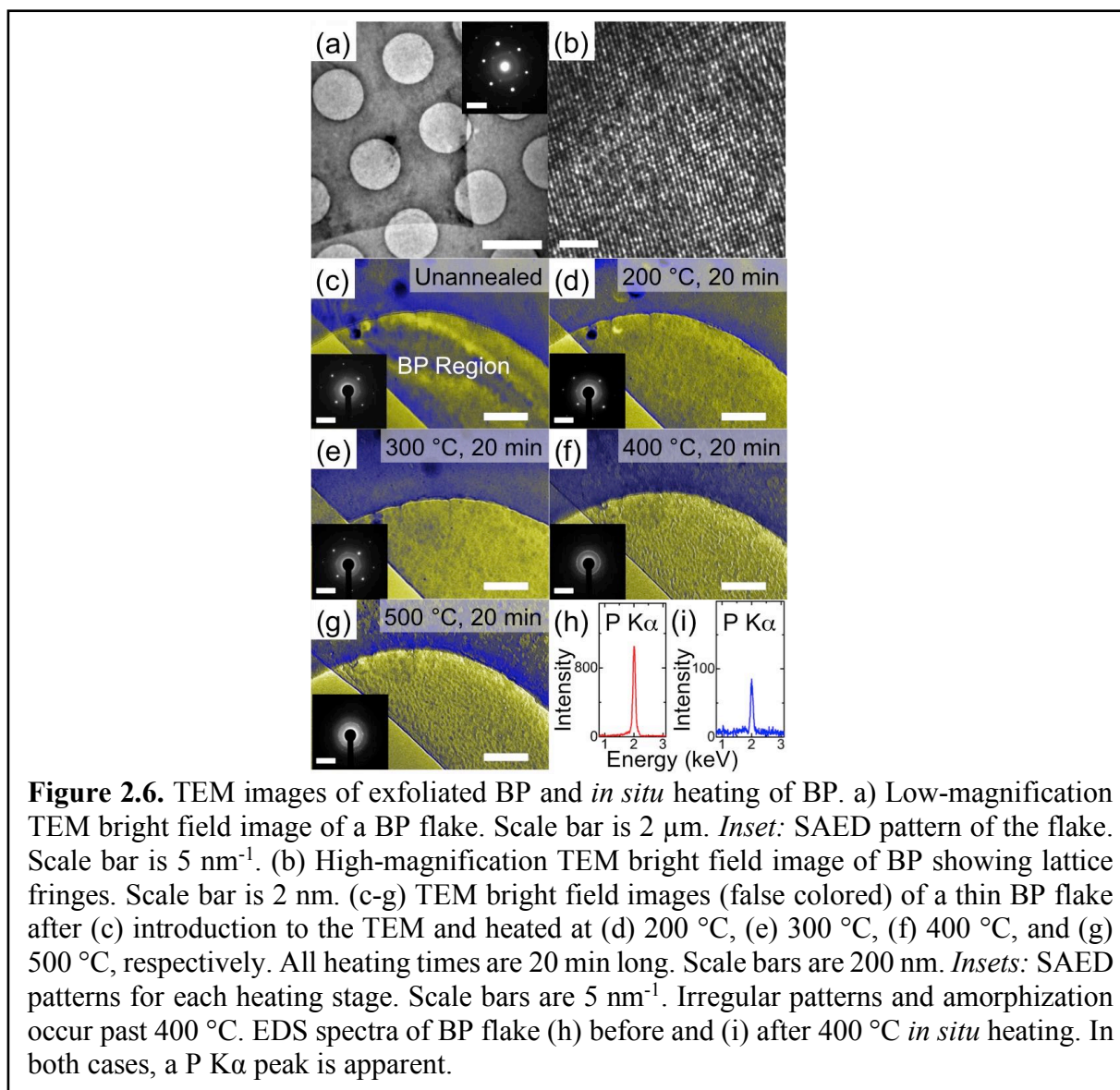
The anisotropic mechanical properties of BP are also a direct result of its highly anisotropic crystal structure. By performing atomic force microscopy indentation on lithographically defined BP ribbons along zigzag and armchair directions, the Young's modulus and fracture stress along the zigzag direction were found to be twice that along the armchair direction.^{281,287} This result is consistent with the ridge structure along the zigzag direction and the puckered structure along the armchair direction. This anisotropy in mechanical strength likely explains the observation that mechanically exfoliated BP flakes often have their straight long edges along the zigzag direction.^{278,285} Beyond direct mechanical tests with a physical probe, spatial mapping of the multimode resonance of BP membranes allows for nondestructive determination of crystallographic orientation as shown in **Fig. 2.5c**.²⁸⁷ Due to mechanical anisotropy, each normally degenerate vibrational mode in an isotropic material is split, forming a pair of modes that are offset in frequency. Since the zigzag direction has a higher Young's modulus, which corresponds to a

higher resonant frequency, the nodal line of the high frequency resonance pattern occurs along the armchair direction of BP.

2.2 Thermal Stability of BP

Although bulk BP is the most thermodynamically stable phosphorus allotrope, it can suffer from electrochemical and ambient oxidation.^{17,290,291} Since nanomaterials often show lower decomposition temperatures compared to their bulk counterparts, similar effects can be expected for 2D BP. Furthermore, even for bulk BP, there is little consensus on basic thermal stability parameters. Therefore, it is important to clarify thermal phenomena in 2D BP before it can be effectively employed in applications. To this end, we quantitatively assess the thermal decomposition of mechanically exfoliated BP via *in situ* S/TEM, allowing for chemical, morphological, and crystallographic decomposition intermediates to be determined by SAED, electron energy loss spectroscopy (EELS), energy-dispersive X-ray spectroscopy (EDS), and X-ray photoelectron spectroscopy (XPS).

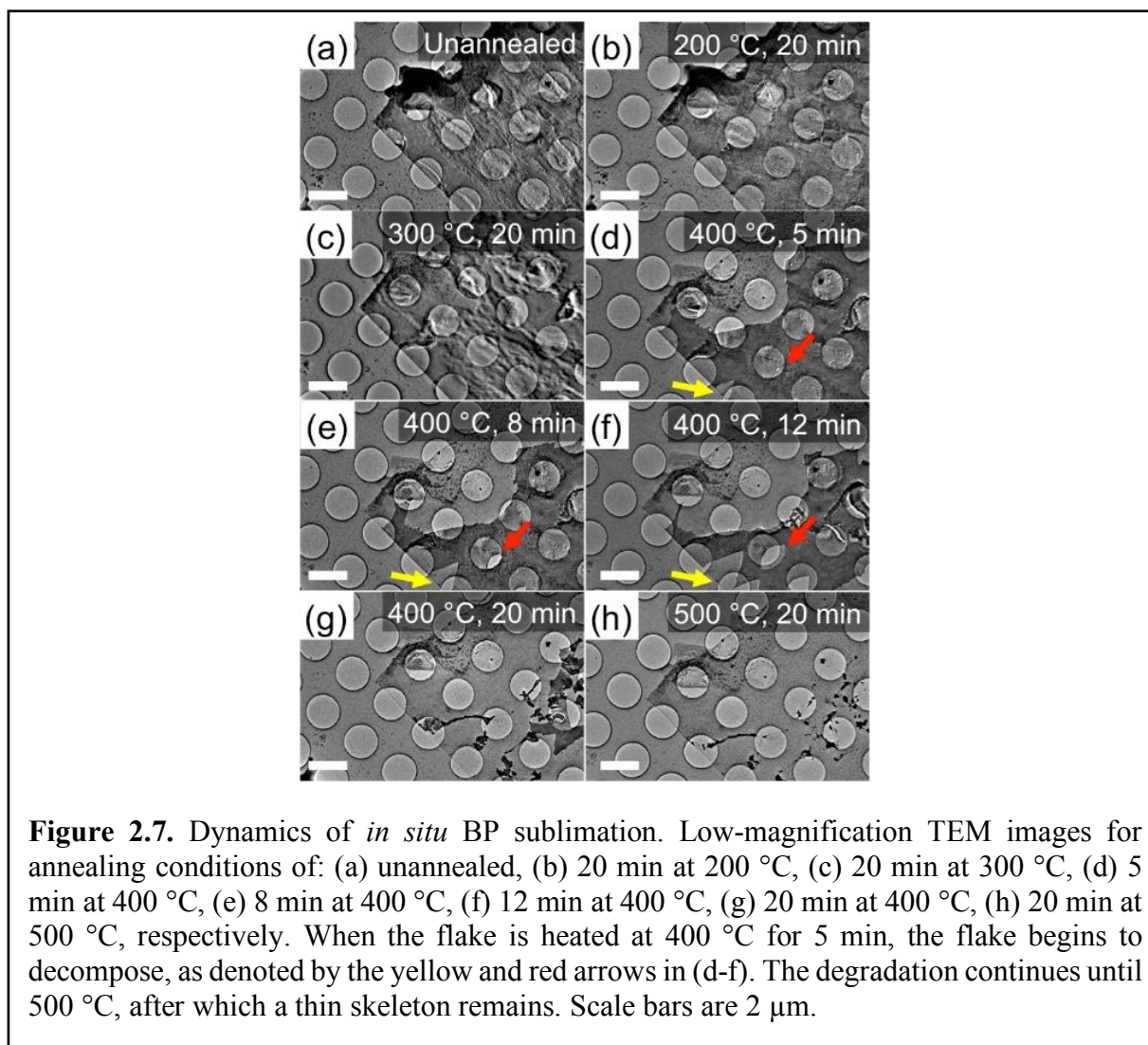
Fig. 2.6a reveals a bright field TEM image for an exfoliated BP flake, where the orthorhombic crystalline character is confirmed in the inset SAED pattern. **Fig. 2.6b** is a high-magnification image of BP showing lattice fringes. To minimize the influence of the electron beam while maintaining spatial resolution, a 120 to 200 keV acceleration voltage is used, and the sample is moved into the beam only when imaging (see Supporting Information for more details). The BP flakes are stored in dry N₂ until TEM is performed. **Figs. 2.6a,b** indicate that the BP flakes are



crystalline with no entrapped species¹⁷ or ambient degradation evident.²⁹¹ **Figs. 2.6c-g** show the edge of a BP flake at different annealing conditions with the insets providing the corresponding SAED patterns. Compared with the unannealed case (**Fig. 2.6c**) after 20 min of 200 $^{\circ}\text{C}$ annealing (**Fig. 2.6d**). The flake appears unchanged after further 300 $^{\circ}\text{C}$ annealing for 20 min (**Fig. 2.6e**) with SAED patterns showing unchanged BP crystal orientation. After annealing at 400 $^{\circ}\text{C}$ for 20 min (**Fig. 2.6f**), irregular patterns appear, and the SAED pattern indicates BP amorphization. The flake remains amorphous after 500 $^{\circ}\text{C}$ annealing for 20 min (**Fig. 2.6g**). EDS spectra for the flake

before (**Fig. 2.6h**) and after (**Fig. 2.6i**) annealing exhibit a P K α peak at 2 keV that decreases in intensity after annealing. This decrease can be attributed to the lower interaction volume in thinner BP flakes, as detailed below.

Fig. 2.7 considers the dynamics of BP amorphization at 400 °C, using low magnification



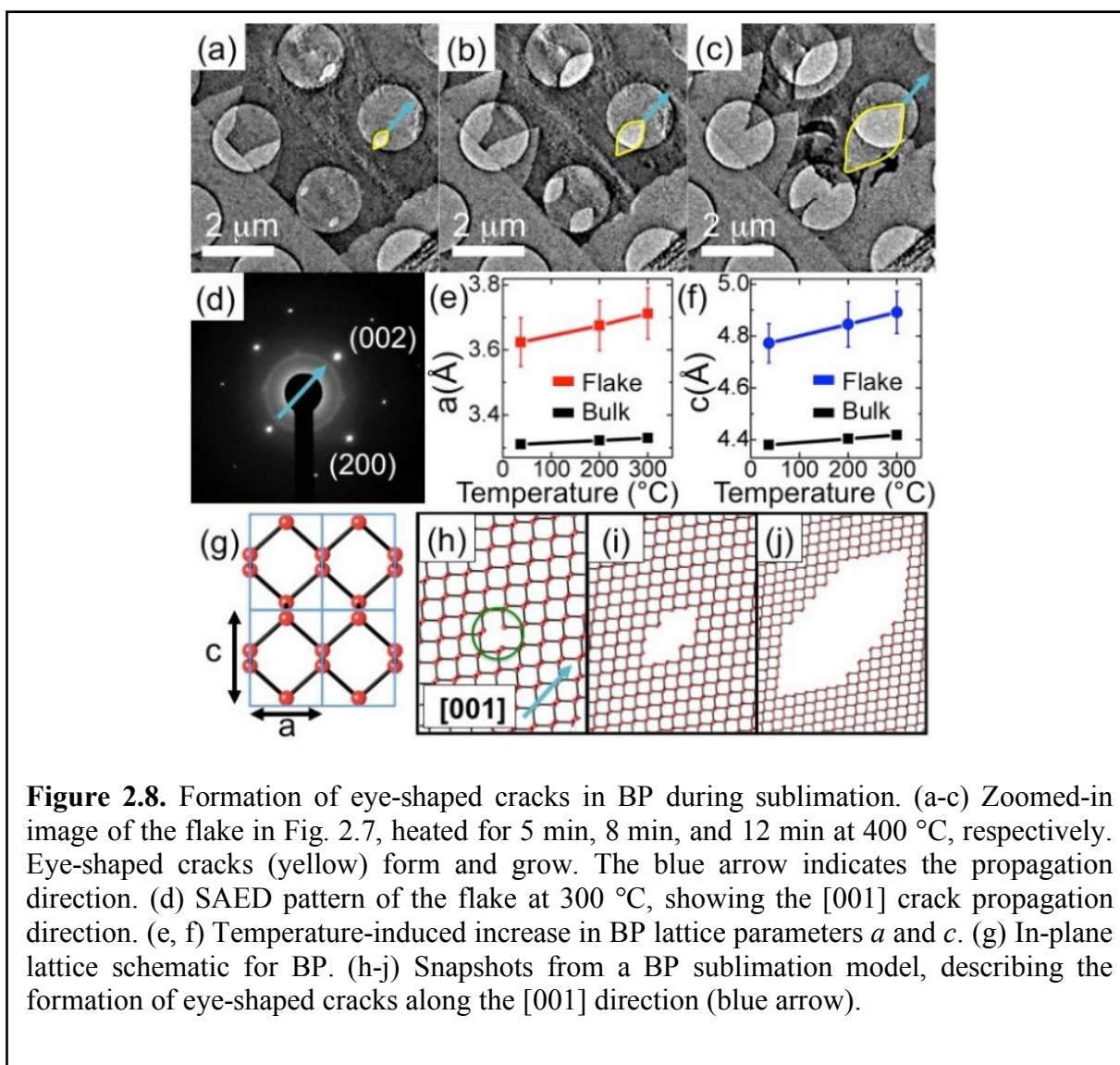
images of the flake from **Fig. 2.6**. **Figs. 2.7a-c** highlight the invariance of the flake to heating up to 300 °C. However, when the flake is heated at 400 °C for 5 min, the flake edge retracts, leaving a thin layer behind (**Fig. 2.7d**). Additional BP decomposition proceeds from the edges until 20 min exposure (**Figs. 2.7e-g**), after which a thin skeleton predominantly remains. This thin skeleton

withstands an additional 20 min of annealing at 500 °C (**Fig. 2.7h**) where it remains continuous over the holes of the Quantifoil TEM support. The SAED patterns and EDS spectra in **Figs. 2.6f-i** reveal that the skeleton is an amorphous phosphorus structure. Since a phosphorus skeleton remains and no liquid-like features appear during decomposition, the BP degradation in **Figs. 2.7d-g** appears to proceed by BP sublimation and not melting. Since the BP flakes transferred onto the TEM grid are 10 to 40 nm thick, their suppressed thermal decomposition temperature compared to the melting point of bulk BP is consistent with other low dimensional nanomaterials with high surface area to volume ratios.

BP sublimation occurs at flake edges and defects, and then propagates as eye-shaped cracks. **Figs. 2.8a-c** give higher magnification images of this crack evolution as the flake is heated to 400 °C for 5 min, 8 min, and 12 min, respectively. In **Fig. 2.8d**, a SAED pattern for this flake (taken at 300 °C) indicates that all cracks are along the [001] direction. Similar to the sublimation of graphene,²⁹² cracks grow larger and coalesce, but, unlike graphene, the BP cracks maintain a regular shape during sublimation. As such, the crystallographic structure of BP appears important in the decomposition mechanism. We first consider the effects of the *a-c* plane (hereafter “in-plane”) thermal expansion as the source of the oriented cracks. We can further estimate the coefficients of thermal expansion (CTE) values for the *a* and *c* lattice parameters using our SAED patterns. **Figs. 2.8e-f** examine six BP flakes and determine average *a* and *c* values from the SAED data. The error bar for each data point consists of standard deviation and TEM system error, estimated to be ±1%. We find that the CTE values of exfoliated BP flakes along the [100] and [001] directions are $\alpha_a = (90.3 \pm 6.4) \times 10^{-6}/^{\circ}\text{C}$ and $\alpha_c = (93.2 \pm 12.7) \times 10^{-6}/^{\circ}\text{C}$. Since the two in-

plane CTE values for exfoliated BP flakes are nearly identical, thermal expansion does not appear to be the main cause for the anisotropic, eye-shaped cracks.

However, the anisotropic, buckled atomic structure (**Fig. 2.8g**) of BP suggests a mechanism for the eye-shaped crack formation. For bulk BP, each phosphorus atom has three single bonds with two in-plane bonds and a third out-of-plane bond. Assuming that sublimation begins with a

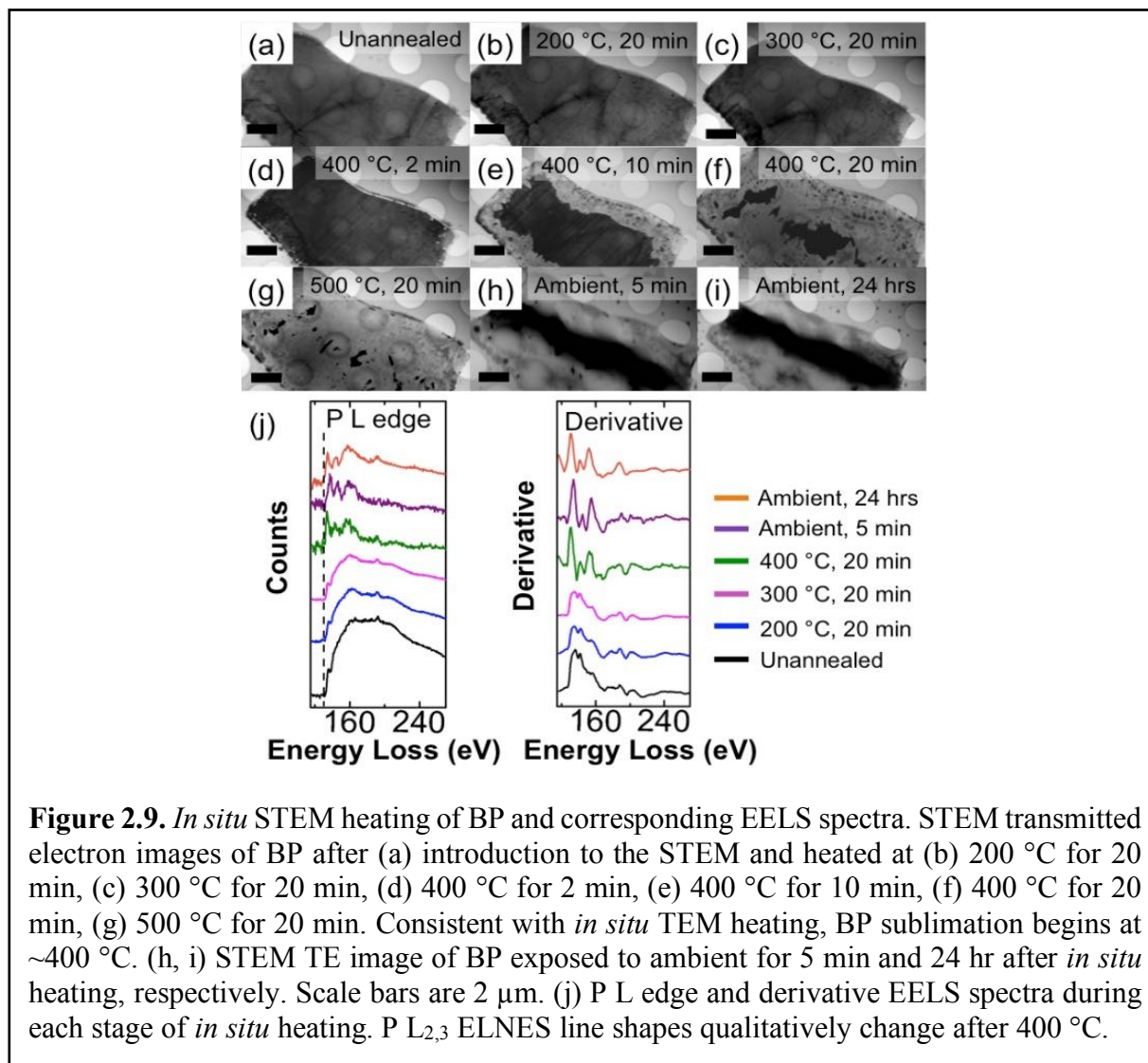


vacancy defect, denoted by a green circle in **Fig. 2.8h**, BP decomposition then continues by removal of P atoms along the perimeter. The perimeter P atoms surrounding the growing crack fall

into several categories including P atoms with only one bond to the surrounding crystal and P atoms with two bonds to the surrounding crystal. The second category can be further subdivided into P atoms with two in-plane bonds and P atoms with one in-plane bond and one out-of-plane bond. Assuming that P atoms with only one bond desorb first followed by P atoms with two in-plane bonds and finally P atoms with one in-plane bond and one out-of-plane bond, then the crack will evolve in an anisotropic manner that is consistent with the observed eye-shape along the [001] direction. Snapshots of this proposed sublimation model are shown in **Figs. 2.8h-j**. For BP multilayers, formation of cracks in one layer will expose the next inner layer, which initiates sublimation at the same point. Hence, sublimation of BP multilayers will also exhibit eye-shaped cracks as observed experimentally in **Fig. 2.8**.

Concurrent *in situ* STEM heating and EELS measurements provide chemical information for the BP decomposition process. **Figs. 2.9a-g** contain the transmission electron images for a range of annealing conditions. After 20 min annealing at 500 °C, the sample is cooled *in situ* to 37 °C, upon which it is exposed to ambient conditions (~26 °C, relative humidity ~38%) for 5 min. The dark contrast in the TE images in **Fig. 2.9h** implies that the flake has become thicker after ambient exposure. In addition, the flake is invariant to additional ambient treatment, as evidenced by the 24 hr ambient exposure preceding the image in **Fig. 2.9i**. **Fig. 2.9j** shows the EELS spectra taken at different annealing conditions for the extracted and normalized P L_{2,3} edge at 132 eV.

To better highlight the change in the energy-loss near-edge structure (ELNES), the derivatives of the EELS P L_{2,3} edge are presented in **Fig. 2.9j**. The existence of the P L_{2,3} edge



after 400°C annealing indicates that the thin skeleton contains P, in agreement with EDS spectrum shown in **Fig. 2.6i**. The ELNES of the P $L_{2,3}$ is invariant before 400°C annealing and changes its line shape qualitatively at 400°C, denoting a different P bonding state. The P $L_{2,3}$ ELNES modifications after ambient exposure are negligible, implying a similar P oxidation state before and after ambient.

A previous study²⁹³ showed that heating bulk BP to 777 °C at ~0.5 GPa pressure produces a 0.3-0.5 mm thick layer of red P on the BP crystal surface. Brazhkin *et al.* also produced a phase diagram for bulk black and red P, showing a phase transition between the black and red phases at

597 °C. This solid red P exists until 620 °C without applied pressure. In general, red P is a highly reactive, amorphous structure. These characteristics suggest that the thin skeleton remaining after BP decomposition is related to red P. Furthermore, previous work has shown that BP degrades in ambient conditions.¹⁷ Oxygenated H₂O has been suggested as a source for BP ambient degradation,¹⁷ and red P is even more hygroscopic than BP. The rapid gettering of oxygenated H₂O by red P following ambient exposure is a plausible explanation for the observed increase in thickness observed in **Figs. 2.9h, i**.

In summary, a suite of atomically precise microscopy and spectroscopy techniques reveals *in situ* thermal decomposition of exfoliated BP at ~400 °C. The high surface area and nanoscale thickness of exfoliated BP likely explains the lower decomposition temperature relative to bulk BP. Sublimation is initiated with the formation of eye-shaped cracks along the [001] direction in a manner consistent with the anisotropic in-plane atomic structure of BP. After thermal decomposition, an amorphous red P like skeleton persists, as inferred from ambient exposure, SAED, EELS, and XPS data. Overall, this study provides insight into the thermal limits of 2D BP, thus facilitating the development of suitable processing methods for BP-based devices.

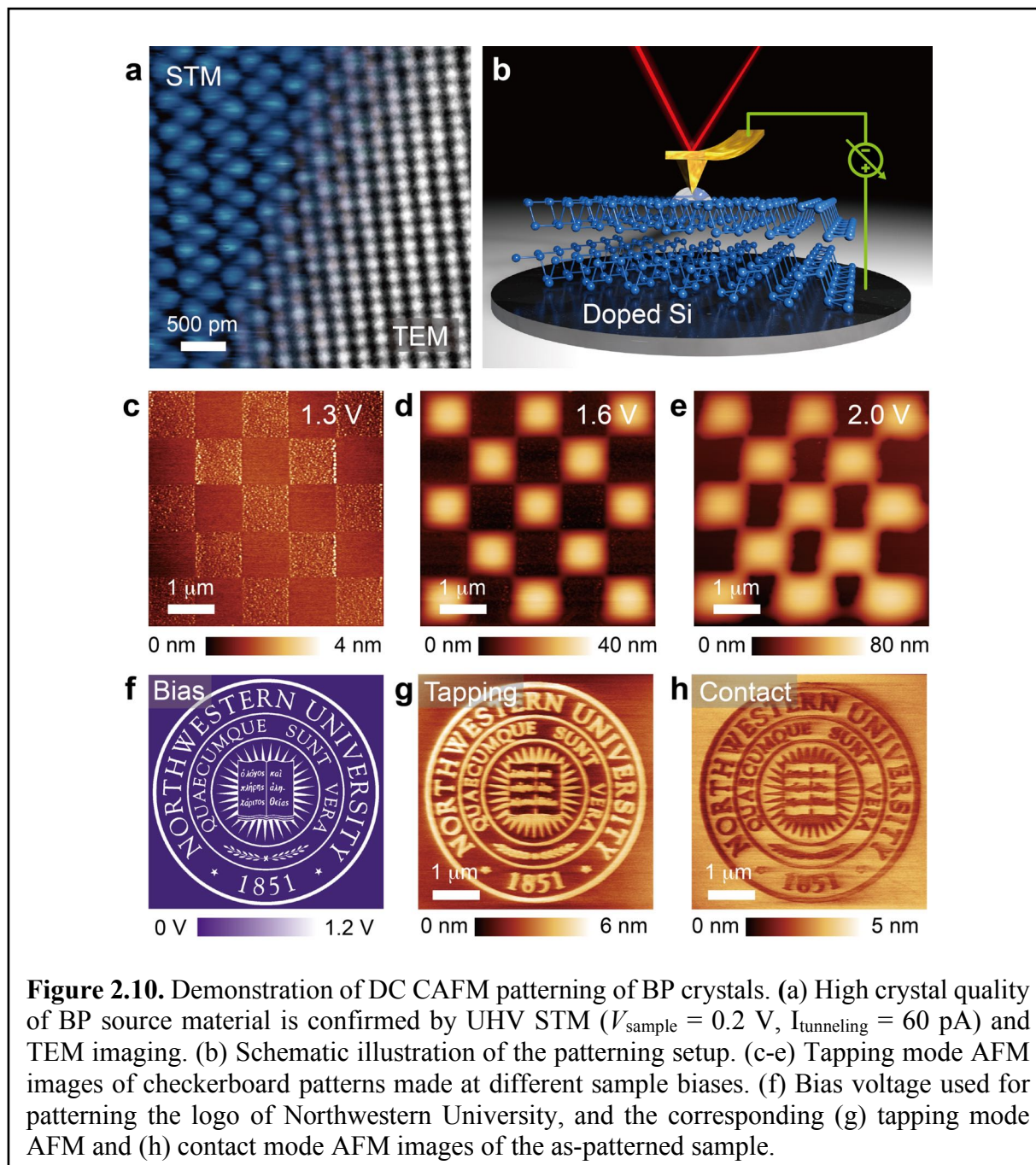
2.3 Patterning and Thinning of BP via Scanning Probe Nanolithography

While BP has been exploited in a range of applications including high-mobility field-effect transistors,²⁵² broadband photodetectors,^{255,294,295} ultrafast terahertz devices,²⁹⁶ and high-sensitivity gas sensors,^{297,298} the absence of large-area growth methods has limited the production of thin BP layers primarily to mechanical exfoliation and solution processing,^{19,299} both of which lack precise control over flake thickness and lateral size. Even at the laboratory scale, the fabrication of large and thin 2D nanomaterials remains challenging. To control thickness, 2D

nanomaterials can be first exfoliated and then thinned, as has been demonstrated for transition metal dichalcogenides through plasma³⁰⁰ and laser oxidation treatments.³⁰¹ Similar thinning methods have also recently been applied to BP.^{302,303} Since plasma etching occurs over large areas and laser oxidation is spatially limited by optical diffraction, localized thinning and patterning at the nanoscale are not available or severely hindered. On the other hand, scanning probe nanolithography is renowned for its high spatial resolution down to the atomic scale, suggesting that this approach may overcome the limitations of plasma etching and laser oxidation.^{304,305}

Herein, we take advantage of the high spatial resolution of scanning probe nanolithography and the tendency of BP to oxidize in ambient conditions to realize lateral nanopatterning and layer-by-layer thinning of BP using CAFM. In particular, layer-by-layer thinning of BP is achieved through direct current (DC) local anodic oxidation in a manner analogous to silicon³⁰⁶ and graphene.²⁰³ This process generates liquid-like patterning byproducts, which are identified as phosphorus oxoacids by Raman spectroscopy and time-of-flight secondary ion mass spectrometry (ToF-SIMS). The oxoacids are readily removed by water rinsing, leaving locally thinned BP regions whose thickness can be controlled by the magnitude and duration of the applied DC bias. In addition, an alternating current (AC) method is further demonstrated that allows patterning and thinning of BP on insulating 300 nm SiO₂/Si substrates, which are widely used for optically identifying thin BP flakes and subsequent device fabrication. BP field-effect transistors (FETs) with patterned channel regions show significant increases in current on-off ratios up to a factor of 50 without significantly compromising on-state current. With these DC and AC biasing conditions, nanoscale BP structures can be realized with on-demand geometries that are not accessible by other patterning or thinning approaches. The generality of this technique suggests that it can be

widely applied to other 2D nanomaterials, with broad implications for the exploration of thickness-dependent nanomaterial properties and in-plane homojunction devices.³⁰⁷



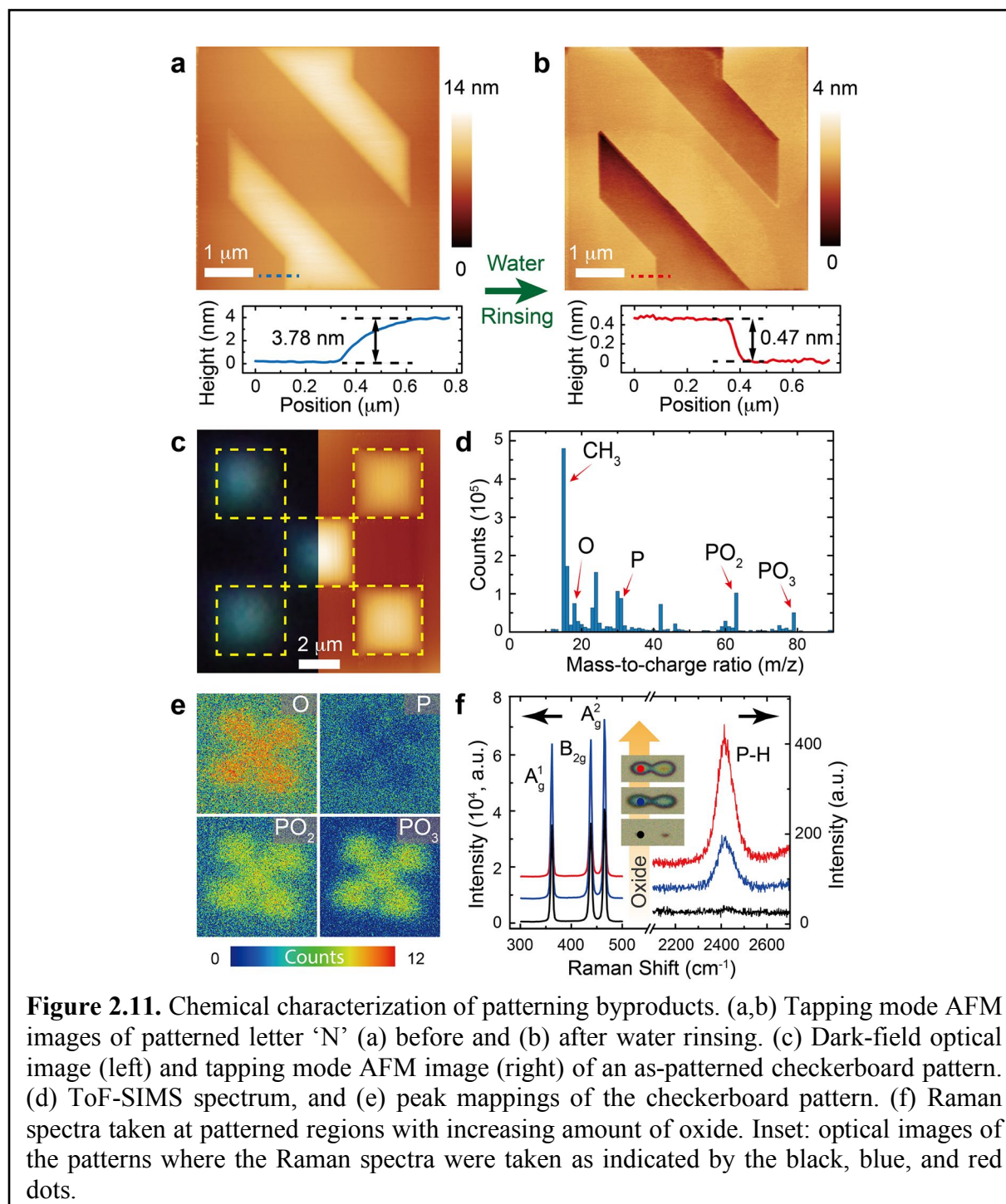
The quality of the BP crystal preceding nanopatterning was verified with UHV STM and TEM, as shown in **Fig. 2.10a**. Due to the high surface sensitivity of STM and the puckered

structure of BP, the local electronic density of states that provides STM imaging contrast mainly results from the upper atoms of the top BP layer, resulting in zigzag rows in the STM image.²⁶⁴ Conversely, all AB stacked BP layers contribute to the TEM image, giving rise to a rectangle-like lattice. The ordered atomic lattices observed in both STM and TEM indicate high material quality. Figure 1b schematically illustrates the patterning setup, where the BP crystal or mechanically exfoliated BP flakes sit on top of an n⁺-doped silicon wafer. During nanopatterning, an adjustable bias voltage is applied to the sample with the CAFM tip grounded in ambient conditions (the relative humidity ranges between 20% and 50% in this work).

By controlling the amplitude of the bias voltage during contact mode CAFM scanning, checkerboard patterns are fabricated on a freshly exfoliated BP crystal. In **Fig. 2.10c-e**, tapping mode AFM images are shown for patterning voltages between 1.3 V and 2.0 V. The patterned regions appear as protrusions and increase in height with higher bias. Arbitrary patterns can be realized through precise voltage control during scanning. For example, **Fig. 2.10f** shows a voltage-encoded version of the Northwestern University logo, with the color encoding the applied sample bias (0–1.2 V) at each pixel. After patterning, the tapping mode AFM image in **Fig. 2.10g** shows protruded features corresponding to high bias regions in agreement with **Fig. 2.10c-e**, whereas the contact mode AFM image in **Fig. 2.10h** indicates the opposite, namely depressions in the high bias regions. In contact mode AFM imaging, the AFM tip can scan a solid BP surface under a liquid; whereas, in tapping mode AFM imaging, the tip can track the morphology of a liquid on BP. Thus, the contrast differences between **Figs. 2.10g,h** suggest the consumption of BP and formation of a liquid-like surface layer in the patterned regions.

These liquid-like features are readily rinsed away by water, as demonstrated in **Fig. 2.11a,b**, where tapping mode AFM images of a patterned letter ‘N’ at 1.2 V before and after 10 s water

rinsing give opposing contrast. The insets indicate line profiles across the same patterning

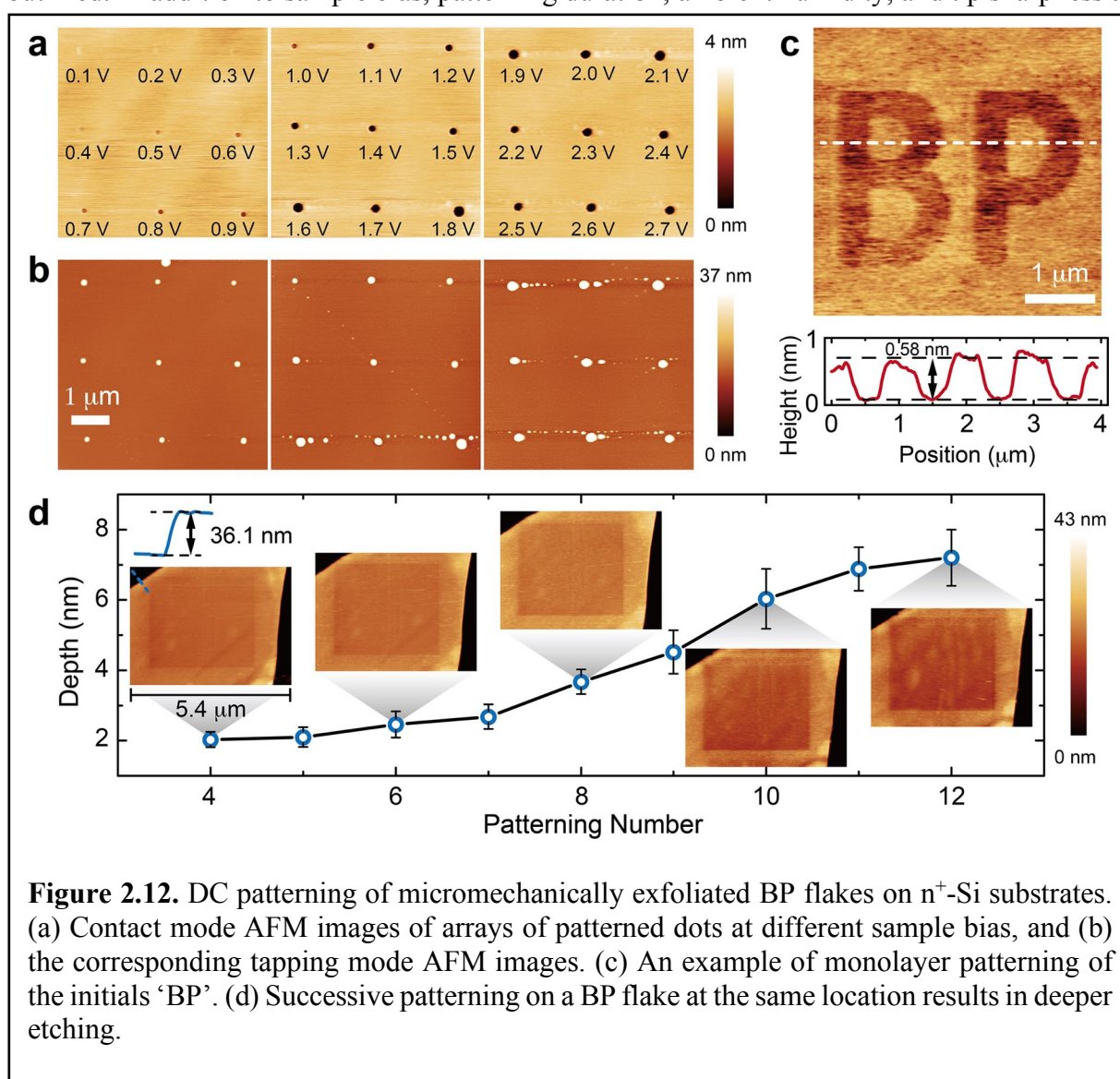


boundary before (blue dashed line) and after (red dashed line) rinsing, which reveal a ~ 0.47 nm step height at the thinned regions of the bulk-like BP crystal, corresponding to the removal of

monolayer phosphorene. The ease of removal of BP patterning byproducts through water rinsing is in contrast to the HF and HCl treatments that are required to remove patterning byproducts on Si,³⁰⁶ graphene,²⁰³ and MoS₂.³⁰⁸

Since only positive sample bias results in effective patterning and thinning, the underlying mechanism is likely to be local anodic oxidation driven by the strong electric field at the tip apex.³⁰⁶ To further probe the chemical identity of the liquid-phase patterning product, a checkerboard pattern was prepared for ToF-SIMS measurements. The dark-field optical microscope (left) and tapping mode AFM (right) images of the as-patterned sample are provided in **Fig. 2.11c**. **Fig. 2.11d** reveals the primary peaks of the ToF-SIMS spectrum acquired across the patterned area. The peaks corresponding to O, PO₂, and PO₃ species suggest that CAFM patterning oxidizes the BP substrate. However, since BP is known to oxidize spontaneously in ambient environment,¹⁷ we further mapped the spatial distributions of O, P, PO₂, and PO₃ in **Fig. 2.11e**. This spatial mapping confirms that the oxygenated species are concentrated at the patterned areas instead of resulting solely from spontaneous oxidation in ambient conditions. Furthermore, the liquid nature of the patterning product can be explained by the fact that phosphorus oxides are known to rapidly absorb water (e.g., P₄O₁₀ is used as a dehydrating agent³⁰⁹) to form phosphorus oxoacids. Indeed, as shown in **Fig. 2.11f**, Raman spectra of the patterned regions with increasing oxide content (inset) show not only BP Raman modes (A_g^1 at $\sim 362\text{ cm}^{-1}$, B_{2g} at $\sim 438\text{ cm}^{-1}$, A_g^2 at $\sim 465\text{ cm}^{-1}$), but also a broad increasing peak at $\sim 2416\text{ cm}^{-1}$ corresponding to the Raman active P–H stretching mode^{310,311} of phosphorus oxoacids (e.g., H₃PO₄). Based on **Figs. 2.11a,b**, the volume expansion ratio at the patterned region is ~ 5.1 , which is close to the expected volume expansion of BP to H₃PO₄ (~ 4.5). The presence of other phosphorus oxoacids and ambient water likely also play a role in determining the exact volume expansion ratio.

In addition to patterning on thick BP crystals, we explored the extension of this method to mechanically exfoliated BP flakes on conductive Si substrates. **Figs. 2.12a,b** show contact mode and tapping mode AFM images, respectively, of a series of patterned points on an exfoliated BP flake on n^+ -doped Si, using different tip biases with a dwell time of ~ 5 s at each point. Corroborating previous observations, higher biases lead to increased etching. Moreover, the two sets of images show opposing contrast due to the different imaging mechanisms previously outlined. In addition to sample bias, patterning duration, ambient humidity, and tip sharpness also

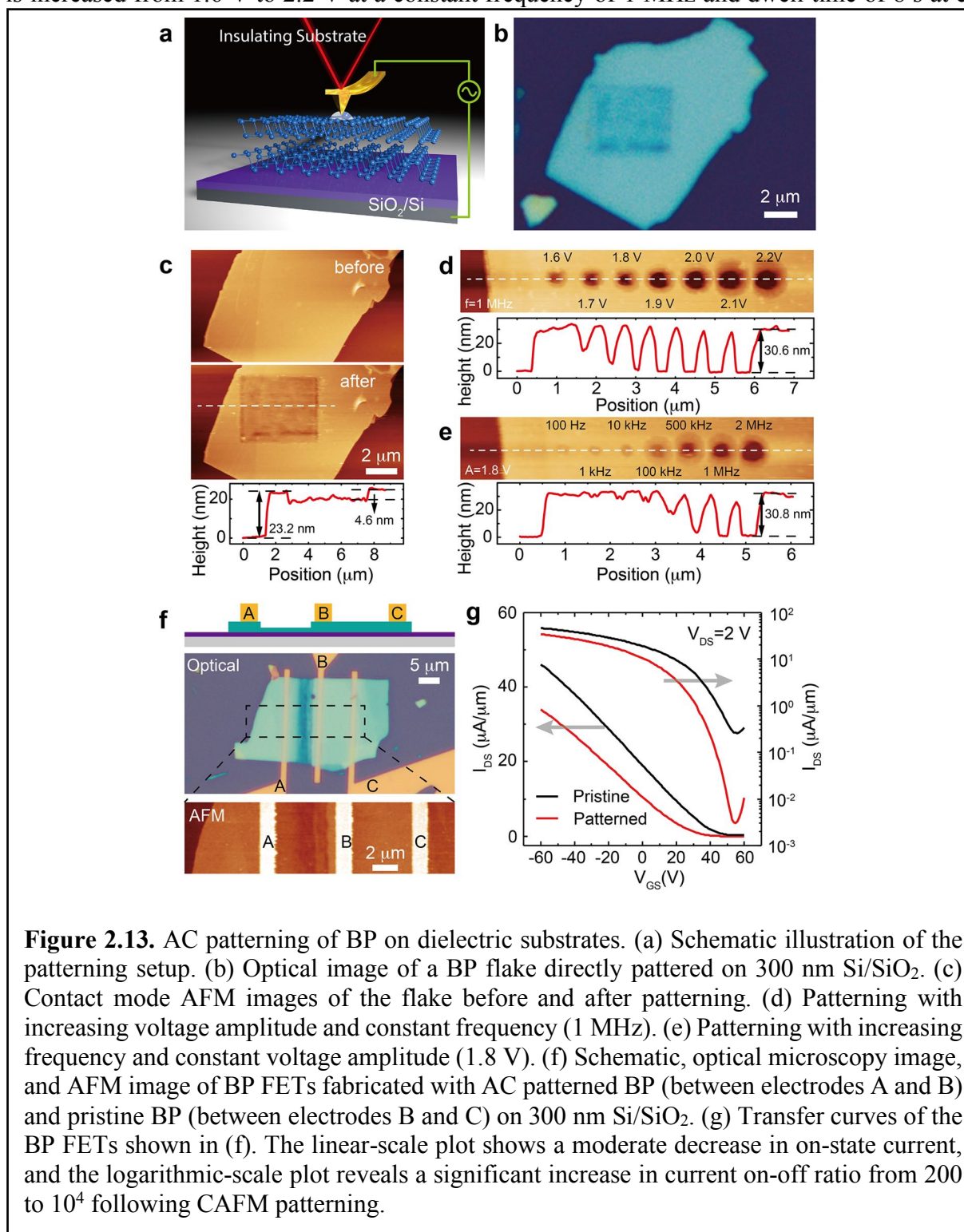


affect the degree of thinning.³⁰⁶ **Fig. 2.12c** shows that layer-by-layer etching is achieved on mechanically exfoliated BP at a sample bias of 0.8 V, as attested by the 0.58 nm line profile depth. Successive patterning can also be applied in the same region to gradually thin flakes down. For example, **Fig. 2.12d** shows a rectangular region of a ~36.1 nm thick BP flake that is repeatedly patterned at 1.2 V with no rinsing between patterning steps. The thinning depth increases monotonically with each patterning step, as evidenced by the resulting series of contact mode AFM images in **Fig. 2.12d**.

Thus far, BP patterning and thinning has been achieved with DC bias voltages on conductive substrates, as is typical for scanning probe anodic oxidation.^{203,306,312} However, it is more common for 2D nanomaterials to be deposited on 300 nm SiO₂/Si substrates to enable identification of monolayer and few-layer flakes with optical microscopy.³¹³ In addition, the substrate SiO₂ layer can act as a gate dielectric for field-effect transistors. **Fig. 2.13a** introduces a simple but effective method for patterning on 300 nm SiO₂/Si substrates, where an AC bias voltage is applied between the underlying n⁺-doped Si substrate and the CAFM tip. Under AC bias, the capacitive impedance of the SiO₂ layer becomes finite: $Z = (j\omega C)^{-1}$, where ω is the angular frequency of the AC voltage and C is the capacitance. As a proof of concept, **Fig. 2.13b** shows a mechanically exfoliated BP flake on a 300 nm SiO₂/Si substrate after AC patterning and water rinsing. In this case, the applied voltage is a 1 MHz AC sinusoidal wave with an amplitude of 2 V. Contact mode AFM images before and after patterning are shown in **Fig. 2.13c**, with the line profile after patterning provided as an inset. From this measurement, it can be seen that ~4.6 nm (9 layers) of BP has been removed from the original 23.2 nm thick BP flake.

As established in **Figs. 2.10** and **2.12**, higher DC bias voltages result in increased BP oxidation, in agreement with literature reports of anodic oxidation of other materials.^{203,306}

Similarly, as shown in the contact mode AFM image in **Fig. 2.13d**, when the AC voltage amplitude is increased from 1.6 V to 2.2 V at a constant frequency of 1 MHz and dwell time of 8 s at each



point, the etching depth increases until the 30.6 nm flake is etched all the way down to the SiO₂/Si substrate. Also, the lateral dimensions of the etched pits increase due to the stray electric field exceeding the patterning threshold at locations away from the tip apex. In **Fig. 2.13e**, AC patterning at different frequencies but with the same voltage amplitude (1.8 V) and dwell time (8 s) also reveals increased oxidation at higher frequency. Because the tip-sample contact resistance is in series with the capacitive impedance of the SiO₂ layer, the decrease of the latter at higher frequency results in an increased potential drop across the tip-sample junction, giving rise to higher local electric fields.

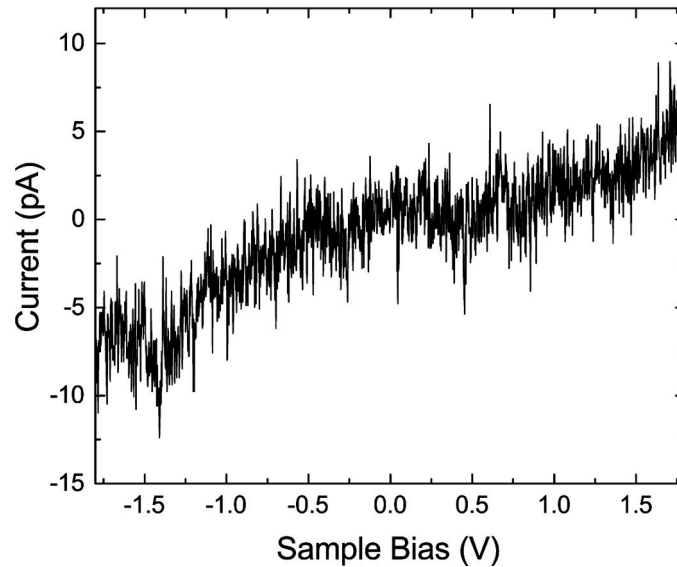
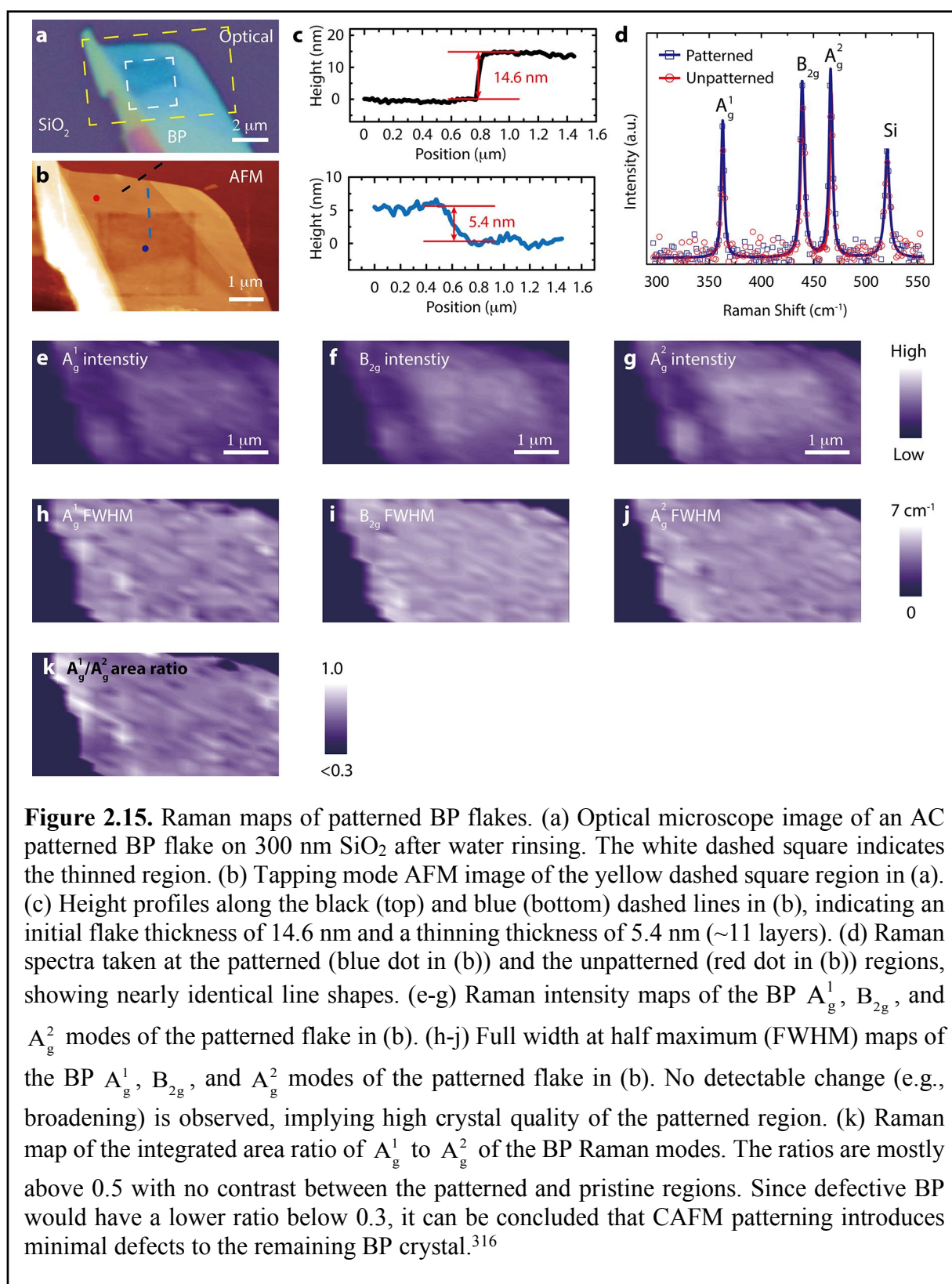


Figure 2.14. Extraction of contact resistance from I - V relationship. The conductive AFM tip is in contact with a BP flake on n⁺-doped Si wafer while varying the applied sample bias. From the resulting I - V curve, the contact resistance is estimated to be $\sim 2 \times 10^{11} \Omega$.

More specifically, the typical contact resistance between the CAFM tip and BP flakes is $\sim 2 \times 10^{11} \Omega$ (**Fig. 2.14**), which is much larger than the sheet resistance ($\sim 10^6 \Omega/\text{sq}^{314}$) of BP flakes. Therefore, the BP flake will have an almost spatially uniform potential distribution during CAFM patterning. In addition, the BP flake and the n⁺-Si substrate form a capacitor with capacitance of $\sim \epsilon S/d$, where ϵ is the dielectric constant of BP ($\sim 10\epsilon_0^{315}$), S is the flake area (on the order of 10^2



μm^2) and d is the thickness of SiO₂ (300 nm). The resulting capacitive impedance varies from

$\sim 10^{11} \Omega$ to $10^7 \Omega$ when the AC frequency changes from 10^2 Hz to 10^6 Hz. The resulting increase in the local electrical field at the tip-sample junction leads to enhanced BP oxidation when patterning at high frequency.

The high crystallinity of patterned BP flakes is preserved as first evidenced by non-detectable broadening of BP Raman modes and high integrated area ratio of A_g^1 to A_g^2 Raman modes as shown in **Fig. 2.15**. Cross-sectional TEM (XTEM) imaging (**Fig. 2.16**) of a patterned BP flake shows a ~ 3.9 nm thick surface oxidation layer in the patterned regions that is comparable to the ~ 3.7 nm thick oxide layer in the pristine BP regions, indicating that the BP structural integrity is preserved following patterning. To demonstrate the electrical performance of patterned BP flakes and potential applications of the CAFM thinning method, FETs with patterned/thinned channels are compared with FETs fabricated from non-patterned regions of the same flake. In **Fig. 2.13f**, with the AC patterning method, a ~ 17 nm thick flake is partially thinned down by 7-8 nm and three electrodes are fabricated after the flake is rinsed in water, as shown in the schematic and in optical microscopy and AFM images. The performance of the patterned device with electrodes A and B is compared to that of the pristine device with electrodes B and C as shown in **Fig. 2.13g**. The patterned devices show minor changes in the on-state current and hole mobility from 113 to $96 \text{ cm}^2 \text{ V}^{-1} \text{ s}^{-1}$, while the current on-off ratio is dramatically increased from 200 to 10^4 due to substantial reductions in the off-state current. Given the well-known increase of current on-off ratio with thinner BP flakes,²⁵² the observed differences in electrical transport can be primarily attributed to changes in flake thickness, thus showing the advantages of direct AC CAFM patterning in improving device performance.

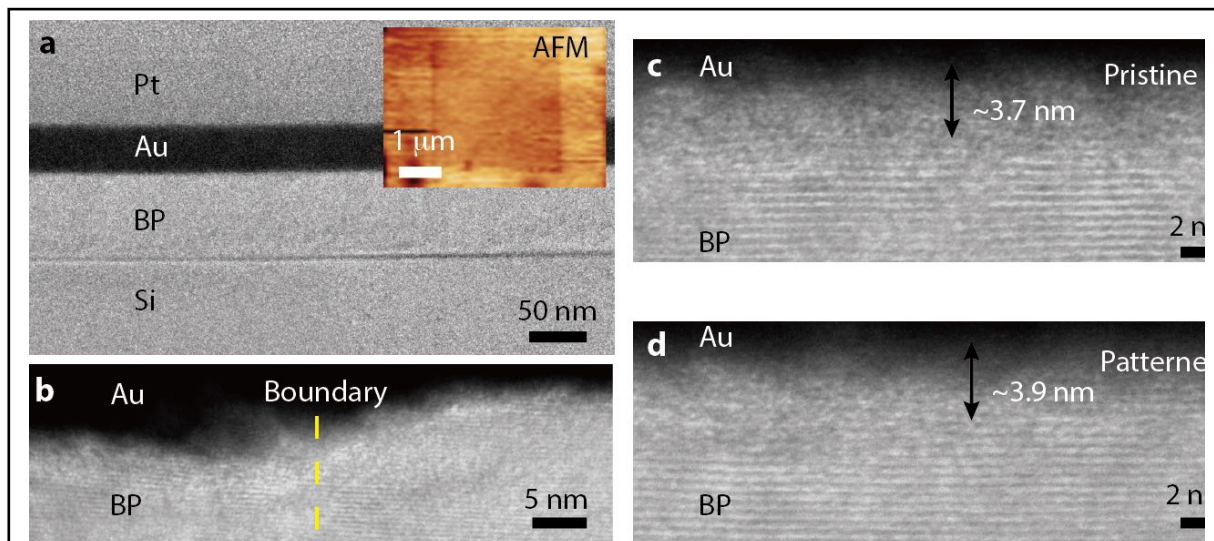


Figure 2.16. XTEM images of patterned BP. (a) XTEM image of the PT/Au/BP/Si structure. Pt and Au are coated to protect BP from damage. Inset: AFM image of as-patterned BP on Si (~ 4 nm thinner in the patterned square). (b) XTEM image of the boundary between patterned and pristine BP regions. (c) XTEM image of the pristine BP region. The BP lattice is present under an amorphous surface layer of ~ 3.7 nm. (d) XTEM image of the patterned BP region showing a similar amorphous layer of ~ 3.9 nm above the crystalline BP lattice. These results shows that the BP crystallinity is preserved after CAFM patterning and water rinsing.

In summary, we have demonstrated controlled patterning and thinning of BP with nanoscale lateral resolution and layer-by-layer thinning using CAFM. The patterning mechanism is consistent with anodic oxidation as evidenced by the formation of oxidized phosphorus species. The oxidized phosphorus gets water from the environment, resulting in a liquid-phase patterning byproduct that is easily removed by water rinsing. Finally, we extend this method to AC biasing conditions to enable BP flake patterning on commonly utilized dielectric substrates and demonstrated significant improvements in the current modulation of BP FETs. The flexibility of this patterning method suggests that it can be broadly applied to other studies including the generation of arbitrary BP edges that would allow for the exploration of orientation-dependent edge properties (e.g., structural reconstruction,²⁶³ edge functionalization,³¹⁷ and edge

intercalation¹⁷). The patterning methods demonstrated here can likely be extended to other 2D nanomaterials and their heterostructures, thereby allowing the generation of geometrically well-defined samples for both fundamental studies and device prototyping.

Chapter 3: MoS₂ Monolayers on EG: Defect Engineering and Chemical Functionalization

This chapter is based partially on the following publications and preprint:

X. Liu, I. Balla, H. Bergeron, and M. C. Hersam, Point Defects and Grain Boundaries in Rotationally Commensurate MoS₂ on Epitaxial Graphene, *Journal of Physical Chemistry C* **2016**, *120*, 20798-20805.

X. Liu*, I. Balla*, H. Bergeron, G. P. Campbell, M. J. Bedzyk, and M. C. Hersam, Rotationally Commensurate Growth of MoS₂ on Epitaxial Graphene, *ACS Nano* **2016**, *10*, 1067-1075.

X. Liu, V. K. Sangwan, I. Balla, C. Zhong, H. Bergeron, E. A. Weiss, and M. C. Hersam, Mixed-Dimensional Heterostructures of MoS₂ with C8-BTBT on Graphene with Well-Ordered Interfaces, in preparation.

*These authors contribute equally

3.1 Introduction: TMDC Monolayers and Heterostructures with Graphene

The advent of graphene and the subsequent extensive research studying this superlative material^{2,318,319} have demonstrated the unique opportunities and challenges associated with materials in the atomically thin limit such as 2D BP discussed in the previous chapter. Similar to graphene and BP, TMDC monolayers³²⁰ exhibit unique material properties compared to their bulk counterparts. As a result of the numerous combinations of transition metals with chalcogen elements,¹²⁰ the diverse family of TMDC compounds³²¹ offers electronic properties ranging from semiconducting (*e.g.*, MoS₂^{20,21}), to metallic (*e.g.*, NbTe₂^{13,14}) to superconducting (*e.g.*, NbSe₂¹⁰). In addition to being abundant in nature as molybdenite, MoS₂ is one of the most studied 2D TMDCs with potential applications in electronics and optoelectronics due to its desirable physical properties.^{322,323} Since monolayer MoS₂ possesses a direct optical band gap of 1.9 eV in the visible range³²⁴ and a relatively high quantum yield,²¹ it is especially promising for applications in photodetectors.^{325,326} The break of spin degeneracy due to the lack of inversion symmetry in

monolayer MoS₂ also makes it possible to fabricate valleytronic devices controlled by circularly polarized light,^{327,328} thereby offering further opportunities for quantum electronics.

Compared to isolated 2D materials, heterostructures composed of stacked 2D materials allow the exploration of fundamental interfacial interactions and novel electronic functionality beyond what could be offered by a single material. Furthermore, van der Waals interactions enable versatile integration of dissimilar materials without dangling bonds. The relaxed constraint of lattice matching not only allows vertical stacking of 2D layers with clean and abrupt interfaces,³²¹ but also mediates effective coupling of materials with different dimensions.^{329,330} Such mixed-dimensional heterostructures^{329,331} further expand the family of van der Waals systems beyond all-2D materials that are limited by lack of controllable doping and low net photon absorption. In that context, particularly interesting heterojunction candidates are small molecule organic semiconductors that typically act as a 0D material due to highly localized molecular orbitals. The combination of such organic layers with inorganic 2D materials have gained significant popularity recently for optoelectronic,^{323,332} energy-harvesting^{181,333} and light-emitting applications.³³⁴ In addition to the desired physical properties (e.g., mechanical flexibility, lightweight, tunability by functional groups), the high processing throughput and potential as a seeding layer for subsequent chemistry³³⁵ makes such mixed-dimensional heterostructures highly competitive compared to all-2D heterostructures, where large area growth has only been realized in limited material systems.³³⁶

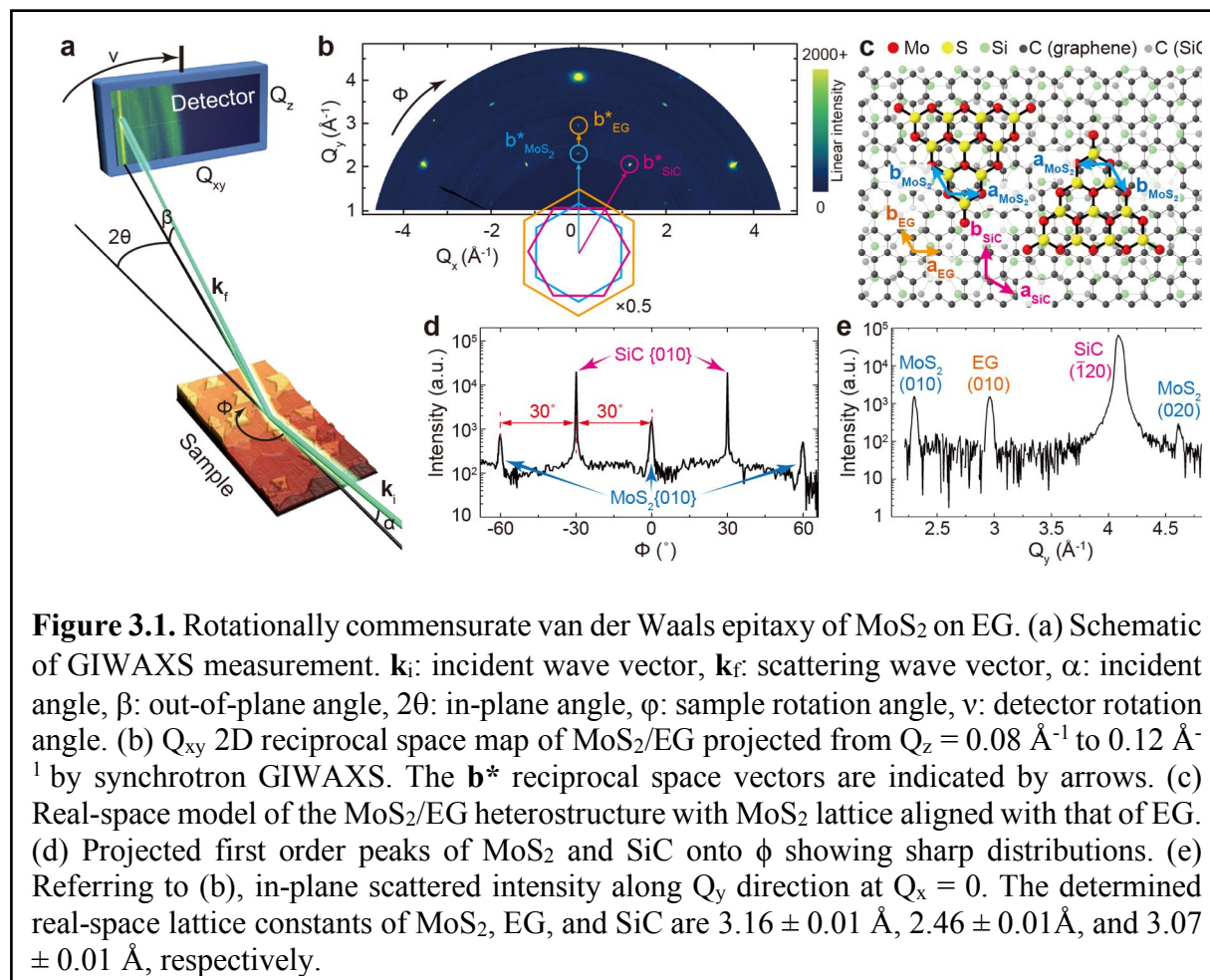
From among the 2D material library consisting of semimetals (e.g., graphene^{15,16}), insulators (e.g., boron nitride²² and Bi₂Se₃²³), and semiconductors (e.g., BP¹⁷⁻¹⁹ and TMDCs^{337,338}), the combination of MoS₂ with graphene^{339,340} shows great potential for next generation electronic and optoelectronic applications due to complementary carrier mobilities and optical responsivities.³⁴¹

Additionally, the MoS₂/graphene heterostructure has been shown to be an excellent catalyst for hydrogen evolution reactions³⁴² and a promising anode material for Li-ion batteries.³⁴³

The properties of MoS₂/graphene heterostructures depend strongly on the underlying substrate and the graphene synthesis technique. Epitaxial graphene (EG) grown on SiC by the preferential thermal desorption^{344,345} of silicon from SiC not only offers uniform large-area synthesis of graphene, but also provides technological advantages over alternative methods such as CVD and mechanical exfoliation. For example, fine control of the growth temperature enables homogeneous monolayer or bilayer EG at the wafer scale,³⁴⁶⁻³⁴⁸ while post-annealing in hydrogen allows decoupling of EG from the underlying SiC substrate.¹⁶ The high quality and cleanliness of EG is evidenced by its high carrier mobility³⁴⁹ of 45,000 cm²V⁻¹s⁻¹ and observation of the quantum hall effect.³⁵⁰ Furthermore, the interaction between graphene and the SiC substrate can be tailored *via* intercalation of different atomic species.³⁵¹

Given the underlying SiC substrate as well as the different electronic characteristics of EG (*e.g.*, substrate-induced n-type doping^{352,353}), CVD synthesis of MoS₂ on EG is expected to differ from that on graphite or CVD graphene, giving rise to novel structural and electronic interactions between the two materials. While MoSe₂ has been grown on EG by molecular beam epitaxy,^{354,355} recent reports of MoS₂ grown by CVD on graphite^{338,356,357} and EG^{358,359} resulted in non-epitaxial growth, where the orientation of the MoS₂ crystals was not controlled. Furthermore, the atomic-scale electronic and structural properties of MoS₂/EG heterostructures have not been thoroughly established. Towards these ends, we have successfully achieved rotationally commensurate growth of atomically thin MoS₂ crystals on EG by van der Waals epitaxy (**Fig. 3.1**), where MoS₂ is found to preferentially grow with lattice aligned with EG, suggesting EG may be a promising substrate for van der Waals epitaxial growth of other emerging 2D nanomaterials in addition to providing a

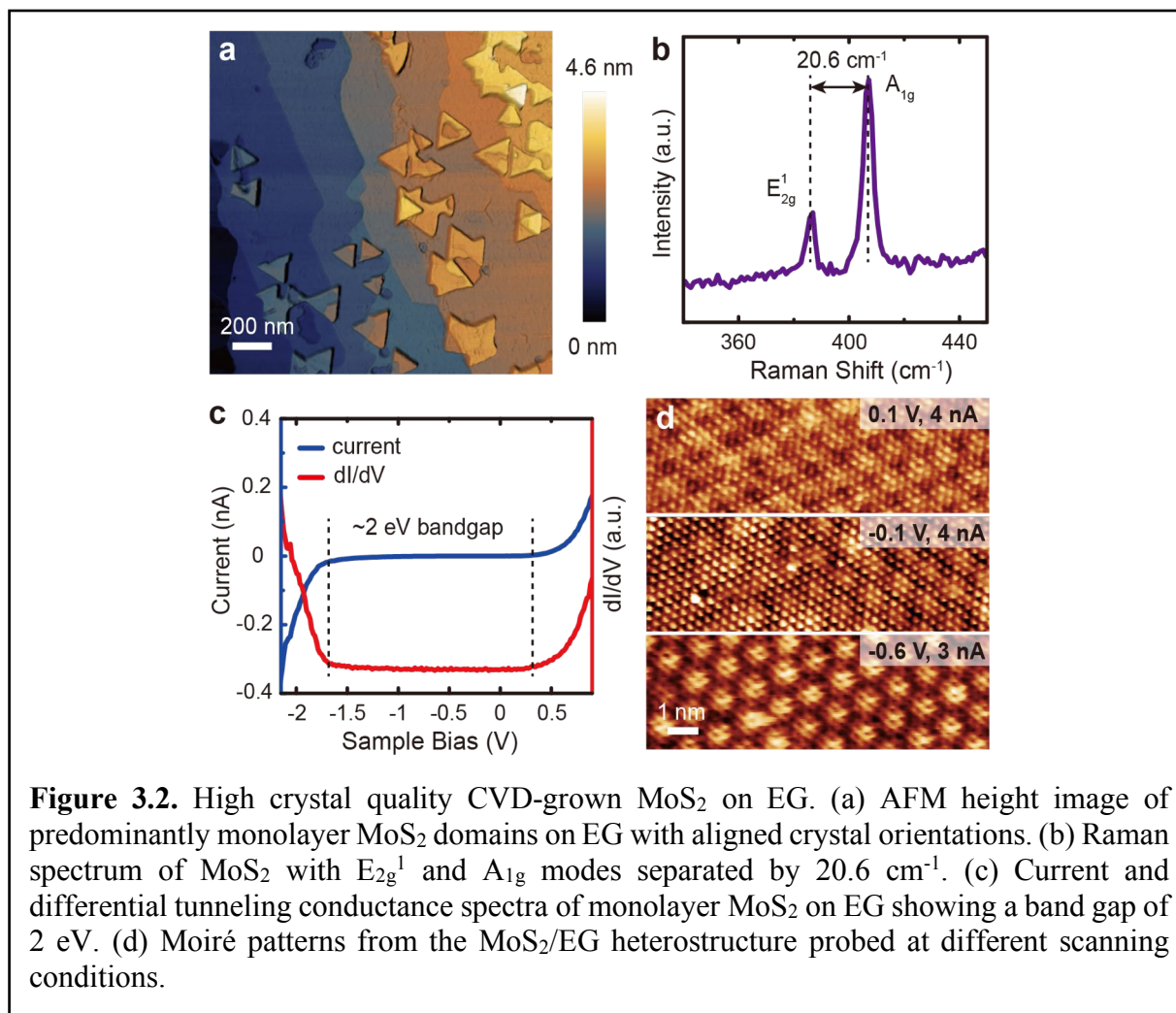
well-defined platform for the future study and application of MoS₂/graphene heterostructures. In



the following sections, we explore the intrinsic crystal defects including point and line defects in MoS₂/EG heterostructures as well as a mixed-dimensional heterostructure based on such platform with a molecular semiconductor 2,7-dioctyl[1]benzothieno[3,2-b][1]benzothiophene (C8-BTBT).

3.2 Point and Line defects in Rotationally Commensurate MoS₂/EG Heterostructures

Despite the attractive properties of monolayer MoS₂, its relatively low experimentally observed carrier mobility³⁶⁰ presents limitations in many high-performance applications. Previous work has suggested that intrinsic structural defects such as vacancies and GBs are the main sources of this degraded mobility.^{361,362} Furthermore, the fact that MoS₂ field-effect transistors perform poorly in

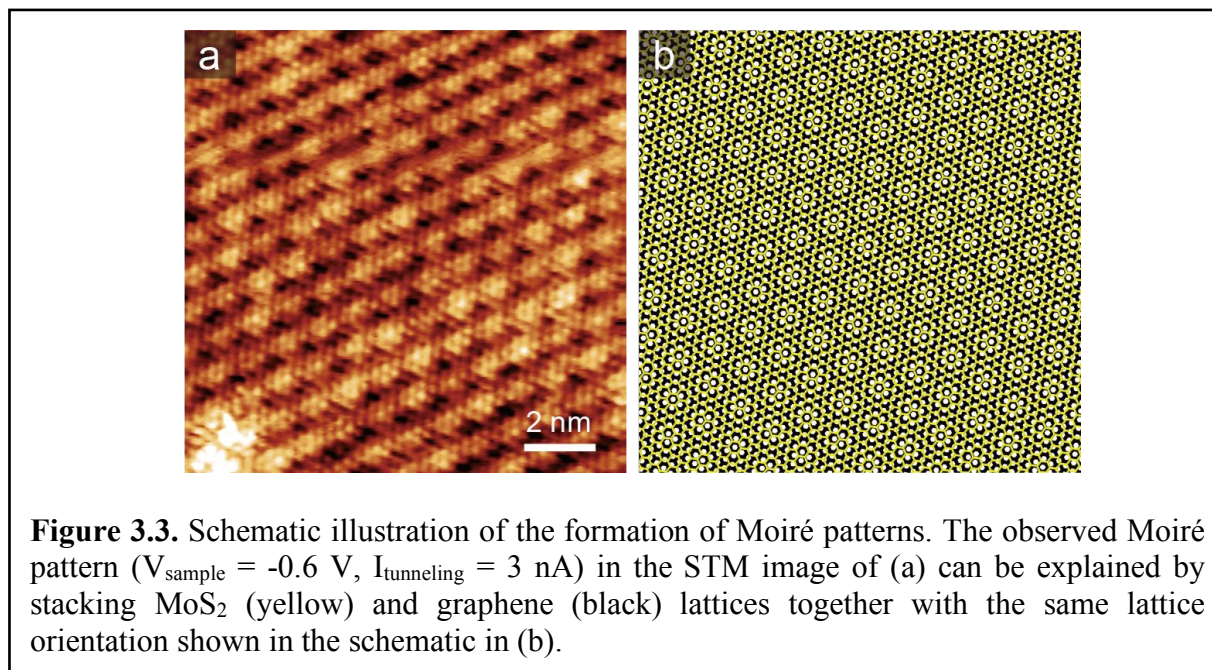


ambient compared to vacuum conditions implicates surface defects as sites of chemisorbed extrinsic scattering centers.^{363,364} On the other hand, defect engineering presents pathways for modifying material properties, especially when the preparation of large-scale monolayer MoS₂ relies primarily on CVD^{165,339,358,365} and solution-phase exfoliation,^{337,366} where high defect density is expected. For example, anisotropic defects in related 2D materials (e.g., graphene and black phosphorus¹⁸) are being explored in separation technologies as nanopores. Gate-tunable MoS₂ memristors based on GB migration¹⁹² present another example where structural defects have been exploited to reveal novel functionalities.

A comprehensive understanding of MoS₂ structural defects at the atomic scale would facilitate the rational design of defect engineering for desired material properties. Although various studies of monolayer MoS₂ defects have been carried out by S/TEM,^{54,365,367-371} concurrent structural and electronic characterization of monolayer MoS₂ defects with STM/STS is relatively unexplored.³⁵⁶ Towards this end, we perform here UHV STM/STS measurements of CVD-grown monolayer MoS₂ on EG, focusing on the structural and electronic properties of intrinsic defects. Previously, we have demonstrated the growth of rotationally commensurate MoS₂ on EG,¹⁶⁵ which offers several technological advantages, including consistent material quality and preferential formation of 30° and 60° GBs. The investigation of point defects and GBs in the MoS₂/EG system is thus of particular interest because of the strain-free nature of the monolayer MoS₂ and the predictability in GB orientations enabled by the rotational commensurability.³⁷²

The as-grown MoS₂/EG sample was imaged by AFM as shown in **Fig. 3.2a**. The vast majority of monolayer MoS₂ triangle domains are aligned as a result of rotational commensurability. The high quality of MoS₂ is revealed by Raman spectroscopy, as shown in **Fig. 3.2b**, where the in-plane E_{2g}¹ (386.5 cm⁻¹) and out-of-plane A_{1g} (407.1 cm⁻¹) Raman modes³⁷³ are separated by 20.6 cm⁻¹, corresponding to monolayer MoS₂.³⁷⁴ The STS-measured band gap of ~2 eV in **Fig. 3.2c** further indicates good material quality.¹⁶⁵ Due to the large mismatch between the lattice constants of MoS₂ (3.16 Å) and EG (2.46 Å), which prevents direct epitaxy but allows van der Waals epitaxy of MoS₂, a Moiré superstructure is expected to develop.³⁵⁴ As shown in **Fig. 3.2d**, Moiré patterns with different levels of contrast but same periodicities are observed at different scanning conditions by UHV STM. To observe Moiré patterns, the tunneling current must be modulated by both the top MoS₂ and underlying EG layers concurrently, which implies that the appearance of Moiré patterns is dependent on tunneling conditions.³⁷⁵ At certain tunneling

conditions, Moiré patterns can disappear, as observed both in previous literature³⁷⁶ and in our experiments. The relatively high tunneling current used in **Fig. 3.2d** ensures an effective overlap between the electron wave functions from both the MoS₂ and EG layers, thus allowing STM observation of the Moiré patterns. A schematic illustration of the observed Moiré patterns is provided in **Fig. 3.3**, which further confirms that the MoS₂ lattice is well-aligned with that of the EG.



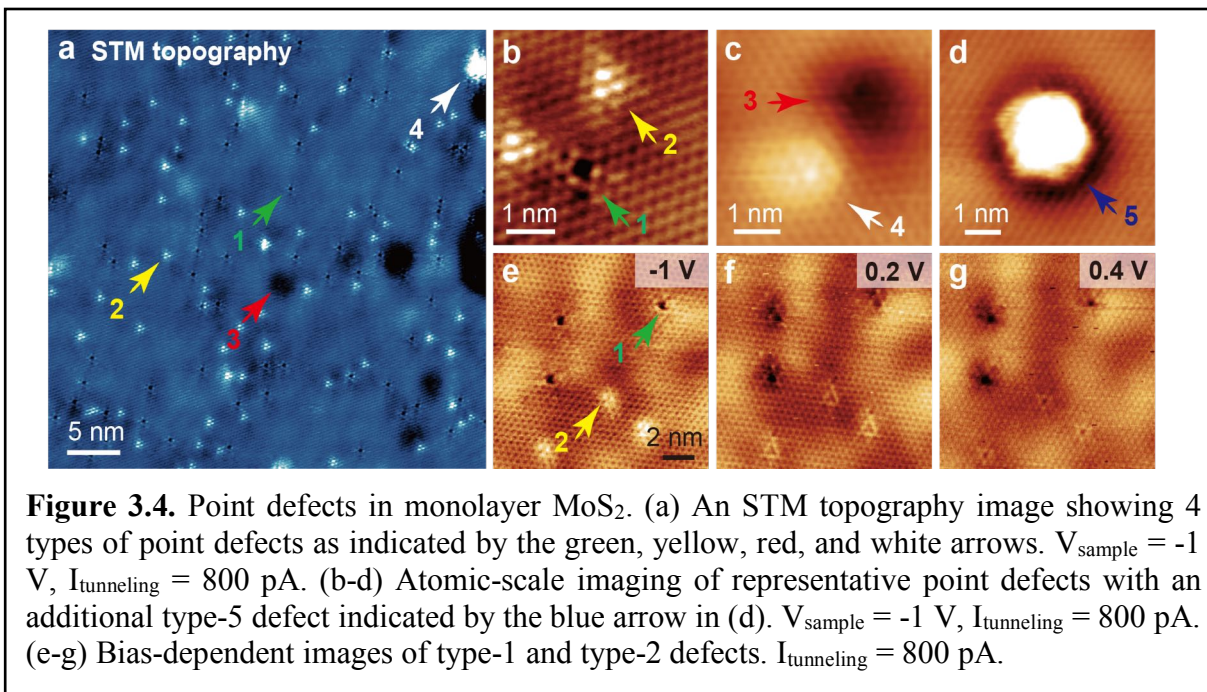
Although the monolayer MoS₂ crystal domains are flat over relatively large length scales as imaged by AFM (**Fig. 3.2a**), several types of point defects are present when examined at the atomic scale in STM. For example, **Fig. 3.4a** is an STM topography image of the monolayer MoS₂ surface recorded at $V_{\text{sample}} = -1$ V with the crystal lattice resolved and decorated with apparently bright and dark defects. Four types of atomic defects are identified and labeled as type-1 to type-4 with each indicated by a green, yellow, red, and white arrow, respectively. From **Fig. 3.4a**, the majority of point defects can be characterized as type-1 and type-2, with respective areal densities of $4.2 \times 10^{12}/\text{cm}^2$ and $3.8 \times 10^{12}/\text{cm}^2$. Averaging over several images, the total defect density is ~ 8

$\times 10^{12}/\text{cm}^2$, which is lower than the reported defect densities of MoS₂ directly grown or mechanically exfoliated onto SiO₂.^{362,368} This low defect density can likely be attributed to the registry of MoS₂ with EG, and is consistent with the high crystal quality that is expected for van der Waals epitaxy.^{66,377}

High-resolution STM images showing type-1 to type-4 defects are shown in **Fig. 3.4b** and **c** with an additional type-5 defect shown in **Fig. 3.4d**. The type-1 and type-2 defects have well-defined structures in which the type-1 defect appears as a depression and the type-2 defect consists of 3 bright protrusions. Chalcogen vacancy defects in TMDCs (e.g., sulfur vacancies in MoS₂³⁶⁸ and selenium vacancies in TiSe₂³⁷⁸) are common, and their prevalence is explained by the low vacancy formation energy of chalcogen atoms as calculated by density functional theory (DFT), whereas metal vacancies are energetically unfavorable.^{368,379,380} Hence, it is likely that type-1 defects are sulfur monovacancies, which is consistent with previous literature that assigned apparent depressions in STM images to chalcogen vacancies.^{378,381,382}

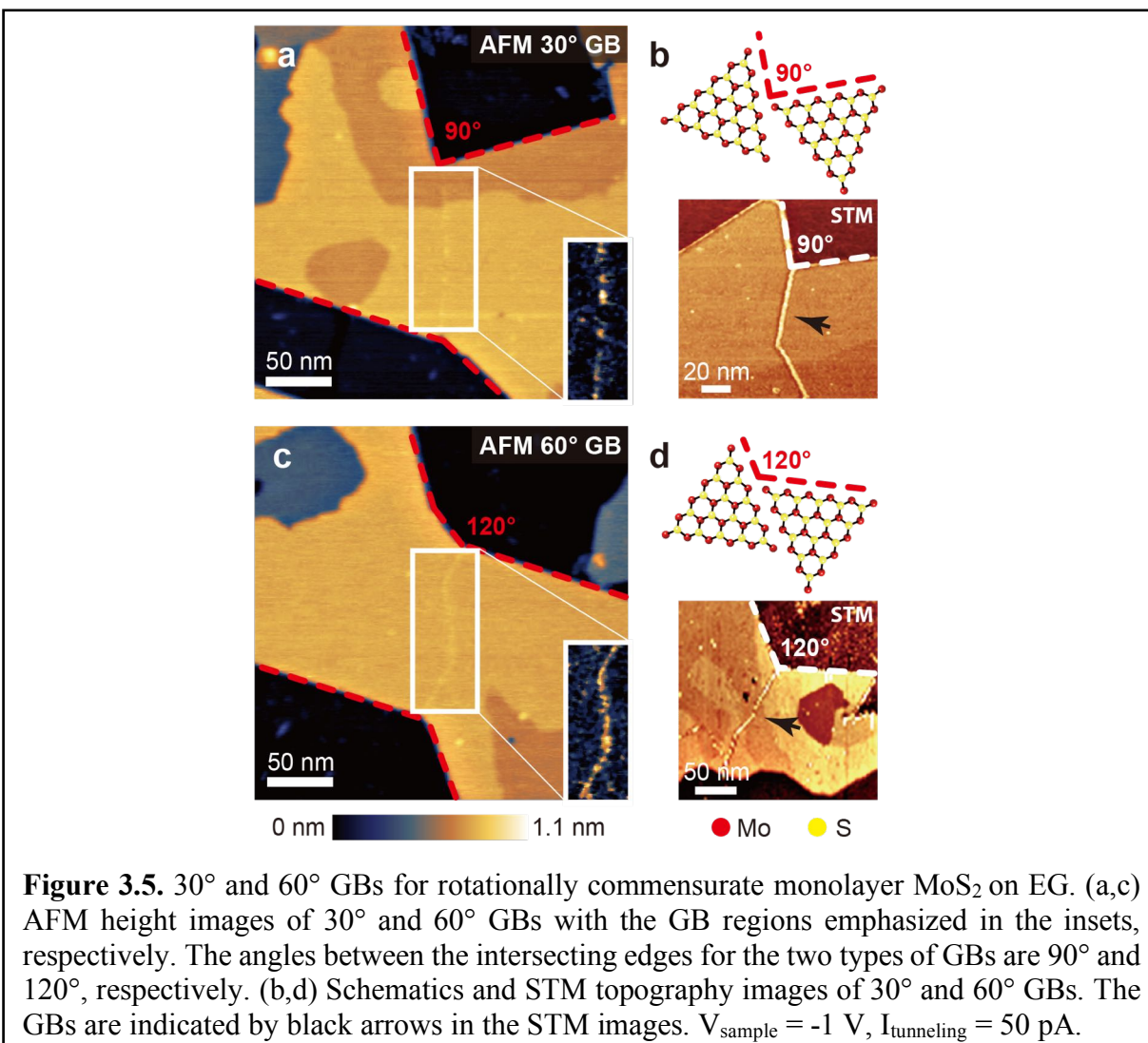
Type-2 defects appear as aligned triangles formed by three point protrusions. Such structures have been experimentally observed in TiSe₂ and assigned to Ti interstitial atoms.³⁸² However, given the much higher formation energy of interstitial Mo defects in comparison to S interstitials,³⁷⁹ type-2 defects are more likely to be S interstitials, which implies that the type-1 and type 2 defects are possibly Frenkel pairs. Although Frenkel defects in non-layered bulk materials are associated with high formation energy, the empty sites in the van der Waals gap between MoS₂ and EG may effectively lower the activation energy in this case.³⁸³ Alternatively, considering the low formation energy of sulfur divacancies,³⁶⁸ such defects can also be prevalent. Indeed, recent work³⁸⁴ suggests that sulfur divacancies also appear as triangular protrusions in simulated STM images. Therefore, type-2 defects are also consistent with a sulfur divacancy model.

The type-3 and type-4 defects shown in **Fig. 3.4c** do not have well-defined boundaries and vary in size (**Fig. 3.4a**). The continuous MoS₂ lattice through the defect area indicates that the



origin of these defects is likely to be subsurface (*e.g.*, defects in the underlying EG or the bottom sulfur layer in monolayer MoS₂). Finally, the type-5 defect in **Fig. 3.4d** appears as an adsorbed particle, possibly originating from the CVD source materials. The depression surrounding the particle may result from an electron depletion zone, which can be caused by Coulomb repulsion from a negatively charged defect. In **Figs. 3.4e-g**, the bias-dependent behavior of type-1 and type-2 defects are provided. At different biases, type-1 defects do not show obvious changes in appearance, whereas type-2 defects develop depressions at their centers. In both filled and empty states images, type-1 defects appear as depressions, which suggests the presence of physical pits in topography as would be expected for sulfur vacancies.

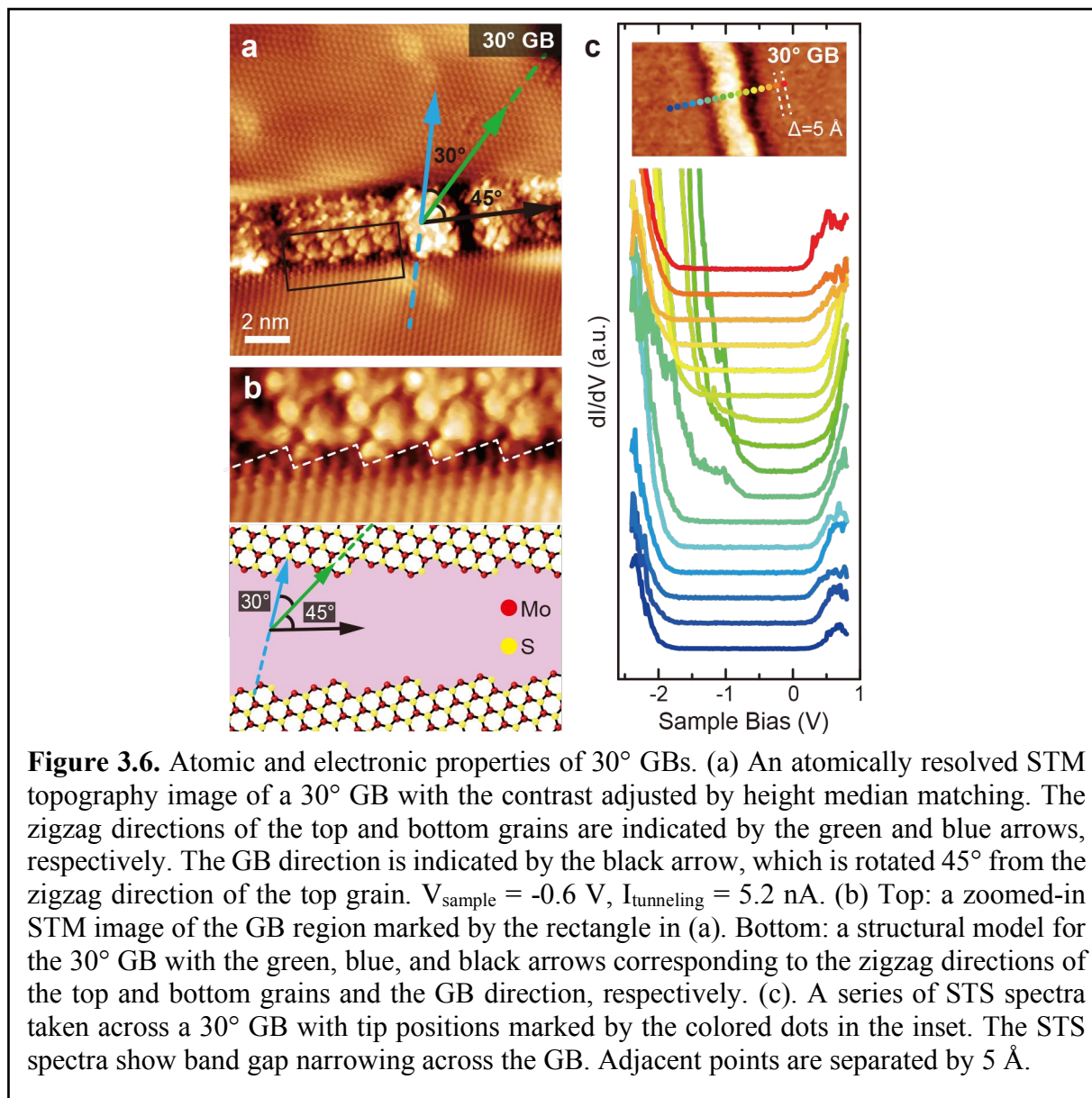
A second class of structural defects in 2D materials are line defects, including dislocations and GBs. Compared to zero-dimensional point defects, which are primarily imaged with atomic resolution methods, one-dimensional GBs can be detected at larger length scales. Driven by the



importance of understanding GBs in the 2D limit, a number of approaches have been developed to visualize MoS₂ GBs including preferential oxidation of GBs,³⁸⁵ nonlinear optics,^{386,387} and stacking of MoS₂ bilayers.³⁸⁸ As a consequence of rotational commensurability, the GBs of MoS₂ grown on EG are restricted to tilt angles of 30° and 60°. **Fig. 3.5a** is an AFM topography image of a 30° GB for monolayer MoS₂ on EG. The formation of such GBs involves a 30° rotated crystal domain as shown in the schematic of **Fig. 3.5b**, where the angle between two triangular domain edges is 90°. Although domains with 30° rotated angles are less energetically favorable than aligned domains, the small fluctuations of binding energies with respect to rotation angle in van

der Waals heterostructures implies that a secondary crystal orientation may still be present experimentally.³⁸⁹ Because the 30° rotated domains comprise only 14% of the total crystals as quantified in our previous work,¹⁶⁵ 30° GBs are the minority species. While the 30° GB is weakly resolved by AFM as shown in **Fig. 3.5a** and its inset, a GB of the same type shows stronger contrast in the STM topography image in **Fig. 3.5b**, likely due to electronic effects that will be explored further later. In addition, **Fig. 3.5c** shows an AFM image of a 60° GB with the inset emphasizing the GB region. A schematic and STM image of a 60° GB are shown in **Fig. 3.5d**. These 60° GBs are twin GBs resulting from two triangular domains with opposite orientations.³⁶⁷ Due to the three-fold symmetry of the MoS₂ lattice, the resulting GB has a 60° tilt angle. Again, with likely electronic contributions, the 60° GBs show significant contrast in STM, appearing as bright protrusions.

Further understanding of MoS₂ GBs is gained through atomic-resolution UHV STM imaging. In particular, **Fig. 3.6a** shows a high-resolution STM image of a 30° GB, where the arrows denote the zigzag directions of the top (green arrow) and bottom (blue arrow) domains separated by the GB. Since GBs are bright protrusions in the filled states images (**Fig. 3.5b,d**), height median matching is performed on **Fig. 3.6a** so that both the domain interior regions and the GB structure show observable contrast in the image. Unlike the disordered GBs found in CVD graphene where the GBs are curved,³⁹⁰ most GBs in MoS₂ are observed to be straight. The orientation of the 30° GB in **Fig. 3.6a** is denoted by the black arrow, which has a 45° rotation angle with respect to the zigzag direction of the top grain (green arrow). The GB possesses discontinuities and exhibits segments of ordered structure. The apparent width of the GB is ~2.3 nm, which is larger than the expected few lattice constant width from S/TEM.^{54,365} However, the fact that constant current STM images are a convolution of real space and electronic structure



makes STM imaging sensitive to local electronic properties in addition to atomic structure. The electronic disturbance resulting from the GB is expected to have a finite decay distance as discussed in **Fig. 3.7**, which would lead to the GB appearing wider in STM imaging. The higher chemical reactivity of GBs may also result in adsorbed impurities that could contribute to the apparent width of the GBs.

A zoomed-in image of the region marked by the black rectangle in **Fig. 3.6a** is shown in

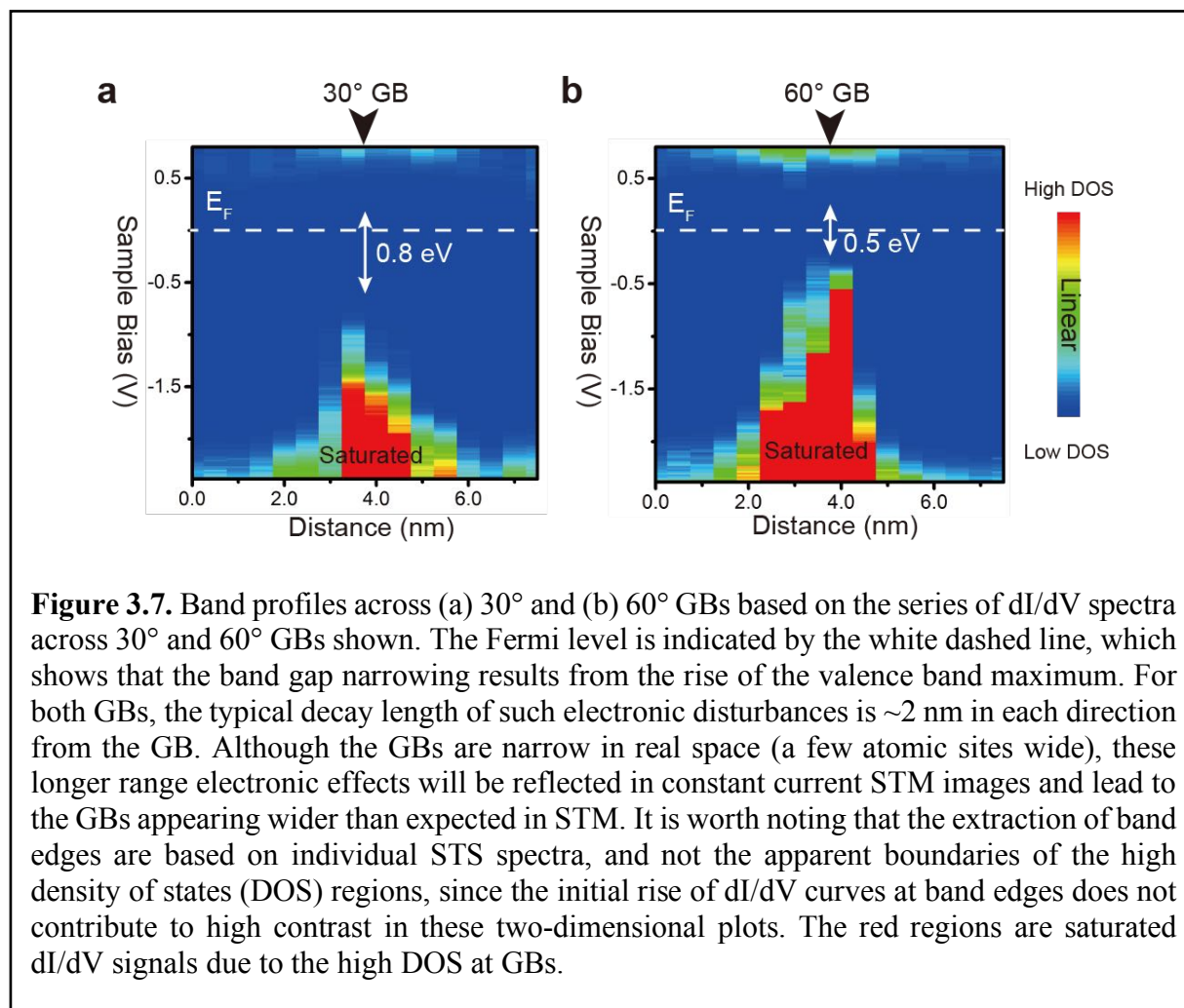
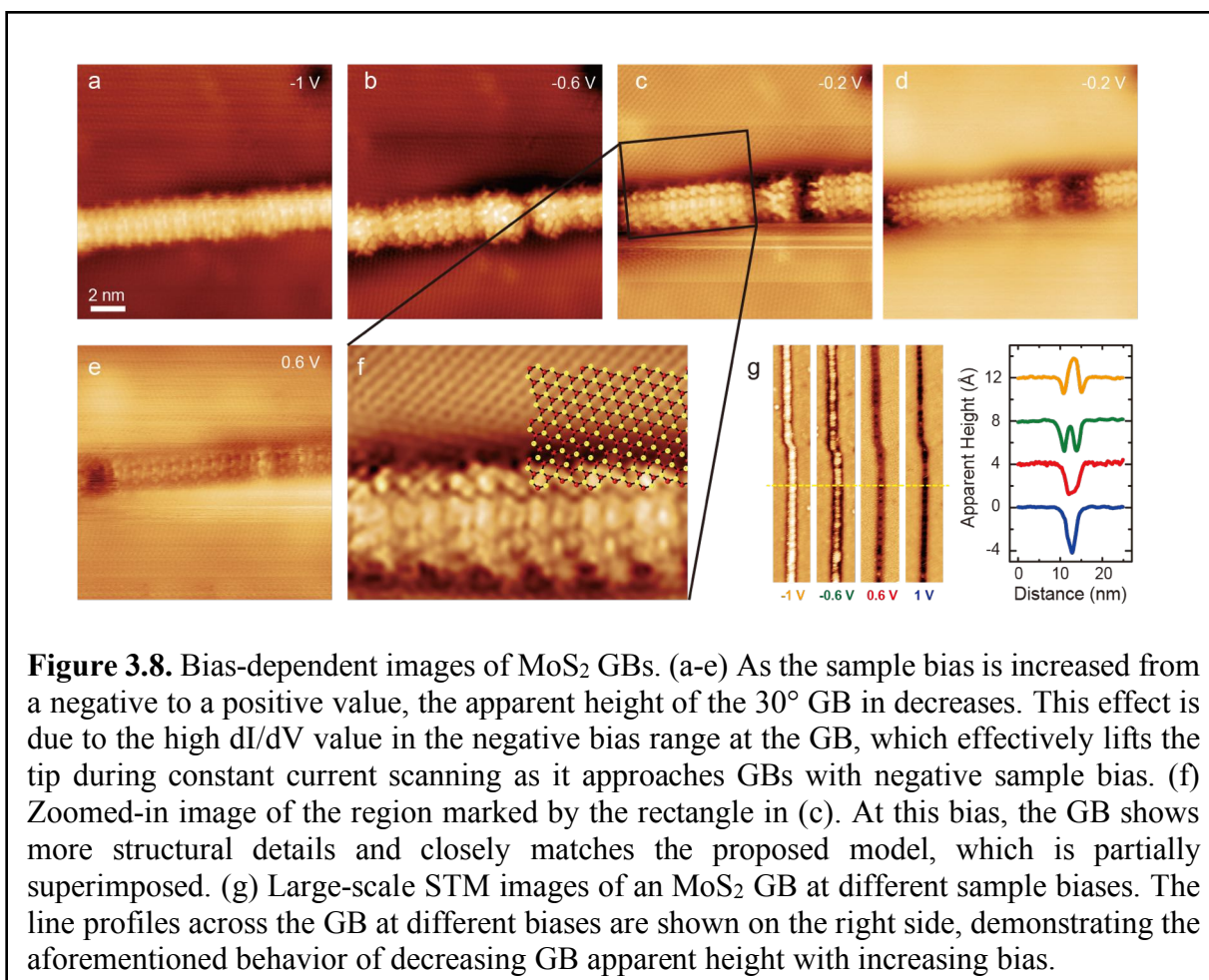


Fig. 3.6b. A linear superstructure is found at the interface between the GB region and the bottom grain as indicated by the white dashed line. Along the GB direction, the periodicity of the superstructure is 4-fold great than that of the bottom lattice. Based upon this superstructure and the orientation of the GB, an atomic model is proposed in the bottom panel of **Fig. 3.6b**. The green and blue arrows correspond to the zigzag lattice orientations of the top and bottom grains, respectively. The pink area represents the GB region bordered by periodic facets along the zigzag direction of the MoS₂ lattice. The periodicity of this superstructure is 4 times greater than that of the lattice, which is consistent with the STM image in the top panel of **Fig. 3.6b**. The resulting GB

orientation as indicated by the black arrow in the schematic is indeed rotated 45° from the zigzag direction of the top grain (green arrow). Hence, this atomic model satisfies the critical observed characteristics of the 30° GB. Bias-dependent images of this GB are provided in **Fig. 3.8**, which show further details that support this proposed structure.

The electronic consequences induced by the 30° GB are explored with STS point spectra taken across the GB, as shown in **Fig. 3.6c**. The distance between two adjacent points in the inset is 5 \AA . Far from the GB region in both domains, the band gaps are uniformly $\sim 2 \text{ eV}$, which is consistent with **Fig. 3.2c** and literature reports of MoS₂ bandgaps on graphite substrates (2.15 eV ,³³⁸ 1.9 eV ³⁵⁷). As the tip moves onto the GB, a band gap reduction to $\sim 0.8 \text{ eV}$ (*i.e.*, a reduction of $\sim 1.2 \text{ eV}$) is observed and accomplished primarily by the rise of valence band maximum (VBM).



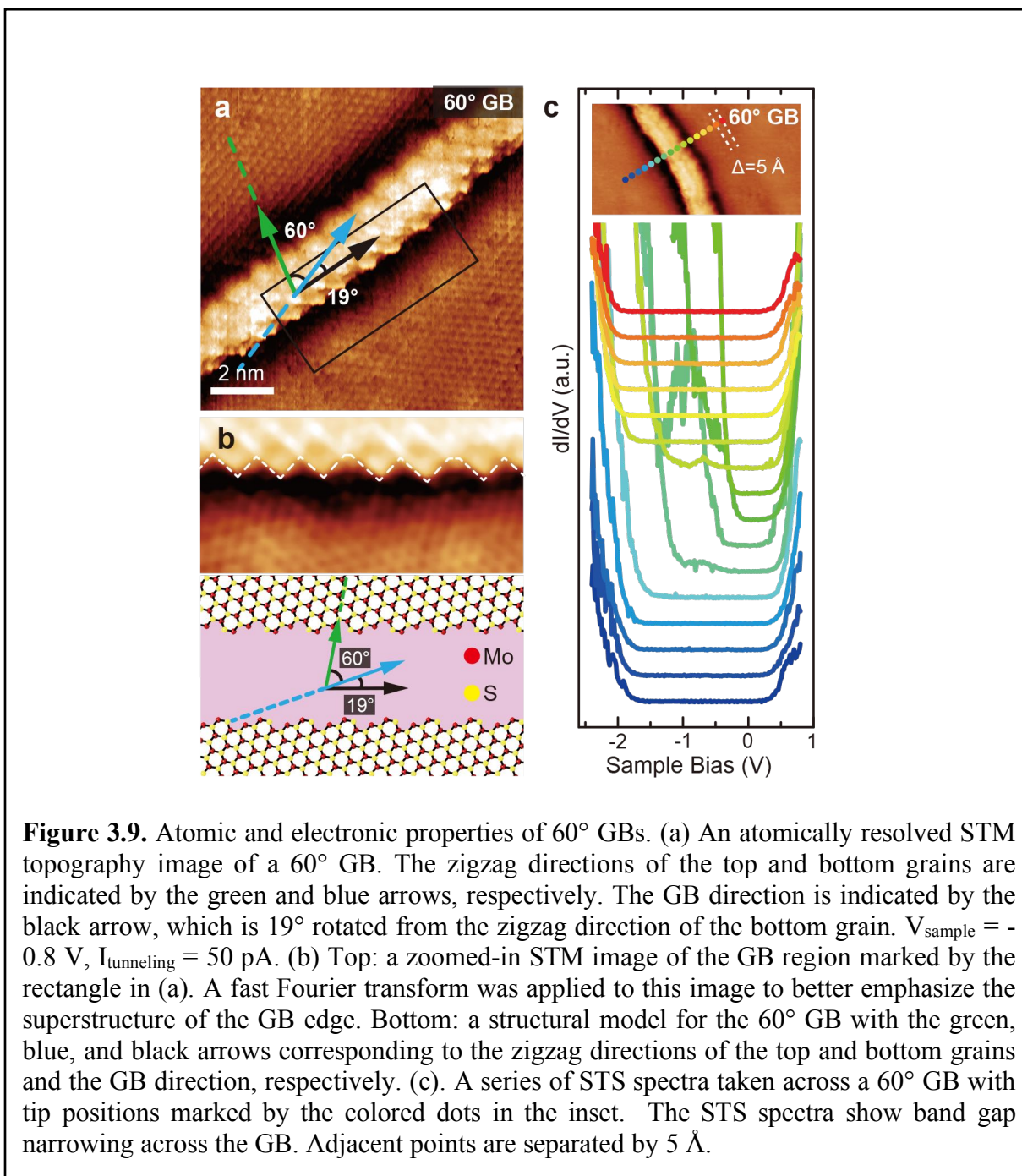
This observation agrees qualitatively with the observed band gap reduction at MoS₂ random tilt GBs (*i.e.*, ~ 0.85 eV at a 18° GB) and the trend that GBs with higher angles possess smaller bandgaps.³⁵⁶ Simulations and S/TEM results of GB structures also suggest that lattice distortions, point defects, and atoms with different coordination from the bulk lattice can be present in GBs.^{54,361,365,391} Furthermore, the resulting higher chemical reactivity due to local strain (*e.g.*, from sulfur vacancies³⁹²) and/or under-coordinated atoms may lead to oxidation and adsorption of impurities at GBs. All of these factors may contribute to additional electronic states in the band gap and/or close to the band edges, leading to the reduced band gap at GBs.

A more common 60° GB is examined at the atomic scale in **Fig. 3.9**. The green and blue arrows in **Fig. 3.9a** represent the respective zigzag directions of the top and bottom grains rotated by 60° from each other. In this case, the GB has a rotation angle of 19° from the bottom grain (blue arrow) indicated by the black arrow. The width of this GB is approximately 2 nm, which is slightly smaller than that of the 30° GB. The zoomed-in periodic superstructure in **Fig. 3.9b** shows a periodicity 3 times that of the MoS₂ lattice along the GB direction. The proposed atomic model includes similar faceted interfaces with the corresponding periodicity in the superlattice. The resulting 19° GB direction relative to the zigzag direction of the bottom grain within the model again matches the orientation measured experimentally by STM. Since STM topography images are a convolution of physical and electronic structure, determining the detailed atomic structure in the GB region is difficult. It has been proposed that a disordered transition region in monolayer MoS₂ exists to accommodate the local strain in a 18° tilt GB.³⁵⁶ In addition, an STEM-based study⁵⁴ showed that 60° GBs (*i.e.*, twin GBs) are $\sim 20^\circ$ rotated from the zigzag direction of the MoS₂ lattice, which is consistent with the 19° rotation observed here. Our structure model is further confirmed by their GB structure model consisting of primarily 8-4-4 membered rings at the

interface of the GB, and the two grains being faceted with the same structure proposed in **Fig.**

3.9b.

Electronically, the 60° GB shows a slightly larger band gap reduction to ~ 0.5 eV primarily



due to the rise of the VBM, as demonstrated by the series of STS spectra taken across the GB

shown in **Fig. 3.9c**. This trend is consistent with literature precedent where larger tilt angles result in smaller band gaps in monolayer MoS₂ on graphite.³⁵⁶ The larger apparent height of the GB compared to grain interiors imaged at negative sample biases in **Fig. 3.9** can be explained by the higher differential tunneling conductance, which is proportional to the sample density of states (DOS), from -0.5 V to -2 V, when the tip is above the GBs. The increased DOS drives the tip farther away from the GBs to maintain a constant tunneling current during STM imaging. This electronic effect also explains why the apparent height of GBs decreases at positive biases as shown in **Fig. 3.8**.

In summary, a detailed study of the intrinsic structural defects of rotationally commensurate CVD-grown monolayer MoS₂ on EG has been carried out at the atomic scale using STM and STS. Five types of point defects, including atomically resolved vacancies and interstitials, were observed and occurred at lower areal density than alternative monolayer MoS₂ sample preparation methods likely due to the nature of van der Waals epitaxy of MoS₂ on EG. GBs were found to be more clearly imaged by STM than AFM due to their pronounced electronic contrast. STS shows band gap narrowing at 30° and 60° GBs, resulting from additional DOS close to the VBM. Based on the relative orientations of the GBs and the periodicities of the observed superlattices, consistent structural models were proposed for each type of GB. Overall, this study provides fundamental insights and a basis for ongoing efforts to realize defect engineering in 2D TMDCs,^{393,394} especially for commensurate heterostructures enabled by substrates like graphene where predictable GB orientations are present.

3.3 Mixed-Dimensional Heterostructures of C8-BTBT with MoS₂/EG

While device-scale demonstrations and fundamental charge/energy transfer studies of organic/monolayer-MoS₂ heterostructures are heavily reported in literatures,^{181,190,332,395,396} molecular scale characterizations of the ordered organic/MoS₂ interface remain largely unexplored. Especially, though the combination of MoS₂ with the organic p-type semiconductor pentacene results in gate-tunable photovoltaic p-n heterojunctions,¹⁹⁰ the disordered molecular layer at the interface is potentially responsible for the longer characteristics time (~6 ps) for hole transfer from MoS₂ to pentacene than typical 2D-2D heterojunctions.^{67,72} Given the importance of interfaces in vertical heterostructures, it is highly desirable to identify an organic semiconductor that is not only technologically relevant when integrated with MoS₂, but also self-assembles into ordered structures at the interfaces. One of the candidates is C8-BTBT, a large bandgap (~3.9 eV) p-type

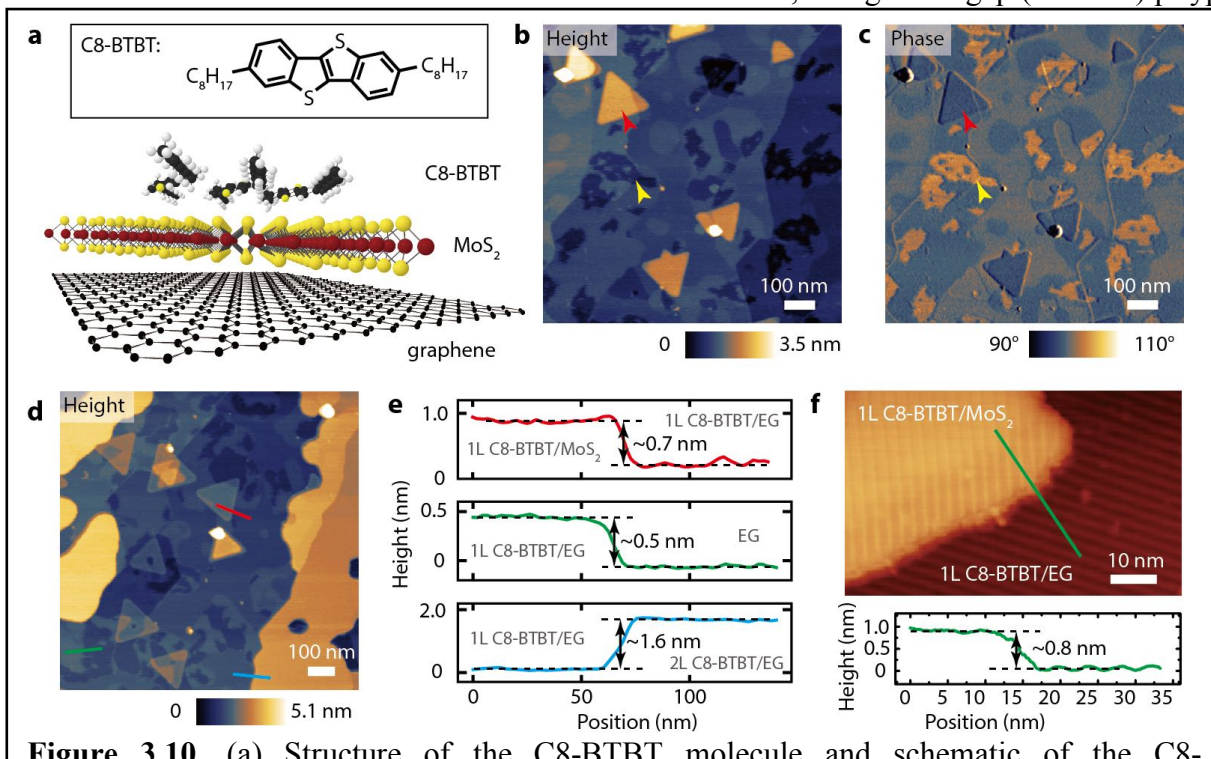
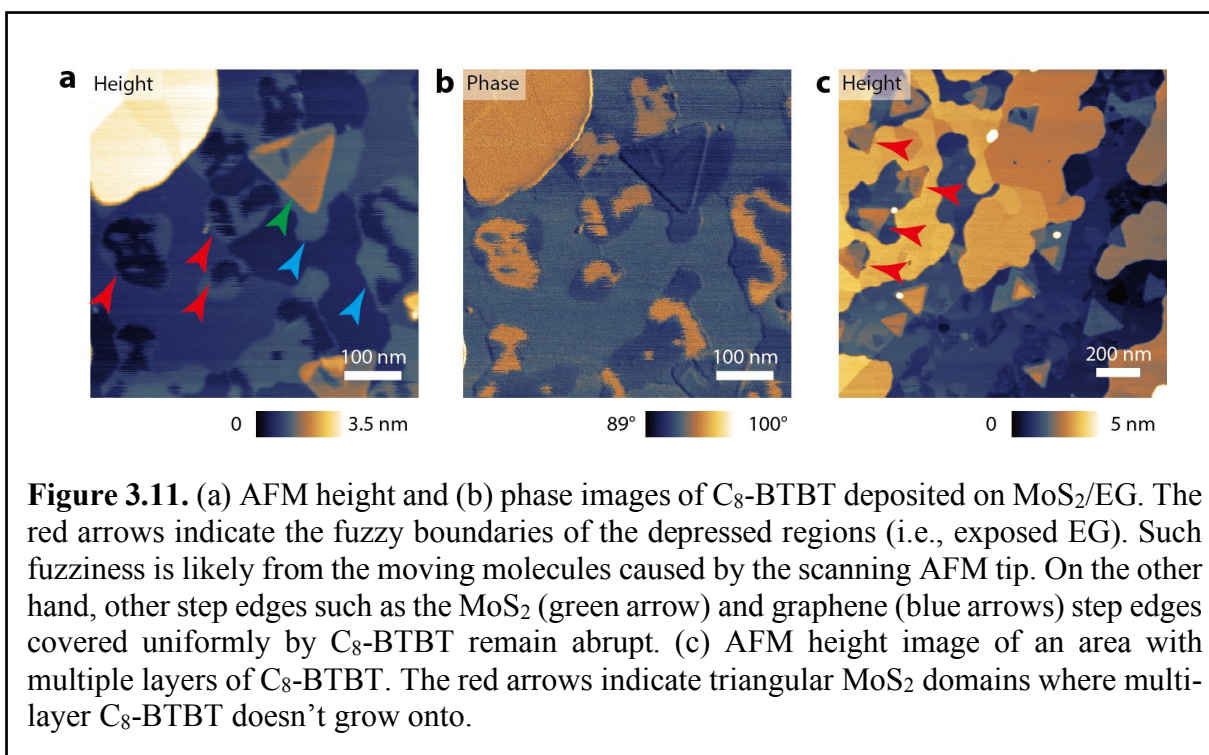


Figure 3.10. (a) Structure of the C8-BTBT molecule and schematic of the C8-BTBT/MoS₂/graphene mixed-dimensional heterostructure. (b) AFM height and (c) phase image of sub-monolayer C8-BTBT deposited on MoS₂/EG. (d) AFM height image of an area with bilayers of C8-BTBT. (e) Extracted height profiles from the corresponding traces shown in d. (f) STM image of the MoS₂/EG boundary covered by monolayer C8-BTBT. Inset: extracted height profile measured along the green line.

semiconductor that has recently gained a lot of attention. It is among the highest mobility organic molecules with demonstrated carrier mobility up to $43 \text{ cm}^2\text{V}^{-1}\text{s}^{-1}$ in thin film transistors.^{397,398} The self-assembly structure of C8-BTBT has been illustrated on semimetal graphene and insulating hBN nanoflakes obtained via mechanical exfoliation.³⁹⁹⁻⁴⁰² However, p-n heterojunction between semiconductors is desired for ubiquitous electronics and optoelectronics applications. Though the integration with n-type MoS₂ is highly interesting, to our knowledge, the molecular ordering of C8-BTBT on MoS₂ remains undetermined. Because molecular ordering can significantly influence the charge and energy transfer processes across the heterojunction,^{330,399} we explore the 0D-2D heterostructure composed of monolayer MoS₂, graphene and C8-BTBT at the molecular scale using UHV STM/STS.

To minimize contamination from exfoliation, high quality rotationally commensurate MoS₂ grown via CVD on EG/SiC^{165,403} is used for the UHV deposition of C8-BTBT. The resulting vertical p-n heterojunction (**Fig. 3.10a**) is a prototype architecture for photodetectors, photovoltaic cell and light-emitting diodes, where the bottom EG acts as a transparent conductor.^{190,329,404-406} Sub-monolayer C8-BTBT deposited on MoS₂/EG exhibits a smooth surface morphology as shown in the AFM height image in **Fig. 3.10b**, implying ordered molecular layers. In addition to the triangular MoS₂ domains indicated by the red arrow and terraces from EG and SiC, regions of depressions indicated by the yellow arrow are present and show enhanced contrast in the phase image of the same region (**Fig. 3.10c**). This can be rationalized by assigning the depressed regions to exposed EG surfaces, whereas the rest of the surface is covered with C8-BTBT layers. Such assignment is first supported by the fuzzy boundaries of the depressed regions when imaged at higher resolution (**Fig. 3.11a,b**), consistent with mobile molecules found at a molecular domain boundary during AFM imaging. **Fig. 3.10d** shows another area with additional layers of C8-BTBT.

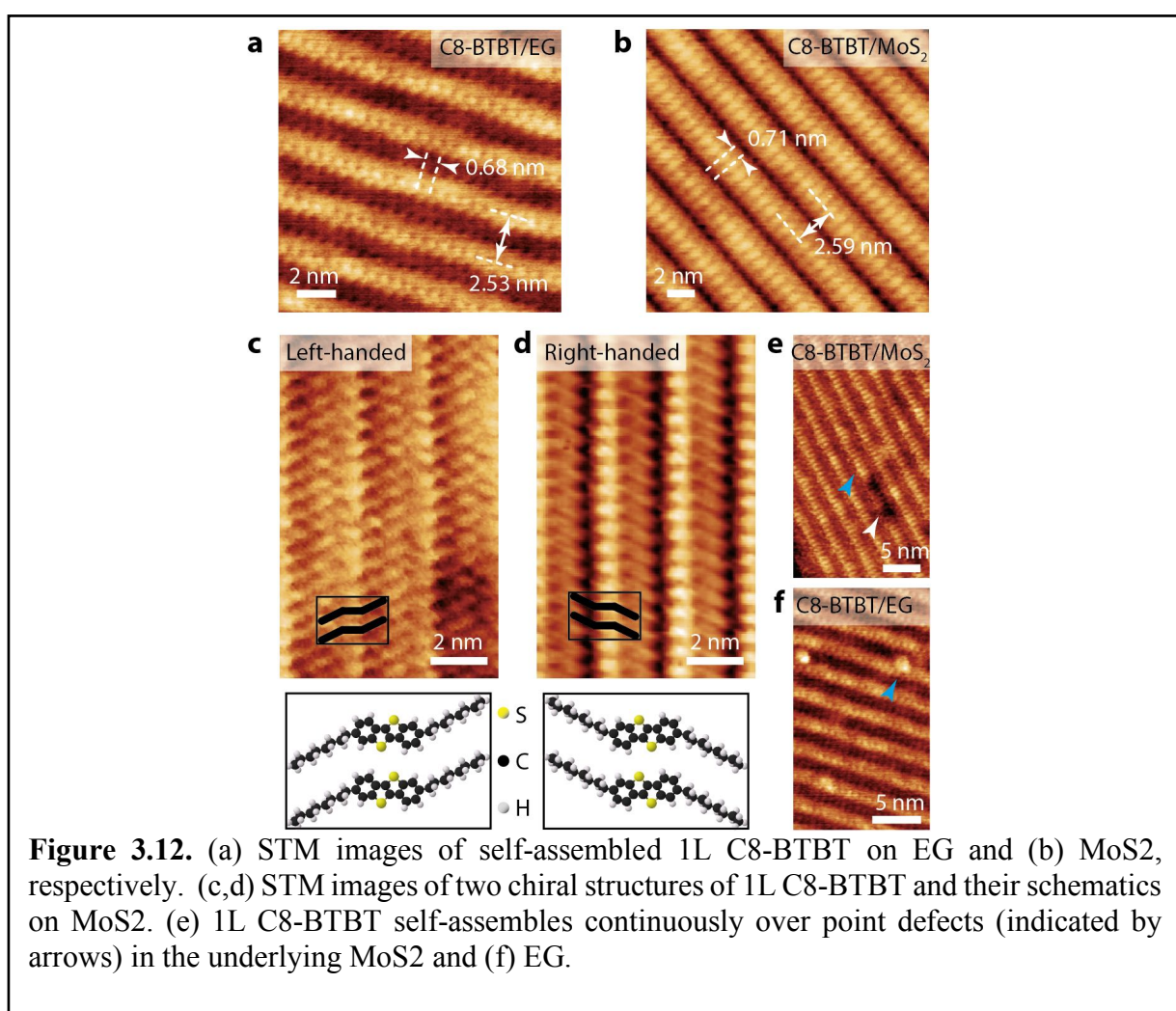
The step edge profiles across a MoS₂ layer (red), a depressed region boundary (green), and a thicker C₈-BTBT layer boundary (blue) are shown in **Fig. 3.10e**, where the step heights of 0.7 nm, 0.5 nm, and 1.6 nm are extracted, respectively. The 0.7 nm step height corresponds well to the thickness of a monolayer MoS₂, suggesting identical C₈-BTBT thicknesses atop MoS₂ and EG. The 0.5 nm step height matches the reported thickness of a monolayer (1L) of C₈-BTBT on



graphene with a lying-down configuration,⁴⁰⁰ supporting our assignment of the depressed regions as bare EG. Finally, the 1.6 nm step height is expected for the second layer (2L) of C₈-BTBT on graphene adopting a semi-standing-up configuration, where individual molecules are vertically self-assembled but with a considerate tilt angle.⁴⁰⁰ Therefore, we have obtained the heterostructure composed of 1L C₈-BTBT over monolayer MoS₂ on EG, further confirmed by the STM image shown in **Fig. 3.10f**, where rows of C₈-BTBT molecules are present on both MoS₂ and EG with an expected monolayer MoS₂ step height of ~0.8 nm. It is worth noting that while regions of exposed EG exist under sub-monolayer C₈-BTBT coverage (**Fig. 3.10b**), no exposed regions of

MoS₂ are detected. At higher coverages (**Fig. 3.10d**), the 2L C8-BTBT instead nucleates on 1L C8-BTBT/EG regions and avoids 1L C8-BTBT/MoS₂ domains as shown in **Fig. 3.11c**. Such phenomena of preferential adsorption have been observed in other material systems such as organics on borophene²⁴ and GaSe,⁴⁰⁷ and could potentially be explained by the difference of adsorption enthalpies of the molecules.

While multilayers of undoped C8-BTBT is too insulating for stable STM imaging, the



structure of self-assembled 1L C8-BTBT on EG and MoS₂ could be resolved at the molecular scale as shown in **Fig. 3.12a,b**, respectively. Both structures appear as linear chains with similar widths (2.53 and 2.59 nm on EG and MoS₂, respectively) and periodic intra-chain segments (0.68 and

0.71 nm on EG and MoS₂, respectively), suggesting similar or identical self-assembly structures of 1L C8-BTBT on both surfaces. Such dimensions are in agreement with the structure of 1L C8-BTBT adopting the lying-down configuration.⁴⁰¹ However, this result contrasts previously reported standing-up configuration of 1L C8-BTBT on MoS₂ surfaces inferred only from step height measurements from atomic force microscopy.⁴⁰⁸ Higher resolution images of C8-BTBT on MoS₂ reveal two chiral structures that have not been observed previously (**Fig. 3.12c,d**), though they are expected from the geometry of individual C8-BTBT molecules. The two arrangements of the molecules are shown schematically at the bottom of **Fig. 3.12c,d**. Though the point defect density of such rotationally commensurate MoS₂ is almost an order of magnitude smaller than MoS₂ grown on amorphous oxide substrate,⁴⁰³ a large number of point defects do exist as local protrusions and depressions as shown in **Fig. 3.13a**. Similarly, protruded point defects are commonly observed on bare EG surfaces after graphitization in UHV (**Fig. 3.13b**). As shown in **Fig. 3.12e,f** and **Fig. 3.13c-e** upon the deposition of 1L C8-BTBT, the molecules are found to self-assemble conformably and continuously across such protruded (blue arrows) and depressed (white arrow) point defects without being perturbed. Furthermore, the molecular stripes also extend across the step edges of single EG layers (**Fig. 3.13e**). Such relative insensitivity to surface defects of MoS₂ and EG leads to a lower defect density in 1L C8-BTBT, a highly desirable property for obtaining highly ordered C8-BTBT layers with well-defined organic-inorganic interfaces, as well as templating subsequent surface chemistry.

Since the CVD grown MoS₂ adopts triangular domain shapes, the crystallographic orientation of MoS₂ could be inferred even when the atomic lattices could not be resolved with the

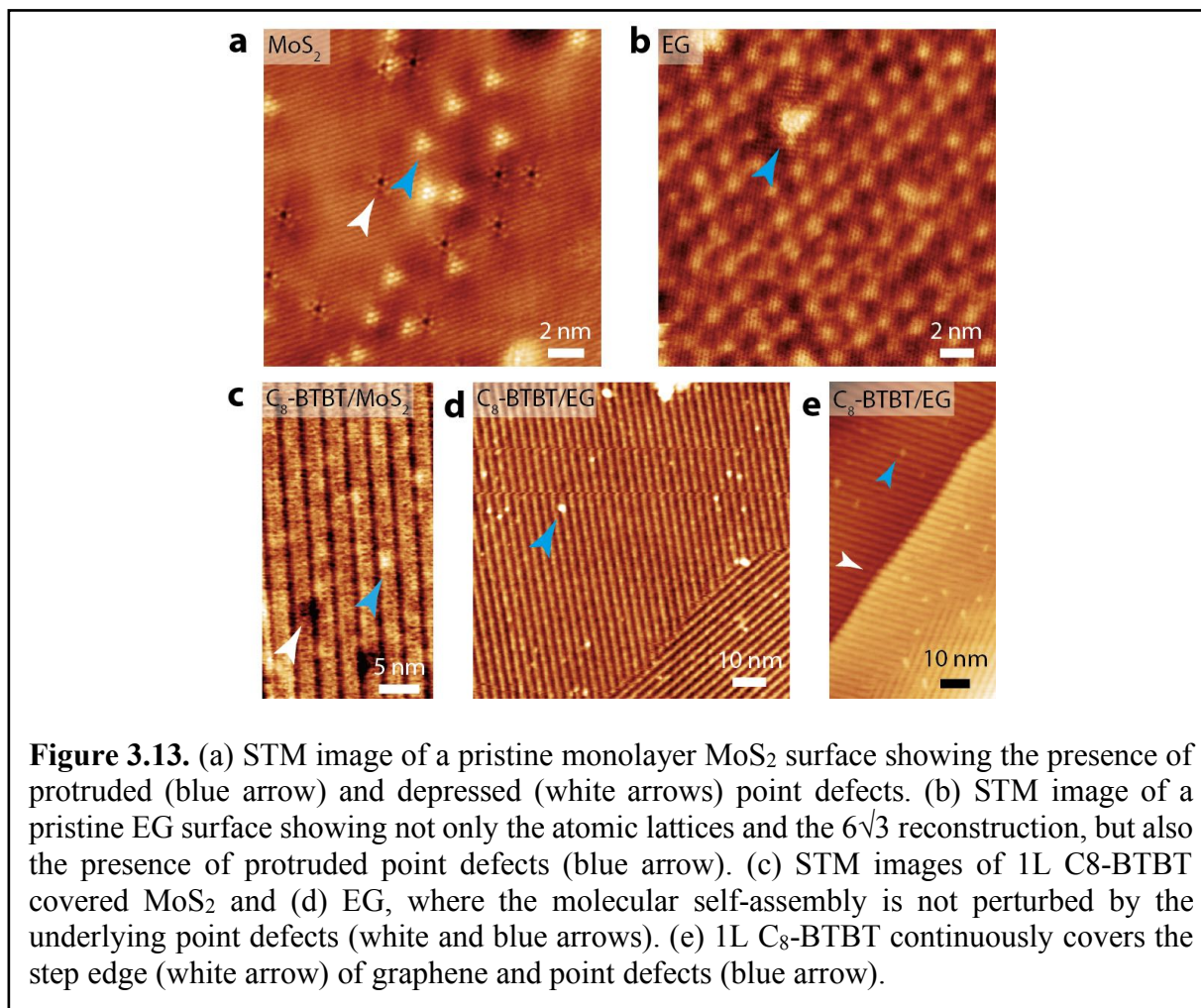


Figure 3.13. (a) STM image of a pristine monolayer MoS₂ surface showing the presence of protruded (blue arrow) and depressed (white arrows) point defects. (b) STM image of a pristine EG surface showing not only the atomic lattices and the $6\sqrt{3}$ reconstruction, but also the presence of protruded point defects (blue arrow). (c) STM images of 1L C₈-BTBT covered MoS₂ and (d) EG, where the molecular self-assembly is not perturbed by the underlying point defects (white and blue arrows). (e) 1L C₈-BTBT continuously covers the step edge (white arrow) of graphene and point defects (blue arrow).

C₈-BTBT over-layers. Though MoS₂ possesses a 3-fold symmetry, 1L C₈-BTBT covering a MoS₂ flake typically forms a single crystalline domain. If we define the acute angle between the C₈-BTBT stripe orientation (red lines) and the MoS₂ domain edge as α (inset of **Fig. 3.14a**), this angle is on average about 68° across 19 domains, as shown in **Fig. 3.14a**, indicating preferred registry of C₈-BTBT on MoS₂. If the triangular MoS₂ domains are assumed to have Mo-terminated edges, the relative orientation of 1L C₈-BTBT can be deduced as schematically shown in **Fig. 3.14b**. Together with the predictable GBs (30° and 60°) of MoS₂ resulting from rotational commensurability on EG,⁴⁰³ such rotational registry with MoS₂ renders the types of GBs in 1L C₈-BTBT highly limited, minimizing uncertainties in charge carrier scattering at GBs. For instance,

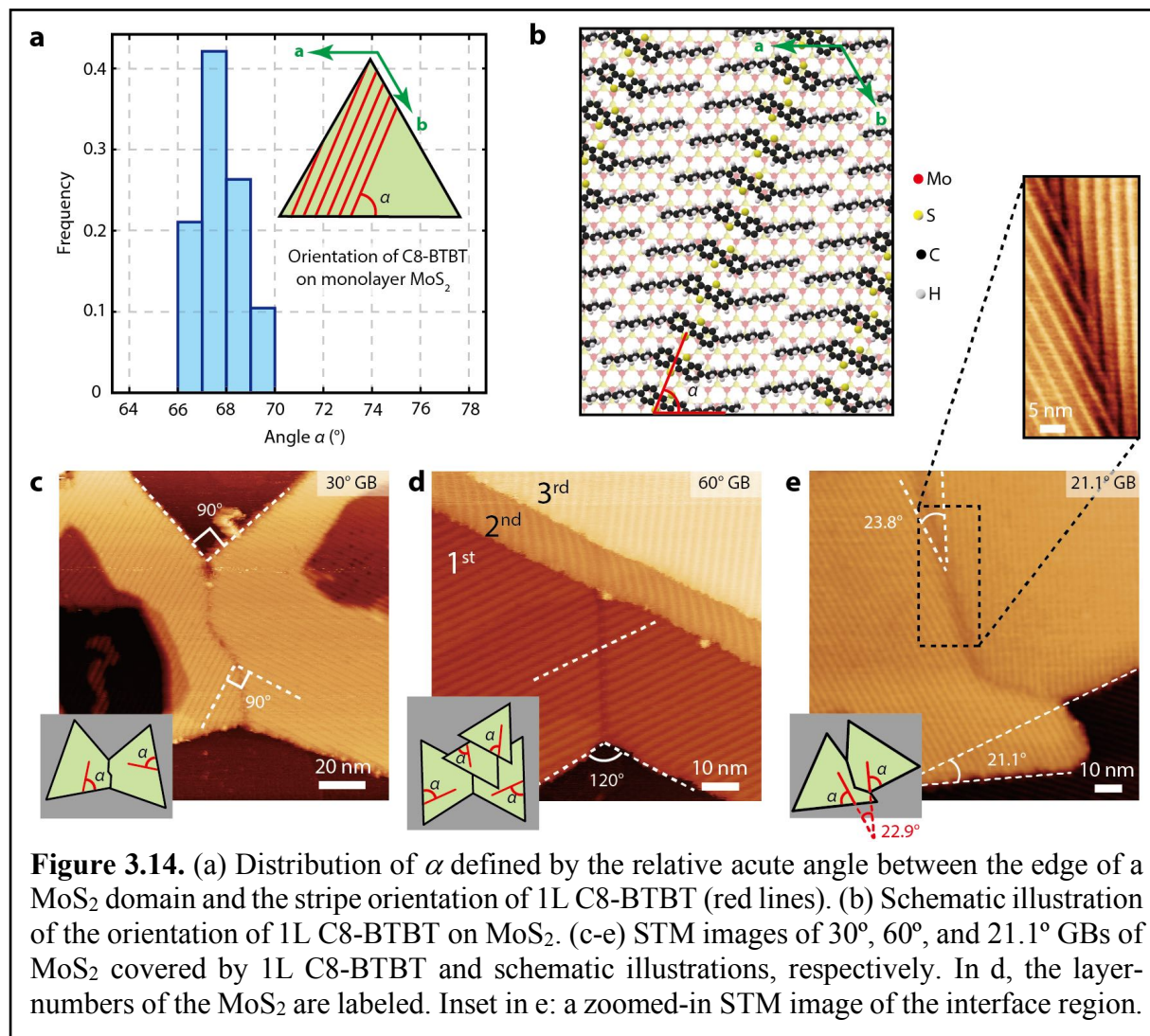
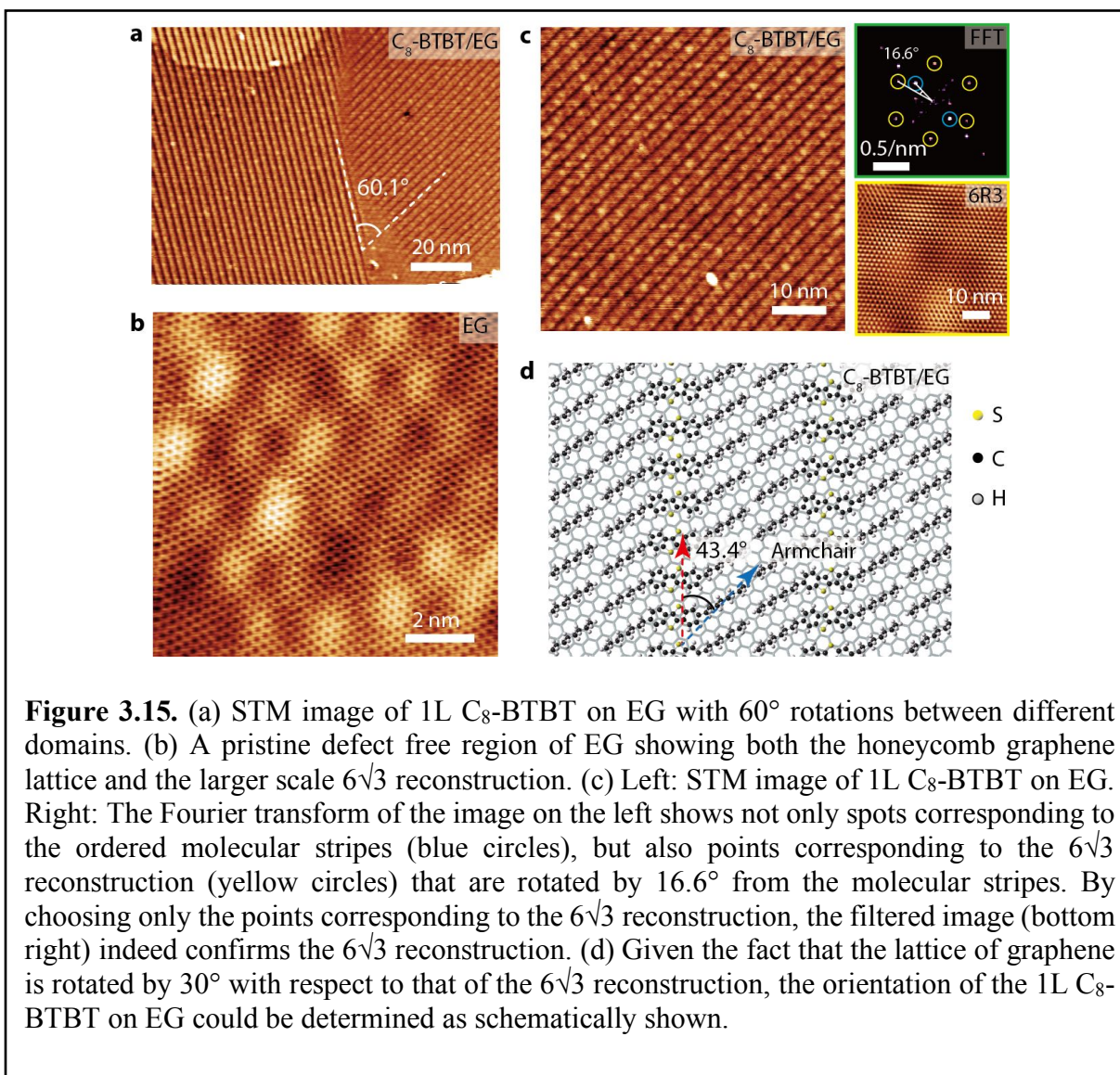


Figure 3.14. (a) Distribution of α defined by the relative acute angle between the edge of a MoS₂ domain and the stripe orientation of 1L C8-BTBT (red lines). (b) Schematic illustration of the orientation of 1L C8-BTBT on MoS₂. (c-e) STM images of 30°, 60°, and 21.1° GBs of MoS₂ covered by 1L C8-BTBT and schematic illustrations, respectively. In d, the layer-numbers of the MoS₂ are labeled. Inset in e: a zoomed-in STM image of the interface region.

Fig. 3.14c-e shows STM images of 1L C8-BTBT self-assembly across the commonly observed 30°, 60° and a rarely observed random 21.1° MoS₂ GB, respectively. The orientation of the 1L C8-BTBT on each domain is indicated by the white dashed lines, and schematically shown in the insets, in agreement with the above-determined angle of α . Especially, for the 21.1° GB in **Fig. 3.14e**, the expected relative angle between adjacent C8-BTBT domains is 22.9°, in close agreement with the measured angle of 23.8°. In **Fig. 3.14d**, the orientations of C8-BTBT are different on the three layers of MoS₂, but still agree with the model in **Fig. 3.14b**. Though MoS₂ GBs are known to present additional electronic features that decay into each domain over a length scale (~3-4 nm)

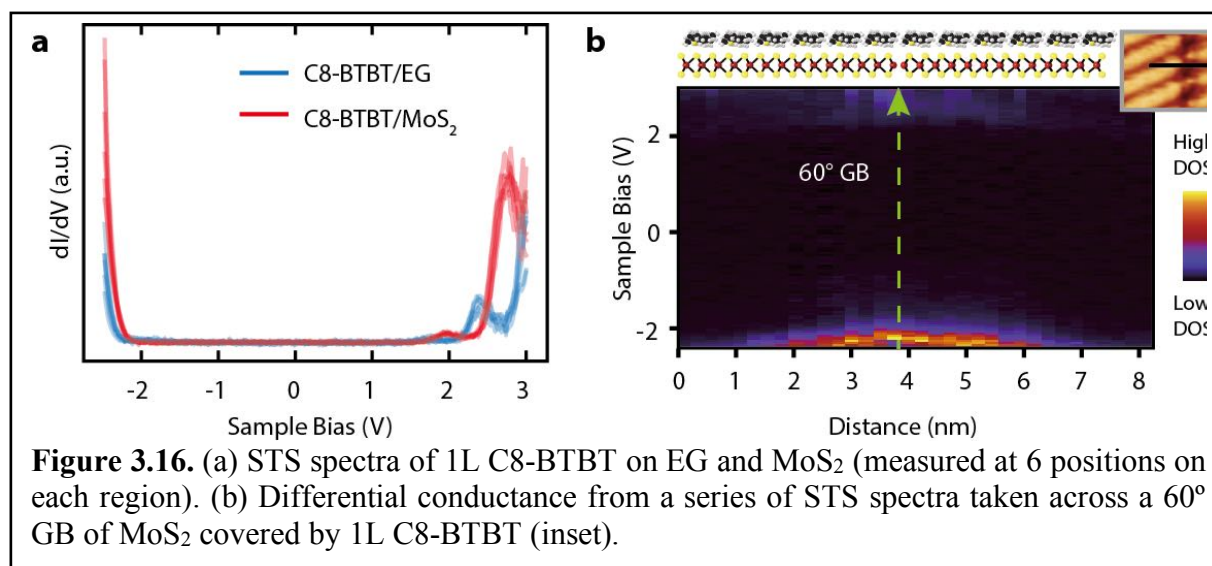
larger than the size of an individual C₈-BTBT molecule,⁴⁰³ the molecules assemble and join abruptly at the GBs shown in the inset of **Fig. 3.14e** as an example. Again, this result demonstrates the high tolerance of C₈-BTBT self-assembly with respect to substrate inhomogeneity due to strong inter-molecular interactions, in contrast to site-specific self-assembly of molecules on



textured surfaces.^{409,410} For 1L C₈-BTBT on EG, different domains are expected to rotate by 60° in accordance with the 6-fold symmetric EG surface (**Fig. 3.15a**). A similar approach is used to

deduce the relative orientation of 1L C8-BTBT on EG, which is in agreement with earlier computational results (**Fig. 3.14b-d**).⁴⁰¹

Electronically, the differential conductance, which is proportional to the sample density of states, of 1L C8-BTBT on EG and MoS₂ are shown in **Fig. 3.16a** (6 curves each) measured by point STS. The resulting curves are similar from which a gap of ~ 4 eV is measured. Interestingly,



the Fermi level lies around the center of the gap suggesting an intrinsic instead of a p-type character of 1L C8-BTBT reported from TFTs measured in ambient.^{397,398} This could likely be explained by the complete depletion of the 1L C8-BTBT when interfaced with the n-type MoS₂ and the intrinsically n-type doped EG⁴¹¹ due to the small thickness of the molecular layer, as well as the lack of p-type atmospheric doping that is typically experienced in thin film transistors measurements in ambient⁴¹² since the sample in this study is fully prepared and measured in UHV. By performing a series of STS measurements across the GB of 1L C8-BTBT over a 60° MoS₂ GB (**Fig. 3.16b** inset), the gap size is observed to decrease by ~ 0.3 eV at the GB. This value is a much smaller than the ~ 1.5 eV band gap reduction we previously determined on bare 60° MoS₂ GBs,⁴⁰³

implying 1L C8-BTBT layer can effectively screen the local electronic states of the underlying MoS₂.

In summary, we have identified C8-BTBT as a promising molecule that will form well-defined interfaces with n-type MoS₂. We demonstrated the fabrication of C8-BTBT/MoS₂/EG mixed-dimensional heterostructures with all components obtained from bottom up growth that is compatible with large-area processing. The first C8-BTBT layer is found to self-assemble into expected chiral structures on mono- and few-layer MoS₂ adopting a lying-down configuration identical to that on graphene. The relative orientations of C8-BTBT molecules with MoS₂ and graphene are determined. Moreover, the C8-BTBT layer is found to be highly tolerant to underlying structural and electronic variations caused by lattice defects in 2D materials as evidenced from the continuous self-assembly of the molecules over point defects, abrupt interfaces at MoS₂ GBs and step edges, and minor variations of the density of states across MoS₂ GBs. These results will likely inform on-going efforts in developing highly efficient hybrid TMDC-based optoelectronic and photovoltaic devices.

Chapter 4: Borophene: Characterization, Functionalization, and Passivation

This chapter is based partially on the following publications and preprints:

X. Liu, Z. Zhang, L. Wang, B. I. Yakobson, and M. C. Hersam, Intermixing and Periodic Self-Assembly of Borophene Line Defects, *Nature Materials* **2018**, *17*, 783–788

X. Liu, Z. Wei, I. Balla, A. J. Mannix, N. P. Guisinger, E. Luijten, and M. C. Hersam, Self-Assembly of Electronically Abrupt Borophene/Organic Lateral Heterostructures, *Science Advances* **2017**, *3*, e1602356.

X. Liu, L. Wang, S. Li, M. S. Rahn, B. I. Yakobson, and M. C. Hersam, Resolving atomic lattice structures of borophene polymorphs with functionalized probes, in preparation.

X. Liu, M. S. Rahn, E. B. Aklile, and M. C. Hersam, Oxidation and Effective Passivation of Borophene, in preparation.

4.1 Introduction to Borophene

Direct synthetic pathways in the atomically thin limit enable 2D materials that are not layered in the bulk.⁹⁴ The rapid ascent of graphene has driven extensive interest in additional atomically thin elemental 2D materials including phosphorene,²⁵² stanene,³⁰ and most recently, borophene.^{11,12} Unlike the naturally layered structures of bulk graphite and black phosphorus, boron exhibits significantly more complex and diverse bulk structures due to the rich bonding configurations among boron atoms.⁴¹³⁻⁴¹⁵ Studies of atomically thin boron sheets, collectively referred to as borophene,^{11,12} primarily relied on theoretical predictions⁴¹⁶⁻⁴¹⁸ until recent studies experimentally demonstrated borophene synthesis on Ag(111) substrates. Theoretical calculations predict multiple possible borophene polymorphs that possess similar formation energies but different arrangements of hollow hexagons (HHs) in an otherwise triangular lattice.^{416,419,420} Such polymorphic nature of borophene,^{418,421} rooted in the rich bonding configurations among boron

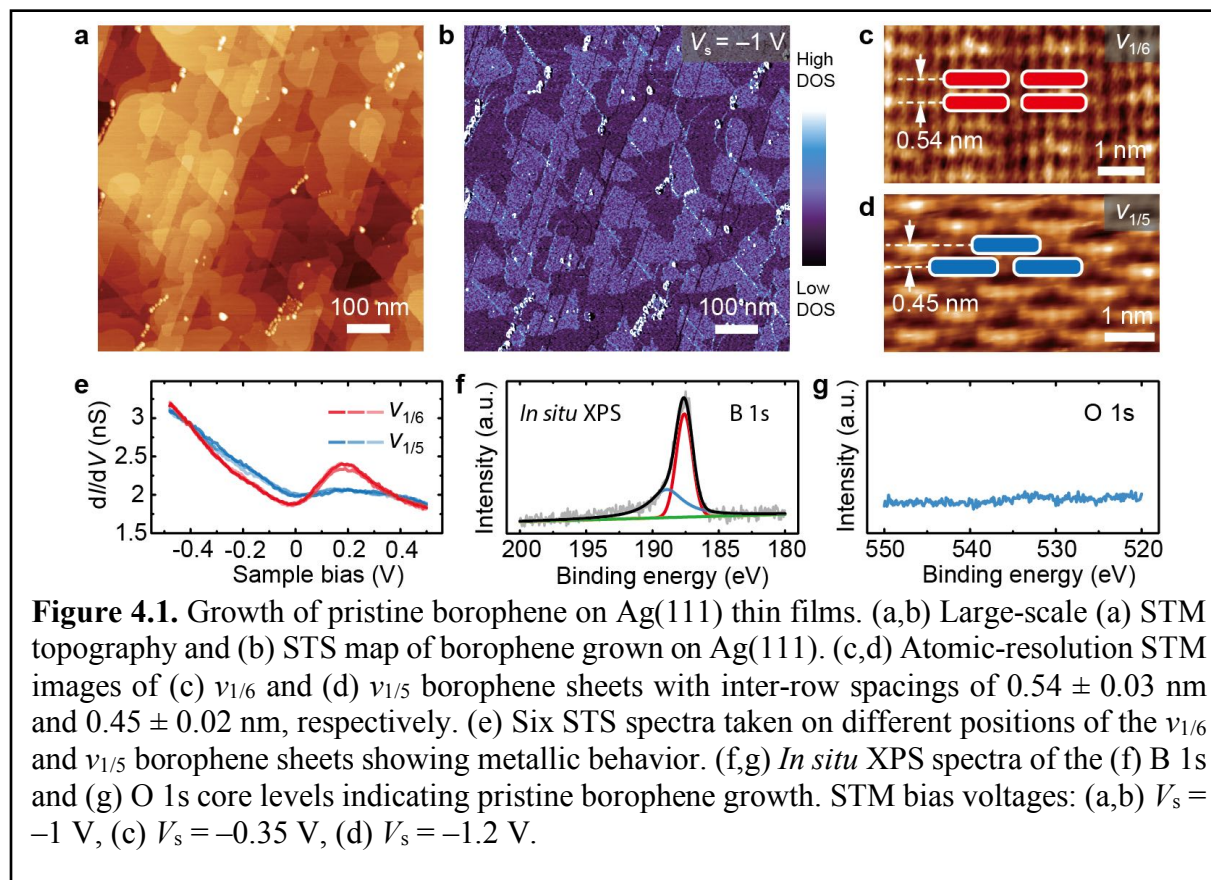
atoms, further distinguishes it from most other 2D materials and offers an additional tuning knob for tailoring material properties.

Indeed, experimental studies have revealed multiple borophene phases whose relative occurrence depends on the growth conditions.^{11,12} The growth substrate plays a major role in stabilizing borophene and determining its structural properties such as substrate-induced undulations⁴²² and the shift of the structural ground state when grown on substrates compared to vacuum.⁴¹⁹ Practically, borophene stability is an important factor towards realistic applications including transferring borophene onto other substrates. Theoretically, both dynamic stability⁴²³ and instability⁴²⁴ of free-standing borophene have been reported as indicated by the absence and presence of imaginary portions of the phonon spectrum, respectively. Compared to semiconducting bulk boron, borophene is an anisotropic metal^{11,12,422,425} with unique surface chemistry that strongly influences molecular self-assembly, which will be detailed later.²⁴ Moreover, experimental evidence for massless Dirac fermions,²⁵ theoretically predicted superconductivity,⁴²⁶ and a tendency of defect self-assembly (the following section)⁴²⁷ expand its desirable characteristics, making borophene a highly promising platform for novel material physics with potential utility in next-generation electronic technologies.

4.2 Defects in Borophene

While most theoretical predictions have assumed perfect crystalline structures, defects are inevitable in as-grown borophene, necessitating atomic-scale studies of defects. Although extensive research has explored point and line defects in graphene^{428,429} and transition metal dichalcogenide monolayers,^{54,368,403} borophene defects remain essentially unexplored. Here, we

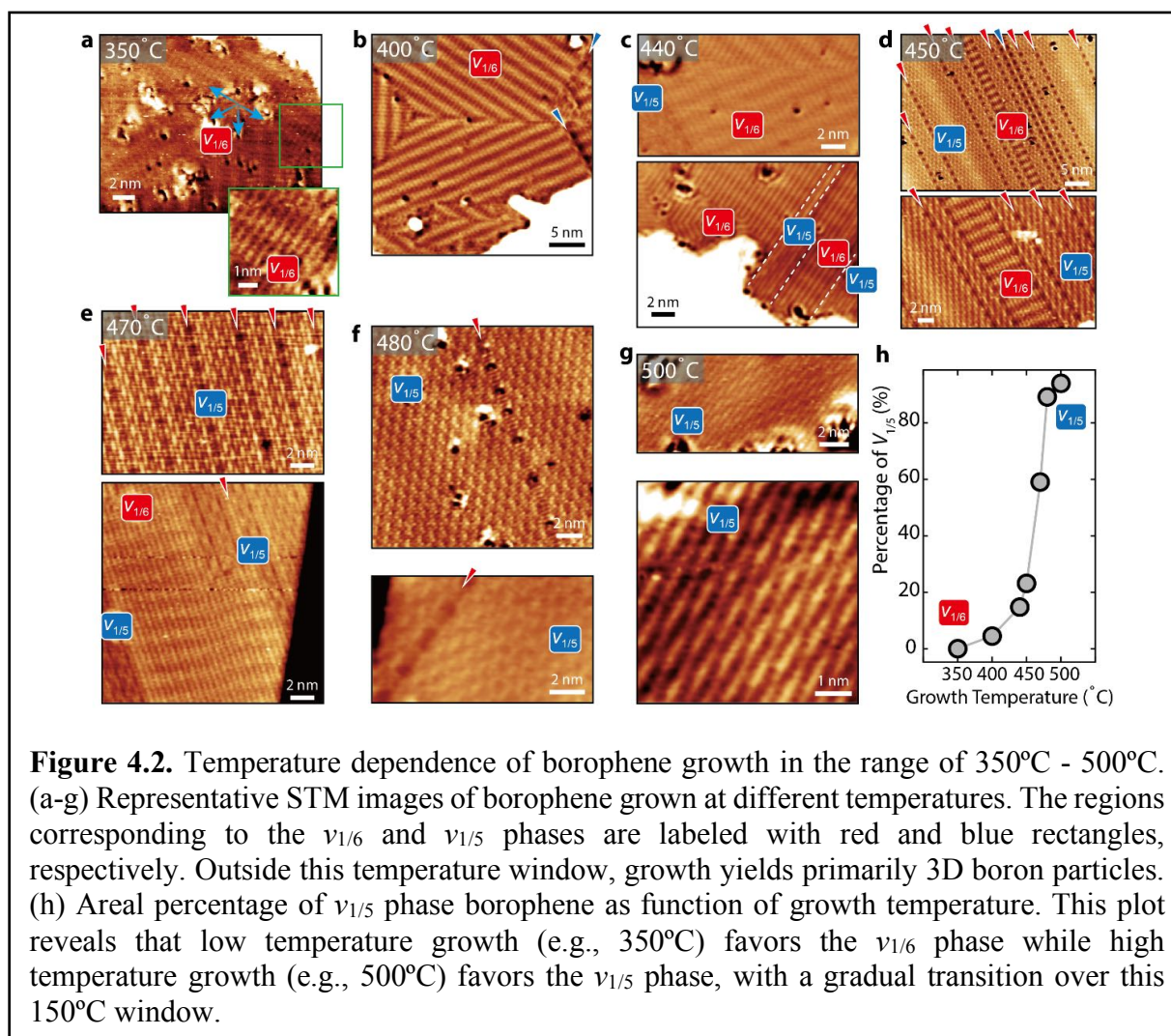
perform an atomically-resolved study of borophene under growth conditions that concurrently



yield multiple borophene phases and thus relatively high concentrations of line defects.

Fig. 4.1a shows an STM image of sub-monolayer borophene following deposition of boron on Ag(111) in UHV. The bright dots correspond to small boron particles that are typically present as minority species after borophene growth.^{11,12,24} Due to the convolution of topographic and electronic structure in STM imaging, the borophene islands appear as depressions under these imaging conditions, consistent with previous reports.^{11,12,24} Atomically thin island structures have also been observed for sub-monolayer coverage of metals deposited on surfaces⁴³⁰ and nitridized metal surfaces.⁴³¹ However, those islands are either alloys with the substrate or covalently bonded to the substrates, which is distinct from the weaker noncovalent interaction between borophene and the silver substrate. The borophene islands of the same region are more clearly distinguished

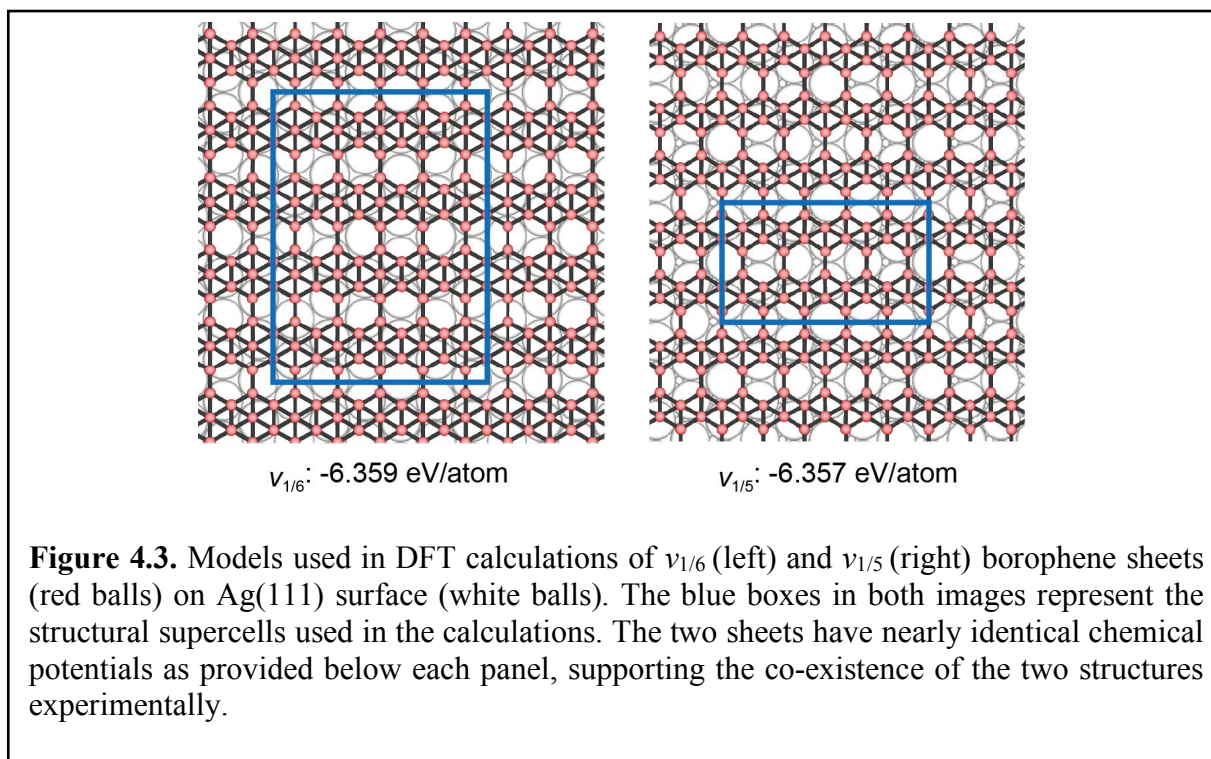
in the STS (dI/dV) map (Fig. 4.1b) as brighter domains. At substrate growth temperatures between



440°C and 470°C, two distinct borophene phases are consistently observed, corresponding to the $\nu_{1/6}$ and $\nu_{1/5}$ structures with HH concentrations being $\nu = 1/6$ and $1/5$, respectively ($\nu = n/N$, where n is the number of HHs in an otherwise triangular lattice with N lattice sites).^{11,12,24} The temperature dependence of borophene growth over a wider temperature window is given in Fig. 4.2, which shows a gradual transition from $\nu_{1/6}$ to $\nu_{1/5}$ phase borophene as the growth temperature is increased from 350°C to 500°C. DFT calculations (in collaboration with Prof. Boris Yakobson's group at Rice University) show similar chemical potentials and thus similar thermal stabilities of these two

phases ($\nu_{1/6}$: -6.359 eV/atom, $\nu_{1/5}$: -6.357 eV/atom, **Fig. 4.3**) in agreement with previous studies.^{416,419}

Atomic-scale STM images of the two phases are provided in **Fig. 4.1c** and **d**, respectively.



While the repeating rectangular structural units are aligned in adjacent rows in the $\nu_{1/6}$ sheet (indicated with red rectangles; inter-row spacing: 0.54 ± 0.03 nm), these units are staggered resembling a brick-wall pattern in the $\nu_{1/5}$ sheet (indicated with blue rectangles; inter-row spacing: 0.45 ± 0.02 nm) in agreement with previous work.¹² Both sheets are metallic as evidenced by the dI/dV curves taken on each phase at 300 K (**Fig. 4.1e**). In **Fig. 4.1f**, the *in situ* X-ray photoelectron spectrum of the B1s core-level is fit with two sub-peaks (187.6 eV and 188.9 eV) corresponding to distinct B-B bonds. The absence of oxidized boron peaks around 192 eV⁴³² coupled with minimal O1s core-level signal (**Fig. 4.1g**) confirms the pristine nature of borophene.

Fig. 4.4a shows a spatial derivative image of the STM topography (**Fig. 4.4b**), which more clearly reveals that the larger borophene island is composed of both $\nu_{1/6}$ and $\nu_{1/5}$ sheets with

respective line defects indicated by the blue and red arrow heads. The line defects in the $\nu_{1/6}$ sheet

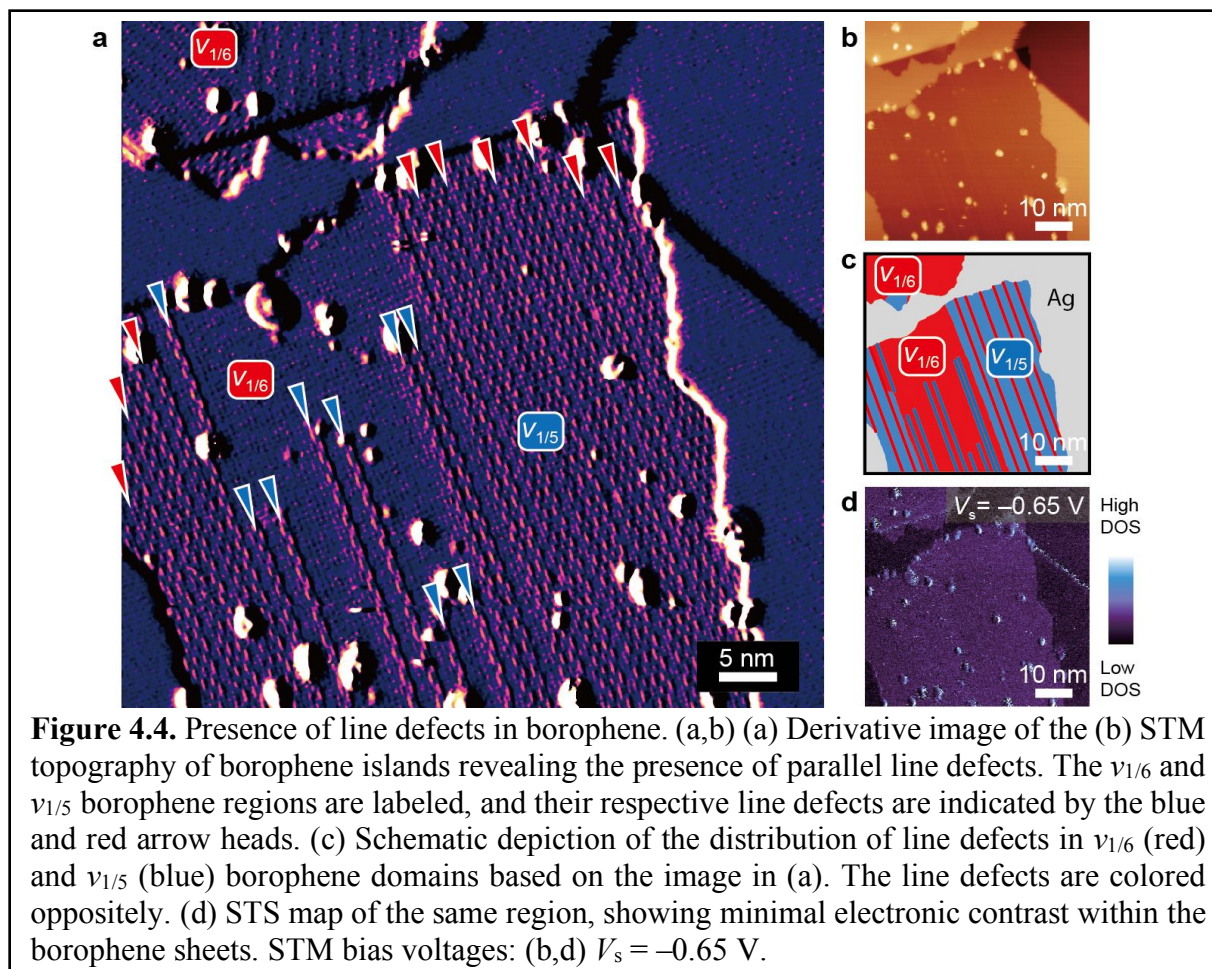
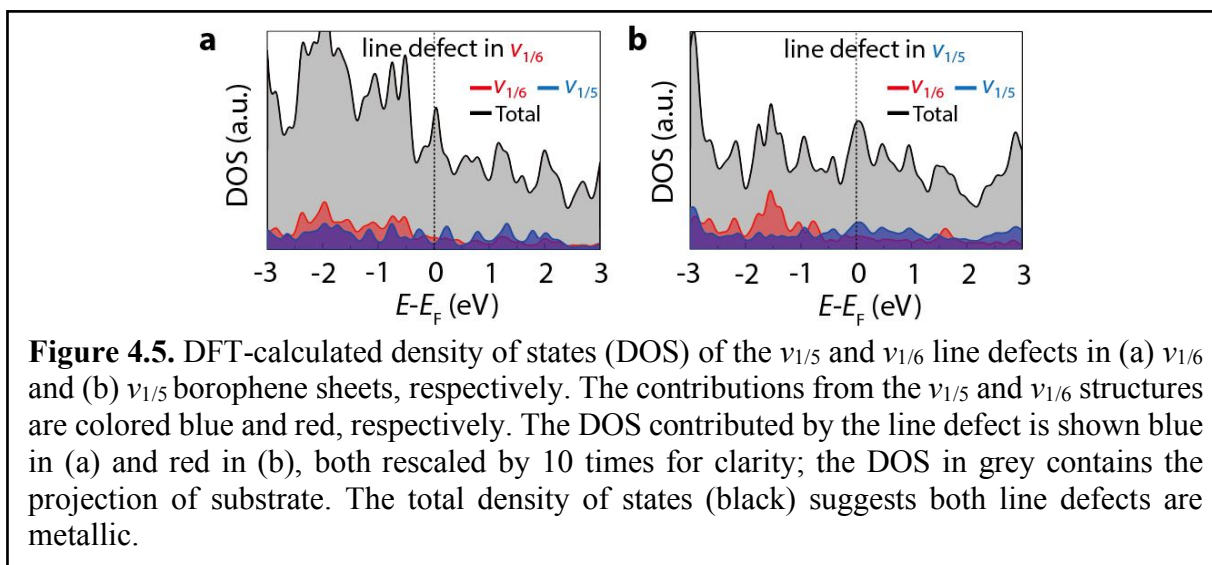


Figure 4.4. Presence of line defects in borophene. (a,b) (a) Derivative image of the (b) STM topography of borophene islands revealing the presence of parallel line defects. The $\nu_{1/6}$ and $\nu_{1/5}$ borophene regions are labeled, and their respective line defects are indicated by the blue and red arrow heads. (c) Schematic depiction of the distribution of line defects in $\nu_{1/6}$ (red) and $\nu_{1/5}$ (blue) borophene domains based on the image in (a). The line defects are colored oppositely. (d) STS map of the same region, showing minimal electronic contrast within the borophene sheets. STM bias voltages: (b,d) $V_s = -0.65$ V.

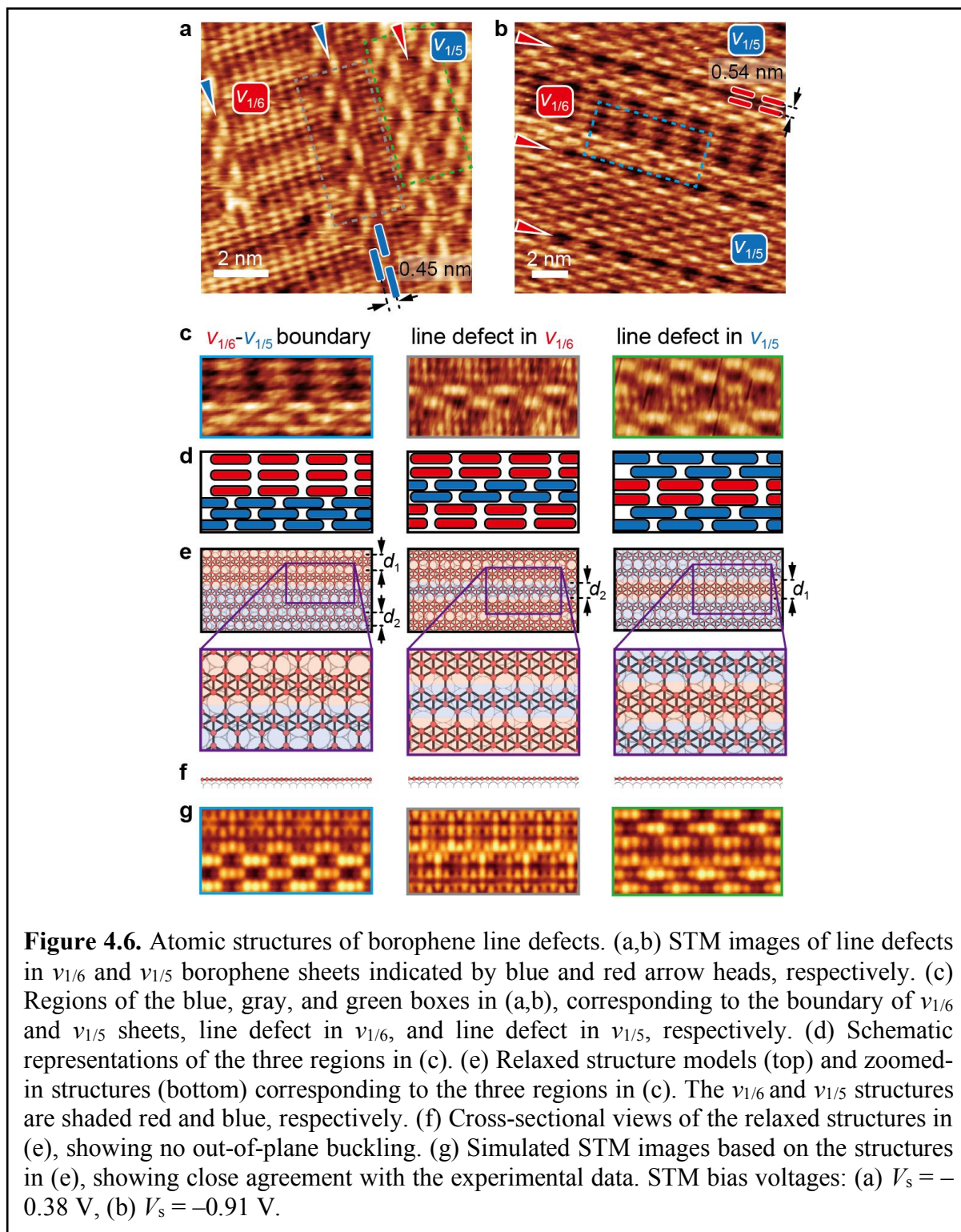
resemble the brick-wall structure of the $\nu_{1/5}$ sheet, suggesting non-unique assignments of phase boundaries. This phase intermixing is schematically shown in **Fig. 4.4c**, where the $\nu_{1/6}$ and $\nu_{1/5}$ sheets are colored red and blue, and the corresponding line defects are colored blue and red. Despite the relatively high density of line defects, STS mapping of the same region at 300 K reveals minimal contrast (**Fig. 4.4d**). DFT calculations confirm the metallic nature of the line defects (**Fig. 4.5**), implying minimal impact on the electronic properties of metallic borophene at room temperature.



Atomically resolved STM images are provided in **Fig. 4.6a** and **b**, where line defects in $\nu_{1/6}$ and $\nu_{1/5}$ sheets are indicated by blue and red arrow heads, respectively. The line defect in the $\nu_{1/6}$ ($\nu_{1/5}$) sheet is represented by staggered (aligned) blue (red) rectangles in **Fig. 4.6a,b**, suggesting the line defect in the $\nu_{1/6}$ domain resembles the unit of a $\nu_{1/5}$ sheet and vice versa. In addition, the respective inter-row spacings of the line defects in $\nu_{1/6}$ and $\nu_{1/5}$ sheets are 0.45 ± 0.02 nm (denoted as d_2) and 0.54 ± 0.03 nm (denoted as d_1), matching those of the $\nu_{1/5}$ and $\nu_{1/6}$ sheets.

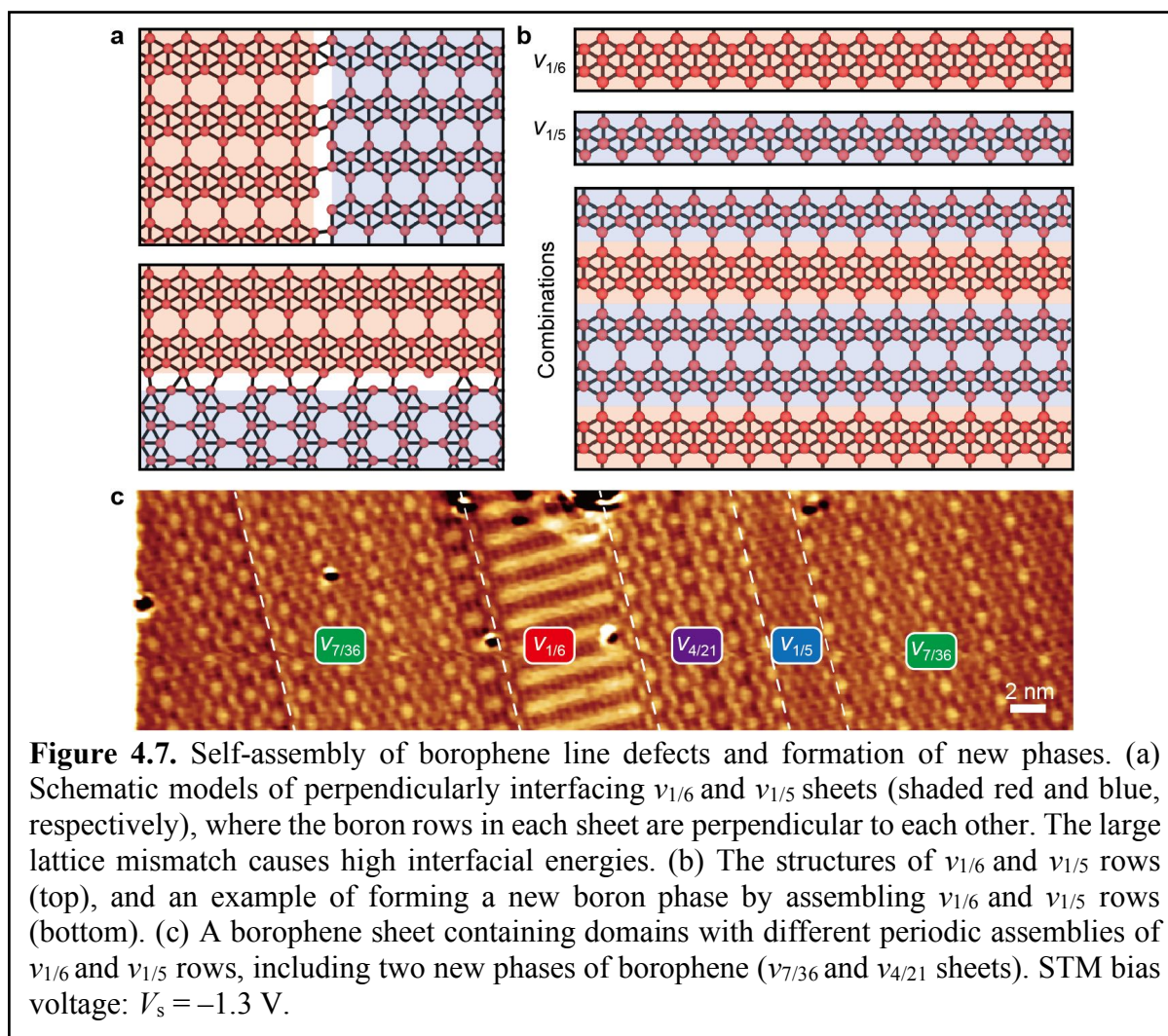
We further compare our experimental observations with DFT modeling that takes into account contributions from the Ag substrate (see details in the Methods section). The regions enclosed by the blue, gray, and green boxes in **Fig. 4.6a,b** are displayed in **Fig. 4.6c**, corresponding to the phase boundary of the $\nu_{1/5}$ and $\nu_{1/6}$ sheets (blue), and line defects in $\nu_{1/6}$ (gray) and $\nu_{1/5}$ (green) sheets, respectively. These images are schematically depicted using the aforementioned red and blue rectangle structural units in **Fig. 4.6d** for clear comparison. Corresponding structural models were generated using a large supercell (up to 800 atoms), with the DFT-relaxed structures shown in **Fig. 4.6e**. The templating effect of the substrate results in epitaxial growth of the two phases with parallel HH rows. The registry of the two lattices along the horizontal rows further allows the

$\nu_{1/6}$ and $\nu_{1/5}$ sheets (shaded red and blue, respectively) to connect seamlessly and exhibit an



atomically smooth phase boundary, as shown by the zoomed-in images in **Fig. 4.6e**. In other words,

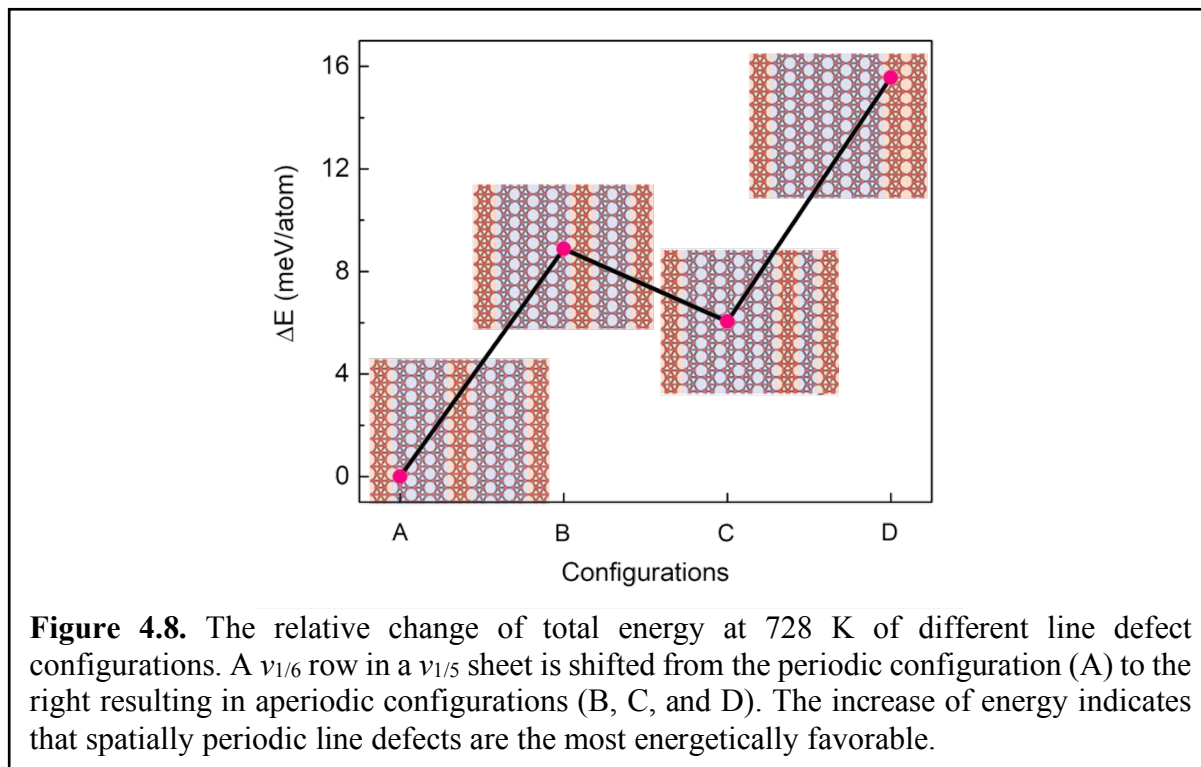
each line defect is a row of the $\nu_{1/5}$ or $\nu_{1/6}$ structure inserted in the $\nu_{1/6}$ or $\nu_{1/5}$ sheet, respectively. The cross-sectional views of the DFT-relaxed structures on Ag(111) are shown in **Fig. 4.6f**, revealing no observable out-of-plane distortion even at phase boundaries, which contributes to their high stability. The calculated values $d_1 = 0.51$ nm and $d_2 = 0.43$ nm agree well with the experimentally measured values. In addition, the simulated STM images in **Fig. 4.6g** based on the



structures in **Fig. 4.6e** are in excellent agreement with the experimental STM images, thus corroborating the proposed structures.

The perfect lattice match along the HH rows at the phase boundaries results in a negligible interface energy, in contrast to substantial interface energies in other configurations due to large

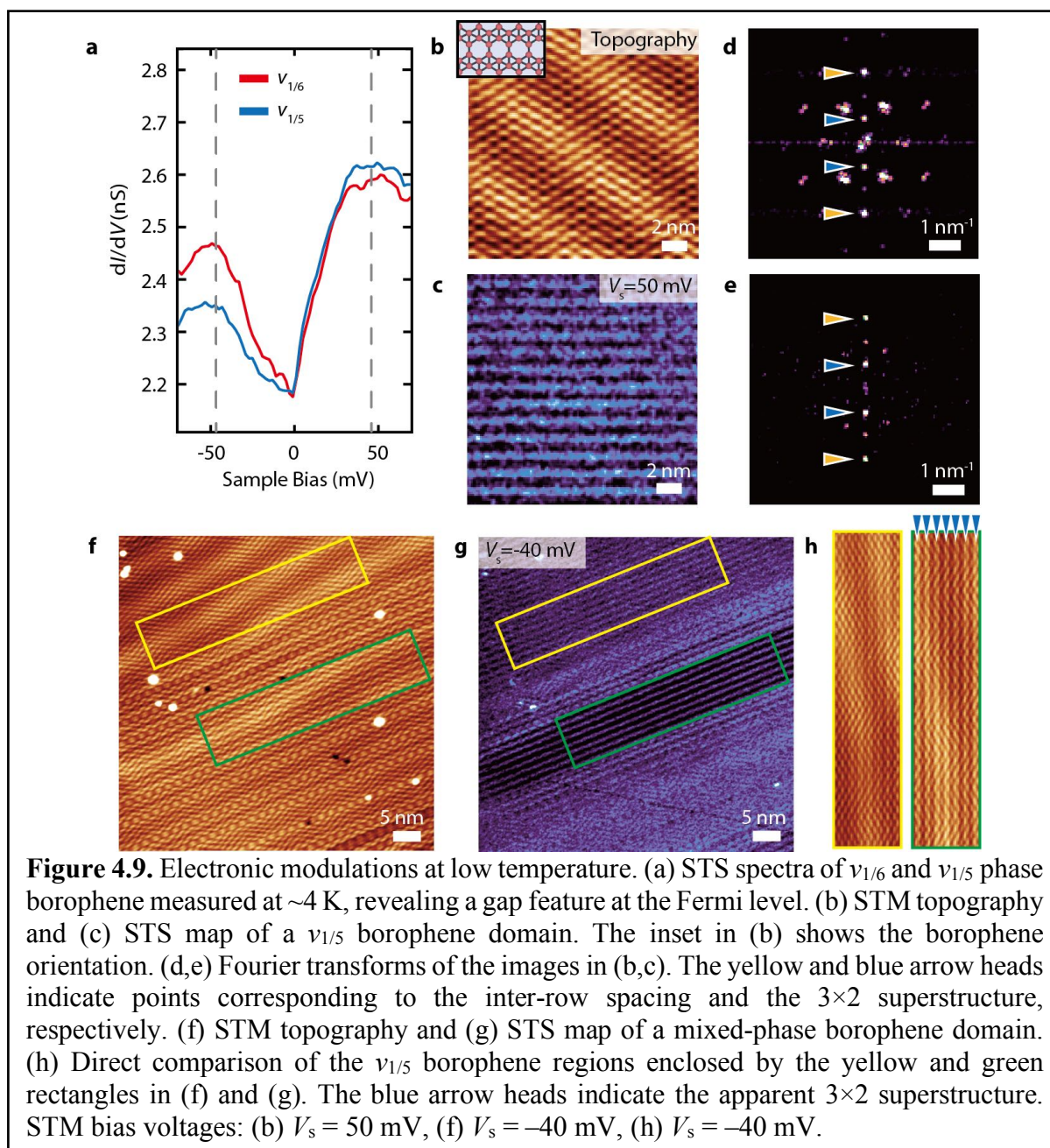
lattice mismatches (schematically shown in **Fig. 4.7a**). This anisotropic intermixing phenomenon is in contrast to silicene, which is also a synthetic 2D material with multiple phases.^{433,434} Despite



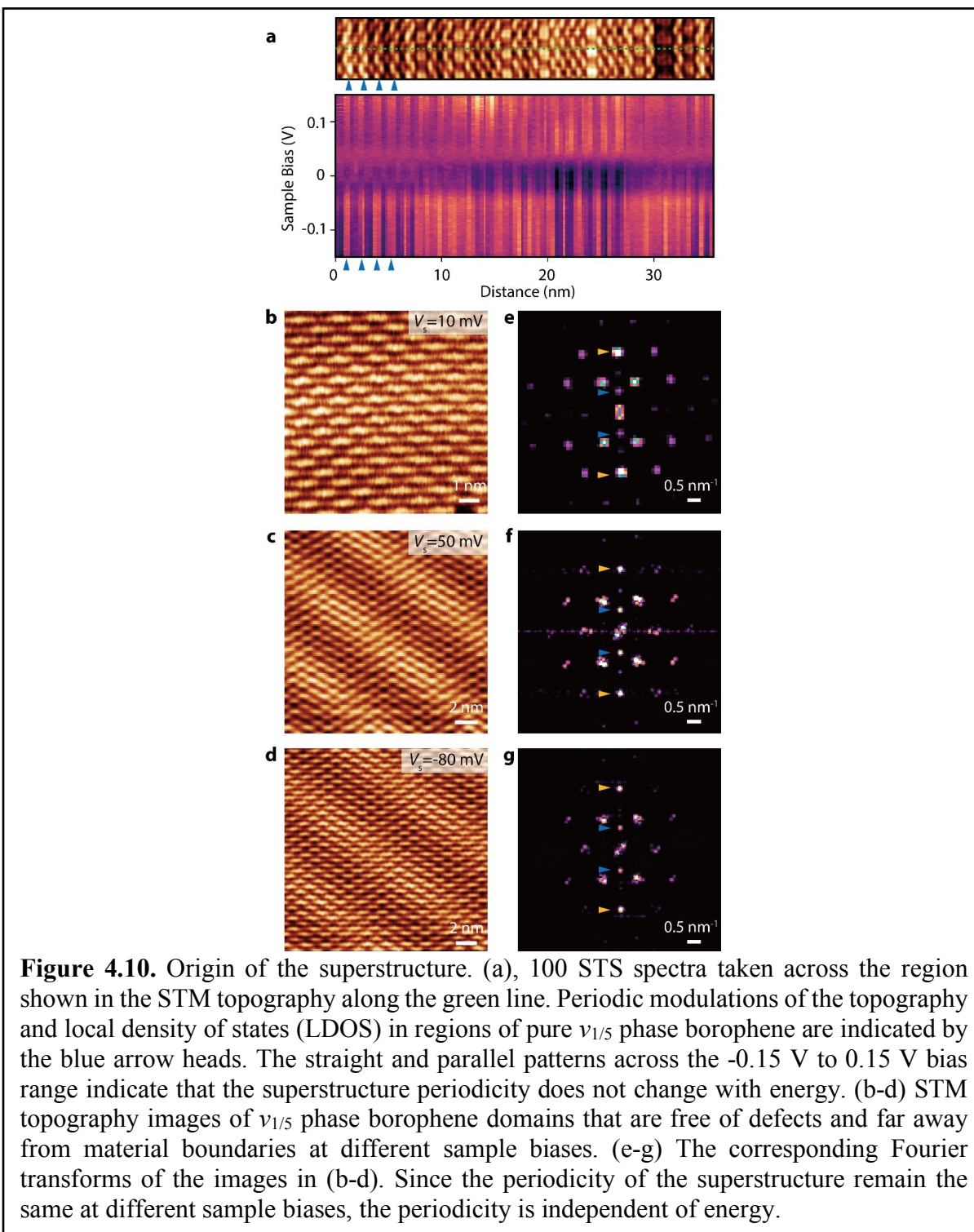
the subtle structural differences among silicene phases, the phase boundaries are complex, leading to isolated domains without phase intermixing,^{434,435} which can be attributed to the rotationally distinct registry of each silicene phase with the substrate and the weak capability of silicon to form variable chemical bonds. On the other hand, the $\nu_{1/6}$ and $\nu_{1/5}$ borophene sheets are highly anisotropic and share the same lattice parameters and rotational registry with Ag(111) along HH rows,^{12,425} emphasizing the importance of the Ag substrate in templating the coherent assembly of different borophene rows with sharp interfaces and the resulting well-defined line defects. This result also highlights how structural anisotropy in 2D materials not only results in anisotropic materials properties, but also influences the nature of crystal defects.

The lattice registry along the HH rows suggests the $\nu_{1/6}$ and $\nu_{1/5}$ rows can act as building blocks to assemble into additional 2D borophene sheets (**Fig. 4.7b**), partially facilitated by the

noncovalent nature of the interaction between borophene and the substrate. While this framework



seemingly accommodates arbitrary combinations of $\nu_{1/6}$ and $\nu_{1/5}$ rows, line defects often show local periodicity (**Fig. 4.4a**). This observation is explored with DFT calculations, including finite temperature contributions and substrate interactions, by shifting one line defect (e.g., a $\nu_{1/6}$ row in a $\nu_{1/5}$ sheet) off its periodic position (**Fig. 4.8**). The total energy increases as the line defect is

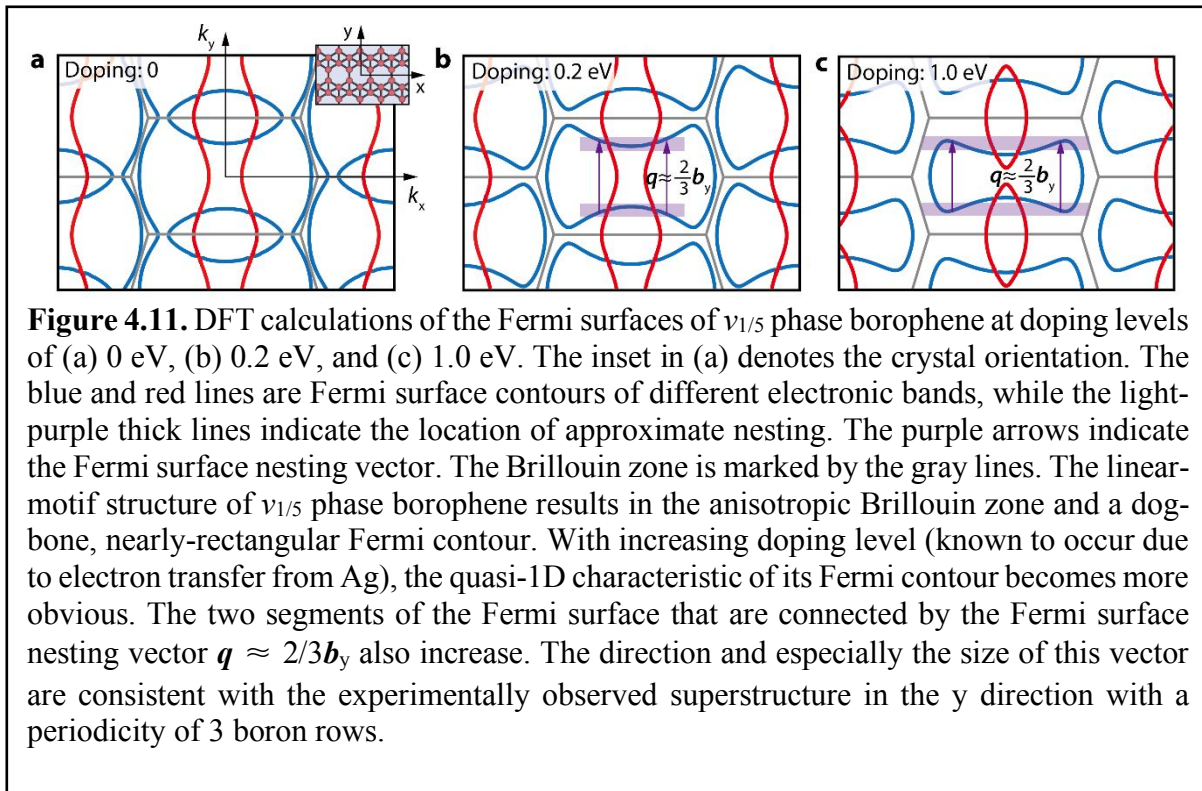


displaced from its periodic position, rendering the structure with periodic line defects as the ground state, which is consistent with the different amounts of charge transfer from the Ag substrate to

the $\nu_{1/5}$ and $\nu_{1/6}$ rows due to their different HH concentrations.⁴²⁰ Since crystals are defined by atomic ordering and structural periodicity, borophene domains with periodic assemblies of $\nu_{1/6}$ and $\nu_{1/5}$ rows can be equivalently viewed as new borophene phases. For example, **Fig. 4.7c** shows a borophene domain displaying different regions defined by line defects with distinct periodic lengths, as separated by the white dashed lines. The HH concentration of a periodic assembly of m $\nu_{1/6}$ and n $\nu_{1/5}$ units in a supercell is $\nu = (m + n)/(6m + 5n)$. In this manner, we identify two new borophene polymorphs in **Fig. 4.7c**, whose supercells are composed of one $\nu_{1/6}$ unit assembled with three and six $\nu_{1/5}$ rows, with $\nu = 4/21$ and $7/36$, respectively.

With increased energy resolution at low temperatures (~ 4 K), a gap at the Fermi level is revealed in the STS spectra of $\nu_{1/5}$ and $\nu_{1/6}$ phase borophene (**Fig. 4.9a**) with two shoulders at $\sim \pm 45$ mV. Moreover, periodic modulations appear in the STS map (**Fig. 4.9c**) of $\nu_{1/5}$ phase borophene (**Fig. 4.9b**), which are better visualized in the Fourier transforms of the topography and the STS map as respectively shown in **Fig. 4.9d,e**. The points indicated by the yellow arrow heads correspond to the inter-row spacing of 0.45 nm, and the blue arrow heads indicate points from a superstructure with ~ 1.33 nm periodicity corresponding to 3 boron rows. The borophene orientation is schematically shown in the inset of **Fig. 4.9b**. Since the unit cell of $\nu_{1/5}$ phase borophene contains 2 boron rows, this superstructure can be categorized as 3×2 . This periodicity is independent of energy and is inconsistent with a Moiré pattern or Friedel oscillations, as detailed in **Fig. 4.10**. Specifically, we rule out the possibility of this superstructure being a Moiré pattern since the distance across 2 $\nu_{1/5}$ boron rows (instead of 3) corresponds to 3 Ag(111) lattice spacings

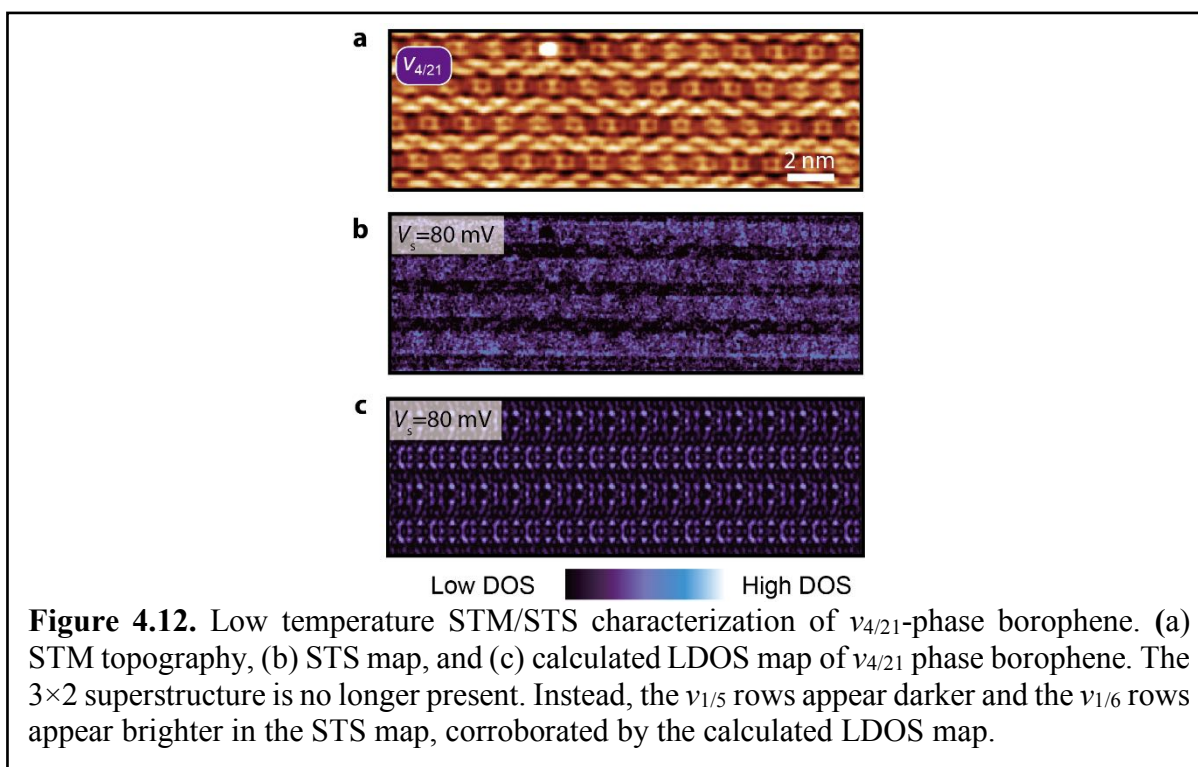
(which gives rise to the staggered brick-wall pattern). The fact that the superstructure is present on defect-free and boundary-free borophene regions with uniform modulations (panels **b-d**, top part of **Fig. 4.9f**) suggests that Friedel oscillations, whose amplitude decays away from perturbation centers, cannot explain the observed phenomenon. Given those observations and the metallic nature of borophene, the superstructure is consistent with a CDW, which is corroborated with DFT analysis (**Fig. 4.11**). **Fig. 4.9f,g** shows the topography and STS map of a mixed-phase borophene region, respectively. While the borophene in the yellow rectangle is within a larger $\nu_{1/5}$ region, the borophene in the green rectangle is confined by two line defects. The electronic modulation is enhanced in the confined region (**Fig. 4.9g**), but with the same periodicity. The topography of the two regions are directly compared in **Fig. 4.9h**, where the superstructure is readily visible in the



topography of the confined $\nu_{1/5}$ region as indicated by the blue arrow heads. In $\nu_{4/21}$ phase borophene, the 3×2 modulation is absent, which is expected given the very narrow $\nu_{1/5}$ regions

(Fig. 4.12).

In summary, we have performed atomic scale characterization of line defects in $\nu_{1/6}$ and $\nu_{1/5}$ borophene sheets, revealing that the line defects in each phase adopt the structure of the other phase and preferentially self-assemble into periodic arrays, resulting in the formation of new phases of borophene. This work thus establishes line defects (i.e., $\nu_{1/6}$ and $\nu_{1/5}$ rows) as the building blocks for a multitude of borophene crystalline phases with a single tuning parameter being the mixing ratio of the two rows. This blurring of the definition of crystalline domains and line defects in borophene is enabled by the similarities of the $\nu_{1/6}$ and $\nu_{1/5}$ lattice constants, atomic registry with the Ag(111) substrate, and the high structural anisotropy. Since the line defects in borophene possess similar metallic structure to the pristine $\nu_{1/6}$ and $\nu_{1/5}$ sheets, the electronic properties of

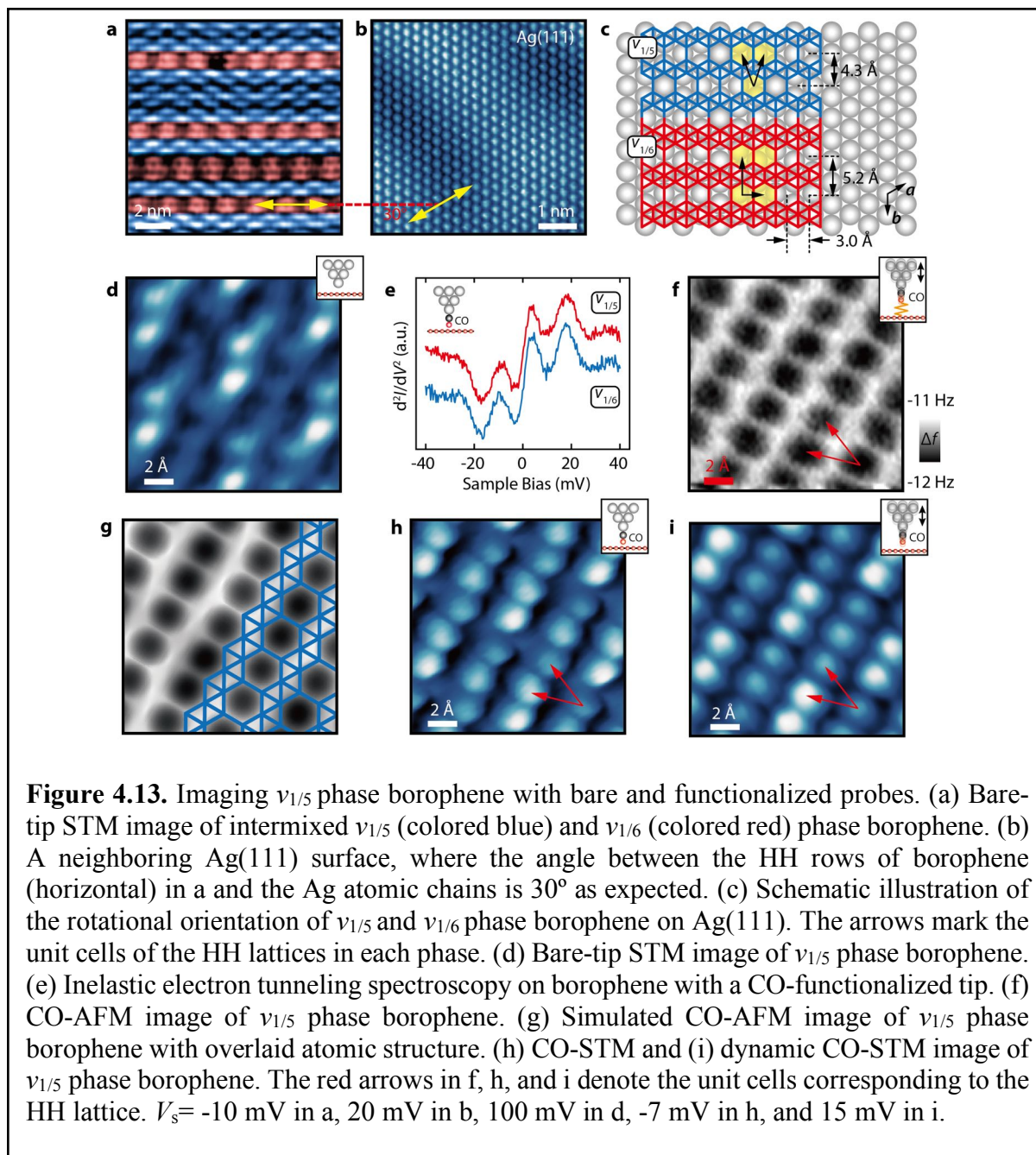


borophene are relatively unperturbed by its underlying structural complexities at room temperature, although subtle electronic modulations consistent with a CDW are observable in the low

temperature limit. In addition, 2D material-based faceted nanotubes with highly tunable electronic properties^{436,437} have been theoretically predicted but not yet realized. Two strategies proposed with phosphorus involve laterally stitched 2D polymorphs⁴³⁶ and a single phase 2D sheet but with parallel line defects.⁴³⁷ Mixed-phase borophene addresses both of these strategies concurrently by offering not only parallel line defects, but also equalizing line defects with borophene polymorphs. The periodic arrangement of line defects may further lead to highly symmetric nanotube cross-sections, which are otherwise difficult to engineer. Given the differences in physical (e.g., bending stiffness,⁴²⁵ thermal conductivity⁴²³) and electrochemical (e.g., ion adsorption and migration on borophene-based battery anodes⁴³⁸) properties of the two phases, borophene sheets with tunable characteristics could be imagined under various periodic line defect arrangements. For example, mixed-phase borophene may offer structurally-tunable near-infrared plasmonic devices.⁴³⁹ Overall, this study reveals the unique nature and implications of line defects on the structure and properties of borophene, which will inform future fundamental studies including the investigation of interactions between CDWs and defects, predicted superconductivity,⁴²⁶ and observed Dirac cones²⁵ in mixed-phase borophene in addition to emerging efforts to realize borophene-based applications.

4.3 CO-Functionalized Scanning Probe Microscopy of Borophene Structures

As mentioned above, borophene lattice is characterized by periodic arrangement of HHs in an otherwise triangular lattice. Together with such complicated lattice structures, borophene's polymorphism adds to the complexities and challenges to unambiguously resolve and identify borophene structures experimentally. Indeed, real-space imaging of borophene structures has so far been limited to conventional metal-tip STM.^{11,12,24,427} The highly convoluted nature of



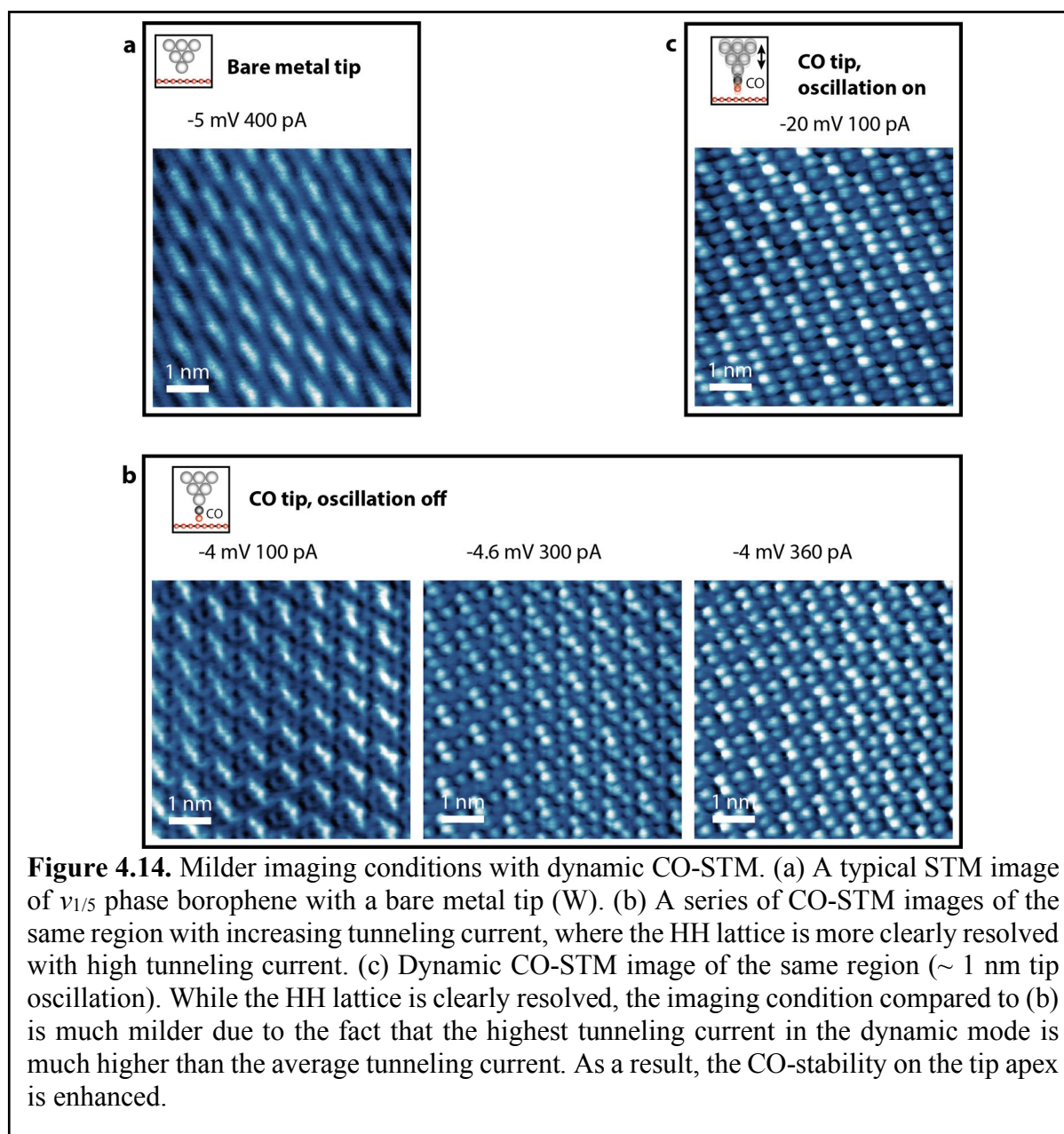
experimental STM images and Moiré superlattices with underlying substrates render direct identification of complex borophene structures non-intuitive. While further clues could be obtained when corroborated with first-principle calculations, simulated images have been shown to be non-determining for certain structures.^{11,440} Therefore, a highly accessible and

straightforward experimental method would be greatly desirable if it unambiguously determines the atomic structures of borophene polymorphs and provides solid grounds for the hitherto more prevailing computational studies of borophene.

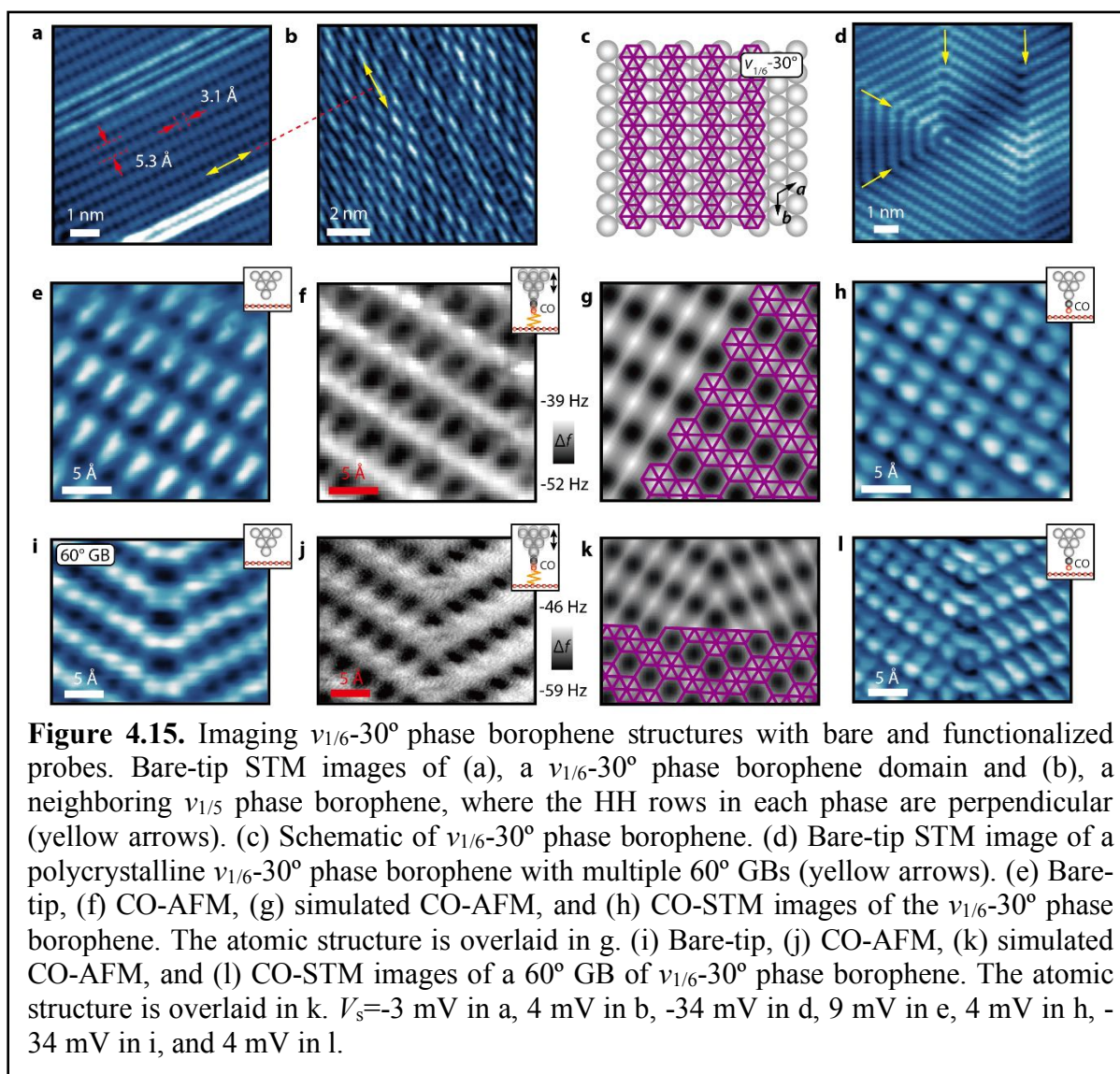
Since the first evidence of enhanced spatial resolution with pentacene-functionalized tips⁴⁴¹, CO,¹⁶⁶ H₂,^{153,442} Xe,⁴⁴³ and the more recent CuO_x tip-functionalizations^{444,445} have been established to purposely reveal greater spatial details down to the subatomic regime. Though still under debate,¹⁷¹ these techniques seemingly resolve inter- and intra-molecular chemical bonds.^{157,446} While such methods have been largely applied to carbon-based molecular or graphitic systems, for the first time we use CO-AFM to reveal features that are consistent with boron-boron covalent bonds, expanding the phase space of this technique. We further identify CO-STM⁴⁴⁷ as an equivalently powerful yet much less demanding and more accessible method in unambiguously resolving borophene structures. The improved spatial resolution allows us to directly verify previously proposed borophene structural models and identify multiple borophene polymorphs with different rotational alignments on Ag(111). In particular, a partial growth transition from rotationally commensurate to incommensurate borophene phases is observed at high growth temperatures.

Borophene polymorphs are characterized by different arrangements and concentrations of HHs in an otherwise 2D triangular lattice. **Fig. 4.13a** shows a conventional bare-tip STM image of intermixed $\nu_{1/5}$ (colored blue) and $\nu_{1/6}$ (colored red) phase borophene grown at a previously established temperature of $\sim 450^\circ\text{C}$.⁴²⁷ Comparing to the atomic lattice of the Ag(111) growth substrate (**Fig. 4.13b**), the horizontal HH row directions of both phases are aligned 30° rotated with respect to the Ag atomic chains (directions *a* or *b* in **Fig. 4.13c**), consistent with previously proposed structural models as shown in **Fig. 4.13c**.¹² For $\nu_{1/5}$ and $\nu_{1/6}$ phase borophene, the HHs

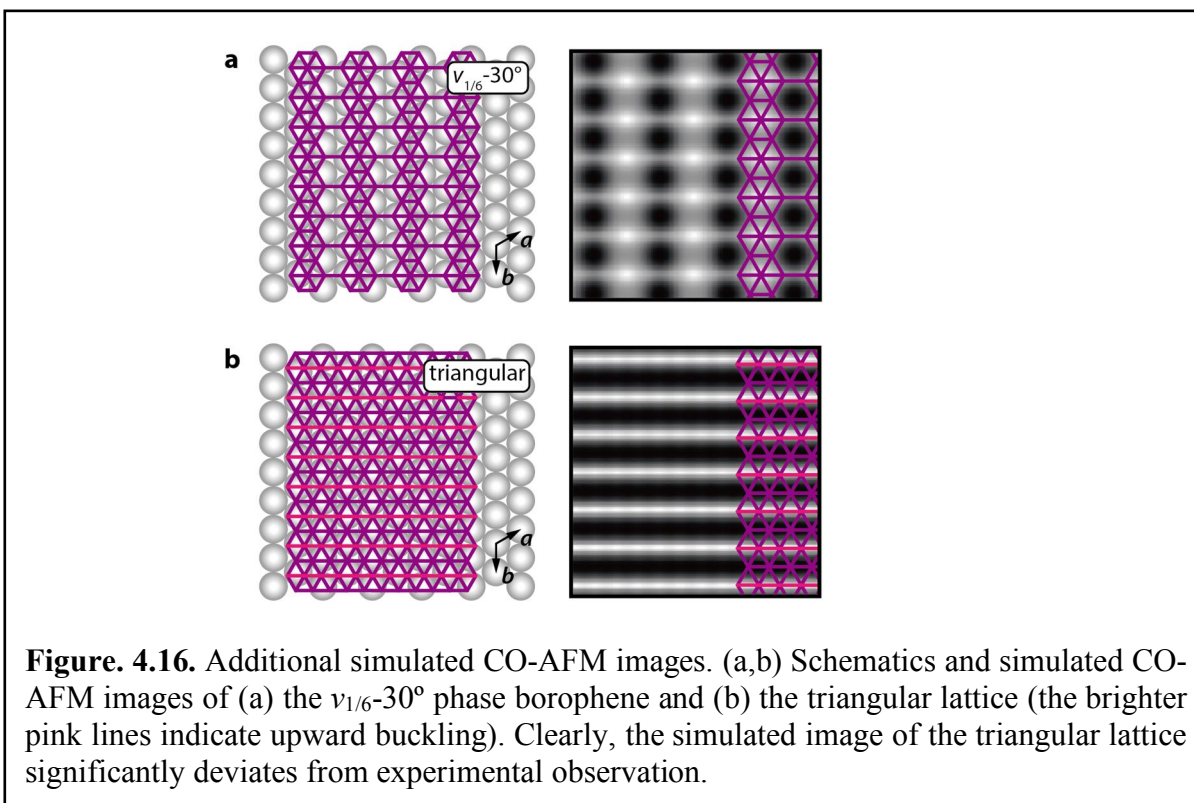
are arranged in a staggered and aligned manner, respectively, with the unit cells of the HH lattices indicated by the black arrows. High-resolution STM imaging of $\nu_{1/5}$ phase borophene with a bare metal tip (**Fig. 4.13d**) reveals a strong brick-wall type Moiré pattern modulating finer features. **Fig. 4.13e** shows the characteristic inelastic electron tunneling spectra of CO obtained on borophene after decorating the metal tips with a CO molecule (hindered translation and rotation modes at 3.2 and 17.6 meV, respectively), confirming successful tip functionalization.⁴⁴⁸ In contrast to the STM image in **Fig. 4.13d**, the constant height CO-AFM image in **Fig. 4.13f** readily resolves the HH lattice and verifies the proposed $\nu_{1/5}$ phase borophene structure, where the HHs are separated by bright ridges at positions expected for boron-boron covalent bonds. In good agreement with the experimental image, **Fig. 4.13g** shows a simulated CO-AFM image^{154,449} with an overlaid $\nu_{1/5}$ phase atomic structure. While apparent bonding structures of the 6-membered boron rings (i.e., HHs) are clearly resolved, little contrast is seen at the triangular boron lattice, where only 3-membered boron rings exist. This is not unexpected given the fact that 4-membered carbon rings were not resolved in literature.⁴⁵⁰ Nonetheless, resolving the HH lattice would be sufficient for determining the structures of borophene polymorphs.⁴¹⁸ Given the highly-demanding nature of non-contact AFM in terms of instrumentation and operation, we demonstrate that CO-STM provides equivalent structural information of borophene with better accessibility as shown in **Fig. 4.13h**. Compared to the bare-tip STM image in **Fig. 4.13d**, a lattice of staggered protrusions (red arrows) matching the HH lattice are clearly resolved in addition to the less-obvious Moiré pattern. By running the CO-STM in the dynamic mode,⁴⁵¹ i.e., with an oscillating STM tip, such contrast could be further enhanced (**Fig. 4.13i**) at a much milder imaging condition (**Fig. 4.14**), which is highly desirable for better CO stability on the tip apex.



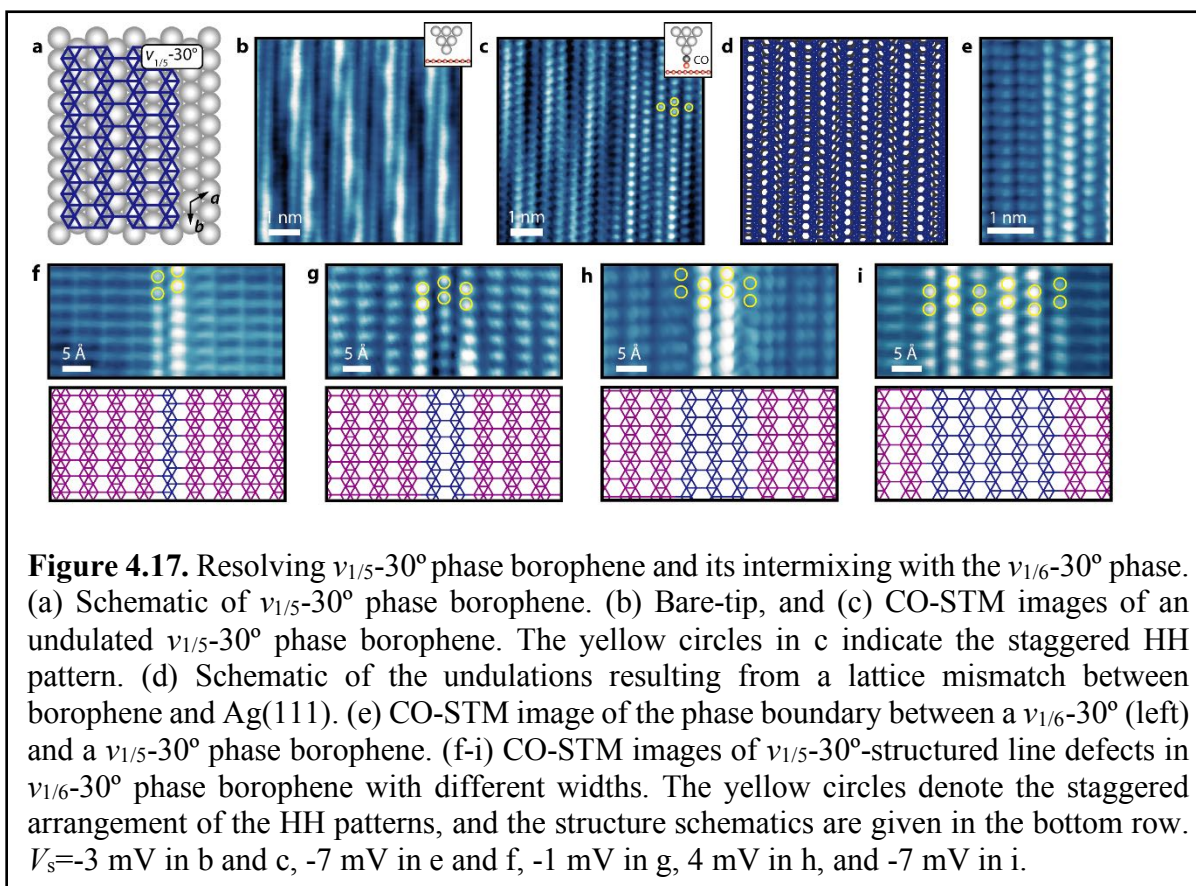
At higher growth temperatures ($\sim 500^\circ\text{C}$), $\nu_{1/5}$ phase borophene dominates⁴²⁷ while another phase with a rectangular lattice begins to appear (**Fig. 4.15a**). This structure was first observed in high temperature growth and assigned to a buckled triangular lattice.¹¹ The $3 \text{ \AA} \times 5 \text{ \AA}$ lattice constants are also indicative of the $\nu_{1/6}$ phase borophene, which should grow at a lower temperature.¹² However, the absence of a linear Moiré pattern typically seen in the $\nu_{1/6}$ phase



borophene suggests such phase might be the $\nu_{1/6}$ sheet on Ag(111) with a different orientation as suggested previously.^{422,452} Indeed, instead of being parallel as in the $\nu_{1/6}$ phase (Fig. 4.13c), the HH rows of this sheet are perpendicular to those of a neighboring $\nu_{1/5}$ phase borophene in Fig. 4.15b (yellow arrows). We thus tentatively assign such phase as $\nu_{1/6}$ - 30° as schematically shown in Fig. 4.15c, indicating that the sheet is rotated by 30° on Ag(111) compared to the $\nu_{1/6}$ phase. A polycrystalline domain of such phase with 60° grain boundaries (GB; yellow arrows) is shown in Fig. 4.15d. Figs. 4.15e,f are high-resolution STM and CO-AFM images of the $\nu_{1/6}$ - 30° phase



borophene, respectively, where the aligned HHs are clearly resolved in **Fig. 4.15f** with neighboring HHs separated by bright ridges at positions expected for boron-boron covalent bonds. In **Fig. 4.15g**, the simulated CO-AFM image with an overlaid atomic structure is again in good agreement with experimental observations, confirming our structural assignment as $\nu_{1/6}$ -30°. On the other hand, simulated CO-AFM images of a buckled triangular lattice deviate from the experimental image (**Fig. 4.16**). Compared to the bare tip STM image, each bright protrusion becomes two with inequivalent brightness in the CO-STM image in **Fig. 4.15h**. A series of bare-tip STM, CO-AFM and CO-STM images of a 60° GB in $\nu_{1/6}$ -30° phase borophene is shown in **Fig. 4.15i**, **j**, and **l**, respectively. Based on the apparent bonding positions resolved in **Fig. 4.15j**, we propose an atomic structure of the GB seamlessly connecting adjacent grains (**Fig. 4.15k**). It yields a simulated CO-AFM image (**Fig. 4.15k**) in good agreement with experimental observation, further supporting our assignment of the phase as $\nu_{1/6}$ -30°.



As established previously, intermixing of $\nu_{1/5}$ and $\nu_{1/6}$ phase borophene takes place when the two phases have rotationally aligned HH rows.⁴²⁷ It would thus be expected to have $\nu_{1/5}$ - 30° phase borophene (schematically shown in **Fig. 4.17a**) intermixed with $\nu_{1/6}$ - 30° at appropriate growth conditions. Indeed, at a higher growth temperature ($\sim 550^\circ\text{C}$), an undulated structure appears as shown in the bare-tip STM image in **Fig. 4.17b**, previously known as the striped phase¹¹ and assigned as induced by Ag surface reconstruction under a $\nu_{1/6}$ - 30° sheet.⁴²² **Fig. 4.17c** is the CO-STM image of the same region as in **Fig. 4.17b**, and we determine that this phase adopts the $\nu_{1/5}$ sheet structure as evidenced from the staggered arrangement of protrusions (yellow circles) representing the HH lattice. Instead of a brick-wall type Moiré pattern seen in the $\nu_{1/5}$ phase, the large-scale undulation comes from a $\sim 4\%$ larger inter-HH spacing along the HH rows than the interatomic spacing of the underlying Ag, which is reproduced qualitatively in **Fig. 4.17d** by

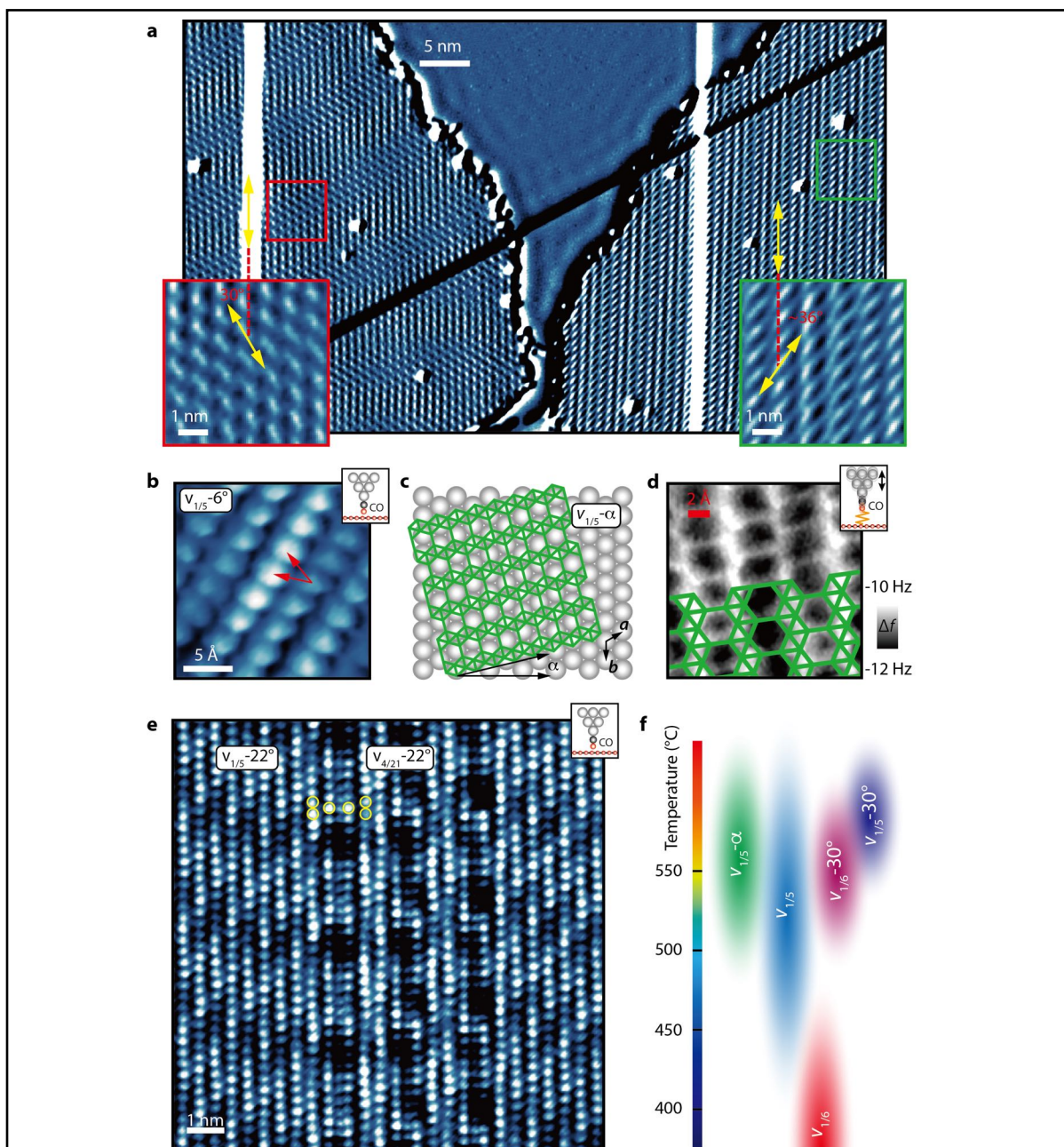


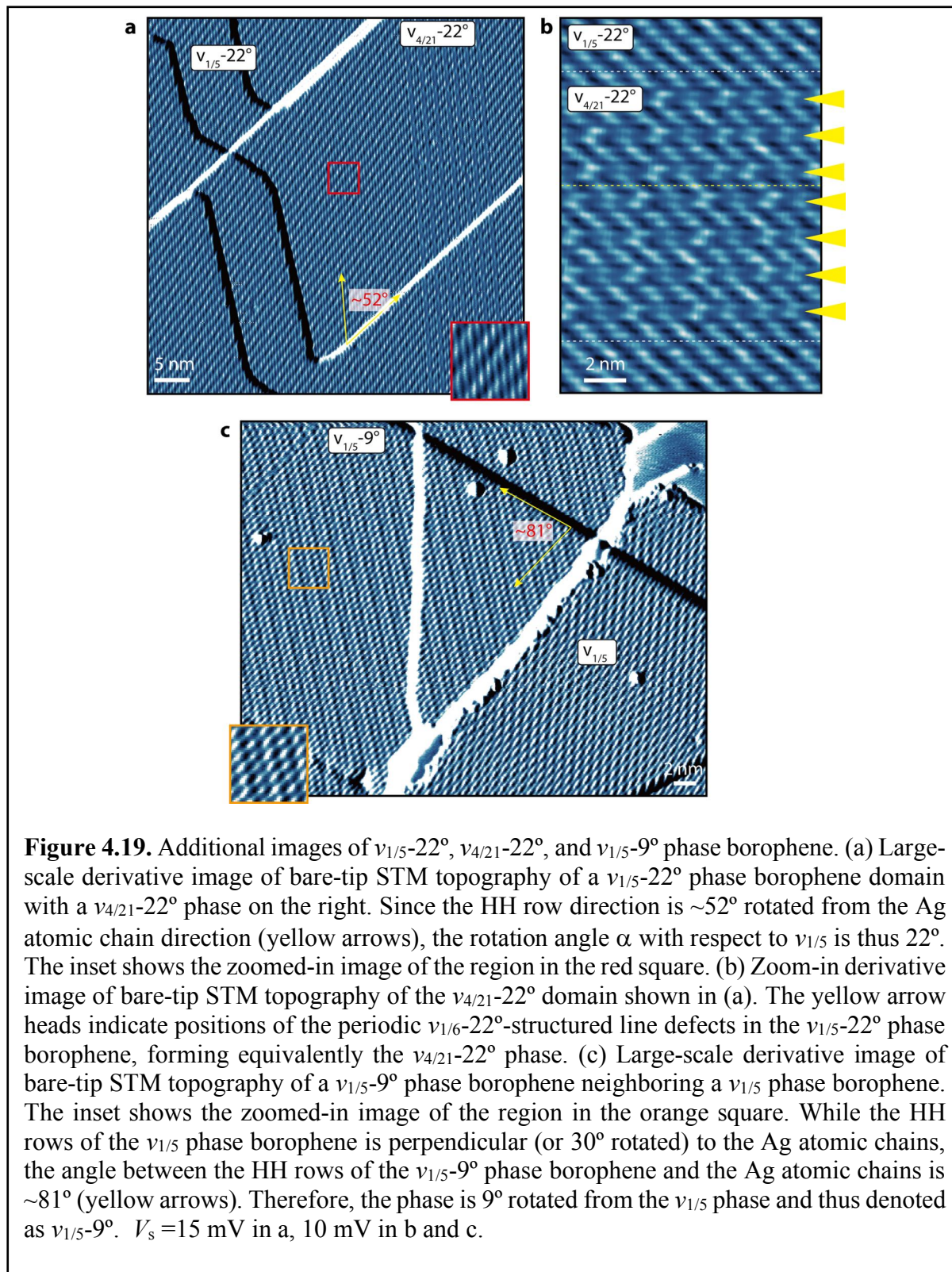
Figure 4.18. Imaging rotationally incommensurate phases of borophene with functionalized probes. (a) Derivative image of bare-tip STM topography of a $\nu_{1/5}$ (left) and $\nu_{1/5}-6^\circ$ (right) phase borophene domains. The insets are the zoomed-in images in the red and green squares. (b) CO-STM image of the $\nu_{1/5}-6^\circ$ phase borophene. (c) Schematic of rotationally incommensurate borophene phases, where α denotes the angle by which the sheet is rotated from $\nu_{1/5}$ phase borophene. (d) CO-AFM image of the $\nu_{1/5}-6^\circ$ phase borophene with overlaid atomic structure. (e) CO-STM image of a $\nu_{1/5}-22^\circ$ phase borophene with self-assembled $\nu_{1/6}-22^\circ$ -structured line defects. (f) Qualitative phase diagram of borophene growth with respect to temperature. $V_s = 190$ mV in a, -2 mV in b, and 22 mV in e.

rotating a $\nu_{1/5}$ phase borophene by 30° on Ag(111). The coexistence of such structure with $\nu_{1/6}-30^\circ$

phase borophene with parallel HH rows and a seamless phase boundary is shown in the CO-STM image in **Fig. 4.17e**, confirming a rotation angle of 30° and thus the phase as $\nu_{1/5}\text{-}30^\circ$. Since phase intermixing starts with line defects in each phase adopting the structure of the other phase,⁴²⁷ we identify various $\nu_{1/5}\text{-}30^\circ$ -structured line defects in $\nu_{1/6}\text{-}30^\circ$ phase borophene with different widths as shown in the top row of **Fig. 4.17f-i** (CO-STM images). The yellow circles denote the staggered HH pattern in the $\nu_{1/5}\text{-}30^\circ$ regions, while the corresponding structures are given in the bottom row.

From $\nu_{1/6}$, $\nu_{1/5}$ to $\nu_{1/6}\text{-}30^\circ$ and $\nu_{1/5}\text{-}30^\circ$ phase borophene, all could be considered rotationally commensurate since the HH rows are aligned along high symmetry directions of the Ag(111) surface. At similar conditions where $\nu_{1/6}\text{-}30^\circ$ and $\nu_{1/5}\text{-}30^\circ$ phase borophene grow, a new structure is observed as shown in the derivative image of bare-tip STM topography in **Fig. 4.18a**. As seen in the zoomed-in inset images, the borophene domain on the left is $\nu_{1/5}$ phase borophene with a characteristic brick-wall type Moiré pattern (red square), whereas the domain on the right shows a distorted brick-wall type Moiré pattern (green square), suggesting a different phase from what has been observed so far. The CO-STM image of such domain shown in **Fig. 4.18b** reveals a HH lattice with staggered protrusions (red arrows), again, indicative of $\nu_{1/5}$ borophene sheet. Due to the $\sim 36^\circ$ (instead of 30° for $\nu_{1/5}$) angle between the directions of HH rows and Ag atomic chains (vertical direction, **Fig. 4.18a**), such borophene sheet is the $\nu_{1/5}$ phase rotated by 6° and is thus denoted as $\nu_{1/5}\text{-}6^\circ$. Such rotationally incommensurate $\nu_{1/5}$ sheet is generally depicted in **Fig. 4.18c** as $\nu_{1/5}\text{-}\alpha$, where α is the rotation angle by which the sheet deviates from the $\nu_{1/5}$ phase. CO-AFM image of such phase with an overlaid atomic structure in **Fig. 4.18d** confirms the assignment as a $\nu_{1/5}$ sheet. In addition to $\alpha=6^\circ$, other rotationally incommensurate phases such as $\nu_{1/5}\text{-}9^\circ$ and $\nu_{1/5}\text{-}22^\circ$ phase borophene have been observed (**Fig. 4.19**). As an example, the CO-STM image in **Fig. 4.18e** resolves the HH lattice of a $\nu_{1/5}\text{-}22^\circ$ phase borophene with periodically self-assembled $\nu_{1/6}\text{-}$

22° line defects in the middle, as evidenced by the staggered and aligned HH patterns indicated by



the yellow circles, respectively. Equivalently, the self-assembled line defects form a $v_{4/21}$ - 22° phase (another example is shown in **Fig. 4.19**), a borophene sheet that is observed previously in non-rotated borophene growth (i.e., $\alpha=0$)⁴²⁷. Based on the observations discussed above and established previously, the phase diagram of borophene growth with respect to temperature could be qualitatively summarized as in **Fig. 4.18f**, where each phase is represented by an oval and overlapping ovals indicate coexistence. As temperature increases, a partial growth transition from rotationally commensurate phases to incommensurate phases takes place with multiple phases coexisting at high temperatures. The existence of rotationally incommensurate phases further supports that borophene layers are chemically discrete from the underlying Ag surface.⁴⁵³

In summary, we have utilized CO-functionalized scanning probes to image and determine the atomic lattice structures of various borophene polymorphs. Compared to CO-AFM, we identify CO-STM as an alternative and comparatively more accessible technique to unambiguously determine borophene structures. With these methods, we verified proposed structure models of borophene, and for the first time we have resolved features consistent with boron-boron covalent bonds. The structures of the previously observed rectangular lattice and striped phase borophene have been clarified. Interestingly, $v_{1/5}$ and $v_{1/6}$ sheets are shown to be the unifying structures for all the observed phases so far, and a partial growth transition from rotationally commensurate $v_{1/5}$ and $v_{1/6}$ phase to rotationally incommensurate phases takes place at high temperatures. The knowledge gained in this work highlights the utility of CO-AFM and CO-STM in fundamentally understanding emerging nanomaterials. Given the large number of computational reports on this new material with various atomic models, this study unambiguously sets the foundation on the structures of borophene polymorphs grown at different temperatures. This blueprint for borophene

growth and characterization will guide the on-going experimental and theoretical work around borophene and other emerging synthetic 2D materials towards realistic applications.

4.4 Non-Covalent Functionalizations of Borophene: a Borophene-Organic Lateral Heterostructure

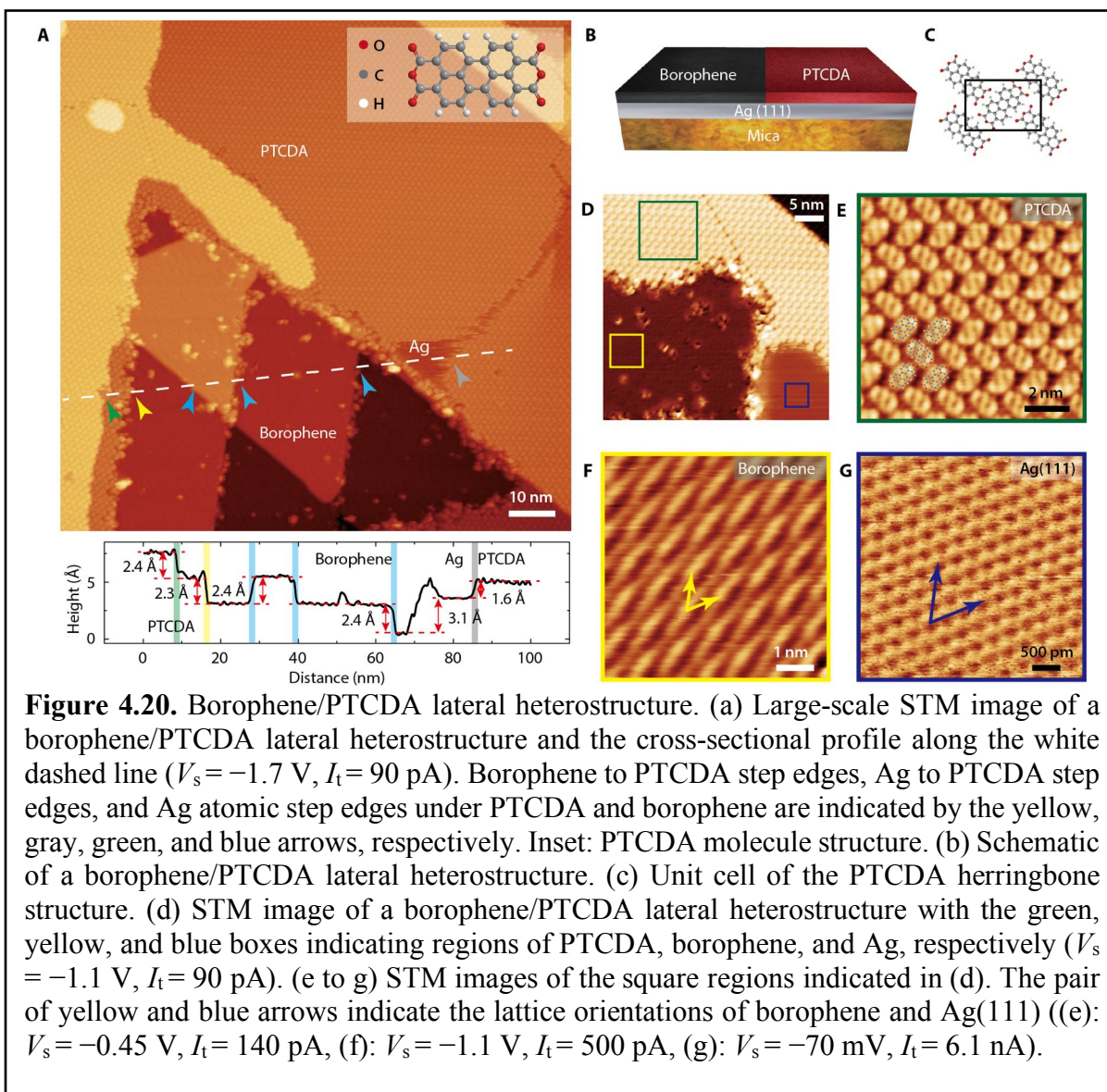
As an emerging 2D material, borophene has thus far only been studied in isolation, whereas nearly all technological applications will require the integration of borophene with other materials. Of particular interest are electronically abrupt lateral heterostructures, which have been widely explored in other 2D materials due to their novel electronic properties.^{196,454-457} For example, atomically well-defined lateral heterostructures between graphene and hexagonal boron nitride⁴⁵⁴ have revealed spatially confined boundary states with STS.⁴⁵⁸ It should be noted, however, that methods for experimentally realizing atomically clean and abrupt lateral heterojunctions remain challenging for many 2D material systems.^{196,455,457,459} For example, the growth front of the first 2D material can be easily contaminated, which can disrupt the subsequent growth of the second 2D material and/or lead to ill-defined interfacial regions. Alloying and intermixing during the growth of 2D material lateral heterostructures also prevents abrupt interfaces.^{456,460}

Here, we report the first experimental demonstration and characterization of a borophene lateral heterostructure with the molecular semiconductor PTCDA. Initially, submonolayer homogeneous-phase borophene is grown on Ag(111) on mica substrates by electron-beam evaporation of a pure boron source. Subsequent deposition of PTCDA results in preferential assembly on Ag(111), ultimately resulting in the presence of dense and well-ordered PTCDA monolayers that form lateral heterostructures with the borophene flakes. PTCDA is known to self-assemble on a variety of substrates including metals,⁴⁶¹ semimetals,⁴⁶² semiconductors,⁴⁶³

oxides,⁴⁶⁴ and salt crystals.⁴⁶⁵ The fact that it does not self-assemble on borophene is thus initially unexpected, but leads to the desirable formation of lateral heterostructures with borophene.

It has been reported that the electronic properties of self-assembled monolayers can be tuned by neighboring materials.⁴⁶⁶ In particular, the noncovalent interaction of PTCDA with silver substrates leads to a delocalized 2D band state with a parabolic dispersion.⁴⁶⁷ It should also be noted that noncovalent van der Waals interactions are prevalent in electronic devices based on 2D^{321,468} and mixed-dimensional heterostructures³²⁹ as discussed in CHAPTER 1. For example, van der Waals coupled organic lateral heterostructures have been demonstrated as gate-tunable p-n diodes.⁴⁵⁹ It has also been reported that van der Waals coupled electronic states play an important role in determining the electronic structure and optical properties of double-walled carbon nanotubes.⁴⁶⁹ For the case of borophene and PTCDA, *in situ* XPS verifies the absence of covalent bonding between borophene and PTCDA since the B 1s peak remains virtually unchanged following the formation of borophene/PTCDA lateral heterostructures. Using molecular dynamics (MD) simulations, we demonstrate that these observations are consistent with a lower adsorption enthalpy of PTCDA on borophene and the formation of a hydrogen bonding network between adsorbed PTCDA molecules. UHV STM and STS measurements further show that these lateral borophene/PTCDA heterostructures are electronically abrupt at the molecular-scale. In addition to elucidating the unique chemistry of borophene, this work has clear implications for borophene-based nanoelectronics.

Similar as before, the growth of submonolayer borophene ($v_{1/5}$ phase in this case) is achieved by electron-beam evaporation of a pure boron rod that is directed toward a Ag(111) thin film (~300 nm thick) on mica substrate in UHV. To functionalize borophene with organics, deposition of PTCDA is achieved by thermally evaporating PTCDA molecules from an alumina-



coated crucible. Fine-tuning of the evaporation temperature and duration allows precise, layer-by-layer growth of self-assembled PTCDA on Ag(111). **Fig. 4.20a** shows a large-scale STM image following PTCDA deposition onto a submonolayer borophene on Ag(111) substrate. The large triangular-shaped domain at the lower half of the image is a bare borophene island surrounded by a PTCDA monolayer and a small patch of clean Ag(111).

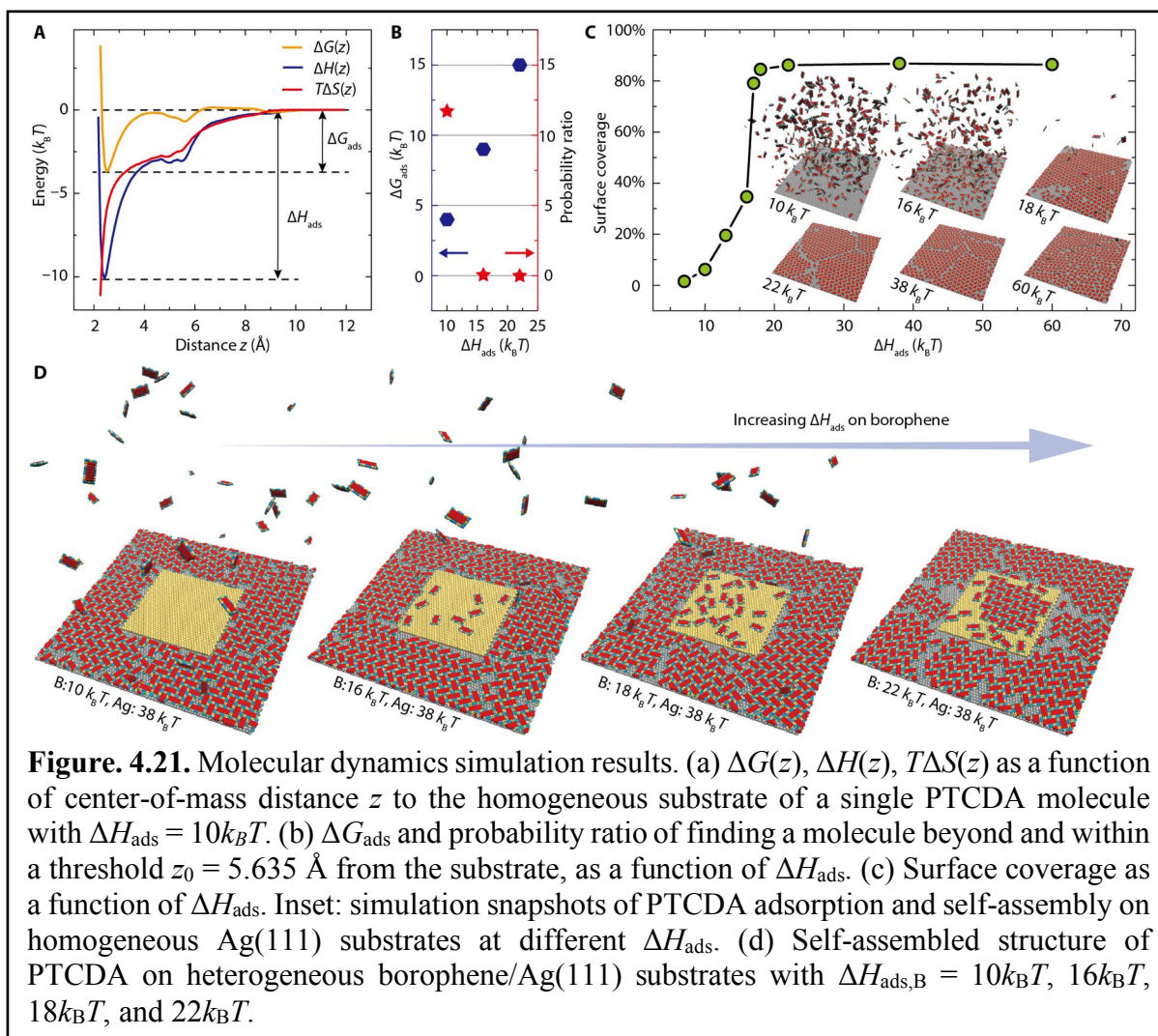
The preferential assembly of PTCDA on Ag(111) compared to borophene leads to the spontaneous formation of borophene/PTCDA lateral heterostructures. Due to the presence of steps

in the underlying Ag(111) substrate, the geometry of the borophene/PTCDA lateral heterostructure is better understood through the cross-sectional profile along the white dashed line (**Fig. 4.20a**), where each step height has been labeled. The measured step heights of 2.4 Å across the PTCDA layer (green arrow) and borophene region (blue arrows) correspond to a single atomic step height on Ag(111) (2.36 Å)⁴⁷⁰ as a result of the carpet-mode growth of PTCDA and borophene over Ag step edges. The apparent step height of 2.3 Å from borophene to monolayer PTCDA (yellow arrow) is explained by the sum of the 0.7 Å step height from borophene to Ag (111) and the 1.6 Å step height from Ag(111) to monolayer PTCDA (gray arrow). Therefore, the borophene/PTCDA lateral heterostructure consists of borophene laterally interfacing with a monolayer of self-assembled PTCDA on Ag(111) as shown schematically in **Fig. 4.20b**. This situation is analogous to the preferential assembly of *meso*-tetramesitylporphyrins on clean Cu(001) compared to nitrogen-modified Cu(001), which has been attributed to the lower polarizability of nitrogen-modified Cu(001) and thus decreased van der Waals interaction with non-covalently bonded molecular adlayers.⁴⁷¹

The self-assembly motif adopted by PTCDA on Ag(111) is the well-known herringbone structure.^{467,472} **Fig. 4.20c** shows the unit cell of this structure, which is more directly observed in **Fig. 4.20d** and **e**. In particular, the green, yellow, and blue squares in **Fig. 4.20d** highlight regions of PTCDA, borophene, and bare Ag, respectively. The zoomed-in STM images of each region are shown in **Fig. 4.20e-g**, with the unit cell of PTCDA schematically overlaid in **Fig. 4.20e**. The relative lattice orientation of homogeneous-phase borophene and Ag(111) is denoted by the pairs of yellow and blue arrows in **Fig. 4.20f-g**, which are parallel to each other and thus indicate registry between the two materials.

To explore the effect of competing adsorption on the self-assembly of molecules on heterogeneous substrates, in collaboration with Zonghui Wei from Prof. Erik Luijten's group at Northwestern University, we employ MD simulations at a fixed temperature $T = 300$ K, which matches the experimental conditions. Since we are interested in large-scale collective effects that are not accessible through *ab initio* calculations, we reduce the PTCDA molecules to a coarse-grained representation capable of forming lateral hydrogen bonds as well as adsorption on the substrate. The Ag(111) substrate is represented as a hexagonally close-packed lattice, with interatomic spacing 2.898 Å. The excluded-volume interactions are modeled with shifted-truncated Lennard-Jones (LJ) potentials and the attractions are represented by LJ potentials. Whereas the hydrogen bonding strength is kept fixed, we systematically vary the enthalpy of adsorption per molecule, ΔH_{ads} , which we define as the magnitude of the relative enthalpy $\Delta H(z) = H(z) - H(\infty)$ upon adsorption at $z = z_G$. The relative Gibbs free energy $\Delta G(z)$ and entropy $\Delta S(z)$ are similarly defined. Here, z is the distance from the substrate and z_G is the position where $\Delta G(z)$ takes its minimum. To set the scale of ΔH_{ads} , we first quantify the loss of entropy upon adsorption of a single coarse-grained PTCDA molecule via thermodynamic integration. As shown in **Fig. 4.21a**, at $\Delta H_{\text{ads}} = 10k_B T$ we find a Gibbs free energy of adsorption ΔG_{ads} of approximately $4k_B T$, implying an entropy loss $\sim 6k_B$ for a fully adsorbed PTCDA molecule. The functional form of the entropy loss (namely, logarithmic in surface separation $z - z_G$) can be rationalized through estimation of the loss in degrees of freedom upon adsorption.

To confirm the calculation of $\Delta G(z)$, we directly probe the probability of finding a single molecule within a certain distance from the substrate. Specifically, for a threshold $z_0 = 5.635$ Å, we find a ratio $P(z > z_0)/P(z < z_0) \approx 10.99$, in relatively good agreement with the value 11.76 computed by integration of $\Delta G(z)$. As ΔH_{ads} is increased from $10k_B T$ to $16k_B T$ and $22k_B T$, ΔG_{ads}



increases accordingly and the probability of finding a single PTCDA molecule near the surface is greatly enhanced in **Fig. 4.21b**. Whereas this follows immediately from the Boltzmann distribution, the situation is more subtle if upon adsorption molecules interact laterally and form a regular surface packing. Thus, we examine self-assembly of PTCDA molecules on a homogeneous Ag(111) substrate as a function of ΔH_{ads} . For molecular adsorption enthalpies of $10k_B T$ and $16k_B T$, we find only moderate adsorption levels (**Fig. 4.21c**), as expected from the significant entropy loss upon adsorption. As ΔH_{ads} is increased to $18k_B T$, we observe significant surface coverage, with the adsorbed molecules arranged in the herringbone structure found experimentally in **Fig. 4.20d,e**

(inset of **Fig. 4.21c**). Increase of ΔH_{ads} to $22k_{\text{B}}T$ and $38k_{\text{B}}T$ does not lead to an appreciable change, but at even higher adsorption enthalpy ($60k_{\text{B}}T$), a large number of defects are observed. We note that these adsorption enthalpies leading to almost full surface coverage are within the range found in density functional theory calculations ($0.5\text{--}3\text{ eV}$),⁴⁷² and we proceed to employ $\Delta H_{\text{ads,Ag}} = 38k_{\text{B}}T$ for the study of competing adsorption on borophene/Ag(111) surfaces. The abrupt increase in surface coverage as a function of ΔH_{ads} is consistent with a first-order transition (**Fig. 4.21c**).

To model the formation of lateral heterostructures on heterogeneous substrates of borophene grown on Ag(111), we add a second hexagonally close-packed lattice layer partially covering the original substrate, to represent a borophene island (yellow islands in **Fig. 4.21d**). Within the context of our coarse-grained model and considering that the atomic structure of homogeneous-phase borophene is not well-established, we choose the same structure for the borophene island, to focus on the energy barriers posed by domain edges and, most importantly, the role of competitive binding. The latter is investigated by fixing $\Delta H_{\text{ads,Ag}}$ on Ag(111) at $38k_{\text{B}}T$ per molecule and then systematically varying the adsorption enthalpy on borophene, $\Delta H_{\text{ads,B}}$. As illustrated in **Fig. 4.21d**, PTCDA molecules self-assemble on Ag(111) in all cases and gradually adsorb and self-assemble on the borophene island as $\Delta H_{\text{ads,B}}$ is increased. As expected, negligible adsorption takes place for $\Delta H_{\text{ads,B}}$ below $18k_{\text{B}}T$. However, even for $\Delta H_{\text{ads,B}} = 18k_{\text{B}}T$, where we find full coverage and self-assembly for a homogeneous substrate, low, unordered coverage occurs on the borophene, owing to the competing adsorption by the Ag(111) substrate. Moreover, the energy barrier at the boundary causes the coverage on Ag(111) to terminate abruptly at the edge of the borophene island. Only when $\Delta H_{\text{ads,B}}$ is increased to $22k_{\text{B}}T$, self-assembly occurs on both substrates. It is important to note that for the study of competitive binding the total number of PTCDA molecules in the system must be limited to the amount needed for full coverage of the

Ag(111). Since our model does not permit multi-layer adsorption, at higher PTCDA availability adsorption on borophene will occur as well once the Ag(111) is fully covered and $\Delta H_{\text{ads,B}}$ is increased to a sufficiently high level. Interestingly, the hydrogen bonding responsible for the formation of the herringbone structure plays a role in suppressing accumulation of PTCDA on the less adsorbing substrate, since at dilute coverage molecules cannot form lateral hydrogen bonds (**Fig. 4.21d**, second and third panel). Therefore, within the limitations of the coarse-grained model and the assumption that differences in adsorption are not governed by surface geometry, we find that a PTCDA adsorption enthalpy on borophene of less than $\sim 16k_{\text{B}}T$ (0.4 eV), combined with a differential in PTCDA adsorption enthalpy between Ag(111) and borophene of several $k_{\text{B}}T$ (~ 0.1 eV), is sufficient to fully explain the experimental observations.

Fig. 4.22a displays *in situ* XPS spectra of borophene before and after PTCDA deposition. Consistent with the absence of PTCDA on the borophene surface, the B 1s core-level peak is essentially unchanged following PTCDA deposition with the exception of a small downshift (< 0.2 eV) to lower binding energy. On the other hand, in response to the PTCDA monolayer on the surrounding Ag(111) surface, the C 1s spectrum in **Fig. 4.22b** shows a significant increase in peak intensity, where the two sub-peaks at 284.3 eV and 287.6 eV correspond to the perylene core and carbonyl groups in PTCDA.⁴⁷³ The small presence of C preceding PTCDA deposition can be attributed to trace amounts of adventitious carbon for Ag on mica. In **Fig. 4.20a**, relatively few individual PTCDA molecules are present atop borophene primarily at points that align with underlying Ag step edges. Charge transfer between metallic borophene and these sparsely adsorbed PTCDA molecules, as well as the PTCDA molecules at the borophene/PTCDA lateral heterojunction interface, presumably leads to the minor peak shift in the B 1s core-level spectrum.

Consistent with this interpretation, charge transfer between PTCDA and conventional metallic substrates, including Ag, results in the LUMO shifting below the Fermi level.^{461,467,472,474,475}

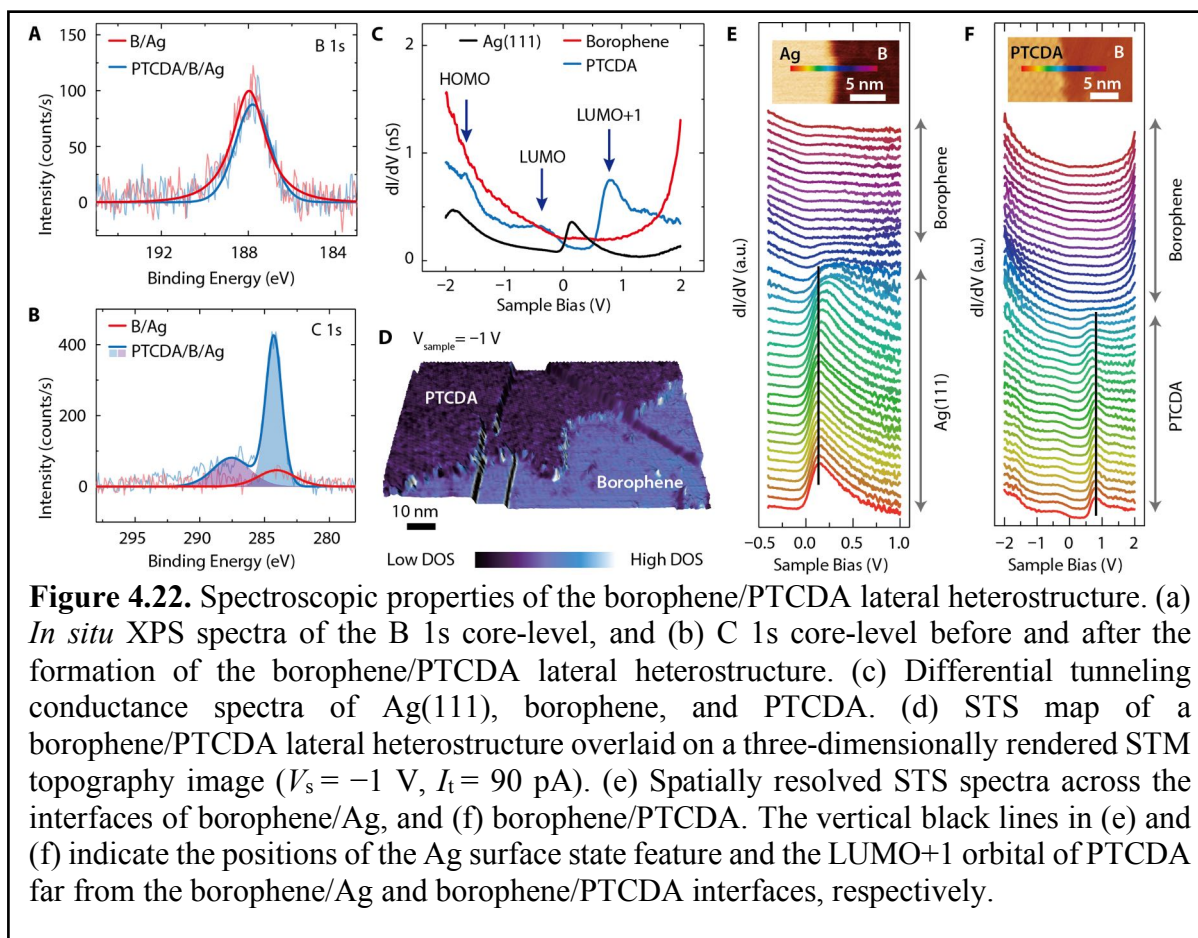


Figure 4.22. Spectroscopic properties of the borophene/PTCDA lateral heterostructure. (a) *In situ* XPS spectra of the B 1s core-level, and (b) C 1s core-level before and after the formation of the borophene/PTCDA lateral heterostructure. (c) Differential tunneling conductance spectra of Ag(111), borophene, and PTCDA. (d) STS map of a borophene/PTCDA lateral heterostructure overlaid on a three-dimensionally rendered STM topography image ($V_s = -1$ V, $I_t = 90$ pA). (e) Spatially resolved STS spectra across the interfaces of borophene/Ag, and (f) borophene/PTCDA. The vertical black lines in (e) and (f) indicate the positions of the Ag surface state feature and the LUMO+1 orbital of PTCDA far from the borophene/Ag and borophene/PTCDA interfaces, respectively.

To further probe electronic interactions between borophene and PTCDA, STS characterization is performed on the borophene/PTCDA lateral heterostructure substrate. Specifically, STS spectra are presented in **Fig. 4.22c** for clean Ag(111), borophene, and monolayer PTCDA. The lineshape and features for the PTCDA STS spectrum agree well with literature precedent for the highest occupied molecular orbital (HOMO, -1.7 eV), LUMO (-0.3 eV), and LUMO+1 (0.8 eV).^{467,472,475} **Fig. 4.22d** shows a rendered three-dimensional topography image of the lateral heterostructure with superimposed STS mapping at a sample bias of -1 V. The relative electronic DOS between borophene and PTCDA is in agreement with **Fig. 4.22c**. The degree of

interfacial electronic interaction is further explored by a series of STS spectra taken across both the Ag/borophene and PTCDA/borophene interfaces with lateral displacements of 3.0 Å and 3.8 Å between adjacent points in **Fig. 4.22e** and **f**, respectively. In **Fig. 4.22e**, far from the interface, both borophene and Ag(111) show characteristic bulk properties. A small upshift (~ 0.05 eV) of the Ag surface state feature to higher energy is observed when approaching the interface from Ag(111). The transition in the STS spectra from PTCDA to borophene is abrupt and takes place within 1-2 nm in **Fig. 4.22f**, similar to the size of a PTCDA molecule. A small downshift of ~ 0.15 eV of the LUMO+1 state is observed when approaching the junction from PTCDA, likely due to the weak van der Waals interactions between the junction PTCDA molecules and borophene. Compared to the additional features in the STS spectra and the large transition distance due to the presence of edge states and transition regions at MoS₂ edges and grain boundaries,^{165,356,403} the borophene/PTCDA lateral heterojunction is noteworthy in terms of its electronic abruptness at the single nanometer length scale.

In summary, self-assembled borophene/PTCDA lateral heterostructures with structurally and electronically abrupt interfaces have been realized by sequential deposition of B and PTCDA on Ag(111). The borophene/PTCDA lateral heterostructures occur spontaneously, which is consistent with molecular dynamics simulations that show that a higher enthalpy of adsorption on Ag(111) and the lateral hydrogen bonding between adsorbed PTCDA molecules leads to preferential assembly of PTCDA on Ag(111) compared to borophene. The weak chemical interaction between borophene and PTCDA is further corroborated by *in situ* XPS measurements. Molecular-resolution STM/STS shows that borophene/PTCDA lateral heterostructures are electronically abrupt with a transition in the DOS from borophene to PTCDA occurring over the length scale of a single PTCDA molecule.

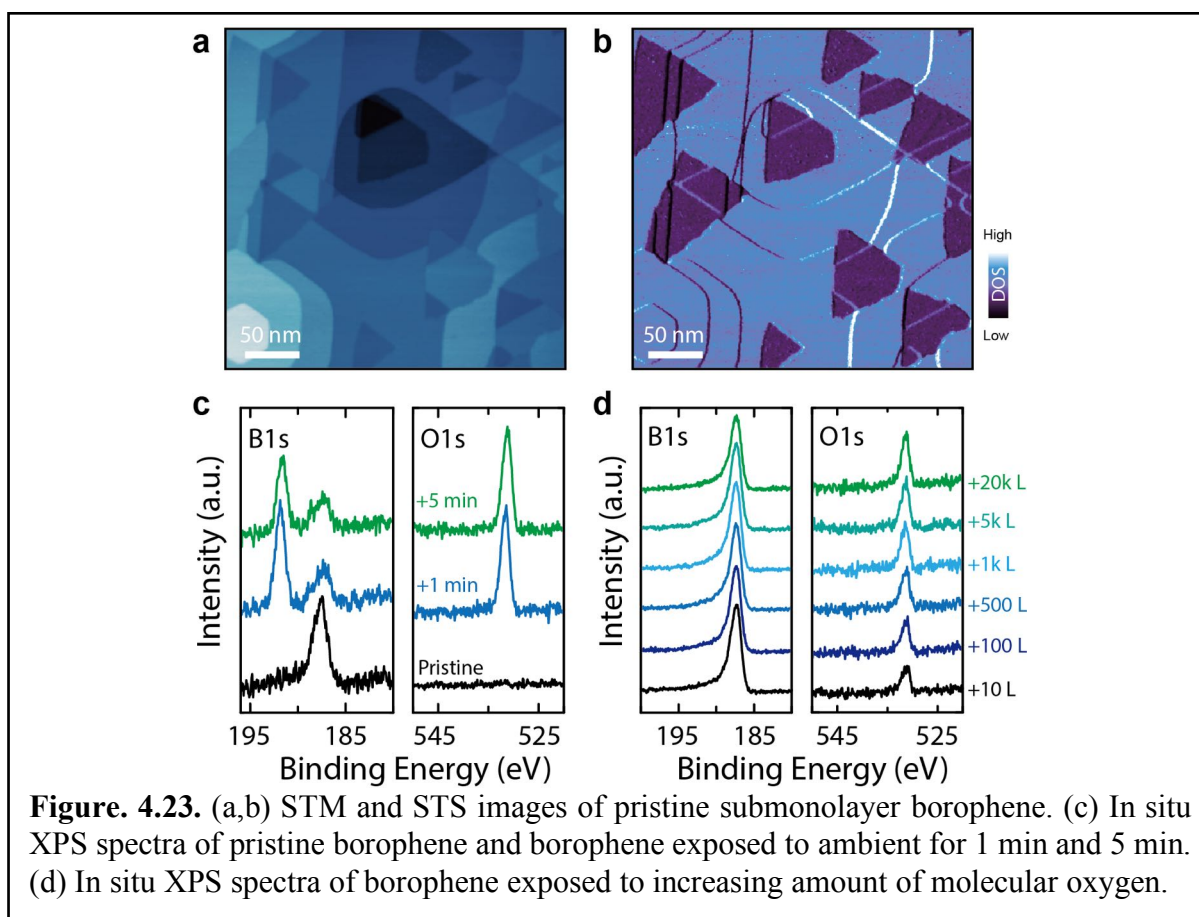
The borophene/PTCDA lateral heterostructure forms a metal/semiconductor lateral heterojunction that has the potential to be exploited in an analogous manner to metal/semiconductor junctions and graphene/organic junctions⁴⁷⁶ for electronic applications (e.g., resistive switching based on metal/PTCDA/metal junctions⁴⁷⁷). For such purposes, transfer schemes will need to be developed to realize borophene-based heterostructures on insulating substrates. However, the development of a transfer scheme that does not chemically damage the borophene itself is nontrivial due to the largely unknown chemistry of borophene. The laterally interfacing PTCDA layers could also serve as a template for additional chemistry, thereby facilitating the formation of other borophene heterostructures. Given the lack of knowledge on borophene chemistry, the increasing interest in lateral heterostructures, and difficulties in obtaining abrupt lateral interfaces free from contamination^{455,459} and alloy formation⁴⁵⁶ in other 2D materials, this work represents an important step forward for emerging efforts in borophene-based heterostructures.

4.5 Borophene Oxidation and Effective Passivation

To realize any borophene-based electronic applications, it is required to remove borophene from its growth environment, i.e., UHV chambers. Furthermore, such atomically thin layers of boron has to be isolated from the metallic growth substrate of Ag and withstand processing steps necessary for device fabrications. Given the high reactivity of borophene in ambient conditions,^{11,12} it is thus of vital importance to understand the oxidation of borophene and develop an effective passivation scheme in UHV to mitigate borophene oxidation.

Figs. 4.23a,b show typical STM and STS images of as-grown borophene, where the triangular-shaped borophene islands are immediately distinguishable from the STS map. In situ

XPS spectra in **Fig. 4.23c** reveals the chemically pristine nature of borophene without any B1s peaks associated with oxidized boron, which would otherwise appear at ~ 192 eV. Similarly, minimum oxygen is detected in the O1s core level scan as expected from growth in UHV conditions. After exposing the pristine borophene sample to ambient for 1 min, an obvious oxidized boron peak is seen in the B1s core level spectrum together with a high O1s peak. No obvious further changes are seen by further exposing the sample to ambient for another 5 min.

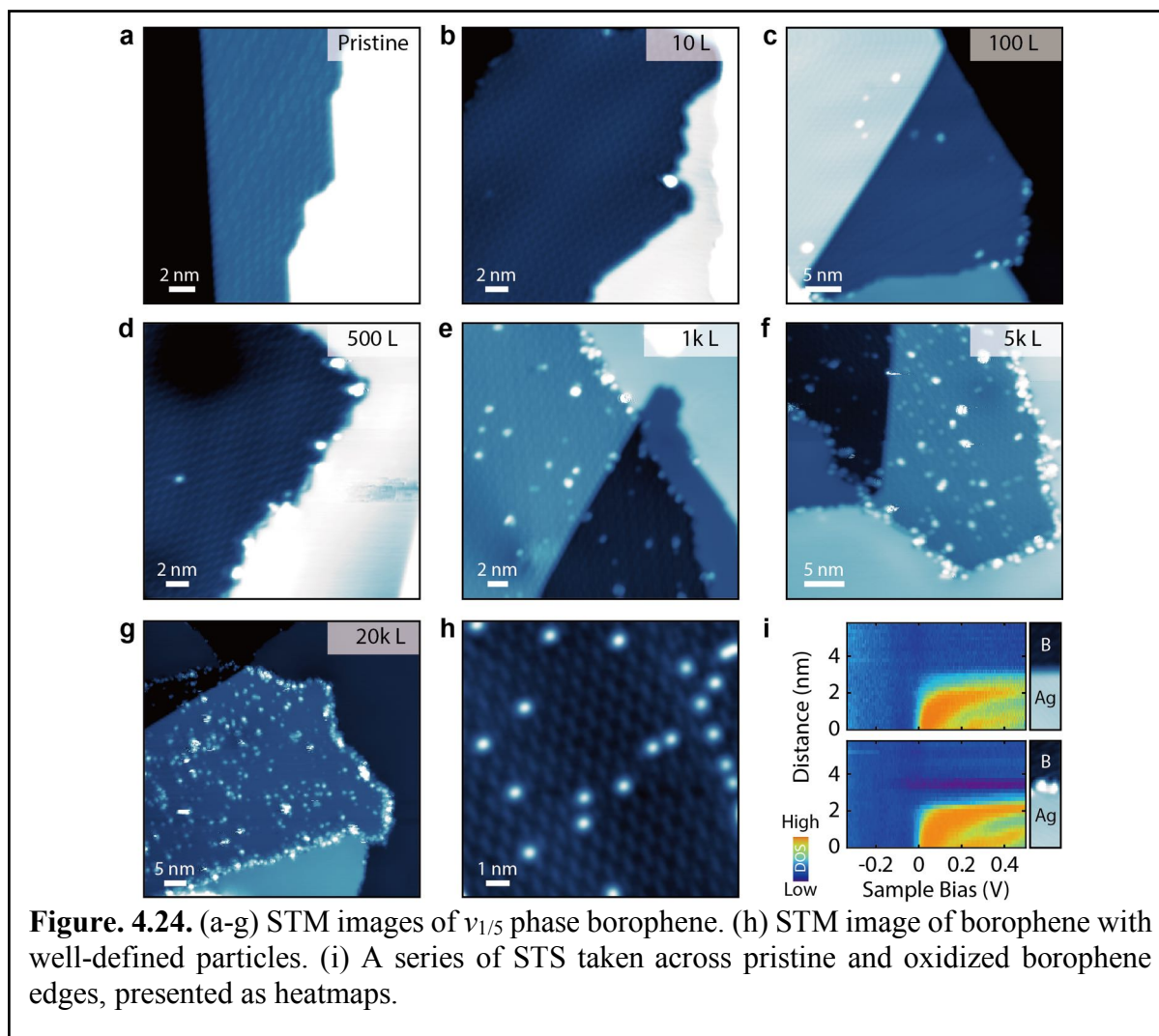


Such result is directly indicative of the high ambient-instability of borophene towards oxidation.

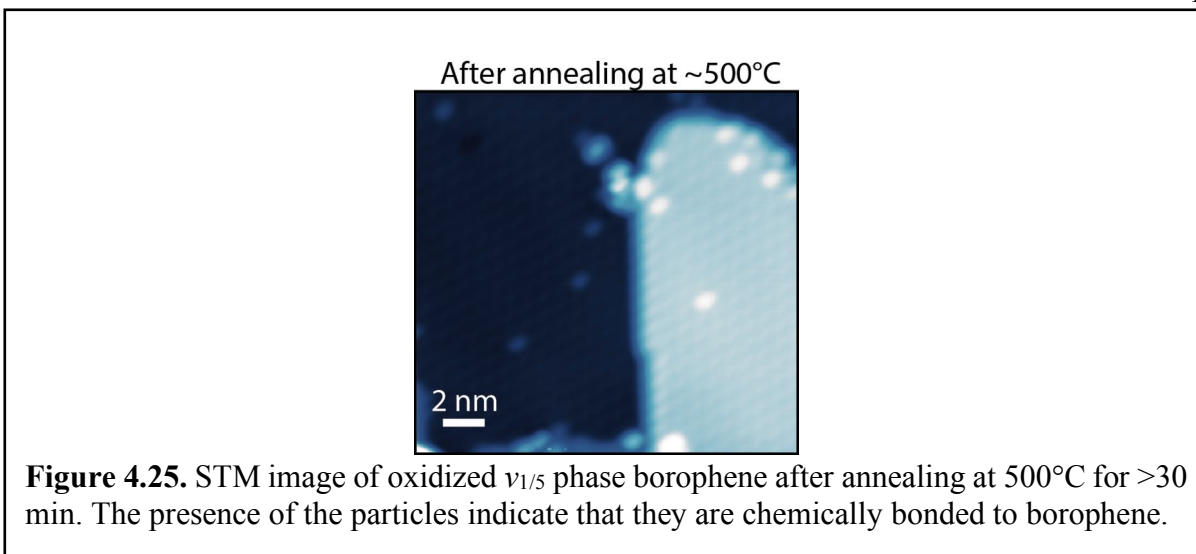
To study the oxidation behavior of borophene in pure oxygen environment, a pristine borophene sample is exposed to different doses of molecular oxygen in UHV. **Fig. 4.23d** demonstrates the evolution of the B1s and O1s core-level peaks with increasing oxygen doses. While no detectable oxidation of borophene is seen from B1s core levels up to 20k Langmuir (L, $1 \text{ L} = 10^{-6} \text{ Torr} \times 1 \text{ s}$)

of oxygen exposure, the O1s peak gradually increases, which would be expected if any physisorbed oxygen molecules are present.

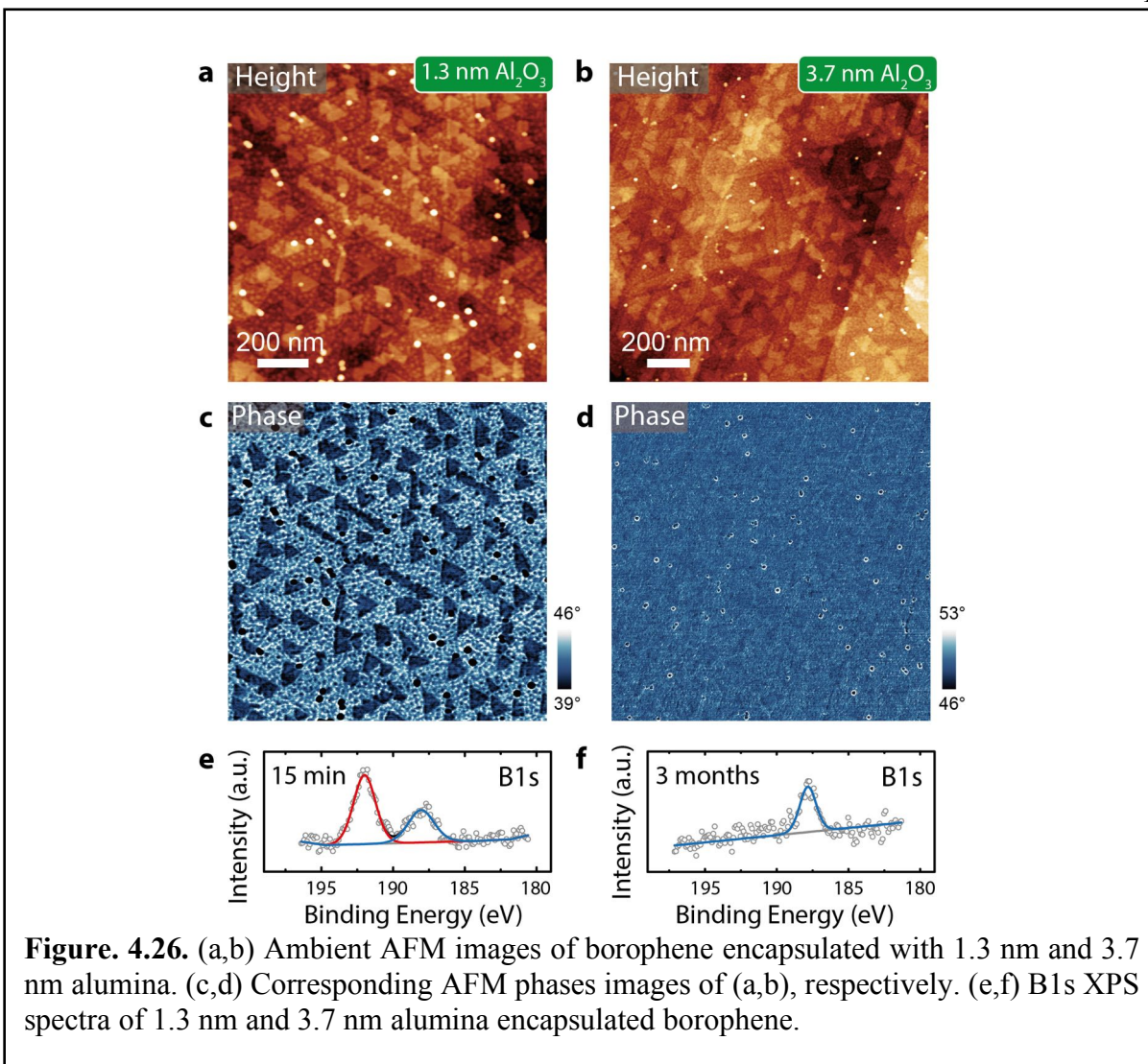
To further explore the possible reactions between borophene and oxygen at the nanoscale beyond the detection limit of XPS, atomic-resolution STM images of borophene exposed to different amounts of oxygen are given in **Figs. 4.24a-g**. Pristine $v_{1/5}$ phase borophene (**Fig. 4.24a**) shows atomically flat surfaces with clean and abrupt domain edges. Exposure to increasing



amounts of molecular oxygen leads to decoration of the edges and basal planes of borophene with small particles, indicative of possible reactions with oxygen. While the density of particles at the

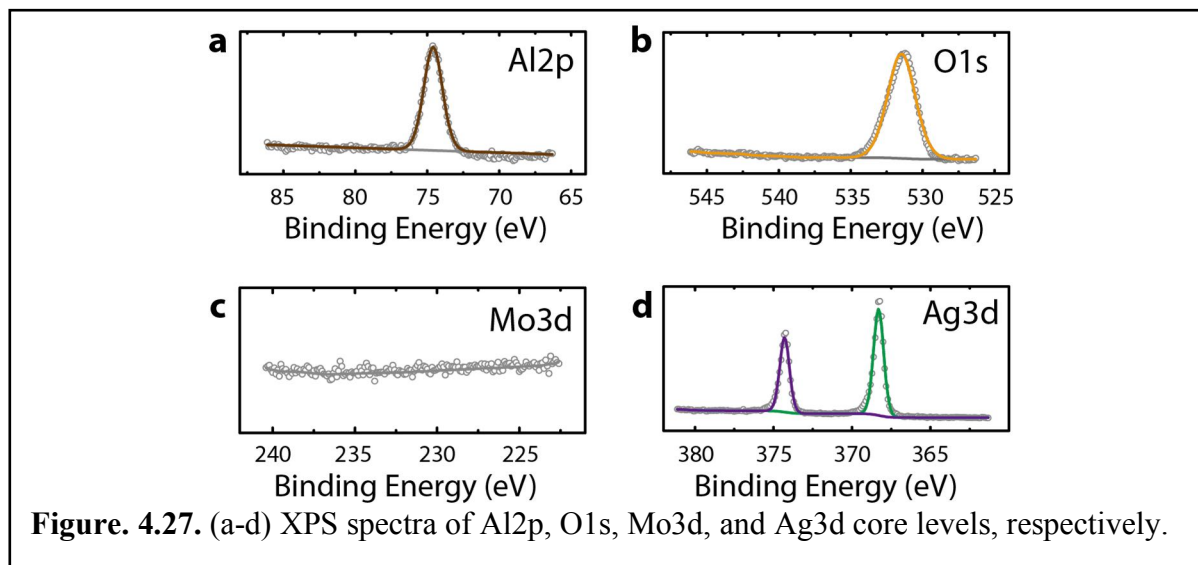


edges saturates after the exposure of 5k L oxygen in **Fig. 4.24f**, the particle density in the basal plane continues to increase (**Fig. 4.24g**). Though the particles on the basal plane vary in size, a large percentage of such particles are in the form of small and uniform round protrusions as shown in **Fig. 4.24h**. The diameter of such well-defined particles is ~ 0.5 nm, indicative of either physisorbed O_2 molecules or chemically bonded O atoms. The fact that $\sim 500^\circ\text{C}$ annealing of such oxidized sample do not fully remove those particles (**Fig. 4.25**) supports the assignment of chemically bonded O atoms. Further DFT calculations would be required to unravel the true nature of those particles. The electronic disturbance imposed by the oxidized borophene edges is investigated as shown in **Fig. 4.24i**. A series of STS spectra taken across a pristine and an oxidized borophene edges are presented as heatmaps on the top and bottom parts of **Fig. 4.24i**, respectively. At positive sample biases, a sharp transition from low borophene DOS to high Ag(111) surface state takes place across the pristine edge, whereas a sharp decrease of DOS at the oxidized edge is seen, consistent with the expected more insulating nature of boron-oxides.

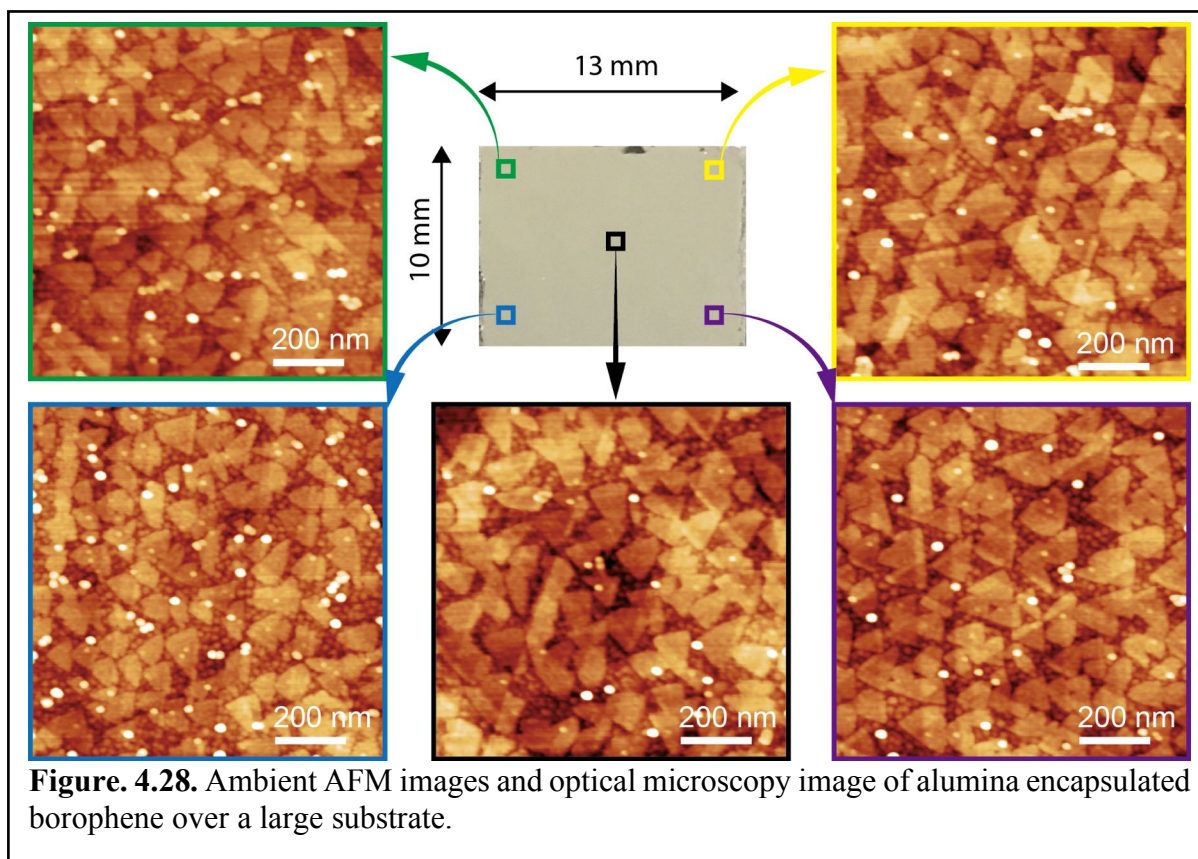


Our previous study has explored the possibility of evaporating Si in UHV as an capping layer to passivate borophene. While such Si-passivated borophene remains pristine for a short amount of time (2 days), oxidation eventually takes place likely due to the diffusion of ambient species through the Si capping layer. Furthermore, the semiconducting nature of Si would complicate any further electrical transport measurements performed on borophene. Therefore, it's highly desirable to identify a method of passivating borophene in UHV with a physically dense and electrically insulating thin film. Since alumina has been shown in the past as an effective passivation layer for BP, we explored UHV deposition of alumina on pristine borophene via

electron beam evaporation from a Mo crucible. **Figs. 4.26a,b** show ambient AFM images of alumina-passivated borophene with nominally 1.3 nm and 3.7 nm alumina. In both cases, the capped borophene triangles are visible, suggesting highly smooth alumina layers, though the



borophene islands are more blurry under the thicker 3.7 nm alumina layer. The corresponding AFM phase images are shown in **Fig. 4.26c,d**. While no obvious phase contrast is seen in the case of 3.7 nm alumina-passivated borophene (**Fig. 4.26d**), borophene triangles show distinct phase contrast in the case of 1.3 nm alumina-passivated borophene (**Fig. 4.26c**), suggesting incomplete passivation. As a result, 15 min of ambient exposure of 1.3 nm alumina-passivated borophene results in significant oxidation (**Fig. 4.26e**). On the other hand, minimum oxidation of borophene with 3.7 nm alumina encapsulation layer is seen even after 3 months (**Fig. 4.26f**), confirming successful passivation over long period of time. As expected, Al2p and O1s core levels show obvious peaks (**Figs. 4.27a,b**). The absence of detectable Mo3d signals (**Fig. 4.27c**) confirms that no Mo (crucible material) is deposited onto the sample. As expected, no splitting or shift of Ag3d peaks (**Fig. 4.27d**) is seen. Finally, we demonstrate the capability of producing high coverage



encapsulated borophene over large areas (13 mm by 10 mm) in **Fig. 4.28**. The AFM images taken across the sample surface show high-quality borophene growth with uniform coverages.

In summary, we characterized at the atomic scale borophene oxidation in pure molecular oxygen environment, where oxidation was found to take place at both borophene edges and basal planes, and developed an effective method of passivating borophene in UHV via electron beam evaporation of alumina. Those advancements will likely facilitate the realization of borophene-based applications in the near future.

Chapter 5: Summary and Future Outlook

This chapter is based partially on the following publication:

X. Liu, and M. C. Hersam, Interface Characterization and Control of 2D Materials and Heterostructures, *Advanced Materials*, **2018**, DOI: 10.1002/adma.201801586.

5.1 Summary

In summary, I've demonstrated my PhD research work on characterizing and controlling the properties of three emerging 2D materials and their heterostructures. In Chapter 1, I briefly reviewed fundamental surface and interface phenomena and common nanoscale characterization approaches. In Chapter 2, I showed the first experimental test of 2D BP thermal stability via in situ S/TEM and spectroscopy methods, revealing a 400°C decomposition temperature. Taking advantage of the ambient instability of BP and the high-spatial resolution of AFM, I utilized CAFM to demonstrate nanopatterning and layer-by-layer thinning of BP using both DC and AC biases on conductive and insulating substrates, respectively. This generalizable approach enabled dramatic enhancement of current modulation in FETs made with AC CAFM-thinned BP channels. In Chapter 3, I explored the intrinsic structure defects of rotationally commensurate monolayer MoS₂ grown on EG, where 5 types of point defects and two types of GBs were atomically resolved. The defects density was found to be much lower than rotationally incommensurate MoS₂ layers. The integration of MoS₂/EG with C8-BTBT resulted in well-defined vertical interfaces. The structure of self-assembled C8-BTBT monolayers was illustrated, and it was illustrated that the molecular layer was insensitive to structural defects and electronic perturbations in the substrates. In Chapter 4, I interrogated line defects in borophene at the atomic scale, and revealed phase intermixing at appropriate growth conditions. The line defects in each phase were found to adopt

the structure of the other phase and energetically preferred spatially periodic self-assembly, giving rise to equivalently new phases of borophene, blurring the traditional distinction between crystals and defects. Low temperature STM/STS measurements further revealed a CDW modulated by line defects. Using CO-functionalized probes, for the first time I revealed features that were consistent with boron-boron covalent bonds. CO-STM was identified as an equivalently effective yet less demanding technique in resolving the lattice structures of borophene. In an effort to integrate borophene with other materials, non-covalent functionalization with PTCDA resulted in spontaneous formation of a borophene/PTCDA lateral heterostructure with electronically abrupt interfaces. Covalent modification of borophene was also investigated via UHV molecular oxygen dosing. Finally, an effective in situ passivation scheme using Al_2O_3 was demonstrated, which protected borophene from ambient oxidation for longer than 3 months.

5.2 Future Outlook

As the first 2D material, graphene has been studied for more than a decade, and still unexpected and exciting new physics is being discovered now and then. Within the scope of the material systems presented in this thesis, there are many foreseeable future directions that are highly relevant to on-going research and thus worth further research efforts. Beyond the materials we have been studying, we should remain open-minded and keep looking for new opportunities offered by new materials.

5.2.1. BP and Bulk van der Waals Materials

While only a small fraction of the large family of layered van der Waals materials have been studied in the form of exfoliated thin layers, a number of them share similar material

characteristics with BP – they have potentially interesting or largely unexplored material properties, but they are reactive in ambient conditions, and no bottom-up growth methods for producing mono- and few-layer flakes have been developed yet. For device- and circuit-scale demonstrations, the technical advantage of uniform thin 2D layers over mechanically exfoliated flakes is obvious. More fundamentally, a great percentage of studies on such exfoliated materials concerns flakes thicker than 5 nm, where the unique quantum confinement and resulting interesting physical properties offered by a true 2D lattice becomes negligible. Therefore, the identification of bottom-up growth methods via CVD, PVD, or MBE would not only open up new opportunities by introducing materials that is otherwise not accessible in the 2D limit, but also enable characterizations and reveal material properties that would not otherwise be possible. Taking BP as an example, direct STM/STS characterizations of pristine mono- and few-layer samples have not been achieved even after 5 years of its ‘rediscovery’ as a 2D material. One of the biggest difficulties is surface degradation for samples prepared ex situ and transferred into UHV. Similarly, in situ growth of high-quality vertical/lateral 2D heterostructures involving monolayer BP is not possible due to surface and edge contaminations. Taking the existing knowledge of bulk phase diagrams of phosphorus allotropes, opportunities exist for growing BP monolayers in UHV via thermal cycling (e.g., graphitization of phosphorus-implanted SiC), compound decomposition (e.g., thermal decomposition of InP, GaP wafers covered with graphene), and direct MBE growth using valved P-sources in UHV on catalytic metal surfaces (careful decontamination setups might be necessary). If such growth could be achieved, in situ growth of heterostructures would be straightforward. Especially, CVD growth of BN would provide a high-quality capping layer that protects BP from degradation.

5.2.2. Synthetic 2D Materials

A common characteristic of synthetic 2D materials (e.g., borophene, stanene, germanene) is their ambient-instability and relatively strong interactions with the substrate. Taking the latest synthetic 2D material borophene as an example, it has not yet been isolated from its growth substrate Ag. Part of the difficulty is its high reactivity, which requires a passivation layer and extremely clean and effective mechanical or chemical treatments to remove Ag. The important role of the metal substrates in stabilizing such templated 2D material might fundamentally prevent borophene from being detached from the growth substrates. However, effective passivation schemes of borophene with alumina have only been developed recently, and thus great opportunities exist in isolating borophene from Ag in the near future. Having borophene on other dielectric or semiconducting substrates would immediately allow charge transport measurements, for example, to test the predicted superconductivity. Quenching effect by the Ag substrate would also be eliminated and thus many optical measurements could be performed more effectively. Meanwhile, limited work has demonstrated functionalizations of borophene. Covalent chemical functionalization with molecular ammonia or cracked ammonia may potentially lead to edge passivation or conversion of borophene to BN. Depositing intercalation species like Si could potentially lift borophene from the Ag substrate, creating quasi-freestanding borophene, which would be ideal for both in situ STM/STS studies and transferring borophene off Ag. Alternatively, growing borophene on submonolayer NaCl islands on Ag(111) may potentially lead to borophene islands partially extended to NaCl surfaces due to the templating effect of edges, creating borophene on insulators. Taking advantage of the selective self-assembly of organics on Ag(111) around borophene as demonstrated in Chapter 4, mixed-dimensional heterostructures between borophene and bottom-up GNRs could be achieved with appropriate molecular precursors. Within

such lateral heterostructures, the anisotropic electronic properties of borophene could potentially be probed due to the presence of GNRs likely coupling differently to different edges of borophene. The possible reactions of borophene edges with radicals formed during GNR growth might be mitigated by first passivating borophene edges using covalent chemistry.

5.2.3. Research Directions Enabled by New Capabilities

Unlike application-driven research, fundamental studies of condensed matter systems rely heavily on instrumental capabilities. For example, moving from conventional semiconductors with nearly free electrons to strongly correlated materials, the strong correlations produce intriguing phenomena that reveal the important role of interactions. However, the bottleneck in fundamentally understanding strongly correlated electronic matter lies in the lack of experimental platforms that simultaneously provide complex artificial material synthesis and comprehensive structural and electronic characterizations. The recent rise of 2D quantum materials (e.g., 2D superconductors, ferromagnets, quantum spin Hall insulators) is partially made possible by advancements in characterization techniques (e.g., better resolutions, commercial availability, ease of use) in addition to increasingly powerful computational predictions, and the rising interest of the community in technologies enabled by unconventional materials (e.g., topological quantum computing). Including BP, TMDC monolayers, and borophene, more fundamental insights about their band structures and evolutions upon chemical functionalization could be readily probed via ARPES, which would be highly complementary to UHV STM/STS. Such technique is especially useful when the material in study enters the quantum mechanical regime (e.g., at low-temperature with phase transitions). Time-resolved ARPES further enables detection of transient states and carrier dynamics. Another example is experimental characterizations that would be enabled by the

premature yet highly versatile qPlus AFM technique. For example, the combination of MBE growth of pristine 2D materials with qPlus-based UHV KPFM and contact resonance AFM would uniquely reveal electronic and mechanical properties at the atomic level that are otherwise not accessible by other means. Integration of scanning probe methods with other in situ techniques such as charge transport measurements, ultra-fast optical spectroscopy, and magnetic characterization will provide unprecedented fundamental insights at the space-time limit under active and extreme conditions. The recent integration of UHV STM with magnetic spin resonance^{478,479} and radio-frequency excitation^{480,481} is helping advance the temporal resolution and chemical sensitivity of STM. Similarly, the combination of STM and Raman spectroscopy has enabled UHV tip-enhanced Raman spectroscopy as a tool to probe surface chemistry down to the single molecule limit.⁴⁸² Any of the above-mentioned instrumental developments would deepen the understanding of material properties and are thus highly rewarding.

Finally, the application of artificial intelligence to materials research⁴⁸³ is beginning to reshape the discovery of new materials including 2D systems. For example, several developments linking machine learning and data mining⁴⁸⁴ with scanning probe image recognition, analysis, and interpretation have been demonstrated.⁴⁸⁵⁻⁴⁹⁰ Machine learning assisted material discovery,⁴⁹¹ design,⁴⁹² and growth optimization^{493,494} are also gaining momentum. With the vast number of permutations for atomically thin materials and 2D heterostructures, this field is likely to continue its broad impact on fundamental science and applied technology for the foreseeable future.

References

1. Novoselov, K. S. *et al.* Electric field effect in atomically thin carbon films. *Science* **306**, 666–669 (2004).
2. Geim, A. K. & Novoselov, K. S. The rise of graphene. *Nat. Mater.* **6**, 183–191 (2007).
3. Mermin, N. D. & Wagner, H. Absence of ferromagnetism or antiferromagnetism in one- or two-dimensional isotropic Heisenberg models. *Phys. Rev. Lett.* **17**, 1133–1136 (1966).
4. Fradkin, E. Critical behavior of disordered degenerate semiconductors. II. Spectrum and transport properties in mean-field theory. *Phys. Rev. B* **33**, 3263–3268 (1986).
5. Mermin, N. D. Crystalline order in two dimensions. *Phys. Rev.* **176**, 250–254 (1968).
6. Peierls, R. Quelques Proprietes Typiques des Corps Solides. *Ann. I. H. Poincare* **5**, 177–222 (1935).
7. Jiapeng, C., Biao, W. & Yangfan, H. An existence criterion for low-dimensional materials. *J. Mech. Phys. Solids* **107**, 451–468 (2017).
8. Fasolino, A., Los, J. H. & Katsnelson, M. I. Intrinsic ripples in graphene. *Nat. Mater.* **6**, 858–861 (2007).
9. Brivio, J., Alexander, D. T. L. & Kis, A. Ripples and Layers in Ultrathin MoS₂ Membranes. *Nano Lett.* **11**, 5148–5153 (2011).
10. Xi, X. *et al.* Ising pairing in superconducting NbSe₂ atomic layers. *Nat. Phys.* **12**, 139–143 (2015).
11. Mannix, A. J. *et al.* Synthesis of borophenes: Anisotropic, two-dimensional boron polymorphs. *Science* **350**, 1513–1516 (2015).
12. Feng, B. *et al.* Experimental realization of two-dimensional boron sheets. *Nat. Chem.* **8**, 563–568 (2016).
13. Cukjati, D. *et al.* The surface and domain structure of NbTe₂. *J. Cryst. Growth* **237–239**, 278–282 (2002).
14. Nagata, S., Abe, T., Ebisu, S., Ishihara, Y. & Tsutsumi, K. Superconductivity in the metallic layered compound NbTe₂. *J. Phys. Chem. Solids* **54**, 895–899 (1993).
15. Reina, A. *et al.* Large area, few-layer graphene films on arbitrary substrates by chemical vapor deposition. *Nano Lett.* **9**, 30–35 (2009).
16. Emery, J. D. *et al.* Structural consequences of hydrogen intercalation of epitaxial graphene on SiC(0001). *Appl. Phys. Lett.* **105**, 161602 (2014).
17. Wood, J. D. *et al.* Effective Passivation of Exfoliated Black Phosphorus Transistors against Ambient Degradation. *Nano Lett.* **14**, 6964–6970 (2014).
18. Liu, X., Wood, J. D., Chen, K.-S., Cho, E. & Hersam, M. C. In Situ Thermal Decomposition of Exfoliated Two-Dimensional Black Phosphorus. *J. Phys. Chem. Lett.* **6**, 773–778 (2015).
19. Kang, J. *et al.* Solvent exfoliation of electronic-grade, two-dimensional black phosphorus. *ACS Nano* **9**, 3596–3604 (2015).

20. Ganatra, R. & Zhang, Q. Few-Layer MoS₂: A Promising Layered Semiconductor. *ACS Nano* **8**, 4074–4099 (2014).
21. Splendiani, A. *et al.* Emerging Photoluminescence in Monolayer MoS₂. *Nano Lett.* **10**, 1271–1275 (2010).
22. Song, L. *et al.* Large scale growth and characterization of atomic hexagonal boron nitride layers. *Nano Lett.* **10**, 3209–3215 (2010).
23. Zhang, H. *et al.* Topological insulators in Bi₂Se₃, Bi₂Te₃ and Sb₂Te₃ with a single Dirac cone on the surface. *Nat. Phys.* **5**, 438–442 (2009).
24. Liu, X. *et al.* Self-assembly of electronically abrupt borophene/organic lateral heterostructures. *Sci. Adv.* **3**, e1602356 (2017).
25. Feng, B. *et al.* Dirac Fermions in Borophene. *Phys. Rev. Lett.* **118**, 096401 (2017).
26. Tao, L. *et al.* Silicene field-effect transistors operating at room temperature. *Nat. Nanotechnol.* **10**, 227–231 (2015).
27. Mannix, A. J., Kiraly, B., Fisher, B. L., Hersam, M. C. & Guisinger, N. P. Silicon growth at the two-dimensional limit on Ag(111). *ACS Nano* **8**, 7538–7547 (2014).
28. Vogt, P. *et al.* Silicene: Compelling Experimental Evidence for Graphenelike Two-Dimensional Silicon. *Phys. Rev. Lett.* **108**, 155501–5 (2012).
29. Dávila, M. E., Xian, L., Cahangirov, S., Rubio, A. & Le Lay, G. Germanene: a novel two-dimensional germanium allotrope akin to graphene and silicene. *New J. Phys.* **16**, 095002 (2014).
30. Zhu, F.-F. *et al.* Epitaxial growth of two-dimensional stanene. *Nat. Mater.* **14**, 1020–1025 (2015).
31. Saxena, S., Chaudhary, R. P. & Shukla, S. Stanene: Atomically Thick Free-standing Layer of 2D Hexagonal Tin. *Sci. Rep.* **6**, 31073 (2016).
32. Li, L. *et al.* Direct observation of the layer-dependent electronic structure in phosphorene. *Nat. Nanotechnol.* **12**, 21–25 (2017).
33. Novoselov, K. S. *et al.* Two-dimensional gas of massless Dirac fermions in graphene. *Nature* **438**, 197–200 (2005).
34. Balushi, Al, Z. Y. *et al.* Two-dimensional gallium nitride realized via graphene encapsulation. *Nat. Mater.* **15**, 1166–1171 (2016).
35. Finnis, M. W. & Heine, V. Theory of lattice contraction at aluminium surfaces. *J. Phy. F Met. Phys.* **4**, L37–L41 (1974).
36. Finnis, M. W. The energy and elastic constants of simple metals in terms of pairwise interactions. *J. Phy. F Met. Phys.* **4**, 1645–1656 (1974).
37. Smoluchowski, R. Anisotropy of the Electronic Work Function of Metals. *Phys. Rev.* **60**, 661–674 (1941).
38. Davis, H. L., Hannon, J. B., Ray, K. B. & Plummer, E. W. Anomalous Interplanar Expansion at the (0001) Surface of Be. *Phys. Rev. Lett.* **68**, 2632–2635 (1992).
39. Adams, D. L., Nielsen, H. B. & Van Hove, M. A. Quantitative-Analysis of Low-Energy-Electron Diffraction - Application to Pt(111). *Phys. Rev. B* **20**, 4789–4806 (1979).
40. Xu, M. L. & Tong, S. Y. Multilayer relaxation for the clean Ni(110) surface. *Phys. Rev. B* **31**, 6332–6336 (1985).
41. Holub-Krappe, E., Horn, K., Frenken, J. W. M., Krans, R. L. & Van Der Veen, J. F. Multilayer relaxation at the Ag(110) surface. *Surf. Sci. Lett.* **188**, 335–349 (1987).

42. Frenken, J. W. M., Van Der Veen, J. F., Barnett, R. N., Landman, U. & Cleveland, C. L. Multilayer relaxation at the Pb(110) surface. *Surf. Sci.* **172**, 319–336 (1986).
43. Adams, D. L., Nielsen, H. B. & Andersen, J. N. Oscillatory relaxation of the Cu(110) surface. *Surf. Sci.* **128**, 294–310 (1983).
44. Bersuker, I. B. Manipulation of structure and properties of two-dimensional systems employing the pseudo Jahn-Teller effect. *FlatChem* **6**, 11–27 (2017).
45. Chowdhury, C., Jahiruddin, S. & Datta, A. Pseudo-Jahn-Teller Distortion in Two-Dimensional Phosphorus: Origin of Black and Blue Phases of Phosphorene and Band Gap Modulation by Molecular Charge Transfer. *J. Phys. Chem. Lett.* **7**, 1288–1297 (2016).
46. Jose, D. & Datta, A. Structures and chemical properties of silicene: unlike graphene. *Acc. Chem. Res.* **47**, 593–602 (2014).
47. Opik, U. & Pryce, M. H. L. Studies of the Jahn Teller Effect .1. a Survey of the Static Problem. *P. R. Soc.-Math. Phys. Sc.* **238**, 425–447 (1957).
48. Ivanov, A. S. *et al.* Pseudo Jahn–Teller Origin of Buckling Distortions in Two-Dimensional Triazine-Based Graphitic Carbon Nitride (g-C₃N₄) Sheets. *J. Phys. Chem. C* **119**, 12008–12015 (2015).
49. Thayer, G. E., Hannon, J. B. & Tromp, R. M. Shape and stability of self-assembled surface domains. *Nat. Mater.* **3**, 95–98 (2004).
50. Kodambaka, S., Khare, S. V., Petrov, I. & Greene, J. E. Two-dimensional island dynamics: Role of step energy anisotropy. *Surf. Sci. Rep.* **60**, 55–77 (2006).
51. Medhekar, N. V., Shenoy, V. B., Hannon, J. B. & Tromp, R. M. Metastability in 2D self-assembling systems. *Phys. Rev. Lett.* **99**, 156102 (2007).
52. Herring, C. Some Theorems on the Free Energies of Crystal Surfaces. *Phys. Rev.* **82**, 87–93 (1951).
53. Wang, L., Chen, F. & Ji, X. Shape consistency of MoS₂ flakes grown using chemical vapor deposition. *Appl. Phys. Express* **10**, 065201 (2017).
54. van der Zande, A. M. *et al.* Grains and grain boundaries in highly crystalline monolayer molybdenum disulphide. *Nat. Mater.* **12**, 554–561 (2013).
55. Jaramillo, T. F. *et al.* Identification of Active Edge Sites for Electrochemical H₂ Evolution from MoS₂ Nanocatalysts. *Science* **317**, 100–102 (2007).
56. Hinnemann, B. *et al.* Biomimetic Hydrogen Evolution: MoS₂ Nanoparticles as Catalyst for Hydrogen Evolution. *J. Am. Chem. Soc.* **127**, 5308 (2005).
57. Yang, L., Liu, P., Li, J. & Bin Xiang. Two-Dimensional Material Molybdenum Disulfides as Electrocatalysts for Hydrogen Evolution. *Catalysts* **7**, 285 (2017).
58. Sung, J. H. *et al.* Coplanar semiconductor-metal circuitry defined on few-layer MoTe₂ via polymorphic heteroepitaxy. *Nat. Nanotechnol.* **12**, 1064–1070 (2017).
59. Empante, T. A. *et al.* Chemical Vapor Deposition Growth of Few-Layer MoTe₂ in the 2H, 1T', and 1T Phases: Tunable Properties of MoTe₂ Films. *ACS Nano* **11**, 900–905 (2017).
60. Mannhar, J. & Herrnberger, A. The interface is still the device. *Nat. Mater.* **11**, 91 (2012).
61. Cao, Q. *et al.* End-bonded contacts for carbon nanotube transistors with low, size-independent resistance. *Science* **350**, 68–72 (2015).

62. Cao, Q., Tersoff, J., Farmer, D. B., Zhu, Y. & Han, S.-J. Carbon nanotube transistors scaled to a 40-nanometer footprint. *Science* **356**, 1369–1372 (2017).
63. Wang, L. *et al.* One-dimensional electrical contact to a two-dimensional material. *Science* **342**, 614–617 (2013).
64. Lee, M. L., Fitzgerald, E. A., Bulsara, M. T., Currie, M. T. & Lochtefeld, A. Strained Si, SiGe, and Ge channels for high-mobility metal-oxide-semiconductor field-effect transistors. *J. Appl. Phys.* **97**, 011101–28 (2005).
65. Kroemer, H. Quasi-electric fields and band offsets: teaching electrons new tricks (Nobel lecture). *ChemPhysChem* **2**, 490–499 (2001).
66. Koma, A. Van der Waals epitaxy for highly lattice-mismatched systems. *J. Cryst. Growth* **201/202**, 236–241 (1999).
67. Hong, X. *et al.* Ultrafast charge transfer in atomically thin MoS₂/WS₂ heterostructures. *Nat. Nanotechnol.* **9**, 682–686 (2014).
68. Zheng, Q. *et al.* Phonon-Assisted Ultrafast Charge Transfer at van der Waals Heterostructure Interface. *Nano Lett.* **17**, 6435–6442 (2017).
69. Zhang, J. *et al.* Interlayer-State-Coupling Dependent Ultrafast Charge Transfer in MoS₂/WS₂ Bilayers. *Adv. Sci.* **4**, 1700086 (2017).
70. Garcia-Basabe, Y. *et al.* Ultrafast charge transfer dynamics pathways in two-dimensional MoS₂-graphene heterostructures: a core-hole clock approach. *Phys. Chem. Chem. Phys.* **19**, 29954–29962 (2017).
71. Boulesbaa, A. *et al.* Ultrafast Charge Transfer and Hybrid Exciton Formation in 2D/0D Heterostructures. *J. Am. Chem. Soc.* **138**, 14713–14719 (2016).
72. Bettis Homan, S. *et al.* Ultrafast Exciton Dissociation and Long-Lived Charge Separation in a Photovoltaic Pentacene-MoS₂ van der Waals Heterojunction. *Nano Lett.* **17**, 164–169 (2017).
73. Uchihashi, T. Two-dimensional superconductors with atomic-scale thickness. *Supercond. Sci. Technol.* **30**, 013002 (2016).
74. Hsu, F.-C. *et al.* Superconductivity in the PbO-type structure alpha-FeSe. *Proc. Natl. Acad. Sci. USA* **105**, 14262–14264 (2008).
75. Ge, J.-F. *et al.* Superconductivity above 100 K in single-layer FeSe films on doped SrTiO₃. *Nat. Mater.* **14**, 285–289 (2015).
76. Lee, J. J. *et al.* Interfacial mode coupling as the origin of the enhancement of T(c) in FeSe films on SrTiO₃. *Nature* **515**, 245–248 (2014).
77. Wang, Q.-Y. *et al.* Interface-Induced High-Temperature Superconductivity in Single Unit-Cell FeSe Films on SrTiO₃. *Chinese Phys. Lett.* **29**, 037402 (2012).
78. Coh, S., Cohen, M. L. & Louie, S. G. Large electron–phonon interactions from FeSe phonons in a monolayer. *New J. Phys.* **17**, 073027 (2015).
79. Huang, B. *et al.* Layer-dependent ferromagnetism in a van der Waals crystal down to the monolayer limit. *Nature* **546**, 270–273 (2017).
80. Zhong, D. *et al.* Van der Waals engineering of ferromagnetic semiconductor heterostructures for spin and valleytronics. *Sci. Adv.* **3**, e1603113 (2017).
81. Gruenewald, J. H. *et al.* Engineering 1D Quantum Stripes from Superlattices of 2D Layered Materials. *Adv. Mater.* **29**, 1603798–6 (2016).
82. Nakagawa, N., Hwang, H. Y. & Muller, D. A. Why some interfaces cannot be sharp. *Nat. Mater.* **5**, 204–209 (2006).

83. Ohtomo, A. & Hwang, H. Y. A high-mobility electron gas at the LaAlO₃/SrTiO₃ heterointerface. *Nature* **427**, 423–426 (2004).
84. Thiel, S., Hammerl, G., Schmehl, A., Schneider, C. W. & Mannhar, J. Tunable quasi-two-dimensional electron gases in oxide heterostructures. *Science* **313**, 1942–1945 (2006).
85. Ron, A. *et al.* Solution Monolayer Epitaxy for Tunable Atomically Sharp Oxide Interfaces. *Adv. Mater. Interfaces* **4**, 1700688–6 (2017).
86. Gurman, S. J. Theory of surface states. *Surf. Sci.* **55**, 93–108 (1976).
87. Heine, V. Theory of Surface States. *Phys. Rev.* **138**, A1689–A1696 (1965).
88. Stęślicka, M. From Tamm to Shockley: An historical comment. *Pro. Sur. Sci.* **42**, 11–18 (1993).
89. Zhang, T. *et al.* Experimental demonstration of topological surface states protected by time-reversal symmetry. *Phys. Rev. Lett.* **103**, 266803 (2009).
90. Sarma, Das, S., Freedman, M. & Nayak, C. Majorana zero modes and topological quantum computation. *npj Quantum Inf.* **1**, 15001 (2015).
91. Dai, W. *et al.* Proximity-effect-induced Superconducting Gap in Topological Surface States – A Point Contact Spectroscopy Study of NbSe₂/Bi₂Se₃ Superconductor-Topological Insulator Heterostructures. *Sci. Rep.* **7**, 7631 (2017).
92. He, Q. L. *et al.* Two-dimensional superconductivity at the interface of a Bi₂Te₃/FeTe heterostructure. *Nat. Commun.* **5**, 4247 (2014).
93. Kang, J., Sangwan, V. K., Wood, J. D. & Hersam, M. C. Solution-Based Processing of Monodisperse Two-Dimensional Nanomaterials. *Acc. Chem. Res.* **50**, 943–951 (2017).
94. Mannix, A. J., Kiraly, B., Hersam, M. C. & Guisinger, N. P. Synthesis and chemistry of elemental 2D materials. *Nat. Rev. Chem.* **1**, 0014 (2017).
95. Shi, Y., Li, H. & Li, L.-J. Recent advances in controlled synthesis of two-dimensional transition metal dichalcogenides via vapour deposition techniques. *Chem. Soc. Rev.* **44**, 2744–2756 (2015).
96. Liu, H. Recent Progress in Atomic Layer Deposition of Multifunctional Oxides and Two-Dimensional Transition Metal Dichalcogenides. *J. Mol. Eng. Mater.* **04**, 1640010 (2016).
97. Wong, S. L., Liu, H. & Chi, D. Recent progress in chemical vapor deposition growth of two-dimensional transition metal dichalcogenides. *Prog. Cryst. Growth. Ch* **62**, 9–28 (2016).
98. Hart, L., Dale, S., Hoyer, S., Webb, J. L. & Wolverson, D. Rhenium Dichalcogenides: Layered Semiconductors with Two Vertical Orientations. *Nano Lett.* **16**, 1381–1386 (2016).
99. Liu, X., Ryder, C. R., Wells, S. A. & Hersam, M. C. Resolving the In-Plane Anisotropic Properties of Black Phosphorus. *Small Methods* **1**, 1700143 (2017).
100. Shulenburg, L., Baczewski, A. D., Zhu, Z., Guan, J. & Tomanek, D. The Nature of the Inter layer Interaction in Bulk and Few-Layer Phosphorus. *Nano Lett.* **15**, 8170–8175 (2015).
101. Björkman, T., Gulans, A., Krasheninnikov, A. V. & Nieminen, R. M. van der Waals bonding in layered compounds from advanced density-functional first-principles calculations. *Phys. Rev. Lett.* **108**, 235502 (2012).

102. Ugeda, M. M. *et al.* Characterization of collective ground states in single-layer NbSe₂. *Nat. Phys.* **12**, 92–97 (2016).
103. Magda, G. Z. *et al.* Exfoliation of large-area transition metal chalcogenide single layers. *Sci. Rep.* **5**, 14714 (2015).
104. Desai, S. B. *et al.* Gold-Mediated Exfoliation of Ultralarge Optoelectronically-Perfect Monolayers. *Adv. Mater.* **28**, 4053–4058 (2016).
105. Huang, Y. *et al.* Reliable Exfoliation of Large-Area High-Quality Flakes of Graphene and Other Two-Dimensional Materials. *ACS Nano* **9**, 10612–10620 (2015).
106. Koepke, J. C., Wood, J. D., Horvath, C. M., Lyding, J. W. & Barraza-Lopez, S. Preserving the 7×7 surface reconstruction of clean Si(111) by graphene adsorption. *Appl. Phys. Lett.* **107**, 071603 (2015).
107. Al-Sherbini, A.-S., Bakr, M., Ghoneim, I. & Saad, M. Exfoliation of graphene sheets via high energy wet milling of graphite in 2-ethylhexanol and kerosene. *J. Adv. Res.* **8**, 209–215 (2017).
108. Paton, K. R. *et al.* Scalable production of large quantities of defect-free few-layer graphene by shear exfoliation in liquids. *Nat. Mater.* **13**, 624–630 (2014).
109. Kang, J. *et al.* Stable aqueous dispersions of optically and electronically active phosphorene. *Proc. Natl. Acad. Sci. USA* **113**, 11688–11693 (2016).
110. Dines, M. B. Lithium intercalation via *n*-Butyllithium of the layered transition metal dichalcogenides. *Mater. Res. Bull.* **10**, 287–291 (1975).
111. Zeng, Z. *et al.* Single-Layer Semiconducting Nanosheets: High-Yield Preparation and Device Fabrication. *Angew. Chem.* **123**, 11289–11293 (2011).
112. Nicolosi, V., Chhowalla, M., Kanatzidis, M. G., Strano, M. S. & Coleman, J. N. Liquid Exfoliation of Layered Materials. *Science* **340**, 1226419–1226419 (2013).
113. Park, S. & Ruoff, R. S. Chemical methods for the production of graphenes. *Nat. Nanotechnol.* **5**, 309–309 (2010).
114. Huo, C., Yan, Z., Song, X. & Zeng, H. 2D materials via liquid exfoliation: a review on fabrication and applications. *Sci. Bull.* **60**, 1994–2008 (2015).
115. Sutter, P. W., Flege, J.-I. & Sutter, E. A. Epitaxial graphene on ruthenium. *Nat. Mater.* **7**, 406–411 (2008).
116. Peng, Z. *et al.* Toward the Synthesis of Wafer-Scale Single-Crystal Graphene on Copper Foils. *ACS Nano* **7**, 875–875 (2013).
117. Hao, Y. *et al.* The Role of Surface Oxygen in the Growth of Large Single-Crystal Graphene on Copper. *Science* **342**, 720–723 (2013).
118. Wu, T. *et al.* Fast growth of inch-sized single-crystalline graphene from a controlled single nucleus on Cu-Ni alloys. *Nat. Mater.* **15**, 43–47 (2016).
119. Xu, X. *et al.* Ultrafast epitaxial growth of metre-sized single-crystal graphene on industrial Cu foil. *Sci. Bull.* **62**, 1074–1080 (2017).
120. Chhowalla, M. *et al.* The chemistry of two-dimensional layered transition metal dichalcogenide nanosheets. *Nat. Chem.* **5**, 263–275 (2013).
121. Woehrl, N., Ochedowski, O., Gottlieb, S., Shibusaki, K. & Schulz, S. Plasma-enhanced chemical vapor deposition of graphene on copper substrates. *AIP Adv.* **4**, 047128 (2014).

122. Kang, K. *et al.* Layer-by-layer assembly of two-dimensional materials into wafer-scale heterostructures. *Nature* **550**, 229–233 (2017).
123. Kang, K. *et al.* High-mobility three-atom-thick semiconducting films with wafer-scale homogeneity. *Nature* **520**, 656–660 (2015).
124. Ling, X. *et al.* Role of the Seeding Promoter in MoS₂ Growth by Chemical Vapor Deposition. *Nano Lett.* **14**, 464–472 (2014).
125. Ling, X. *et al.* Parallel Stitching of 2D Materials. *Adv. Mater.* **28**, 2322–2329 (2016).
126. Alaboson, J. M. P. *et al.* Templating Sub-10 nm Atomic Layer Deposited Oxide Nanostructures on Graphene via One-Dimensional Organic Self-Assembled Monolayers. *Nano Lett.* **13**, 5763–5770 (2013).
127. Kim, H. G. & Leek, H.-B.-R. Atomic Layer Deposition on 2D Materials. *Chem. Mater.* **29**, 3809–3826 (2017).
128. Kim, Y. *et al.* Self-Limiting Layer Synthesis of Transition Metal Dichalcogenides. *Sci. Rep.* **6**, 183 (2016).
129. Jurca, T. *et al.* Low-Temperature Atomic Layer Deposition of MoS₂ Films. *Angew. Chem. Int. Ed.* **56**, 4991–4995 (2017).
130. Valdivia, A., Tweet, D. J. & Conley, J. F. Atomic layer deposition of two dimensional MoS₂ on 150 mm substrates. *J. Vac. Sci. Technol. A* **34**, 021515 (2016).
131. Pyeon, J. J. *et al.* Wafer-scale growth of MoS₂ thin films by atomic layer deposition. *Nanoscale* **8**, 10792–10798 (2016).
132. Liu, L., Huang, Y., Sha, J. & Chen, Y. Layer-controlled precise fabrication of ultrathin MoS₂ films by atomic layer deposition. *Nanotechnology* **28**, 195605 (2017).
133. Wang, K., Tai, G., Wong, K. H., Lau, S. P. & Guo, W. Ni induced few-layer graphene growth at low temperature by pulsed laser deposition. *AIP Adv.* **1**, 022141 (2011).
134. Glavin, N. R. *et al.* Synthesis of few-layer, large area hexagonal-boron nitride by pulsed laser deposition. *Thin Solid Films* **572**, 245–250 (2014).
135. Serna, M. I. *et al.* Large-Area Deposition of MoS₂ by Pulsed Laser Deposition With In Situ Thickness Control. *ACS Nano* **10**, 6054–6061 (2016).
136. Yang, Z. *et al.* Wafer-Scale Synthesis of High-Quality Semiconducting Two-Dimensional Layered InSe with Broadband Photoresponse. *ACS Nano* **11**, 4225–4236 (2017).
137. Yang, Z. *et al.* Field-Effect Transistors Based on Amorphous Black Phosphorus Ultrathin Films by Pulsed Laser Deposition. *Adv. Mater.* **27**, 3748–3754 (2015).
138. Yang, Z. & Hao, J. Progress in pulsed laser deposited two-dimensional layered materials for device applications. *J. Mater. Chem. C* **4**, 8859–8878 (2016).
139. Son, J. S. *et al.* Colloidal Synthesis of Ultrathin Two-Dimensional Semiconductor Nanocrystals. *Adv. Mater.* **23**, 3214–3219 (2011).
140. Lin, Z. *et al.* Scalable solution-phase epitaxial growth of symmetry-mismatched heterostructures on two-dimensional crystal soft template. *Sci. Adv.* **2**, e1600993 (2016).

141. Lv, L. *et al.* Generalized colloidal synthesis of high-quality, two-dimensional cesium lead halide perovskite nanosheets and their applications in photodetectors. *Nanoscale* **8**, 13589–13596 (2016).
142. Fei, F. *et al.* Solvothermal Synthesis of Lateral Heterojunction $\text{Sb}_2\text{Te}_3/\text{Bi}_2\text{Te}_3$ Nanoplates. *Nano Lett.* **15**, 5905–5911 (2015).
143. Plashnitsa, V. V. *et al.* Synthetic Strategy and Structural and Optical Characterization of Thin Highly Crystalline Titanium Disulfide Nanosheets. *J. Phys. Chem. Lett.* **3**, 1554–1558 (2012).
144. Peng, Y. Y. *et al.* Hydrothermal synthesis and characterization of single-molecular-layer MoS_2 and MoSe_2 . *Chem. Lett.* **30**, 772–773 (2001).
145. Altavilla, C., Sarno, M. & Ciambelli, P. A Novel Wet Chemistry Approach for the Synthesis of Hybrid 2D Free-Floating Single or Multilayer Nanosheets of $\text{MS}_2@$ oleylamine (M=Mo, W). *Chem. Mater.* **23**, 3879–3885 (2011).
146. Nasilowski, M., Mahler, B., Lhuillier, E., Ithurria, S. & Dubertret, B. Two-Dimensional Colloidal Nanocrystals. *Chem. Rev.* **116**, 10934–10982 (2016).
147. Yang, J., Son, J. S., Yu, J. H., Joo, J. & Hyeon, T. Advances in the Colloidal Synthesis of Two-Dimensional Semiconductor Nanoribbons. *Chem. Mater.* **25**, 1190–1198 (2013).
148. Wong, D. *et al.* Characterization and manipulation of individual defects in insulating hexagonal boron nitride using scanning tunnelling microscopy. *Nat. Nanotechnol.* **10**, 949–U192 (2015).
149. Liu, X. & Lu, Q. A piezo motor based on a new principle with high output force, rigidity and integrity: The Tuna Drive. *Rev. Sci. Instrum.* **83**, 115111–6 (2012).
150. Chen, C. J. *Introduction to Scanning Tunneling Microscopy*. 196–198 (Oxford University Press, 1993). doi:10.1093/acprof:oso/9780199211500.001.0001
151. Hoffman, J. E. Spectroscopic scanning tunneling microscopy insights into Fe-based superconductors. *Rep. Prog. Phys.* **74**, 124513–35 (2011).
152. Weiss, C., Wagner, C., Temirov, R. & Tautz, F. S. Direct Imaging of Intermolecular Bonds in Scanning Tunneling Microscopy. *J. Am. Chem. Soc.* **132**, 11864–11865 (2010).
153. Temirov, R., Soubatch, S., Neucheva, O., Lassise, A. C. & Tautz, F. S. A novel method achieving ultra-high geometrical resolution in scanning tunnelling microscopy. *New J. Phys.* **10**, 053012 (2008).
154. Hapala, P. *et al.* Mechanism of high-resolution STM/AFM imaging with functionalized tips. *Phys. Rev. B* **90**, 085421 (2014).
155. Chiang, C. L., Xu, C., Han, Z. & Ho, W. Real-space imaging of molecular structure and chemical bonding by single-molecule inelastic tunneling probe. *Science* **344**, 885–888 (2014).
156. Boneschanscher, M. P. *et al.* Quantitative Atomic Resolution Force Imaging on Epitaxial Graphene with Reactive and Nonreactive AFM Probes. *ACS Nano* **6**, 10216–10221 (2012).
157. Zhang, J. *et al.* Real-Space Identification of Intermolecular Bonding with Atomic Force Microscopy. *Science* **342**, 611–614 (2013).
158. Welker, J. & Giessibl, F. J. Revealing the Angular Symmetry of Chemical Bonds by Atomic Force Microscopy. *Science* **336**, 444–449 (2012).

159. Wu, R. J. *et al.* Atomic and electronic structure of exfoliated black phosphorus. *J. Vac. Sci. Technol. A* **33**, 060604–12 (2015).
160. Tersoff, J. & Hamann, D. R. Theory and Application for the Scanning Tunneling Microscope. *Phys. Rev. Lett.* **50**, 1998–2001 (1983).
161. Nguyen, G. D. *et al.* Atomically precise graphene nanoribbon heterojunctions from a single molecular precursor. *Nat. Nanotechnol.* **12**, 1077–1082 (2017).
162. Giessibl, F. J. High-speed force sensor for force microscopy and profilometry utilizing a quartz tuning fork. *Appl. Phys. Lett.* **73**, 3956–3958 (1998).
163. Torbruegge, S., Schaff, O. & Rychen, J. Application of the KolibriSensor to combined atomic-resolution scanning tunneling microscopy and noncontact atomic-force microscopy imaging. *J. Vac. Sci. Technol. B* **28**, C4E12–C4E20 (2010).
164. Giessibl, F. J. Advances in atomic force microscopy. *Rev. Mod. Phys.* **75**, 949–983 (2003).
165. Liu, X. *et al.* Rotationally Commensurate Growth of MoS₂ on Epitaxial Graphene. *ACS Nano* **10**, 1067–1075 (2016).
166. Gross, L., Mohn, F., Moll, N., Liljeroth, P. & Meyer, G. The Chemical Structure of a Molecule Resolved by Atomic Force Microscopy. *Science* **325**, 1110–1114 (2009).
167. Moll, N., Gross, L., Mohn, F., Curioni, A. & Meyer, G. The mechanisms underlying the enhanced resolution of atomic force microscopy with functionalized tips. *New J. Phys.* **12**, 125020 (2010).
168. Schneiderbauer, M., Emmrich, M., Weymouth, A. J. & Giessibl, F. J. CO tip functionalization inverts atomic force microscopy contrast via short-range electrostatic forces. *Phys. Rev. Lett.* **112**, 166102 (2014).
169. Guo, C.-S., Xin, X., Van Hove, M. A., Ren, X. & Zhao, Y. Origin of the Contrast Interpreted as Intermolecular and Intramolecular Bonds in Atomic Force Microscopy Images. *J. Phys. Chem. C* **119**, 14195–14200 (2015).
170. Labidi, H. *et al.* Indications of chemical bond contrast in AFM images of a hydrogen-terminated silicon surface. *Nat. Commun.* **8**, 14222 (2017).
171. Hämäläinen, S. K. *et al.* Intermolecular Contrast in Atomic Force Microscopy Images without Intermolecular Bonds. *Phys. Rev. Lett.* **113**, 186102 (2014).
172. Barja, S. *et al.* Charge density wave order in 1D mirror twin boundaries of single-layer MoSe₂. *Nat. Phys.* **12**, 751–756 (2016).
173. Albers, B. J. *et al.* Three-dimensional imaging of short-range chemical forces with picometre resolution. *Nat. Nanotechnol.* **4**, 307–310 (2009).
174. Holscher, H., Langkat, S. M., Schwarz, A. & Wiesendanger, R. Measurement of three-dimensional force fields with atomic resolution using dynamic force spectroscopy. *Appl. Phys. Lett.* **81**, 4428–4430 (2002).
175. Williams, D. B. & Carter, C. B. in *Transmission Electron Microscopy* 3–17 (Springer US, 1996). doi:10.1007/978-1-4757-2519-3_1
176. Zheng, X. *et al.* Robust ultra-low-friction state of graphene via moiré superlattice confinement. *Nat. Commun.* **7**, 13204 (2016).
177. Lee, C. *et al.* Frictional Characteristics of Atomically Thin Sheets. *Science* **328**, 76–80 (2010).

178. Liu, X.-Z. *et al.* Dynamics of atomic stick-slip friction examined with atomic force microscopy and atomistic simulations at overlapping speeds. *Phys. Rev. Lett.* **114**, 146102 (2015).
179. Gallagher, P. *et al.* Switchable friction enabled by nanoscale self-assembly on graphene. *Nat. Commun.* **7**, 10745 (2016).
180. Choi, J. S. *et al.* Friction Anisotropy-Driven Domain Imaging on Exfoliated Monolayer Graphene. *Science* **333**, 607–610 (2011).
181. Shastry, T. A. *et al.* Mutual Photoluminescence Quenching and Photovoltaic Effect in Large-Area Single-Layer MoS₂-Polymer Heterojunctions. *ACS Nano* **10**, 10573–10579 (2016).
182. Gomès, S., Assy, A. & Chapuis, P.-O. Scanning thermal microscopy: A review. *Phys. Status Solidi A* **212**, 477–494 (2015).
183. Majumdar, A. Scanning Thermal Microscopy. *Annu. Rev. Mater. Sci.* **29**, 505–585 (1999).
184. Menges, F., Riel, H., Stemmer, A. & Gotsmann, B. Quantitative thermometry of nanoscale hot spots. *Nano Lett.* **12**, 596–601 (2012).
185. Kim, K., Jeong, W., Lee, W. & Reddy, P. Ultra-high vacuum scanning thermal microscopy for nanometer resolution quantitative thermometry. *ACS Nano* **6**, 4248–4257 (2012).
186. Halbertal, D. *et al.* Nanoscale thermal imaging of dissipation in quantum systems. *Nat. Nanotechnol.* **539**, 407–410 (2016).
187. Lei, C. H., Das, A., Elliott, M. & Macdonald, J. E. Quantitative electrostatic force microscopy-phase measurements. *Nanotechnology* **15**, 627–634 (2004).
188. Burnett, T., Yakimova, R. & Kazakova, O. Mapping of Local Electrical Properties in Epitaxial Graphene Using Electrostatic Force Microscopy. *Nano Lett.* **11**, 2324–2328 (2011).
189. Datta, S. S., Strachan, D. R., Mele, E. J. & Johnson, A. T. C. Surface Potentials and Layer Charge Distributions in Few-Layer Graphene Films. *Nano Lett.* **9**, 7–11 (2009).
190. Jariwala, D. *et al.* Hybrid, Gate-Tunable, van der Waals p-n Heterojunctions from Pentacene and MoS₂. *Nano Lett.* **16**, 497–503 (2016).
191. Chen, K. *et al.* Electronic Properties of MoS₂-WS₂ Heterostructures Synthesized with Two-Step Lateral Epitaxial Strategy. *ACS Nano* **9**, 9868–9876 (2015).
192. Sangwan, V. K. *et al.* Gate-tunable memristive phenomena mediated by grain boundaries in single-layer MoS₂. *Nat. Nanotechnol.* **10**, 403–406 (2015).
193. Tosun, M. *et al.* MoS₂ Heterojunctions by Thickness Modulation. *Sci. Rep.* **5**, 10990 (2015).
194. Li, Y., Xu, C.-Y. & Zhen, L. Surface potential and interlayer screening effects of few-layer MoS₂ nanoflakes. *Appl. Phys. Lett.* **102**, 143110 (2013).
195. Sharma, I. & Mehta, B. R. Enhanced charge separation at 2D MoS₂/ZnS heterojunction: KPFM based study of interface photovoltage. *Appl. Phys. Lett.* **110**, 061602 (2017).
196. Li, M.-Y. *et al.* Epitaxial growth of a monolayer WSe₂-MoS₂ lateral p-n junction with an atomically sharp interface. *Science* **349**, 524–528 (2015).

197. Dumcenco, D. *et al.* Large-Area Epitaxial Monolayer MoS₂. *ACS Nano* **9**, 4611–4620 (2015).
198. Yoo, M. J. *et al.* Scanning single-electron transistor microscopy: Imaging individual charges. *Science* **276**, 579–582 (1997).
199. Martin, J. *et al.* Observation of electron–hole puddles in graphene using a scanning single-electron transistor. *Nat. Phys.* **4**, 144–148 (2007).
200. Li, H. *et al.* Investigation of MoS₂ and Graphene Nanosheets by Magnetic Force Microscopy. *ACS Nano* **7**, 2842–2849 (2013).
201. Li, L. H. & Chen, Y. Electric contributions to magnetic force microscopy response from graphene and MoS₂ nanosheets. *J. Appl. Phys.* **116**, 213904 (2014).
202. Neves, C. S. *et al.* New insights into the use of magnetic force microscopy to discriminate between magnetic and nonmagnetic nanoparticles. *Nanotechnology* **21**, 305706 (2010).
203. Alaboson, J. M. P. *et al.* Conductive Atomic Force Microscope Nanopatterning of Epitaxial Graphene on SiC(0001) in Ambient Conditions. *Adv. Mater.* **23**, 2181–2184 (2011).
204. Kellar, J. A., Alaboson, J. M. P., Wang, Q. H. & Hersam, M. C. Identifying and characterizing epitaxial graphene domains on partially graphitized SiC(0001) surfaces using scanning probe microscopy. *Appl. Phys. Lett.* **96**, 143103–4 (2010).
205. Kobayashi, Y. *et al.* Modulation of electrical potential and conductivity in an atomic-layer semiconductor heterojunction. *Sci. Rep.* **6**, 31223 (2017).
206. Leever, B. J. *et al.* Spatially resolved photocurrent mapping of operating organic photovoltaic devices using atomic force photovoltaic microscopy. *Appl. Phys. Lett.* **92**, 013302 (2008).
207. Hedley, G. J. *et al.* Determining the optimum morphology in high-performance polymer-fullerene organic photovoltaic cells. *Nat. Commun.* **4**, 2867 (2013).
208. Zhao, Z., Chen, X., Wu, H., Wu, X. & Cao, G. Probing the Photovoltage and Photocurrent in Perovskite Solar Cells with Nanoscale Resolution. *Adv. Funct. Mater.* **26**, 3048–3058 (2016).
209. Leblebici, S. Y. *et al.* Facet-dependent photovoltaic efficiency variations in single grains of hybrid halide perovskite. *Nat. Energy* **1**, 16093 (2016).
210. Son, Y. *et al.* Observation of Switchable Photoresponse of a Monolayer WSe₂-MoS₂ Lateral Heterostructure via Photocurrent Spectral Atomic Force Microscopic Imaging. *Nano Lett.* **16**, 3571–3577 (2016).
211. Sonde, S. *et al.* Electrical properties of the graphene/ 4H-SiC(0001) interface probed by scanning current spectroscopy. *Phys. Rev. B* **80**, 241406 (2009).
212. Fisichella, G., Greco, G., Roccaforte, F. & Giannazzo, F. Current transport in graphene/AlGaN/GaN vertical heterostructures probed at nanoscale. *Nanoscale* **6**, 8671–8680 (2014).
213. Lee, G.-H. *et al.* Electron tunneling through atomically flat and ultrathin hexagonal boron nitride. *Appl. Phys. Lett.* **99**, 243114 (2011).
214. Fu, D. *et al.* Mechanically modulated tunneling resistance in monolayer MoS₂. *Appl. Phys. Lett.* **103**, 183105 (2013).

215. Giannazzo, F., Fisichella, G., Piazza, A., Agnello, S. & Roccaforte, F. Nanoscale inhomogeneity of the Schottky barrier and resistivity in MoS₂ multilayers. *Phys. Rev. B* **92**, 081307 (2015).
216. Roy, T. *et al.* Dual-Gated MoS₂/WSe₂ van der Waals Tunnel Diodes and Transistors. *ACS Nano* **9**, 2071–2079 (2015).
217. Lin, Y.-C. *et al.* Atomically thin resonant tunnel diodes built from synthetic van der Waals heterostructures. *Nat. Commun.* **6**, 7311 (2015).
218. Britnell, L. *et al.* Resonant tunnelling and negative differential conductance in graphene transistors. *Nat. Commun.* **4**, 1794 (2013).
219. Bayram, C., Vashaei, Z. & Razeghi, M. AlN/GaN double-barrier resonant tunneling diodes grown by metal-organic chemical vapor deposition. *Appl. Phys. Lett.* **96**, 042103 (2010).
220. Shekhawat, G. S. & Dravid, V. P. Nanoscale imaging of buried structures via scanning near-field ultrasound holography. *Science* **310**, 89–92 (2005).
221. Shekhawat, G. S., Dudek, S. M. & Dravid, V. P. Development of ultrasound bioprobe for biological imaging. *Sci. Adv.* **3**, e1701176 (2017).
222. You, L., Ahn, J.-J., Obeng, Y. S. & Kopanski, J. J. Subsurface imaging of metal lines embedded in a dielectric with a scanning microwave microscope. *J. Phys. D* **49**, 045502 (2015).
223. Gramse, G. *et al.* Nondestructive imaging of atomically thin nanostructures buried in silicon. *Sci. Adv.* **3**, e1602586 (2017).
224. Dinelli, F., Pingue, P., Kay, N. D. & Kolosov, O. V. Subsurface imaging of two-dimensional materials at the nanoscale. *Nanotechnology* **28**, 085706 (2017).
225. Tu, Q. *et al.* Quantitative Subsurface Atomic Structure Fingerprint for 2D Materials and Heterostructures by First-Principles-Calibrated Contact-Resonance Atomic Force Microscopy. *ACS Nano* **10**, 6491–6500 (2016).
226. Soliman, M., Ding, Y. & Tetard, L. Nanoscale subsurface imaging. *J. Phys.: Condens. Matter* **29**, 173001 (2017).
227. Hsu, W.-T. *et al.* Second Harmonic Generation from Artificially Stacked Transition Metal Dichalcogenide Twisted Bilayers. *ACS Nano* **8**, 2951–2958 (2014).
228. Li, Y. *et al.* Probing Symmetry Properties of Few-Layer MoS₂ and h-BN by Optical Second-Harmonic Generation. *Nano Lett.* **13**, 3329–3333 (2013).
229. Youngblood, N., Peng, R., Nemilentsau, A., Low, T. & Li, M. Layer-Tunable Third-Harmonic Generation in Multilayer Black Phosphorus. *ACS Photonics* **4**, 8–14 (2017).
230. Autere, A. *et al.* Rapid and Large-Area Characterization of Exfoliated Black Phosphorus Using Third-Harmonic Generation Microscopy. *J. Phys. Chem. Lett.* **8**, 1343–1350 (2017).
231. Shi, J. *et al.* Cascaded exciton energy transfer in a monolayer semiconductor lateral heterostructure assisted by surface plasmon polariton. *Nat. Commun.* **8**, 35 (2017).
232. Ni, G. X. *et al.* Plasmons in graphene moiré superlattices. *Nat. Mater.* **14**, 1217–1222 (2015).
233. Liu, H. *et al.* High-harmonic generation from an atomically thin semiconductor. *Nat. Phys.* **13**, 262–265 (2017).

234. Fang, H. *et al.* Strong interlayer coupling in van der Waals heterostructures built from single-layer chalcogenides. *Proc. Natl. Acad. Sci. U.S.A.* **111**, 6198–6202 (2014).
235. Wilson, N. R. *et al.* Determination of band offsets, hybridization, and exciton binding in 2D semiconductor heterostructures. *Sci. Adv.* **3**, e1601832 (2017).
236. Yu, H., Wang, Y., Tong, Q., Xu, X. & Yao, W. Anomalous Light Cones and Valley Optical Selection Rules of Interlayer Excitons in Twisted Heterobilayers. *Phys. Rev. Lett.* **115**, 187002 (2015).
237. Nagler, P. *et al.* Interlayer exciton dynamics in a dichalcogenide monolayer heterostructure. *2D Mater.* **4**, 025112 (2017).
238. Rivera, P. *et al.* Observation of long-lived interlayer excitons in monolayer MoSe₂-WSe₂ heterostructures. *Nat. Commun.* **6**, 6242 (2015).
239. Ross, J. S. *et al.* Interlayer Exciton Optoelectronics in a 2D Heterostructure p-n Junction. *Nano Lett.* **17**, 638–643 (2017).
240. Kaplan, D. *et al.* Excitation intensity dependence of photoluminescence from monolayers of MoS₂ and WS₂/MoS₂ heterostructures. *2D Mater.* **3**, 015005 (2016).
241. Huo, N. *et al.* Interlayer coupling and optoelectronic properties of ultrathin two-dimensional heterostructures based on graphene, MoS₂ and WS₂. *J. Mater. Chem. C* **3**, 5467–5473 (2015).
242. Gong, Y. *et al.* Vertical and in-plane heterostructures from WS₂/MoS₂ monolayers. *Nat. Mater.* **13**, 1135–1142 (2014).
243. Kozawa, D. *et al.* Evidence for Fast Interlayer Energy Transfer in MoSe₂/WS₂ Heterostructures. *Nano Lett.* **16**, 4087–4093 (2016).
244. Sonntag, M. D., Pozzi, E. A., Jiang, N., Hersam, M. C. & Van Duyne, R. P. Recent Advances in Tip-Enhanced Raman Spectroscopy. *J. Phys. Chem. Lett.* **5**, 3125–3130 (2014).
245. Gerton, J. M., Wade, L. A., Lessard, G. A., Ma, Z. & Quake, S. R. Tip-enhanced fluorescence microscopy at 10 nanometer resolution. *Phys. Rev. Lett.* **93**, 180801 (2004).
246. Betzig, E., Lewis, A., Harootunian, A., Isaacson, M. & Kratschmer, E. Near Field Scanning Optical Microscopy (NSOM): Development and Biophysical Applications. *Biophys. J.* **49**, 269–279 (1986).
247. Wang, L. & Xu, X. G. Scattering-type scanning near-field optical microscopy with reconstruction of vertical interaction. *Nat. Commun.* **6**, 8973 (2015).
248. Wang, K. *et al.* Interlayer Coupling in Twisted WSe₂/WS₂ Bilayer Heterostructures Revealed by Optical Spectroscopy. *ACS Nano* **10**, 6612–6622 (2016).
249. Chen, H. *et al.* Ultrafast formation of interlayer hot excitons in atomically thin MoS₂/WS₂ heterostructures. *Nat. Commun.* **7**, 12512 (2016).
250. Ceballos, F., Bellus, M. Z., Chiu, H.-Y. & Zhao, H. Ultrafast Charge Separation and Indirect Exciton Formation in a MoS₂-MoSe₂ van der Waals Heterostructure. *ACS Nano* **8**, 12717–12724 (2014).
251. Butler, S. Z. *et al.* Progress, challenges, and opportunities in two-dimensional materials beyond graphene. *ACS Nano* **7**, 2898–2926 (2013).
252. Li, L. *et al.* Black phosphorus field-effect transistors. *Nat. Nanotechnol.* **9**, 372–377 (2014).

253. Xia, F., Wang, H. & Jia, Y. Rediscovering black phosphorus as an anisotropic layered material for optoelectronics and electronics. *Nat. Commun.* **5**, 4458–6 (2014).
254. Yuichi, A., Shoichi, E. & Shin-ichiro, N. Electrical Properties of Black Phosphorus Single Crystals. *J. Phys. Soc. Jpn.* **52**, 2148–2155 (2013).
255. Buscema, M. *et al.* Fast and Broadband Photoresponse of Few-Layer Black Phosphorus Field-Effect Transistors. *Nano Lett.* **14**, 3347–3352 (2014).
256. Tian, H. *et al.* Anisotropic Black Phosphorus Synaptic Device for Neuromorphic Applications. *Adv. Mater.* **28**, 4991–4997 (2016).
257. He, R. *et al.* Coupling and Stacking Order of ReS₂ Atomic Layers Revealed by Ultralow-Frequency Raman Spectroscopy. *Nano Lett.* **16**, 1404–1409 (2016).
258. Liu, X. *et al.* Scanning Probe Nanopatterning and Layer-by-Layer Thinning of Black Phosphorus. *Adv. Mater.* **29**, 1604121 (2017).
259. Lee, S. *et al.* Anisotropic in-plane thermal conductivity of black phosphorus nanoribbons at temperatures higher than 100 K. *Nat. Commun.* **6**, 8573 (2015).
260. Brown, A. & Rundqvist, S. Refinement of the crystal structure of black phosphorus. *Acta Cryst.* **19**, 684–685 (1965).
261. Du, Y. *et al.* Auxetic Black Phosphorus: A 2D Material with Negative Poisson's Ratio. *Nano Lett.* **16**, 6701–6708 (2016).
262. Jiang, J.-W. & Park, H. S. Negative poisson's ratio in single-layer black phosphorus. *Nat. Commun.* **5**, 1–7 (2014).
263. Liang, L. *et al.* Electronic Bandgap and Edge Reconstruction in Phosphorene Materials. *Nano Lett.* **14**, 6400–6406 (2014).
264. Zhang, C. D. *et al.* Surface Structures of Black Phosphorus Investigated with Scanning Tunneling Microscopy. *J. Phys. Chem. C* **113**, 18823–18826 (2009).
265. Qiao, J., Kong, X., Hu, Z.-X., Yang, F. & Ji, W. High-mobility transport anisotropy and linear dichroism in few-layer black phosphorus. *Nat. Commun.* **5**, 1–7 (2014).
266. Yuan, H. *et al.* Polarization-sensitive broadband photodetector using a black phosphorus vertical p–n junction. *Nat. Nanotechnol.* **10**, 707–713 (2015).
267. Wang, X. Highly anisotropic and robust excitons in monolayer black phosphorus. *Nat. Nanotechnol.* **10**, 517–521 (2015).
268. Ling, X. *et al.* Anisotropic Electron-Photon and Electron-Phonon Interactions in Black Phosphorus. *Nano Lett.* **16**, 2260–2267 (2016).
269. Mao, N. *et al.* Optical Anisotropy of Black Phosphorus in the Visible Regime. *J. Am. Chem. Soc.* **138**, 300–305 (2016).
270. Li, D. *et al.* Polarization and Thickness Dependent Absorption Properties of Black Phosphorus: New Saturable Absorber for Ultrafast Pulse Generation. *Sci. Rep.* **5**, 15899 (2015).
271. Tran, V., Soklaski, R., Liang, Y. & Yang, L. Layer-controlled band gap and anisotropic excitons in few-layer black phosphorus. *Phys. Rev. B* **89**, 235319 (2014).
272. Hong, T. *et al.* Polarized photocurrent response in black phosphorus field-effect transistors. *Nanoscale* **6**, 8978–6 (2014).
273. Wu, J., Mao, N., Xie, L., Xu, H. & Zhang, J. Identifying the crystalline orientation of black phosphorus using angle-resolved polarized Raman spectroscopy. *Angew. Chem. Int. Ed.* **54**, 2366–2369 (2015).

274. Ribeiro, H. B. *et al.* Unusual angular dependence of the Raman response in black phosphorus. *ACS Nano* **9**, 4270–4276 (2015).
275. Wang, Y. *et al.* Remarkable anisotropic phonon response in uniaxially strained few-layer black phosphorus. *Nano Res.* **8**, 3944–3953 (2015).
276. Zhang, S. *et al.* Extraordinary Photoluminescence and Strong Temperature/Angle-Dependent Raman Responses in Few-Layer Phosphorene. *ACS Nano* **8**, 9590–9596 (2014).
277. Ling, X. *et al.* Low-Frequency Interlayer Breathing Modes in Few-Layer Black Phosphorus. *Nano Lett.* **15**, 4080–4088 (2015).
278. Kim, J. *et al.* Anomalous polarization dependence of Raman scattering and crystallographic orientation of black phosphorus. *Nanoscale* **7**, 18708–18715 (2015).
279. Lu, W. *et al.* Probing the anisotropic behaviors of black phosphorus by transmission electron microscopy, angular-dependent Raman spectra, and electronic transport measurements. *Appl. Phys. Lett.* **107**, 021906 (2015).
280. Liu, H. *et al.* Phosphorene: An Unexplored 2D Semiconductor with a High Hole Mobility. *ACS Nano* **8**, 4033–4041 (2014).
281. Tao, J. *et al.* Mechanical and Electrical Anisotropy of Few-Layer Black Phosphorus. *ACS Nano* **9**, 11362–11370 (2015).
282. Kim, J. *et al.* Observation of tunable band gap and anisotropic Dirac semimetal state in black phosphorus. *Science* **349**, 723–726 (2015).
283. Fei, R. & Yang, L. Strain-engineering the anisotropic electrical conductance of few-layer black phosphorus. *Nano Lett.* **14**, 2884–2889 (2014).
284. Chaves, A., Low, T., Avouris, P., Çakır, D. & Peeters, F. M. Anisotropic exciton Stark shift in black phosphorus. *Phys. Rev. B* **91**, 155311–7 (2015).
285. Luo, Z. *et al.* Anisotropic in-plane thermal conductivity observed in few-layer black phosphorus. *Nat. Commun.* **6**, 8572 (2015).
286. Jang, H., Wood, J. D., Ryder, C. R., Hersam, M. C. & Cahill, D. G. Anisotropic Thermal Conductivity of Exfoliated Black Phosphorus. *Adv. Mater.* **27**, 8017–8022 (2015).
287. Wang, Z. *et al.* Resolving and Tuning Mechanical Anisotropy in Black Phosphorus via Nanomechanical Multimode Resonance Spectromicroscopy. *Nano Lett.* **16**, 5394–5400 (2016).
288. Fei, R. *et al.* Enhanced Thermoelectric Efficiency via Orthogonal Electrical and Thermal Conductances in Phosphorene. *Nano Lett.* **14**, 6393–6399 (2014).
289. Wang, Y. *et al.* Large anisotropic thermal transport properties observed in bulk single crystal black phosphorus. *Appl. Phys. Lett.* **108**, 092102 (2016).
290. Castellanos-Gomez, A. *et al.* Isolation and characterization of few-layer black phosphorus. *2D Mater.* **1**, 2, (2014).
291. Koenig, S. P., Doganov, R. A., Schmidt, H., Castro Neto, A. H. & Özyilmaz, B. Electric field effect in ultrathin black phosphorus. *Appl. Phys. Lett.* **104**, 103106–5 (2014).
292. Huang, J. Y., Ding, F., Yakobson, B. I., Lu, P., Qi, L., and Li, J., In situ observation of graphene sublimation and multi-layer edge reconstructions. *Proc. Natl. Acad. Sci. U.S.A.* **106**, 10103–10106 (2009).

293. Brazhkin, V. V., Zerr, A. Ju., Relative stability of red and black phosphorus at $P < 1$ GPa. *J. Mater. Sci.* **27**, 2677–2681 (1992).
294. Youngblood, N., Chen, C., Koester, S. J. & Li, M. Waveguide-integrated black phosphorus photodetector with high responsivity and low dark current. *Nat. Photonics* **9**, 247–252 (2015).
295. Huang, M. *et al.* Broadband Black-Phosphorus Photodetectors with High Responsivity. *Adv. Mater.* **28**, 3481–3485 (2016).
296. Viti, L. *et al.* Black Phosphorus Terahertz Photodetectors. *Adv. Mater.* **27**, 5567–5572 (2015).
297. Cui, S. *et al.* Ultrahigh sensitivity and layer-dependent sensing performance of phosphorene-based gas sensors. *Nat. Commun.* **6**, 8632 (2015).
298. Abbas, A. N. *et al.* Black Phosphorus Gas Sensors. *ACS Nano* **9**, 5618–5624 (2015).
299. Yasaei, P. *et al.* High-Quality Black Phosphorus Atomic Layers by Liquid-Phase Exfoliation. *Adv. Mater.* **27**, 1887–1892 (2015).
300. Liu, Y. *et al.* Layer-by-Layer Thinning of MoS₂ by Plasma. *ACS Nano* **7**, 4202–4209 (2013).
301. Tan, C. *et al.* Laser-assisted oxidation of multi-layer tungsten diselenide nanosheets. *Appl. Phys. Lett.* **108**, 083112 (2016).
302. Jia, J. *et al.* Plasma-Treated Thickness-Controlled Two-Dimensional Black Phosphorus and Its Electronic Transport Properties. *ACS Nano* **9**, 8729–8736 (2015).
303. Lu, J. *et al.* Bandgap Engineering of Phosphorene by Laser Oxidation toward Functional 2D Materials. *ACS Nano* **9**, 10411–10421 (2015).
304. Garcia, R., Knoll, A. W. & Riedo, E. Advanced scanning probe lithography. *Nat. Nanotechnol.* **9**, 577–587 (2014).
305. Crommie, M. F., Lutz, C. P. & Eigler, D. M. Confinement of Electrons to Quantum Corrals on a Metal-Surface. *Science* **262**, 218–220 (1993).
306. Avouris, P., Hertel, T. & Martel, R. Atomic force microscope tip-induced local oxidation of silicon: kinetics, mechanism, and nanofabrication. *Appl. Phys. Lett.* **71**, 285–4 (1997).
307. Howell, S. L. *et al.* Investigation of Band-Offsets at Monolayer–Multilayer MoS₂ Junctions by Scanning Photocurrent Microscopy. *Nano Lett.* **15**, 2278–2284 (2015).
308. Donarelli, M. *et al.* Few layered MoS₂ lithography with an AFM tip: description of the technique and nanospectroscopy investigations. *Nanoscale* **7**, 11453–11459 (2015).
309. Onodera, K. *et al.* Nucleosides and related substances. V. A synthetic procedure for nucleosides with the use of phosphorus pentoxide as dehydrating agent. *J. Org. Chem.* **31**, 1291–1292 (1966).
310. Detoni, S., Hadži, D. & Orel, B. Vibrational spectra of crystalline hypophosphorous acid. *J. Mol. Struct.* **33**, 279–288 (1976).
311. Lamrood, P. Y., Ralegankar, S. D. & Harpale, V. M. Applications of Raman Spectroscopy for Chemical Characterization and Protein Conformation of *Agaricus Bisporus* (Lange) Imbach. (*Agaricomycetidae*) Spores. *Int. J. Bioassays* **3**, 3318–3323 (2014).

312. Espinosa, F. M. *et al.* Direct fabrication of thin layer MoS₂ field-effect nanoscale transistors by oxidation scanning probe lithography. *Appl. Phys. Lett.* **106**, 103503–5 (2015).
313. Blake, P. *et al.* Making graphene visible. *Appl. Phys. Lett.* **91**, 063124–3 (2007).
314. Kim, J.-S. *et al.* Toward air-stable multilayer phosphorene thin-films and transistors. *Sci. Rep.* **5**, 8989 (2015).
315. Nagahama, T., Kobayashi, M., Akahama, Y., Endo, S. & Narita, S. Optical Determination of Dielectric-Constant in Black Phosphorus. *J. Phys. Soc. Jpn.* **54**, 2096–2099 (1985).
316. Favron, A. *et al.* Photooxidation and quantum confinement effects in exfoliated black phosphorus. *Nat. Mater.* **14**, 826–832 (2015).
317. Guo, H., Lu, N., Dai, J., Wu, X. & Zeng, X. C. Phosphorene Nanoribbons, Phosphorus Nanotubes, and van der Waals Multilayers. *J. Phys. Chem. C* **118**, 14051–14059 (2014).
318. Secor, E. B., Prabhumirashi, P. L., Puntambekar, K., Geier, M. L. & Hersam, M. C. Inkjet Printing of High Conductivity, Flexible Graphene Patterns. *J. Phys. Chem. Lett.* **4**, 1347–1351 (2013).
319. Xu, C., Wang, X. & Zhu, J. Graphene–Metal Particle Nanocomposites. *J. Phys. Chem. C* **112**, 19841–19845 (2008).
320. Jariwala, D., Sangwan, V. K., Lauhon, L. J., Marks, T. J. & Hersam, M. C. Emerging Device Applications for Semiconducting Two-Dimensional Transition Metal Dichalcogenides. *ACS Nano* **8**, 1102–1120 (2014).
321. Geim, A. K. & Grigorieva, I. V. Van der Waals heterostructures. *Nature* **499**, 419–425 (2013).
322. Ji, Q. *et al.* Epitaxial monolayer MoS₂ on mica with novel photoluminescence. *Nano Lett.* **13**, 3870–3877 (2013).
323. Jariwala, D. *et al.* Gate-tunable carbon nanotube-MoS₂ heterojunction p-n diode. *Proc. Natl. Acad. Sci. U.S.A.* **110**, 18076–18080 (2013).
324. Mak, K. F., Lee, C., Hone, J., Shan, J. & Heinz, T. F. Atomically Thin MoS₂: A New Direct-Gap Semiconductor. *Phys. Rev. Lett.* **105**, 136805 (2010).
325. Lopez-Sanchez, O., Lembke, D., Kayci, M., Radenovic, A. & Kis, A. Ultrasensitive photodetectors based on monolayer MoS₂. *Nat. Nanotechnol.* **8**, 497–501 (2013).
326. Zhang, W. *et al.* Ultrahigh-Gain Photodetectors Based on Atomically Thin Graphene-MoS₂ Heterostructures. *Sci. Rep.* **4**, 3826 (2014).
327. Mak, K. F., McGill, K. L., Park, J. & McEuen, P. L. The valley Hall effect in MoS₂ transistors. *Science* **344**, 1489–1492 (2014).
328. Zeng, H., Dai, J., Yao, W., Di Xiao & Cui, X. Valley polarization in MoS₂ monolayers by optical pumping. *Nat. Nanotechnol.* **7**, 490–493 (2012).
329. Jariwala, D., Marks, T. J. & Hersam, M. C. Mixed-dimensional van der Waals heterostructures. *Nat. Nanotechnol.* **16**, 170–181 (2017).
330. Sangwan, V. K. & Hersam, M. C. Electronic Transport in Two-Dimensional Materials. *Annu. Rev. Phys. Chem.* **69**, 299–325 (2018).
331. Zheng, Y. J. *et al.* Heterointerface Screening Effects between Organic Monolayers and Monolayer Transition Metal Dichalcogenides. *ACS Nano* **10**, 2476–2484 (2016).

332. Choi, J., Zhang, H. & Choi, J. H. Modulating Optoelectronic Properties of Two-Dimensional Transition Metal Dichalcogenide Semiconductors by Photoinduced Charge Transfer. *ACS Nano* **10**, 1671–1680 (2015).
333. Zang, H. *et al.* Nonradiative Energy Transfer from Individual CdSe/ZnS Quantum Dots to Single-Layer and Few-Layer Tin Disulfide. *ACS Nano* **10**, 4790–4796 (2016).
334. Li, P. *et al.* A mixed-dimensional light-emitting diode based on a p-MoS₂ nanosheet and an n-CdSe nanowire. *Nanoscale* **9**, 18175–18179 (2017).
335. Sangwan, V. K. *et al.* Quantitatively enhanced reliability and uniformity of high- κ dielectrics on graphene enabled by self-assembled seeding layers. *Nano Lett.* **13**, 1162–1167 (2013).
336. Hong Wang, F. L. W. F. Z. F. W. Z. Z. L. Two-dimensional heterostructures: fabrication, characterization, and application. *Nanoscale* **6**, 12250–12272 (2014).
337. Kang, J. *et al.* Thickness sorting of two-dimensional transition metal dichalcogenides via copolymer-assisted density gradient ultracentrifugation. *Nat. Commun.* **5**, 5478 (2014).
338. Zhang, C., Johnson, A., Hsu, C.-L., Li, L.-J. & Shih, C.-K. Direct imaging of band profile in single layer MoS₂ on graphite: quasiparticle energy gap, metallic edge states, and edge band bending. *Nano Lett.* **14**, 2443–2447 (2014).
339. Shi, Y. *et al.* van der Waals Epitaxy of MoS₂ Layers Using Graphene As Growth Templates. *Nano Lett.* **12**, 2784–2791 (2012).
340. Yu, L. *et al.* Graphene/MoS₂ hybrid technology for large-scale two-dimensional electronics. *Nano Lett.* **14**, 3055–3063 (2014).
341. Roy, K. *et al.* Graphene-MoS₂ hybrid structures for multifunctional photoresponsive memory devices. *Nat. Nanotechnol.* **8**, 826–830 (2013).
342. Li, Y. *et al.* MoS₂ Nanoparticles Grown on Graphene: An Advanced Catalyst for the Hydrogen Evolution Reaction. *J. Am. Chem. Soc.* **133**, 7296–7299 (2011).
343. Chang, K. & Chen, W. l-Cysteine-Assisted Synthesis of Layered MoS₂/Graphene Composites with Excellent Electrochemical Performances for Lithium Ion Batteries. *ACS Nano* **5**, 4720–4728 (2011).
344. Alaboson, J. M. P. *et al.* Seeding Atomic Layer Deposition of High- κ Dielectrics on Epitaxial Graphene with Organic Self-Assembled Monolayers. *ACS Nano* **5**, 5223–5232 (2011).
345. Karmel, H. J. *et al.* Self-assembled organic monolayers on epitaxial graphene with enhanced structural and thermal stability. *Chem. Commun.* **50**, 8852–8855 (2014).
346. Emtsev, K. V. *et al.* Towards wafer-size graphene layers by atmospheric pressure graphitization of silicon carbide. *Nat. Mater.* **8**, 203–207 (2009).
347. Çelebi, C., Yanık, C., Demirkol, A. G. & Kaya, İ. İ. The effect of a SiC cap on the growth of epitaxial graphene on SiC in ultra high vacuum. *Carbon* **50**, 3026–3031 (2012).
348. Norimatsu, W. & Kusunoki, M. Transitional structures of the interface between graphene and 6H-SiC (0001). *Chem. Phys. Lett.* **468**, 52–56 (2009).
349. Tanabe, S., Sekine, Y., Kageshima, H., Nagase, M. & Hibino, H. Carrier transport mechanism in graphene on SiC(0001). *Phys. Rev. B* **84**, 115458 (2011).

350. Jobst, J. *et al.* Quantum oscillations and quantum Hall effect in epitaxial graphene. *Phys. Rev. B* **81**, 195434 (2010).
351. Riedl, C., Coletti, C., Iwasaki, T., Zakharov, A. A. & Starke, U. Quasi-Free-Standing Epitaxial Graphene on SiC Obtained by Hydrogen Intercalation. *Phys. Rev. Lett.* **103**, 246804 (2009).
352. Fukidome, H. *et al.* Precise control of epitaxy of graphene by microfabricating SiC substrate. *Appl. Phys. Lett.* **101**, 041605 (2012).
353. Eriksson, J. *et al.* The influence of substrate morphology on thickness uniformity and unintentional doping of epitaxial graphene on SiC. *Appl. Phys. Lett.* **100**, 241607 (2012).
354. Ugeda, M. M. *et al.* Giant bandgap renormalization and excitonic effects in a monolayer transition metal dichalcogenide semiconductor. *Nat. Mater.* **13**, 1091–1095 (2014).
355. Zhang, Y. *et al.* Direct observation of the transition from indirect to direct bandgap in atomically thin epitaxial MoSe₂. *Nat. Nanotechnol.* **9**, 111–115 (2013).
356. Huang, Y. L. *et al.* Bandgap tunability at single-layer molybdenum disulphide grain boundaries. *Nat. Commun.* **6**, 6298 (2015).
357. Lu, C.-I. *et al.* Graphite edge controlled registration of monolayer MoS₂ crystal orientation. *Appl. Phys. Lett.* **106**, 181904 (2015).
358. Lin, Y.-C. *et al.* Direct Synthesis of van der Waals Solids. *ACS Nano* **8**, 3715–3723 (2014).
359. Miwa, J. A. *et al.* Van der Waals Epitaxy of Two-Dimensional MoS₂-Graphene Heterostructures in a Ultra-High Vacuum. *ACS Nano* **9**, 6502–6510 (2015).
360. Novoselov, K. S. *et al.* Two-dimensional atomic crystals. *Proc. Natl. Acad. Sci. USA* **102**, 10451–10453 (2005).
361. Enyashin, A. N., Bar-Sadan, M., Houben, L. & Seifert, G. Line Defects in Molybdenum Disulfide Layers. *J. Phys. Chem. C* **117**, 10842–10848 (2013).
362. Qiu, H. *et al.* Hopping transport through defect-induced localized states in molybdenum disulphide. *Nat. Commun.* **4**, 2642 (2013).
363. Qiu, H. *et al.* Electrical characterization of back-gated bi-layer MoS₂ field-effect transistors and the effect of ambient on their performances. *Appl. Phys. Lett.* **100**, 123104 (2012).
364. Park, W. *et al.* Oxygen environmental and passivation effects on molybdenum disulfide field effect transistors. *Nanotechnology* **24**, 095202 (2013).
365. Najmaei, S. Vapour phase growth and grain boundary structure of molybdenum disulphide atomic layers. *Nat. Mater.* **12**, 754–759 (2013).
366. Varrla, E. *et al.* Large-Scale Production of Size-Controlled MoS₂ Nanosheets by Shear Exfoliation. *Chem. Mater.* **27**, 1129–1139 (2015).
367. Lin, J., Pantelides, S. T. & Zhou, W. Vacancy-Induced Formation and Growth of Inversion Domains in Transition-Metal Dichalcogenide Monolayer. *ACS Nano* **9**, 5189–5197 (2015).
368. Hong, J. *et al.* Exploring atomic defects in molybdenum disulphide monolayers. *Nat. Commun.* **6**, 6293 (2015).
369. rkman, T. O. R. B. O. *et al.* Three-fold rotational defects in two-dimensional transition metal dichalcogenides. *Nat. Commun.* **6**, 6736 (2015).

370. Liu, Z. *et al.* Strain and structure heterogeneity in MoS₂ atomic layers grown by chemical vapour deposition. *Nat. Commun.* **5**, 5246 (2014).
371. Zhou, W. *et al.* Intrinsic Structural Defects in Monolayer Molybdenum Disulfide. *Nano Lett.* **13**, 2615–2622 (2013).
372. Robinson, J. A. Growing Vertical in the Flatland. *ACS Nano* **10**, 42–45 (2016).
373. Lee, C. *et al.* Anomalous Lattice Vibrations of Single- and Few-Layer MoS₂. *ACS Nano* **4**, 2695–2700 (2010).
374. Plechinger, G. *et al.* A direct comparison of CVD-grown and exfoliated MoS₂ using optical spectroscopy. *Semicond. Sci. Technol.* **29**, 064008 (2014).
375. Hiebel, F., Mallet, P., Magaud, L. & Veuille, J. Y. Atomic and electronic structure of monolayer graphene on 6H-SiC(0001)(3×3): A scanning tunneling microscopy study. *Phys. Rev. B* **80**, 235429 (2009).
376. Feng, J., Wagner, S. R. & Zhang, P. Interfacial Coupling and Electronic Structure of Two-Dimensional Silicon Grown on the Ag(111) Surface at High Temperature. *Sci. Rep.* **5**, 10310 (2015).
377. Koma, A. & Yoshimura, K. Ultrasharp interfaces grown with Van der Waals epitaxy. *Surf. Sci.* **174**, 556–560 (1986).
378. Peng, J.-P. *et al.* Molecular beam epitaxy growth and scanning tunneling microscopy study of TiSe₂ ultrathin films. *Phys. Rev. B* **91**, 121113–4 (2015).
379. Noh, J.-Y., Kim, H. & Kim, Y.-S. Stability and electronic structures of native defects in single-layer MoS₂. *Phys. Rev. B* **89**, 205417–12 (2014).
380. KC, S., Longo, R. C., Addou, R., Wallace, R. M. & Cho, K. Impact of intrinsic atomic defects on the electronic structure of MoS₂ monolayers. *Nanotechnology* **25**, 375703 (2014).
381. Addou, R., Colombo, L. & Wallace, R. M. Surface Defects on Natural MoS₂. *ACS Appl. Mater. Inter.* **7**, 11921–11929 (2015).
382. Hildebrand, B. *et al.* Doping Nature of Native Defects in 1T–TiSe₂. *Phys. Rev. Lett.* **112**, 197001–5 (2014).
383. Pehlke, E. & Schattke, W. The effect of frenkel defects on the electronic structure of 1T–TiSe₂. *Z. Physik B - Condensed Matter* **66**, 31–37 (1987).
384. González, C., Biel, B. & Dappe, Y. J. Theoretical characterisation of point defects on a MoS₂ monolayer by scanning tunnelling microscopy. *Nanotechnology* **27**, 105702 (2016).
385. Rong, Y. *et al.* Controlled Preferential Oxidation of Grain Boundaries in Monolayer Tungsten Disulfide for Direct Optical Imaging. *ACS Nano* **9**, 3695–3703 (2015).
386. Yin, X. *et al.* Edge nonlinear optics on a MoS₂ atomic monolayer. *Science* **344**, 488–490 (2014).
387. Cheng, J. *et al.* Kinetic Nature of Grain Boundary Formation in As-Grown MoS₂ Monolayers. *Adv. Mater.* **27**, 4069–4074 (2015).
388. Park, S. *et al.* Spectroscopic Visualization of Grain Boundaries of Monolayer Molybdenum Disulfide by Stacking Bilayers. *ACS Nano* **9**, 11042–11048 (2015).
389. Ji, Q. *et al.* Unravelling Orientation Distribution and Merging Behavior of Monolayer MoS₂ Domains on Sapphire. *Nano Lett.* **15**, 198–205 (2015).

390. Koepke, J. C. *et al.* Atomic-Scale Evidence for Potential Barriers and Strong Carrier Scattering at Graphene Grain Boundaries: A Scanning Tunneling Microscopy Study. *ACS Nano* **7**, 75–86 (2013).
391. Zou, X., Liu, Y. & Yakobson, B. I. Predicting Dislocations and Grain Boundaries in Two-Dimensional Metal-Disulfides from the First Principles. *Nano Lett.* **13**, 253–258 (2013).
392. Li, H. *et al.* Activating and optimizing MoS₂ basal planes for hydrogen evolution through the formation of strained sulphur vacancies. *Nat. Mater.* **15**, 48–53 (2016).
393. Kim, I. S. *et al.* Influence of stoichiometry on the optical and electrical properties of chemical vapor deposition derived MoS₂. *ACS Nano* **8**, 10551–10558 (2014).
394. Amani, M. *et al.* Near-unity photoluminescence quantum yield in MoS₂. *Science* **350**, 1065–1068 (2015).
395. Mouri, S., Miyauchi, Y. & Matsuda, K. Tunable photoluminescence of monolayer MoS₂ via chemical doping. *Nano Lett.* **13**, 5944–5948 (2013).
396. Liu, X. *et al.* Photoresponse of an Organic Semiconductor/Two-Dimensional Transition Metal Dichalcogenide Heterojunction. *Nano Lett.* **17**, 3176–3181 (2017).
397. Yuan, Y. *et al.* Ultra-high mobility transparent organic thin film transistors grown by an off-centre spin-coating method. *Nat. Commun.* **5**, 3005–9 (2014).
398. Minemawari, H. *et al.* Inkjet printing of single-crystal films. *Nature* **475**, 364–367 (2011).
399. Zhang, Y. *et al.* Probing Carrier Transport and Structure-Property Relationship of Highly Ordered Organic Semiconductors at the Two-Dimensional Limit. *Phys. Rev. Lett.* **116**, 016602 (2016).
400. Xu, R. *et al.* Unveiling the structural origin of the high carrier mobility of a molecular monolayer on boron nitride. *Phys. Rev. B* **90**, 224106 (2014).
401. He, D. *et al.* Two-dimensional quasi-freestanding molecular crystals for high-performance organic field-effect transistors. *Nat. Commun.* **5**, 5162 (2014).
402. Wu, B. *et al.* Precise, Self-Limited Epitaxy of Ultrathin Organic Semiconductors and Heterojunctions Tailored by van der Waals Interactions. *Nano Lett.* **16**, 3754–3759 (2016).
403. Liu, X., Balla, I., Bergeron, H. & Hersam, M. C. Point Defects and Grain Boundaries in Rotationally Commensurate MoS₂ on Epitaxial Graphene. *J. Phys. Chem. C* **120**, 20798–20805 (2016).
404. Withers, F. *et al.* Light-emitting diodes by band-structure engineering in van der Waals heterostructures. *Nat. Mater.* **14**, 301–306 (2015).
405. Furchi, M. M., Pospischil, A., Libisch, F., Burgdoerfer, J. & Mueller, T. Photovoltaic Effect in an Electrically Tunable van der Waals Heterojunction. *Nano Lett.* **14**, 4785–4791 (2014).
406. Lee, C.-H. *et al.* Atomically thin p-n junctions with van der Waals heterointerfaces. *Nat. Nanotechnol.* **9**, 676–681 (2014).
407. Ueno, K., Sasaki, K., Nakahara, T. & Koma, A. Fabrication of C₆₀ nanostructures by selective growth on GaSe/MoS₂ and InSe/MoS₂ heterostructure substrates. *Applied Surface Science* **130-132**, 670–675 (1998).
408. He, D. *et al.* A van der Waals pn heterojunction with organic/inorganic semiconductors. *Appl. Phys. Lett.* **107**, 183103 (2015).

409. Mao, J. *et al.* Tunability of Supramolecular Kagome Lattices of Magnetic Phthalocyanines Using Graphene-Based Moire Patterns as Templates. *J. Am. Chem. Soc.* **131**, 14136–14137 (2009).
410. Lin, X. *et al.* Intrinsically patterned two-dimensional materials for selective adsorption of molecules and nanoclusters. *Nat. Mater.* **16**, 717–721 (2017).
411. Coletti, C. *et al.* Charge neutrality and band-gap tuning of epitaxial graphene on SiC by molecular doping. *Phys. Rev. B* **81**, 235401 (2010).
412. Piazza, A. *et al.* Graphene p-Type Doping and Stability by Thermal Treatments in Molecular Oxygen Controlled Atmosphere. *J. Phys. Chem. C* **119**, 22718–22723 (2015).
413. Oganov, A. R. *et al.* Ionic high-pressure form of elemental boron. *Nature* **457**, 863–867 (2009).
414. Sergeeva, A. P. *et al.* Understanding Boron through Size-Selected Clusters: Structure, Chemical Bonding, and Fluxionality. *Acc. Chem. Res.* **47**, 1349–1358 (2014).
415. Tang, H. & Ismail-Beigi, S. Novel Precursors for Boron Nanotubes: The Competition of Two-Center and Three-Center Bonding in Boron Sheets. *Phys. Rev. Lett.* **99**, 115501 (2007).
416. Wu, X. *et al.* Two-dimensional boron monolayer sheets. *ACS Nano* **6**, 7443–7453 (2012).
417. Liu, Y., Penev, E. S. & Yakobson, B. I. Probing the Synthesis of Two-Dimensional Boron by First-Principles Computations. *Angew. Chem. Int. Ed.* **52**, 3156–3159 (2013).
418. Penev, E. S., Bhowmick, S., Sadrzadeh, A. & Yakobson, B. I. Polymorphism of Two-Dimensional Boron. *Nano Lett.* **12**, 2441–2445 (2012).
419. Zhang, Z., Yang, Y., Gao, G. & Yakobson, B. I. Two-Dimensional Boron Monolayers Mediated by Metal Substrates. *Angew. Chem. Int. Ed.* **54**, 13022–13026 (2015).
420. Tang, H. & Ismail-Beigi, S. Self-doping in boron sheets from first principles: A route to structural design of metal boride nanostructures. *Phys. Rev. B* **80**, 170 (2009).
421. Zhang, Z., Penev, E. S. & Yakobson, B. I. Two-dimensional materials: Polyphony in B flat. *Nat. Chem.* **8**, 525–527 (2016).
422. Zhang, Z. *et al.* Substrate-Induced Nanoscale Undulations of Borophene on Silver. *Nano Lett.* **16**, 6622–6627 (2016).
423. Tsafack, T. & Yakobson, B. I. Thermomechanical analysis of two-dimensional boron monolayers. *Phys. Rev. B* **93**, 165434 (2016).
424. Wang, H. *et al.* Strain effects on borophene: ideal strength, negative Poisson's ratio and phonon instability. *New J. Phys.* **18**, 073016 (2016).
425. Zhang, Z., Yang, Y., Penev, E. S. & Yakobson, B. I. Elasticity, Flexibility, and Ideal Strength of Borophenes. *Adv. Funct. Mater.* **27**, 1605059 (2017).
426. Penev, E. S., Kutana, A. & Yakobson, B. I. Can Two-Dimensional Boron Superconduct? *Nano Lett.* **16**, 2522–2526 (2016).
427. Liu, X., Zhang, Z., Wang, L., Yakobson, B. I. & Hersam, M. C. Intermixing and periodic self-assembly of borophene line defects. *Nat. Mater.* **17**, 783–788 (2018).

428. Huang, P. Y. *et al.* Grains and grain boundaries in single-layer graphene atomic patchwork quilts. *Nature* **469**, 389–392 (2011).
429. Zhao, L. *et al.* Visualizing individual nitrogen dopants in monolayer graphene. *Science* **333**, 999–1003 (2011).
430. Muzychenko, D. A., Schouteden, K., Panov, V. I. & Van Haesendonck, C. Formation of Co/Ge intermixing layers after Co deposition on Ge(111) 2×1 surfaces. *Nanotechnology* **23**, 435605 (2012).
431. Leibsle, F. M., Dhesi, S. S., Barrett, S. D. & Robinson, A. W. STM observations of Cu(100)- $c(2 \times 2)$ N surfaces: evidence for attractive interactions and an incommensurate $c(2 \times 2)$ structure. *Surf. Sci.* **317**, 309–320 (1994).
432. Xu, T. T. *et al.* Crystalline Boron Nanoribbons: Synthesis and Characterization. *Nano Lett.* **4**, 963–968 (2004).
433. Moras, P., Montes, T. O., Sheverdyeva, P. M., Locatelli, A. & Carbone, C. Coexistence of multiple silicene phases in silicon grown on Ag(111). *J. Phys.: Condens. Matter* **26**, 185001 (2014).
434. Feng, B. *et al.* Evidence of Silicene in Honeycomb Structures of Silicon on Ag(111). *Nano Lett.* **12**, 3507–3511 (2012).
435. Zhuang, J. *et al.* Investigation of electron-phonon coupling in epitaxial silicene by in situ Raman spectroscopy. *Phys. Rev. B* **91**, 161409 (2015).
436. Guan, J., Zhu, Z. & Tománek, D. High Stability of Faceted Nanotubes and Fullerenes of Multiphase Layered Phosphorus: A Computational Study. *Phys. Rev. Lett.* **113**, 226801 (2014).
437. Aierken, Y., Leenaerts, O. & Peeters, F. M. Defect-induced faceted blue phosphorene nanotubes. *Phys. Rev. B* **92**, 104104 (2015).
438. Xiang, P. *et al.* Metallic borophene polytypes as lightweight anode materials for non-lithium-ion batteries. *Phys. Chem. Chem. Phys.* **19**, 24945–24954 (2017).
439. Huang, Y., Shirodkar, S. N. & Yakobson, B. I. Two-Dimensional Boron Polymorphs for Visible Range Plasmonics: A First-Principles Exploration. *J. Am. Chem. Soc.* **139**, 17181–17185 (2017).
440. Luo, Z., Fan, X. & An, Y. First-Principles Study on the Stability and STM Image of Borophene. *Nanoscale Research Letters* **12**, 514 (2017).
441. Repp, J., Meyer, G., Stojković, S. M., Gourdon, A. & Joachim, C. Molecules on insulating films: scanning-tunneling microscopy imaging of individual molecular orbitals. *Phys. Rev. Lett.* **94**, 026803 (2005).
442. Martinez, J. I., Abad, E., González, C., Flores, F. & Ortega, J. Improvement of scanning tunneling microscopy resolution with H-sensitized tips. *Phys. Rev. Lett.* **108**, 246102 (2012).
443. Hapala, P. *et al.* Mapping the electrostatic force field of single molecules from high-resolution scanning probe images. *Nat. Commun.* **7**, 11560 (2016).
444. Moenig, H. *et al.* Submolecular Imaging by Noncontact Atomic Force Microscopy with an Oxygen Atom Rigidly Connected to a Metallic Probe. *ACS Nano* **10**, 1201–1209 (2016).
445. Mönig, H. *et al.* Quantitative assessment of intermolecular interactions by atomic force microscopy imaging using copper oxide tips. *Nat. Nanotechnol.* **13**, 371–375 (2018).

446. Han, Z. *et al.* Imaging the halogen bond in self-assembled halogenbenzenes on silver. *Science* **358**, 206–210 (2017).
447. la Torre, de, B. *et al.* Submolecular Resolution by Variation of the Inelastic Electron Tunneling Spectroscopy Amplitude and its Relation to the AFM/STM Signal. *Phys. Rev. Lett.* **119**, 166001 (2017).
448. Han, Z. *et al.* Probing Intermolecular Coupled Vibrations between Two Molecules. *Phys. Rev. Lett.* **118**, 036801 (2017).
449. Hapala, P., Temirov, R., Tautz, F. S. & Jelínek, P. Origin of High-Resolution IETS-STM Images of Organic Molecules with Functionalized Tips. *Phys. Rev. Lett.* **113**, 226101 (2014).
450. Liu, M. *et al.* Graphene-like nanoribbons periodically embedded with four- and eight-membered rings. *Nat. Commun.* **8**, 14924 (2017).
451. Herz, M., Giessibl, F. J. & Mannhar, J. Probing the shape of atoms in real space. *Phys. Rev. B* **68**, 045301 (2003).
452. Zhong, Q. *et al.* Metastable phases of 2D boron sheets on Ag(1 1 1). *J. Phys.: Condens. Matter* **29**, 095002 (2017).
453. Campbell, G. P. *et al.* Resolving the Chemically Discrete Structure of Synthetic Borophene Polymorphs. *Nano Lett.* **18**, 2816–2821 (2018).
454. Levendorf, M. P. *et al.* Graphene and boron nitride lateral heterostructures for atomically thin circuitry. *Nature* **488**, 627–632 (2017).
455. Duan, X. *et al.* Lateral epitaxial growth of two-dimensional layered semiconductor heterojunctions. *Nat. Nanotechnol.* **9**, 1024–1030 (2014).
456. Huang, C. *et al.* Lateral heterojunctions within monolayer MoSe₂-WSe₂ semiconductors. *Nat. Mater.* **13**, 1096–1101 (2014).
457. Kiraly, B., Mannix, A. J., Hersam, M. C. & Guisinger, N. P. Graphene-Silicon Heterostructures at the Two-Dimensional Limit. *Chem. Mater.* **27**, 6085–6090 (2015).
458. Park, J. *et al.* Spatially resolved one-dimensional boundary states in graphene-hexagonal boron nitride planar heterostructures. *Nat. Commun.* **5**, 5403 (2014).
459. Dhar, B. M. *et al.* Field-effect-tuned lateral organic diodes. *Proc. Natl. Acad. Sci. U.S.A.* **107**, 3972–3976 (2010).
460. Sutter, P., Cortes, R., Lahiri, J. & Sutter, E. Interface formation in monolayer graphene-boron nitride heterostructures. *Nano Lett.* **12**, 4869–4874 (2012).
461. Eremitchenko, M., Schaefer, J. A. & Tautz, F. S. Understanding and tuning the epitaxy of large aromatic adsorbates by molecular design. *Nature* **425**, 602–605 (2003).
462. Wang, Q. H. & Hersam, M. C. Room-temperature molecular-resolution characterization of self-assembled organic monolayers on epitaxial graphene. *Nat. Chem.* **1**, 206–211 (2009).
463. Zebari, A. A. A., Kolmer, M. & Prauzner-Bechcicki, J. S. Characterization of PTCDA nanocrystals on Ge(001):H-(2 × 1) surfaces. *App. Sur. Sci.* **332**, 403–408 (2015).
464. Tekiel, A., Godlewski, S., Budzioch, J. & Szymoński, M. Nanofabrication of PTCDA molecular chains on rutile TiO₂(011)-(2 × 1) surfaces. *Nanotechnology* **19**, 495304 (2008).

465. Burke, S. A. *et al.* Strain induced dewetting of a molecular system: bimodal growth of PTCDA on NaCl. *Phys. Rev. Lett.* **100**, 186104 (2008).
466. Kobayashi, S. *et al.* Control of carrier density by self-assembled monolayers in organic field-effect transistors. *Nat. Mater.* **3**, 317–322 (2004).
467. Temirov, R., Soubatch, S., Luican, A. & Tautz, F. S. Free-electron-like dispersion in an organic monolayer film on a metal substrate. *Nature* **444**, 350–353 (2006).
468. Liu, Y. *et al.* Van der Waals heterostructures and devices. *Nat. Rev. Mater.* **1**, 16042–17 (2016).
469. Liu, K. *et al.* Van der Waals-coupled electronic states in incommensurate double-walled carbon nanotubes. *Nat. Phys.* **10**, 737–742 (2014).
470. Orisaka, S., Minobe, T., Uchihashi, T., Sugawara, Y. & Morita, S. The atomic resolution imaging of metallic Ag(111) surface by noncontact atomic force microscope. *Applied Surface Science* **140**, 243–246 (1999).
471. Otero, R., Gallego, J. M., de Parga, A. L. V., Martín, N. & Miranda, R. Molecular Self-Assembly at Solid Surfaces. *Adv. Mater.* **23**, 5148–5176 (2011).
472. Rohlfing, M., Temirov, R. & Tautz, F. S. Adsorption structure and scanning tunneling data of a prototype organic-inorganic interface: PTCDA on Ag(111). *Phys. Rev. B* **76**, 115421 (2007).
473. Wüsten, J., Ertl, T., Lach, S. & Ziegler, C. Post deposition purification of PTCDA thin films. *Applied Surface Science* **252**, 104–107 (2005).
474. Tautz, F. S. *et al.* Strong electron-phonon coupling at a metal/organic interface: PTCDA/Ag(111). *Phys. Rev. B* **65**, 125405 (2002).
475. Kraft, A. *et al.* Lateral adsorption geometry and site-specific electronic structure of a large organic chemisorbate on a metal surface. *Phys. Rev. B* **74**, 041402 (2006).
476. Kim, K. *et al.* Structural and Electrical Investigation of C₆₀-Graphene Vertical Heterostructures. *ACS Nano* **9**, 5922–5928 (2015).
477. Ruchi Agrawal, Kumar, P. & Ghosh, S. Mechanism of Resistive Switching in 3, 4, 9, 10 Perylenetetracarboxylic Dianhydride (PTCDA) Sandwiched Between Metal Electrodes. *IEEE Trans. Electron Devices* **55**, 2795–2799 (2008).
478. Baumann, S. *et al.* Electron paramagnetic resonance of individual atoms on a surface. *Science* **350**, 417–420 (2015).
479. Thiele, S. *et al.* Electrically driven nuclear spin resonance in single-molecule magnets. *Science* **344**, 1135–1138 (2014).
480. Müllegger, S. *et al.* Radio frequency scanning tunneling spectroscopy for single-molecule spin resonance. *Phys. Rev. Lett.* **113**, 133001 (2014).
481. Kemiktarak, U., Ndukum, T., Schwab, K. C. & Ekinci, K. L. Radio-frequency scanning tunnelling microscopy. *Nature* **450**, 85–88 (2007).
482. Pozzi, E. A. *et al.* Ultrahigh-Vacuum Tip-Enhanced Raman Spectroscopy. *Chem. Rev.* **117**, 4961–4982 (2017).
483. Sacha, G. M. & Varona, P. Artificial intelligence in nanotechnology. *Nanotechnology* **24**, 452002 (2013).
484. Kalinin, S. V. *et al.* Big, Deep, and Smart Data in Scanning Probe Microscopy. *ACS Nano* **10**, 9068–9086 (2016).
485. Ziatdinov, M., Maksov, A. & Kalinin, S. V. Learning surface molecular structures via machine vision. *npj Comput. Mater.* **3**, 303 (2017).

486. Ziatdinov, M. *et al.* Data mining graphene: correlative analysis of structure and electronic degrees of freedom in graphenic monolayers with defects. *Nanotechnology* **27**, 495703 (2016).
487. Sacha, G. M., Rodriguez, F. B. & Varona, P. An inverse problem solution for undetermined electrostatic force microscopy setups using neural networks. *Nanotechnology* **20**, 085702 (2009).
488. Castellano-Hernandez, E. & Sacha, G. M. Ultrahigh dielectric constant of thin films obtained by electrostatic force microscopy and artificial neural networks. *Appl. Phys. Lett.* **100**, 023101 (2012).
489. Woolley, R. A. J., Stirling, J., Radocea, A., Krasnogor, N. & Moriarty, P. Automated probe microscopy via evolutionary optimization at the atomic scale. *Appl. Phys. Lett.* **98**, 253104–4 (2011).
490. Li, Q. *et al.* Quantification of flexoelectricity in PbTiO₃/SrTiO₃ superlattice polar vortices using machine learning and phase-field modeling. *Nat. Commun.* **8**, 2069 (2017).
491. Raccuglia, P. *et al.* Machine-learning-assisted materials discovery using failed experiments. *Nature* **533**, 73–76 (2016).
492. Liu, Y., Zhao, T., Ju, W. & Shi, S. Materials discovery and design using machine learning. *J. Materiomics* **3**, 159–177 (2017).
493. Nikolaev, P., Hooper, D., Perea-Lopez, N., Terrones, M. & Maruyama, B. Discovery of Wall-Selective Carbon Nanotube Growth Conditions via Automated Experimentation. *ACS Nano* **8**, 10214–10222 (2014).
494. Nikolaev, P. *et al.* Autonomy in materials research: a case study in carbon nanotube growth. *npj Comput. Mater.* **2**, 6295 (2016).

Vita

Xiaolong Liu (刘晓龙)

Email: xiaolongliu2013@u.northwestern.edu

Address: 2220 Campus Drive, Cook Hall Room 1059, Evanston, IL 60208

Education

2013-2018 **Ph.D.** in Applied Physics, **Northwestern University** (NU)

2009-2013 **B.S.** in Applied Physics, **University of Science and Technology of China** (USTC)

Research

2013-2018 *Graduate Research Assistant*, Advisor: **Prof. Mark C. Hersam**, NU

- Ultra-high vacuum scanning tunneling microscopy and atomic force microscopy of emerging 2D electronic nanomaterials and heterostructures.

2012-2013 *Undergraduate Research Assistant*, Advisor: **Prof. Jiangfeng Du**, USTC

- Design of microwave resonators for electron paramagnetic resonance.

2012-2013 *Undergraduate Research Assistant*, Advisor: **Prof. Qingyou Lu**, USTC

- Design of high-precision piezoelectric motors for scanning probe microscopy.

Honors and Awards

2019- Kavli Institute Postdoctoral Fellowship, Cornell University

2018 Graduate Student Silver Award, MRS

2018 Chinese Government Award for Outstanding Self-Financed Students Abroad

2017 Dorothy M. and Earl S. Hoffman Award, AVS

2017 Nanometer-Scale Science and Technology Division Student Award, AVS

2017 Cabell Terminal Year Fellowship, NU

2017 Ovshinsky Travel Grant Award, APS

2016 Ryan Fellowship, NU

2016 NNI EnvisioNano Contest, finalist

2016 Certified LabVIEW Associate Developer, National Instruments

2015 Honorable Mention, Science in Society Image Contest 2015

2012 2nd Prize, National Competition of Physics Experiment for College Students

2012 2nd Prize, Animal and Plant Specimen Contest

2012 2nd Prize, Challenge Cup National Science and Technology Innovation Contest

2012 China Construction Bank Elite Scholarship

2012 University-Level Excellence, Research Project for Undergraduates

2012 Honorable Mention, International Mathematical Contest in Modeling, COMAP

2011 1st Prize, 7th Competition of Physical Research (team leader, No.1 of 200+ teams)

2011 & 2010 Outstanding Student Scholarship

2010 Top 16, RoboGame 2010 Robot Competition (team leader)

2010 1st Prize, Science and Technology Innovation Contest (No.1 of 30+ students)

2009 Outstanding Freshman Scholarship

2008 1st Prize, National Physics Olympiad

Professional Service & Outreach

- 2016- Journal referee of *ACS Nano*, *2D Mater.*, *J. Phys. Chem.*, *J. Appl. Phys.*, *J. Vac. Sci. Technol.*, *J. Phys. D: Appl. Phys.*, *Mater. Res. Express*, *Surf. Topogr.*
- 2017 Session Chair, American Physical Society March Meeting 2017 (*session P30: Transition Metal Dichalcogenides: Optical Properties*)
- 2017 Volunteer at Chicago City of Learning - Back to School Jam
- 2015 Judge of Chicago Public Schools Annual Science Fair, Goudy Elementary School
- 2015 Exhibitor at Scientific Image Exhibition at Evanston Township High School
- 2015 Student Volunteer of NU Booth at Google Geek Street Fest, Chicago
- 2014 Scholar, PreScouter Global Scholars Program
- 2011 Volunteer at Hefei Special Education Center to help students with disabilities, Hefei
- 2011 Volunteer as an illustrator at Science and Technology Hall of Hefei, Hefei
- 2009 Member of Publicity Department of Students' Union, USTC

Professional Society Memberships

American Vacuum Society (AVS), American Physical Society (APS), Materials Research Society (MRS)

Teaching

- 2016 - 2018 Mentor of an M.S. and 2 Ph.D. students in Materials Science and Engineering
- 2016 Mat. Sci. 451: Advanced Physics of Materials, teaching assistant
- 2016 Mat. Sci. 396-1, mentor of undergraduate senior project

Publications

(Google Scholar: <https://scholar.google.com/citations?user=WzbeYkAAAAAJ&hl=en>)

- [27] **X. Liu**, and M. C. Hersam, Interface Characterization and Control of 2D Materials and Heterostructures, *Advanced Materials*, **2018**, DOI: 10.1002/adma.201801586.
- [26] **X. Liu**, Z. Zhang, L. Wang, B. I. Yakobson, and M. C. Hersam, Intermixing and Periodic Self-Assembly of Borophene Line Defects, *Nature Materials* **2018**, *17*, 783–788
- [25] J. Kang, S. A. Wells, V. K. Sangwan, D. Lam, **X. Liu**, Z. Sofer, J. Luxa, and M. C. Hersam, Solution-Based Processing of Optoelectronically Active Indium Selenide, *Advanced Materials* **2018**, DOI: 10.1002/adma.201802990.
- [24] Q. Li, Y. Xu, Z. Yao, J. Kang, **X. Liu**, C. Wolverton, M. C. Hersam, J. Wu, and V. P. Dravid, Revealing the Effects of Electrode Crystallographic Orientation on Battery Electrochemistry via the Anisotropic Lithiation and Sodiation of ReS₂, *ACS Nano* **2018**, *12*, 7875-7882.
- [23] C. Sun, M. Shen, A. D. Chavez, A. M. Evans, **X. Liu**, B. Harutyunyan, N. C. Flanders, M. C. Hersam, M. J. Bedzyk, M. O. de la Cruz, and W. R. Dichtel, High Aspect Ratio Nanotubes Assembled from Macrocyclic Iminium Salts, *Proceedings of the National Academy of Sciences of the United States of America* **2018**, DOI: 10.1073/pnas.1809383115
- [22] D. Lam, K.-S. Chen, J. Kang, **X. Liu**, and M. C. Hersam, Anhydrous Liquid-Phase Exfoliation of Pristine Electrochemically-Active GeS Nanosheets, *Chem. Mater.* **2018**, *30*, 2245-2250.
- [21] Y.-L. Wu, N. S. Bobbitt, J. Logsdon, N. Powers-Riggs, J. Nelson, **X. Liu**, T. Wang, R. Snurr, J. Hupp, O. Farha, M. C. Hersam, and M. R. Wasielewski, Tunable Crystallinity and Charge

- Transfer in 2-Dimensional G-Quadruplex Organic Frameworks, *Angew. Chem. Int. Ed.* **2018**, *57*, 3985-3989.
- [20] **X. Liu***, C. R. Ryder*, S. A. Wells, and M. C. Hersam, Resolving the In-Plane Anisotropic Properties of Black Phosphorus, *Small Methods* **2017**, *1*, 1700143.
- [19] **X. Liu**, Z. Wei, I. Balla, A. J. Mannix, N. P. Guisinger, E. Luijten, and M. C. Hersam, Self-Assembly of Electronically Abrupt Borophene/Organic Lateral Heterostructures, *Science Advances* **2017**, *3*, e1602356.
- [18] **X. Liu**, K.-S. Chen, S. A. Wells, I. Balla, J. Zhu, J. D. Wood, and M. C. Hersam, Scanning Probe Nanopatterning and Layer-by-Layer Thinning of Black Phosphorus, *Advanced Materials* **2017**, *29*, 1604121.
- [17] H. Bergeron, V. K. Sangwan, J. J. McMorow, G. P. Campbell, I. Balla, **X. Liu**, M. J. Bedzyk, T. J. Marks, and M. C. Hersam, Chemical Vapor Deposition of Monolayer MoS₂ Directly on Ultrathin Al₂O₃ for Low-Power Electronics, *Applied Physics Letters* **2017**, *110*, 053101.
- [16] **X. Liu**, I. Balla, H. Bergeron, and M. C. Hersam, Point Defects and Grain Boundaries in Rotationally Commensurate MoS₂ on Epitaxial Graphene, *Journal of Physical Chemistry C* **2016**, *120*, 20798-20805.
- [15] **X. Liu***, I. Balla*, H. Bergeron, G. P. Campbell, M. J. Bedzyk, and M. C. Hersam, Rotationally Commensurate Growth of MoS₂ on Epitaxial Graphene, *ACS Nano* **2016**, *10*, 1067-1075.
- [14] P.-C. Chen, **X. Liu**, J. L. Hedrick, Z. Xie, S. Wang, Q.-Y. Lin, M. C. Hersam, V. P. Dravid, and C. A. Mirkin, Polyelemental Nanoparticle Libraries, *Science* **2016**, *352*, 1565-1569.
- [13] J. Kang, V. Sangwan, J. D. Wood, **X. Liu**, I. Balla, D. Lam, and M. C. Hersam, Layer-by-Layer Sorting of Rhenium Disulfide via High-Density Isopycnic Density Gradient Ultracentrifugation, *Nano Letters* **2016**, *16*, 7216-7223.
- [12] L. Li, E. B. Secor, K.-S. Chen, J. Zhu, **X. Liu**, T. Z. Gao, J.-W. T. Seo, Y. Zhao, and M. C. Hersam, High-Performance Solid-State Supercapacitors and Microsupercapacitors Derived from Printable Graphene Inks, *Advanced Energy Materials* **2016**, *6*, 1600909.
- [11] J. Kang, S. A. Wells, J. D. Wood, J.-H. Lee, **X. Liu**, C. R. Ryder, J. Zhu, J. R. Guest, C. A. Husko, and M. C. Hersam, Stable Aqueous Dispersions of Optically and Electronically Active Phosphorene, *Proceedings of the National Academy of Sciences* **2016**, *113*, 11688-11693.
- [10] **X. Liu***, J. D. Wood*, K.-S. Chen, E. Cho, and M. C. Hersam, In Situ Thermal Decomposition of Exfoliated Two-Dimensional Black Phosphorus, *Journal of Physical Chemistry Letters* **2015**, *6*, 773-778.
- [9] J. Zhu, **X. Liu**, M. L. Geier, J. J. McMorow, D. Jariwala, M. E. Beck, W. Huang, T. J. Marks, and M. C. Hersam, Layer-by-Layer Assembled 2D Montmorillonite Dielectrics for Solution-Processed Electronics, *Advanced Materials* **2015**, *28*, 63-68.
- [8] A. J. Mannix, X.-F. Zhou, B. Kiraly, J. D. Wood, D. Alducin, B. D Myers, **X. Liu**, B. L. Fisher, U. Santiago, J. R. Guest, M. J. Yacaman, A. Ponce, A. R. Oganov, M. C. Hersam, and N. P. Guisinger, Synthesis of Borophenes: Anisotropic, Two-Dimensional Boron Polymorphs, *Science* **2015**, *350*, 1513-1516.
- [7] J. Kang, J. D. Wood, S. A. Wells, J.-H. Lee, **X. Liu**, K.-S. Chen, and M. C. Hersam, Solvent Exfoliation of Electronic-Grade, Two-Dimensional Black Phosphorus, *ACS Nano* **2015**, *9*, 3596-3604.

- [6] J. D. Wood*, S. A. Wells*, D. Jariwala, K.-S. Chen, E. Cho, V. K. Sangwan, **X. Liu**, L. J. Lauhon, T. J. Marks, and M. C. Hersam, Effective Passivation of Exfoliated Black Phosphorus Transistors against Ambient Degradation, *Nano Letters* **2014**, *14*, 6964-6970.
- [5] Q. Lu, and **X. Liu**, Double-End Clamping Piezoelectric Motor Utilizing Opposite-direction Rubs to Reduce Friction Force and Control Method, *Chinese Invention Patent* 201210338648.0.
- [4] Z. Wang, J. Du, **X. Liu**, Z. Wei, and X. Rong, Dual-Mode Polarization Cavity with Adjustable Coupling Hole, *Chinese Invention Patent* 201310283144.8.
- [3] M. C. Hersam, and **X. Liu**, Electronically Abrupt Borophene/Organic Lateral Heterostructures and Preparation Thereof, US Patent App. 15892124.
- [2] **X. Liu**, and Q. Lu, A Piezo Motor Based on a New Principle with High Output Force, Rigidity and Integrity: The Tuna Drive, *Review of Scientific Instruments* **2012**, *83*, 115111.
- [1] **X. Liu**, Z. Wei, C. Feng, Y. Duan, Z. Wang, and Z. Zhang, Preparation and Characterization of Magnetic Fluid, *Physics Experimentation* **2012**, *32*, 8.

Manuscripts in revision/preparation:

- [36] B. Kiraly*, **X. Liu***, Z. Zhang, A. J. Mannix, B. L. Fisher, B. I. Yakobson, and M. C. Hersam, and N. P. Guisinger, Nanoscale Templated Borophene Synthesis on Au(111), in revision.
- [35] **X. Liu**, L. Wang, S. Li, M. S. Rahn, B. I. Yakobson, and M. C. Hersam, Resolving atomic lattice structures of borophene polymorphs with functionalized probes, in preparation
- [34] **X. Liu**, V. K. Sangwan, I. Balla, C. Zhong, H. Bergeron, E. A. Weiss, and M. C. Hersam, Mixed-Dimensional Heterostructures of MoS₂ with C8-BTBT on Gra-phene with Well-Ordered Interfaces, in preparation.
- [33] **X. Liu**, L. Wang, I. Balla, H. Bergeron, B. I. Yakobson, and M. C. Hersam, Parallel Line Defects and Migrations in Anisotropic ReS₂/Graphene Vertical Heterostructures, in preparation.
- [32] J. Kang, V. K. Sangwan, H.-Sub. Lee, **X. Liu**, and M. C. Hersam, High-Performance Photodetectors from Solution-Processed Heavily-Doped 2D Gallium Telluride, in revision.
- [31] V. K. Sangwan*, J. Kang*, H.-S. Lee, D. Lam, **X. Liu**, and M. C. Hersam, Solution-Processed Two-Dimensional Semiconductor Thermally Activated Memristors, submitted.
- [30] J. Kang, I. Balla, **X. Liu**, H. Bergeron, S. Kim, C. Wolverton, and M. C. Hersam, Efficient Transfer of Rotationally Commensurate MoS₂ from van der Waals Heterostructure, submitted.
- [29] L. Li, S. Kim, J. Zhu, K.-S. Chen, L. M. Guiney, **X. Liu**, Z. Wang, C. Wolverton, and M. C. Hersam, Toward a Quantitative Understanding of Graphene in Improving Electrochemical Performance of Spinel LiMn₂O₄ Cathodes, in preparation.
- [28] I. Balla, K.-S. Chen, G. P. Campbell, **X. Liu**, M. J. Bedzyk, and M. C. Hersam, Mixed-Dimensional Heterostructure Facilitated by Hierarchical Self-Assembly, in preparation.

*These authors contributed equally to this work.

Oral Presentations and Posters

- 2018 “*Surface and Interface Engineering of van der Waals Nanoelectronic Heterostructures (2018)*”, Office of Naval Research Program Review, UC Berkeley (Poster)
- 2018 “*Surface and Interface Engineering of Borophene*”, 78th Physical Electronics Conference (Oral)

- 2018 “*Atomic-Scale Characterization of Line Defects in Borophene via Ultra-High Vacuum Scanning Tunneling Microscopy and Density Functional Theory*”, Materials Research Society 2018 Spring Meeting & Exhibit (Oral)
- 2018 “*Tailoring Surfaces and Interfaces of Two-Dimensional Material Systems*”, Kavli Institute at Cornell, Cornell University (Oral)
- 2017 “*Surface and Interface Engineering of van der Waals Nanoelectronic Heterostructures (2017)*”, Office of Naval Research Program Review, UC Berkeley (Poster)
- 2017 “*Electronically Abrupt Borophene/organic Lateral Heterostructures*”, American Vacuum Society 64th International Symposium & Exhibition (Oral)
- 2017 “*Van der Waals Heterostructures at the Atomic Scale*”, SPIE NU Chapter (Oral)
- 2017 “*Patterning and Thinning of Black Phosphorus with Scanning Probe Nanolithography*”, American Physical Society March Meeting 2017 (Oral)
- 2016 “*MoS₂/Graphene Heterostructure with Rotational Commensurability*”, American Vacuum Society Prairie Chapter Meeting (Oral)
- 2015 “*Exploring the Thermal Stability of Two-Dimensional Black Phosphorus*”, American Vacuum Society 62nd International Symposium & Exhibition (Oral)
- 2016 “*Rotationally Commensurate MoS₂/Graphene Heterostructure*”, Applied Physics Seminar, Northwestern University (Oral)